

One Decade of Glacier Mass Changes on the Tibetan Plateau Derived from Multisensoral Remote Sensing Data

Dissertation

der Mathematisch-Naturwissenschaftlichen Fakultät
der Eberhard Karls Universität Tübingen
zur Erlangung des Grades eines
Doktors der Naturwissenschaften
(Dr. rer. nat.)

vorgelegt von
Niklas Neckel
aus Aachen

Tübingen
2014

Tag der mündlichen Qualifikation:

21. Juli 2014

Dekan:

Prof. Dr. Wolfgang Rosenstiel

1. Berichterstatter:

Prof. Dr. Volker Hochschild

2. Berichterstatter:

Dr. habil. Tobias Bolch

Contents

Abstract	iii
Zusammenfassung	v
List of Abbreviations	vii
List of Papers	viii
1 Introduction	1
1.1 Motivation	1
1.1.1 Study area	3
1.1.2 Current state of research	5
1.2 Objectives	6
1.3 Structure of the thesis	7
2 Background	8
2.1 Glaciers	8
2.1.1 Measurement of glacier mass balance	10
2.2 International glacier monitoring	12
2.3 Remote sensing	13
2.3.1 Interferometric Synthetic Aperture Radar	15
2.3.2 Laser altimetry	16
2.3.3 Optical stereo photogrammetry	17
3 Research Summary	18
3.1 An overview of the spatial distribution of glacier mass balances on the Tibetan Plateau	18
3.2 Mass balance estimation of a single mountain glacier from ICESat laser altimetry data	19
3.3 Recent mass balance of the Purogangri Ice Cap, Tibet's largest ice cap	20
3.4 Comparing glacier mass balances derived from TanDEM-X and Pléiades data	22
4 Discussion	24

5	Conclusions and outlook	29
	References	31
A	Glacier mass changes on the Tibetan Plateau 2003-2009 derived from ICESat laser altimetry measurements	36
B	Estimation of Mass Balance of the Grosser Aletschgletscher, Swiss Alps, from ICESat Laser Altimetry Data and Digital Elevation Models	54
C	Recent mass balance of the Purogangri Ice Cap, central Tibetan Plateau, by means of differential X-band SAR interferometry	74
D	Glacier variations at Gurla Mandhata (Naimona'nyi), Tibet: a multi-sensoral approach including TanDEM-X, Pléiades and KH-7 Gambit-1	86
	Acknowledgements	107

Abstract

The Tibetan Plateau (TP) with an average altitude of 4,500 meters above sea level is characterized by many glaciers and ice caps. Glaciers are a natural indicator for climate variability in this high mountain environment where meteorological stations are rare or non-existent. In addition, the melt water released from the Tibetan glaciers is feeding the headwaters of the major Asian river systems and contributes to the rising levels of endorheic lakes on the plateau. As many people directly rely on the glacier melt water a continuous glacier monitoring program is necessary in this region. *In situ* measurements of glaciers are important, but are spatial limited due to large logistical efforts, physical constrains and high costs. Remote sensing techniques can overcome this gap and are suitable to complement *in situ* measurements on a larger scale. In the last decade several remote sensing studies dealt with areal changes of glaciers on the TP. However, glacier area changes only provide a delayed signal to a changing climate and the amount of melt water released from the glaciers cannot be quantified. Therefore it is important to measure the glacier mass balance.

In order to estimate glacier mass balances and their spatial differences on the TP, several remote sensing techniques and sensors were synthesized in this thesis. In a first study data from the Ice Cloud and Elevation Satellite (ICESat) mission were employed. ICESat was in orbit between 2003 and 2009 and carried a laser altimeter which recorded highly accurate surface elevation measurements. As in mid-latitudes these measurements are rather sparse glaciers on the TP were grouped into eight climatological homogeneous sub-regions in order to perform a statistical sound analysis of glacier elevation changes. To assess surface elevation changes of a single mountain glacier from ICESat data, an adequate spatial sampling of ICESat measurements need to be present. This is the case for the Grosser Aletschgletscher, located in the Swiss Alps which served as a test site in this thesis.

In another study data from the current TanDEM-X satellite mission and from the Shuttle Radar Topography Mission (SRTM) conducted in February 2000 were employed to calculate glacier elevation changes. In a co-authored study, these estimates could be compared with glacier elevation changes obtained from the current French Pléiades satellite mission. In order to calculate glacier mass balances, the derived elevation changes were combined with assumptions about glacier area and ice density in all studies.

In this thesis contrasting patterns of glacier mass changes were found on the [TP](#). With an [ICESat](#) derived estimate of $-15.6 \pm 10.1 \text{ Gt a}^{-1}$ between 2003 and 2009 the average glacier mass balance on the [TP](#) was clearly negative. However, some glaciers in the central and north-western part of the [TP](#) showed a neutral mass balance or a slightly positive anomaly which was also confirmed by data from the current [TanDEM-X](#) satellite mission. A possible explanation of this anomaly in mass balance could be a compensation of the temperature driven glacier melt due to an increase in precipitation.

Zusammenfassung

Mit einer mittleren Höhe von 4.500 Metern über dem Meeresspiegel weist das tibetische Hochland einen sehr hohen Vergletscherungsgrad auf. Da in den abgelegenen Gebirgsregionen Tibets nur wenige meteorologische Messstationen vorhanden sind, können Gletscher als natürlicher Indikator für Klimaänderungen herangezogen werden. Zudem trägt das Schmelzwasser der tibetischen Gletscher signifikant zu den Quellschüttungen der großen asiatischen Flusssysteme sowie zum Seespiegelanstieg endorheischer Seen auf dem Plateau bei. Dies hat zur Folge, dass viele Menschen direkt von der Gletscherschmelze auf dem Plateau betroffen sind. Eine kontinuierliche Beobachtung der Gletscher ist deshalb von höchster Priorität. Bodenmessungen auf den Gletschern sind zwar wichtig, aber durch die enorme Höhe und Abgeschiedenheit örtlich begrenzt und verbunden mit hohen Kosten und großem logistischen Aufwand. Hier kommt der Fernerkundung eine tragende Rolle zu, da sie in der Lage ist, die räumliche Ausdehnung der Bodenmessungen erheblich zu erweitern. In den letzten Jahren wurden mit Mitteln der Fernerkundung vor allem Flächenänderungen von Gletschern auf dem tibetischen Plateau untersucht. Diese beinhalten allerdings nur ein verzögertes Signal gegenüber Klimaschwankungen und können nicht herangezogen werden, um die Menge des freigewordenen Schmelzwassers zu quantifizieren. Daher ist es wichtig, die Gletschermassenbilanzen zu untersuchen.

In dieser Doktorarbeit wurden unterschiedliche Fernerkundungsansätze miteinander verknüpft, um die Gletschermassenbilanzen auf dem tibetischen Plateau zu erfassen und ihre räumlichen Unterschiede zu quantifizieren. In einer ersten Studie wurden Daten von der Ice Cloud and Elevation Satellite ([ICESat](#)) Mission ausgewertet. Der mit einem hoch genauen Laseraltimeter ausgestattete Satellit war zwischen 2003 und 2009 im Einsatz. Da in den mittleren Breiten die Datendichte der [ICESat](#) Mission begrenzt ist, wurden die Gletscher auf dem Plateau in acht klimatologisch einheitliche und statistisch repräsentative Gruppen zusammengefasst. Um Höhenänderungen für einzelne Gletscher aus [ICESat](#) Messungen abzuleiten, muss eine gewisse räumliche Verteilung der Messungen auf dem Gletscher gewährleistet sein. Dies ist beim großen Aletschgletscher in den Schweizer Alpen der Fall, der in dieser Arbeit als ein Testgebiet gewählt wurde.

In einer weiteren Studie wurden Daten der Shuttle Radar Topography Mission ([SRTM](#)) von 2000 mit Daten der aktuellen [TanDEM-X](#) Mission verglichen, um so die Gletscherdickenänderungen zwischen 2000 und 2012 zu quantifizieren. In einer Studie mit Co-

Autorenschaft konnten diese Ergebnisse noch um Daten der aktuellen französischen Pléiades Satellitenmission erweitert werden. Aus den berechneten Gletscherdickenänderungen der einzelnen Studien konnten unter Annahmen über Gletschergrenzen und Eisdichte Gletschermassenbilanzen berechnet werden.

Die Haupteckentnis dieser Doktorarbeit ist, dass sich die Gletschermassenbilanzen auf dem tibetischen Plateau räumlich deutlich unterscheiden. Zwar sind die mittleren Abschmelzraten von $-15.6 \pm 10.1 \text{ Gt a}^{-1}$ abgeleitet von den Daten der ICESat Mission zwischen 2003 und 2009 deutlich negativ, aber gerade im zentralen und nordwestlichen Teil des Plateaus wurden ausgeglichene oder leicht positive Massenbilanzen berechnet. Diese Anomalie, die auch durch die TanDEM-X Daten bestätigt wird, könnte mit einer Kompensation der Temperatur getriebenen Gletscherschmelze durch höhere Niederschlagsraten zusammenhängen.

List of Abbreviations

AR	Assessment Report
CGI	Chinese Glacier Inventory
CNES	French Space Agency
CoSSC.....	Co-registered Single look Slant range Complex
DEM	Digital Elevation Model
DGPS	Differential Global Positioning System
DInSAR.....	Differential Interferometric Synthetic Aperture Radar
DLR.....	German Aerospace Center
ELA	Equilibrium Line Altitude
ERS	European Remote Sensing Satellite
ERTS.....	Earth Resources Technology Satellite
GLAS	Geoscience Laser Altimeter System
GLIMS	Global Land Ice Measurements from Space
GLOF	Glacial Lake Outburst Flood
GRACE	Gravity Recovery and Climate Experiment
HAR.....	High Asia Reanalysis
ICESat	Ice Cloud and Elevation Satellite
InSAR.....	Interferometric Synthetic Aperture Radar
IPCC	Intergovernmental Panel on Climate Change
NASA	National Aeronautics and Space Administration
NSIDC	National Snow and Ice Data Center
PIC.....	Purogangri Ice Cap
RAR.....	Real Aperture Radar
RGI	Randolph Glacier Inventory
SAR	Synthetic Aperture Radar
SRTM	Shuttle Radar Topography Mission
TanDEM-X.....	TerraSAR-X add-on for Digital Elevation Measurements
TP	Tibetan Plateau
WET	Variability and Trends in Water Balance Components of Benchmark Drainage Basins on the Tibetan Plateau
WGMS	World Glacier Monitoring Service

List of Papers

This cumulative doctoral thesis is based on the following papers. Next to each paper, the authors contribution is highlighted.

- [Paper A](#)

Neckel, N., Kropáček, J., Bolch, T., and Hochschild, V. (2014). Glacier mass changes on the Tibetan Plateau 2003 – 2009 derived from ICESat laser altimetry measurements. *Environmental Research Letters*, 9(1):014009.

Author contribution: study design, data preparation, data analysis, figures and writing.

- [Paper B](#)

Kropáček, J., Neckel, N., and Bauder, A. (2014). Estimation of Mass Balance of the Grosser Aletschgletscher, Swiss Alps, from ICESat Laser Altimetry Data and Digital Elevation Models. *Remote Sensing*, 6(6):5614–5632.

Author contribution: contribution to the study design, contribution to the data preparation and data analysis, contribution to the writing.

- [Paper C](#)

Neckel, N., Braun, A., Kropáček, J., and Hochschild, V. (2013). Recent mass balance of the Purogangri Ice Cap, central Tibetan Plateau, by means of differential X-band SAR interferometry. *The Cryosphere*, 7(5):1623–1633.

Author contribution: study design, data preparation, data analysis, figures and writing.

- [Paper D](#)

Holzer, N., **Neckel, N.**, Buchroithner, M., Gourmelen, N., Colin, J., and Bolch, T. (2014). Glacier variations at Gurla Mandhata (Naimona'nyi), Tibet: a multi-sensoral approach including TanDEM-X, Pléiades and KH-7 Gambit-1. *Remote Sensing of Environment*, in review.

Author contribution: contribution to the study design, Synthetic Aperture Radar ([SAR](#)) data analysis, contribution to the writing.

1 Introduction

1.1 Motivation

Glaciers outside the polar regions are located in mountainous regions and have a large influence on the physical and anthropogenic processes in these areas. Amongst others, glaciers release melt water, are modeling mountain valleys, are affecting the local climate and are adjusting their shape to the prevailing climatic conditions (Cuffey and Paterson, 2010). Mountain glaciers are often located at the headwaters of major river systems and are seasonally affecting their discharge regimes. At the rivers upper reaches the glacier melt water contribution is large, particularly during warm and dry seasons, but decreases further downstream where the river discharge relies more on the amount and seasonality of precipitation. As many people are living along rivers they depend to a varying extent on the water released from glaciers (Kaser et al., 2010; Immerzeel et al., 2010). Furthermore, glaciers react very sensitive to changes in air temperature and precipitation and their changes are considered to be a key indicator for climate variability. Monitoring of glaciers is therefore very important in mountainous regions where meteorological stations are rare or non-existent. While changes in glacier length and area show only a delayed signal to climate variability, the glacier mass balance shows the immediate reaction to climatic changes (e.g. Haeberli, 2011).

In order to asses the amount of melt water released from the glaciers, to estimate their contribution to the global sea-level rise and to study the climate variability on the TP it is important to adequately estimate the mass balance of Tibetan glaciers. However, *in situ* measurements of glacier mass balances are sparse on the TP (Yao et al., 2012) and glacier volume changes and their environmental impact need much more investigation (Kang et al., 2010). The rapid development of remote sensing sensors and associated techniques makes this possible. The great advantage of satellite derived mass balance measurements over *in situ* mass balance measurements is the ability to map glacier elevation changes of large areas in remote regions (Cuffey and Paterson, 2010; Haeberli, 2011). Recent remote sensing studies show the great potential of deriving mass balances of mountain glaciers from optical stereo photogrammetry (e.g. Bolch et al., 2011; Gardelle et al., 2013; Pieczonka et al., 2013)

or laser altimetry (Kääb et al., 2012; Bolch et al., 2013; Gardner et al., 2013) and at the first time remote sensing estimates of glacier mass balances are included in the Intergovernmental Panel on Climate Change (IPCC) Assessment Report (AR) (Vaughan et al., 2013). In this context the Variability and Trends in Water Balance Components of Benchmark Drainage Basins on the Tibetan Plateau (WET) project¹ was initiated in 2011, combining numerical models and satellite observations in order to investigate the coupling of climate and hydrological cycles on TP. This thesis took place within the WET project and focuses on glacier mass balances on the TP derived from multisensoral remote sensing data.

¹more information about the WET project is available on the web via: www.klima.tu-berlin.de/forschung/WET/home.php

1.1.1 Study area

With an average altitude of 4,500 m above sea level and an area of 2.5 million km², the TP is the highest and largest plateau on earth (e.g. Mäder, 1997; Ludwig, 2010). The TP is located between 28-38°N and 80-102°E with a south-to-north extension of 800 km and an east-to-west extension of 1,600 km. On the relatively flat plateau relief gradients of more than 1,000 m are rare and are only found at some mountain ranges such as the Tanggula Mountains, the Nyainqentanglha Range and the Transhimalaya (Miehe, 2004). While parts of the central plateau are draining into endorheic lakes, also the large Asian rivers Indus, Brahmaputra, Salween, Mekong, Yangtze and Huang He are originating on the TP (Figure 1.1).

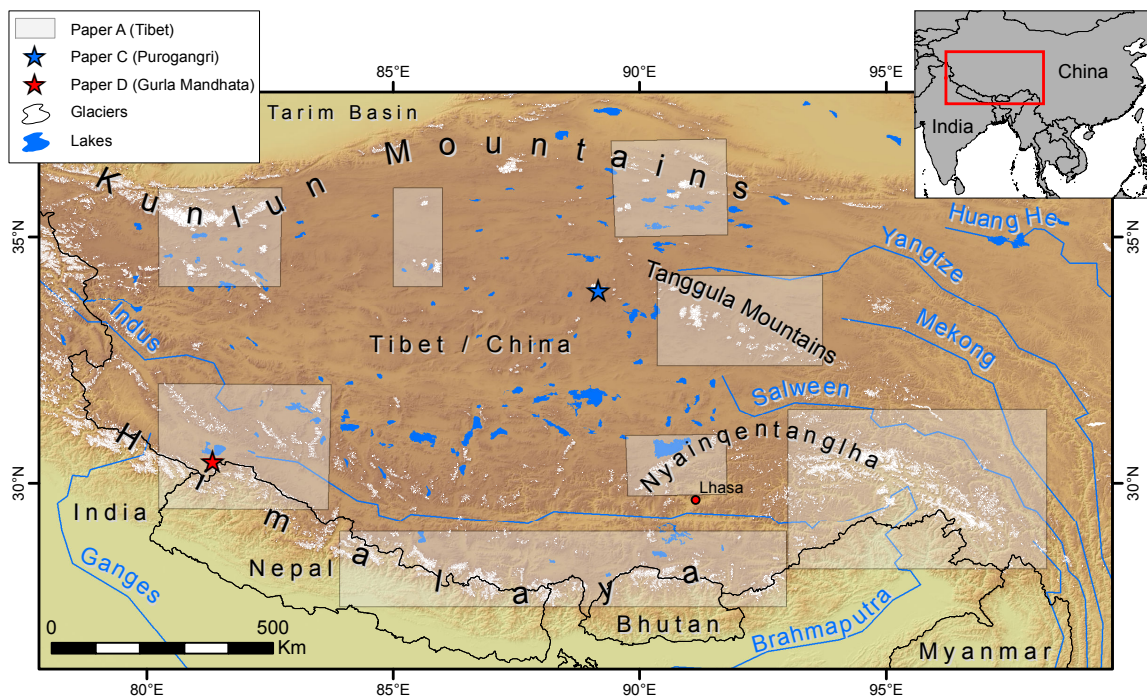


Figure 1.1: Overview of the Tibetan Plateau (TP). Geographic locations of mass balance estimates derived in the thesis papers² are shown next to the places and landmarks mentioned in the text. Glacier outlines are based on the Randolph Glacier Inventory (RGI) (Pfeffer et al., 2014).

With its great altitude the TP is a major topographic barrier and influences the atmospheric circulation at a large scale. It affects the position and magnitude of the

²except for the methodical Paper B which is located in the Swiss Alps.

westerly jet (e.g. Schiemann et al., 2009) and is important for the development of the Asian summer monsoon (e.g. Yihui and Chan, 2005). During winter the climate on the TP is mostly dry, with relatively slight orographic precipitation in some parts of western Tibet (Figure 1.2a). During summer a heat low is characteristic for the TP while the monsoonal depression develops over India. Summer precipitation is concentrated on the eastern part of the plateau while the western TP remains mostly dry (Figure 1.2b). Mean annual precipitation rates reach from less than 50 mm a⁻¹ in the Tarim Basin to more than 6,000 mm a⁻¹ in the foothills of the south-eastern Himalayas (e.g. Böhner, 2006; Maussion et al., 2014). A strong gradient is also found for the mean annual temperatures which reach from 7.7°C in Lhasa at an altitude of 3,490 m to well below 0°C in the northern part of the plateau at an altitude higher than 4,500 m (Miehe et al., 2001).

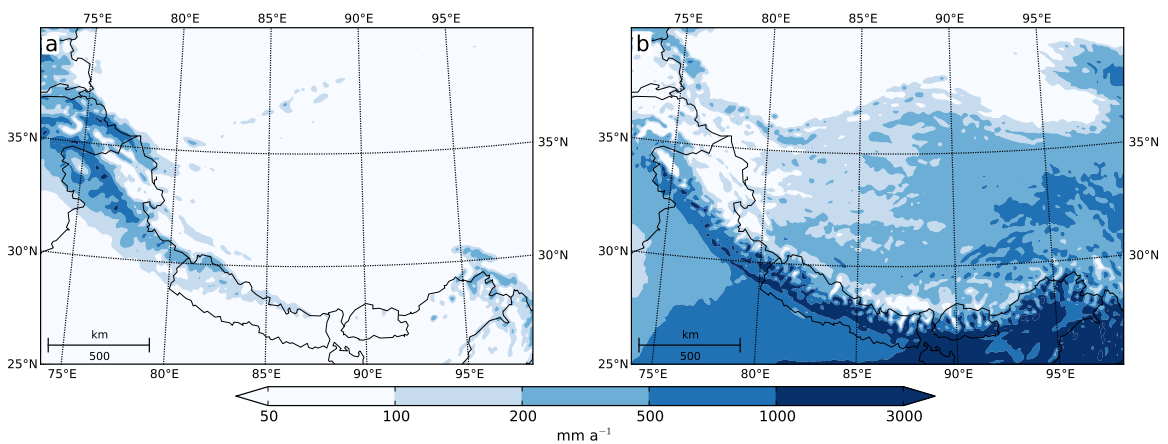


Figure 1.2: Mean December, January, February precipitation (a) and mean June, July, August precipitation (b) between 2001 and 2012 as resolved by the 10 km High Asia Reanalysis (HAR) domain (Maussion et al., 2014).

The temporal pattern in precipitation is also found in the accumulation regime of Tibetan glaciers. While glaciers in the central part of the plateau are accumulating mass predominantly in summer, glaciers in western Tibet receive most snowfall in winter (Maussion et al., 2014). Also different types of glaciers are developing under the different climate regimes. Glaciers in the south-eastern part of the plateau are of maritime type with a temperate thermal regime, while glaciers in the north-western part are of continental type with a cold thermal regime (Shih et al., 1980; Huang, 1990).

1.1.2 Current state of research

First scientific observations of glaciers in High Asia probably date back to the Schlagintweit brothers who investigated glaciers in the Himalaya, Karakoram and Kunlun Mountains during the years 1854 to 1857 (Kick, 1960). In the later 19th and early 20th century several cartographic expeditions were carried out on the TP, which also give some descriptive information about glaciers on the plateau (e.g. Ryder, 1908; Ward and Smith, 1934). In the 1960s Chinese glaciologists started observations on several Tibetan glaciers and conducted some statistical and inventory work (Li and Cheng, 1980). The first Chinese Glacier Inventory (CGI) was initiated in 1979 and internationally published in 2008 (Shi et al., 2009). Today, the glacier area on the TP is estimated between 40,000 km² and 50,000 km², depending on the used glacier inventory and the definition of the Tibetan border (Shi et al., 2009; Zhang et al., 2011; Kang et al., 2010; Pfeffer et al., 2014). Since the 1990s most of the Tibetan glaciers retreated, although some glaciers have advanced (Kang et al., 2010). Several studies revealed heterogeneous patterns of glacier area and length changes on the plateau from satellite imagery, historical maps and aerial photographs dating back to the 1950s (e.g. Ding et al., 2006; Wei et al., 2014). While glaciers on the central and north-western TP were relatively stable or even advancing, glaciers in the south-eastern part of the plateau showed a more rapid retreat. For the western Nyaiqentanglha Range Bolch et al. (2010b) found a decrease in glacier area of $6.1 \pm 3\%$ between 1976 and 2001 from satellite imagery. Significantly smaller rates of glacier area changes were reported for the western Kunlun Mountains, located in the north-western part of the plateau. For this region Shangguan et al. (2007) found a decrease in glacier area of 0.4% between 1970 and 2000 by comparing glacier inventory data with more recent Landsat imagery. These regional differences were also confirmed by Yao et al. (2012) who measured glacier area changes of 82 glaciers between ~ 1970 and ~ 2000 and *in situ* mass balances of 15 glaciers between 2006 and 2010. In a recent study, global glacier mass changes were estimated by combining *in situ* mass balance measurements, data from the Gravity Recovery and Climate Experiment (GRACE) and ICESat data (Gardner et al., 2013). On the TP Gardner et al. (2013) calculated glacier mass balances from ICESat data acquired between 2003 and 2009. Their results show similar regional patterns as the results from Yao et al. (2012), with slightly positive mass balances in the western Kunlun Mountains and the strongest mass loss in the eastern Himalayas (Gardner et al., 2013).

The retreat of glaciers is also reflected in the hydrology of the TP. Several recent studies employed satellite altimetry data to estimate lake-level changes on the TP (Zhang et al., 2011; Kropáček et al., 2012; Phan et al., 2012; Zhang et al., 2013). In total, an average lake-level rise between 0.20 and 0.25 m a⁻¹ was observed on the TP between 2003 and 2009 (Zhang et al., 2011; Phan et al., 2012). Recent studies also reported about increased river discharges (e.g. Yao et al., 2004; Immerzeel et al., 2009)

and an enhancement of glacial debris flows and Glacial Lake Outburst Flood (GLOF) events (Kang et al., 2010). However, the hydrology on the TP is also influenced by changes in snow cover, precipitation and evapotranspiration which are difficult to separate from the signal of glacier changes (e.g. Immerzeel et al., 2009; Zhang et al., 2013). To adequately estimate the amount of melt water released from the Tibetan glaciers, it is important to investigate the current changes in glacier volume in much more detail (Ding et al., 2006; Kang et al., 2010).

1.2 Objectives

The main objective of this thesis is the quantification and interpretation of recent glacier volume and mass changes on the TP and their spatial variability. These results will help to better understand the effects of a changing climate to the water balance on the plateau. Furthermore, the contribution to the global sea-level rise from a large portion of Tibetan glaciers is estimated. Additionally, it is investigated to which amount the observed rise of the local lake levels is induced by glacier melt water.

For this purpose different recent remote sensing datasets and techniques are employed allowing to compare and to discuss the different approaches. First, the suitability of ICESat laser altimetry to derive glacier elevation changes of mountain glaciers is tested. The methodology is proofed at the Grosser Aletschgletscher, located in the Swiss Alps and transferred to the TP in another study. Also the potential of the current TanDEM-X satellite mission to derive geodetic glacier mass balances is proofed for the first time in this thesis. TanDEM-X data are employed at the Purogangri study site and are compared to Pléiades data in a co-authored study at the Gurla Mandhata study site (Figure 1.1). These local results are compared with the Tibet wide ICESat derived mass balance estimates. Furthermore, the remote sensing results are compared to the few existing *in situ* mass balance measurements on the TP (Yao et al., 2012).

Changes in glacier mass balance are closely connected to climate variability. However, as long-term meteorological measurements are sparse on the plateau only some general suggestions concerning the connection between glacier mass balances and climatic forces are made in this thesis.

1.3 Structure of the thesis

This thesis is build on four peer-reviewed papers all addressing, to a varying extent, the objectives described above. Figure 1.1 gives an overview of the study area, including geographic regions for which mass balances could be derived in this thesis.

- **Chapter 1, Introduction** highlights the environmental importance of the topic and gives a short overview of the study area, the current state of research, the objectives and the structure of the thesis.
- **Chapter 2, Background** gives a short introduction on glaciers and mass balance measurements, international glacier monitoring and the applied remote sensing techniques.
- **Chapter 3, Research Summary** gives an overview of the main results of the four papers included in this thesis.
- **Chapter 4, Discussion** discusses the remote sensing techniques applied in this thesis and integrates the results into the wider context of the current environmental research on the TP.
- **Chapter 5, Conclusions and outlook** concludes the thesis and gives an outlook on future and ongoing research, concerning mass balance measurements from remote sensing data with special focus on the TP.

This framework is followed by the four peer-reviewed papers, which are reproduced as published in the respective journal³.

³except for Paper D which is still in review.

2 Background

2.1 Glaciers

Approximately 10% of the earth surface is covered by glacier ice which stores around 75% of the world's freshwater resources (Jansson et al., 2003; Vaughan et al., 2013). The majority of this enormous ice mass is located in the large ice sheets of Greenland and Antarctica. Compared to the polar ice sheets mountain glaciers are comparatively small. However, as they are located in regions with human activity they have, to a varying extent, a direct influence on the local population. The meltwater released from glaciers is used for agricultural and industrial purposes and is an important source for hydropower. Glacial Lake Outburst Floods (GLOFs) and ice/snow avalanches are serious hazards for mountain communities and changes in glacier volume can lead to water resource problems and local lake-level changes (e.g. Richardson and Reynolds, 2000; Kropáček et al., 2012). On a global scale, glaciers are a major contributor to the observed sea-level rise. Between 2003 and 2009 all glaciers globally contributed with 0.71 [0.64 to 0.79] mm a⁻¹ to the global sea-level rise (Church et al., 2013).

In general, a glacier is defined as a “[...] *compact ice mass on land that forms through the recrystallization of snow and moves forward under its own weight. Glaciers form over many years of packed snow in areas where more snow accumulates than it melts.*” (Dobhal, 2011, p. 376). The morphology of a glacier is a function of climate and topography and each glacier on earth is adapted to its very specific geographic location (Benn and Evans, 2010). Besides the two large ice sheets covering Greenland and Antarctica, glaciers can be distinguished into ice caps and mountain glaciers. *Ice caps* are most common in regions with polar to sub-temperate climate conditions and can cover a whole mountain system (Bhutiyani, 2011). The ice of ice caps moves from the interior to the outer regions where faster moving outlet glaciers are common (Benn and Evans, 2010). Compared to ice caps *mountain glaciers* are relatively small. A typical form of a mountain glacier is a valley glacier which forms when ice is discharged into a mountain valley. A prominent example of a valley glacier is the Grosser Aletschgletscher in the Swiss Alps, which was used as a test site in Paper B. Whether a glacier is gaining or losing mass can be treated as a direct response of

the glacier to climate conditions. The glacier mass balance is therefore considered as a key indicator for climate change (e.g. [Haeberli, 2011](#)). Accumulation of mass is mostly related to snowfall while ablation is mainly due to the melting of snow and ice. However, processes such as avalanches, wind drift, deposition, refreezing of meltwater and sublimation of snow and ice can also influence the mass balance of a glacier ([Cuffey and Paterson, 2010](#)). Glacier mass balance is strongly correlated with air temperature and therefore with altitude. While ablation is highest at the lowest part of a glacier it turns to accumulation at higher elevations. The average altitude where accumulation equals ablation over a one-year period is called the Equilibrium Line Altitude (ELA) and separates the accumulation area from the ablation area. The ELA can be treated as a local climate indicator as it reacts very sensitive to changes in air temperature and precipitation. If the annual mass balance of a glacier is positive the ELA moves to a lower altitude, while it rises if the annual mass balance is negative. The ELA is in a steady-state when the annual glacier mass balance is zero, meaning that the glacier mass and geometry are in balance with the prevailing climate conditions ([Bakke and Nesje, 2011](#)).

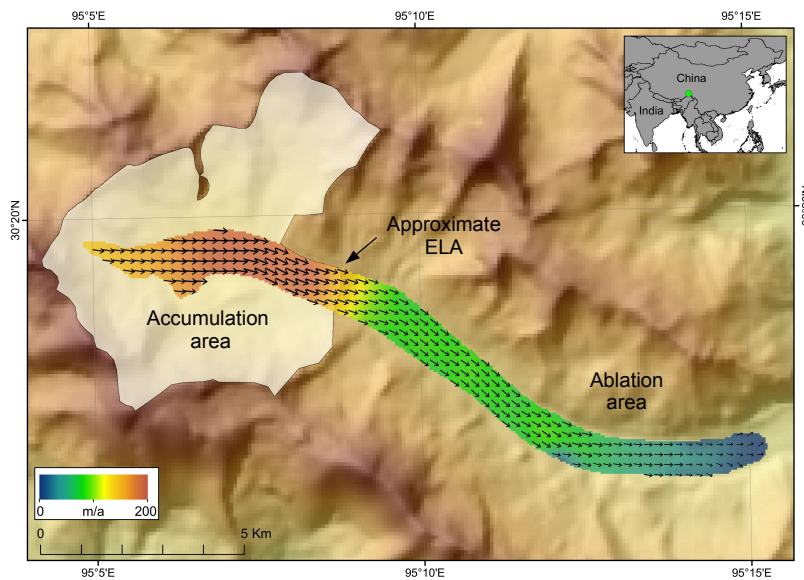


Figure 2.1: TerraSAR-X derived surface velocities of Zepu Kangri glacier located in south-eastern Tibet are shown next to the approximate accumulation area, ablation area and Equilibrium Line Altitude (ELA). A standard deviation of 2.5 m a^{-1} is estimated for the off-glacier displacements which can be used as an error estimate for the derived surface velocities.

Due to gravitational forces and stresses induced by their ice thickness, glaciers flow downhill. This way, the glacier transports ice from the accumulation area to the ablation area in order to maintain in a steady-state. Hereby the ice velocity increases

upstream of the equilibrium line (Figure 2.1) having a downward component and decreases towards the glacier terminus having an upward component (Nye, 1957; Bridge and Demicco, 2008). In general, two mechanisms of glacial flow can be distinguished. (1) *Viscous-plastic deformation of ice* is characterized by laminar flow with a decreasing vertical velocity profile. (2) *Basal slip mechanisms* occur at the margin between the ice and the underlying bed. For this, a slip plane needs to be present, which can be a thin layer of water or a deformable bed, on which the ice starts to slide (Cuffey and Paterson, 2010). How these two main mechanisms of ice motion combine is highly dependent on the thermal properties of the ice and the properties of the underlying bed. Plastic deformation of ice produces relatively slow ice fluxes, whereas basal slip mechanisms enable faster flow velocities. A special form of glacier movement which is common for cold based glaciers is the *Block-Schollen* movement (Battle, 1951). Here the glacier moves *en bloc* over its entire width disintegrating into a scattered mosaic. Also a *glacier surge* is a special form of glacier motion, which describes a sudden advance of a glacier at much higher velocities than the average. Impressive examples of surge-type glaciers are found in the Karakoram (e.g. Hewitt, 2005; Rankl et al., 2014), but are also common in other parts of High Asia.

2.1.1 Measurement of glacier mass balance

The mass balance of a glacier can be determined by several methods. In the following the most important methods will be described briefly with the main focus on the altimetric or geodetic approach which was employed in this thesis.

(1) The direct or glaciological method uses a network of *in situ* accumulation and ablation measurements along the glacier surface (Cuffey and Paterson, 2010; Haeberli, 2011). In order to measure the amount of accumulation, the snow thickness and density is measured in several snow pits in the accumulation area. Additionally, the spatial distribution of accumulation is often mapped by snow probing (Fischer, 2011). The amount of ablation is measured by reading stakes which are drilled into the ice of the ablation area multiplied by the density of ice. The results of all measurements are interpolated over the entire glacier area. To determine the annual mass balance, measurements are mostly taken at the end of the ablation period (Fischer, 2011; Haeberli, 2011).

(2) The hydrological method is based on the subtraction of runoff and evapotranspiration from the precipitation of a glacierized catchment area. The amount of precipitation is estimated from meteorological station data or models while runoff is taken from nearby gauging stations. In the hydrological method large errors can arise due to the extrapolation of point measurements to the whole catchment area

and large distances between the glacier and the next gauging station (Hagg et al., 2004; Cuffey and Paterson, 2010).

(3) The gravitational method uses small changes in the gravity field of the earth to estimate mass changes of glaciers. For this purpose, data from the GRACE satellite mission is employed which was launched in 2002 (e.g. Jacob et al., 2012; Gardner et al., 2013). However, the coarse spatial resolution and difficulties in separating the glaciological from the hydrological signal and the glacial isostatic adjustment induces high uncertainties on the TP (e.g. Jacob et al., 2012).

(4) The altimetric or geodetic method uses two topographic datasets acquired at different times in order to calculate the temporal changes in glacier surface elevation. As the elevation change at one point on the glacier surface is a combination of mass balance and ice flow, geodetic mass balances are only valid when integrated over the total glacier area. For the conversion from volume to mass changes an assumption about the materials density which is gained or lost is required. This value is difficult to determine as the density of the glacier surface varies in time and space and can range between 100 kg m^{-3} (damp new snow) and 917 kg m^{-3} (glacier ice) (Cuffey and Paterson, 2010; Fischer, 2011). Following Sorge's law (Bader, 1954) many studies make use of a constant conversion factor of 900 kg^{-3} (e.g. Rignot et al., 2003; Berthier et al., 2010; Bolch et al., 2011; Pieczonka et al., 2013) assuming that only ice is lost or gained. Other authors use different conversion factors for different zones of the glacier (e.g. Berthier et al., 2007; Käab et al., 2012) or are employing a firn compaction model above the ELA (e.g. Sørensen et al., 2011; Bolch et al., 2013). Based on a firn compaction model adapted for mountain glaciers, Huss (2013) suggests a conversion factor below the ice density. For glaciers under certain conditions, i.e. with a stable mass balance gradient, the presence of a firn area and significant volume changes in a time period of at least five years, Huss (2013) proposed a conversion factor of $850 \pm 60 \text{ kg m}^{-3}$. This best estimate was also used by Fischer (2011) who compared the geodetic mass balance of six Austrian glaciers with *in situ* measured mass balances concluding that a constant conversion factor might be the main uncertainty in the geodetic approach.

2.2 International glacier monitoring

Glaciers were early recognized as natural indicators for climate variability. Therefore, a worldwide monitoring program about ongoing glacier changes was initiated in 1894 (Haeberli, 1998). Since then a comprehensive dataset on glacier variations is developing. Standardized observations on changes in glacier mass, volume, area and length are collected by the World Glacier Monitoring Service (WGMS) and are distributed on the web via <http://www.wgms.ch>. Furthermore, statistical information on the spatial distribution of glaciers all over the world are collected by the WGMS in close cooperation with the National Snow and Ice Data Center (NSIDC) and the Global Land Ice Measurements from Space (GLIMS) initiative. So called glacier inventories are important for various reasons. They form the basis for modeling the future development of glaciers and are essential to calculate glacier mass changes and volumes which are crucial to estimate the actual and potential glacial contribution to the global sea-level rise. The recently published RGI is the first complete inventory of all glaciers on earth except for the polar ice sheets including $\sim 198,000$ glaciers with a total extent of $726,800 \pm 34,000$ km² (Pfeffer et al., 2014). While the expertise of the WGMS is traditionally on *in situ* measurements of glaciers, GLIMS and NSIDC have their focus primarily on remote sensing of glaciers and the associated data management (WGMS, 2014).

2.3 Remote sensing

In general, remote sensing includes all techniques which are able to collect information from an object without being in direct contact with the object under investigation (e.g. Lillesand et al., 2007; Rees and Pellikka, 2010). For this, remote sensing relies on electromagnetic energy transmitted and/or acquired at a specific wavelength (Figure 2.2). Remote sensing, as used in this thesis, can further be restricted to sensors mounted on airborne and space-borne platforms. First aerial photographs date back

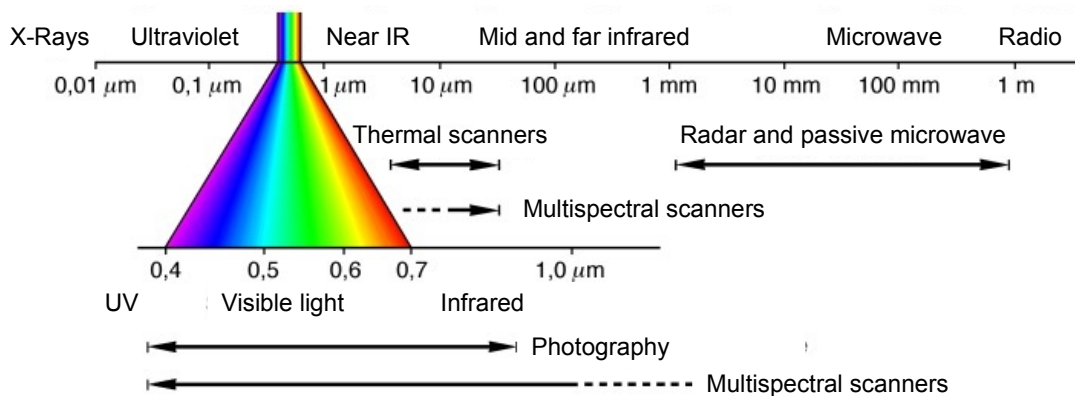


Figure 2.2: Electromagnetic spectrum as covered by common remote sensing systems. Modified after [Albertz \(2009\)](#).

to 1858 and were taken from a hot-air balloon over Paris ([Albertz, 2009](#)). Passive remote sensing, which uses only the natural radiation, advanced from aerial photography in order to obtain more information from other parts of the electromagnetic spectrum. Sensors were soon mounted on airplanes and active remote sensing sensors, which are actively transmitting an electromagnetic signal, developed after the invention of the radar during World War II ([Rees and Pellikka, 2010](#)). First remote sensing experiments from space-borne platforms date back to the American Apollo program in the 1960s ([Albertz, 2009](#)). The probably most significant development for geoscience was the launch of the first Landsat satellite in 1972. Landsat, alias Earth Resources Technology Satellite (ERTS), was the first satellite in orbit which systematically acquired repetitive, medium resolution multispectral data ([Lillesand et al., 2007](#)). Since then the Landsat family provides continuous multispectral satellite data in its currently eighth generation. For glaciology, the Landsat archive is one of the most important primary data sources ([Bindschadler et al., 2001](#)). Amongst others, Landsat data is routinely employed for glacier inventories ([Bolch et al., 2010a,b](#); [Frey et al., 2012](#); [Pfeffer et al., 2014](#)), ELA monitoring (e.g. [Bindschadler et al., 2001](#)), measurements of glacier area changes and length changes (e.g. [Ding et al., 2006](#); [Bolch](#)

et al., 2010b; Wei et al., 2014) as well as for estimating glacier surface velocities (Heid and Kääb, 2012). For the semi-automatic classification of glaciers the start of the Landsat Thematic Mapper Mission in 1982 is important to notice. With its seven multispectral bands between 0.45 μm and 2.35 μm wavelength, band ratios are routinely applied to map clean ice and snow areas (e.g. Bolch et al., 2010a; Frey et al., 2012).

Space-borne radar remote sensing started with the launch of Seasat in 1978. The Seasat mission lasted only for 99 days due to a system failure, but showed the great potential of space-borne SAR for various applications in geoscience (Lillesand et al., 2007). A SAR system is an imaging radar system which stores the intensity and phase information of the backscattered signal in a two-dimensional array. Only SAR systems are used on space-borne platforms, as the along-track resolution of Real Aperture Radar (RAR) systems is strongly dependent on the aperture angle, which increases with the distance between the sensor and the ground. As the aperture angle is a function of the wavelength and the antenna length, a very long antenna would be needed to improve the angular resolution and hence the along-track resolution of a space-borne RAR (e.g. Lillesand et al., 2007; Albertz, 2009). Therefore, a SAR synthesizes a long radar antenna by constantly transmitting radar pulses while moving over a target on the ground. During the SAR processing the overlapping footprints are coherently stacked taking into account the Doppler history of the individual ground targets.

The great advantage of a SAR is the ability to map in all weather conditions during all daytimes. However, the side-looking geometry of a SAR can cause some problems when working in mountainous terrain such as the TP. Due to the side-looking geometry, the radar backscatter from higher elevations (e.g. mountain tops) is received earlier than from lower elevations. In the resulting SAR image slopes facing in the direction of the SAR are appearing shortened (foreshortening) and higher elevations can superimpose the surrounding part of the scene (layover) (e.g. Rott, 2009; Shugar et al., 2010).

Similar as optical remote sensing data, SAR images are widely used in glaciology. For example can SAR images be used to derive glacier outlines, to detect different glacier facies and to derive glacier surface velocities by means of feature or speckle tracking. The latter is shown in Figure 2.1, where surface velocities were derived from two TerraSAR-X Stripmap scenes, acquired in 2008 and 2009 over the south-eastern part of the TP. In this example, surface velocities could be derived by image cross-correlation techniques employing the freely available IMCORR software (Scambos et al., 1992). Another powerful SAR technique is Interferometric Synthetic Aperture Radar (InSAR) which will be described in the next section.

2.3.1 Interferometric Synthetic Aperture Radar

Today **InSAR** is routinely employed for a wide range of applications in geoscience. In glaciology it is mainly used to derive surface velocities and topographical information of glaciers, ice caps, ice sheets and ice shelves (e.g. [Kwok and Fahnestock, 1996](#); [Joughin et al., 1998](#); [Drews et al., 2009](#); [Neckel et al., 2012](#)). **InSAR** uses the difference in phase information of two **SAR** acquisitions. The interferometric phase is a precise measurement of the difference in path length between both data takes, where the path length is the distance between the **SAR** and the illuminated target. The geophysical information of the interferometric phase is strongly related to the acquisition setup of the **SAR** sensors. The interferometric phase of a single-pass system such as TerraSAR-X and its add-on for Digital Elevation Measurements (**TanDEM-X**) is induced by the different viewpoints of the satellites and hence by the surface topography. The interferometric phase of a repeat-pass system includes additional information such as the surface displacement between the dates of data acquisition. A prominent example of a repeat-pass **InSAR** satellite mission is the European Remote Sensing Satellite (**ERS**) tandem mission which was conducted between 1995 and 1996 with an acquisition interval of one day (e.g. [Kramer, 2002](#)). For **InSAR** to work it is essential that the phase of the target remains stable in both **SAR** acquisitions. This assumption is normally met for single-pass systems with an adequate baseline configuration, but temporal decorrelation of the phase is a critical issue for repeat-pass acquisitions. Due to this fact, single-pass systems are preferable for topographic mapping (e.g. [Rott, 2009](#)). In this thesis data from two single-pass **InSAR** missions were employed to map the topography of Tibetan glaciers.

(1) The **SRTM** was conducted during 11 days in February 2000, resulting in two almost global Digital Elevation Models (**DEMs**) ([Rabus et al., 2003](#); [Farr et al., 2007](#)). One **DEM** was acquired in C-band with a wavelength of 5.6 cm and a carrier frequency of 5.3 GHz and is available at a grid posting of three arc seconds. The other **DEM** was acquired in X-band with a wavelength of 3.1 cm and a carrier frequency of 9.3 GHz and is available at a spatial resolution of one arc second ([Hoffmann and Walter, 2006](#)). As the X-band **SAR** system was operated with a swath width of 45 km it shows large data gaps when compared to the C-band **DEM** which was acquired with a swath width of 225 km ([Rabus et al., 2003](#); [Farr et al., 2007](#)).

(2) The **TanDEM-X** satellite mission is still in orbit but experimental Co-registered Single look Slant range Complex (**CoSSC**) images were available to the author through proposal *XTI_GLAC1054*. TerraSAR-X was launched in June 2007 followed by its twin satellite **TanDEM-X** in June 2010. Both satellites are equipped with a X-band **SAR** system and are run by the German Aerospace Center (**DLR**). The data used in this thesis were acquired in bistatic mode, i.e. with one transmitting antenna and two antennas simultaneous receiving the backscattered signal (Figure 2.3a). Out of the interferometric phase of these **SAR** images **DEMs** with a high spatial resolution could

be derived and compared to the [SRTM DEMs](#) in order to map temporal variations in glacier thickness.

2.3.2 Laser altimetry

Laser altimetry is an active remote sensing technique which measures the two-way travel time of an emitted light pulse which is reflected at the surface. Similar to [InSAR](#) it is routinely employed in geoscience to derive surface elevations. For this purpose laser altimeters are operated from airborne and space-borne platforms. In this thesis data from the Geoscience Laser Altimeter System ([GLAS](#)) mounted on-board the [ICESat](#) were employed (Figure 2.3b). The [ICESat](#) mission was conducted between 2003 and 2009 by the National Aeronautics and Space Administration ([NASA](#)). During its 18 campaigns large amounts of elevation measurements were acquired by the [GLAS](#). The laser channel for surface altimetry operates at a wavelength of 1064 nm. Laser footprints on the ground are spaced at about 172 m along track and have a diameter of about 70 m (e.g. [Zwally et al., 2002](#); [Brenner et al., 2003](#); [Schutz et al., 2005](#)). Surface elevations are obtained from the maximum peaks of Gaussian functions fitted to the returned signals of the footprints. Several [ICESat](#) data products are freely available via the [NSIDC](#). Due to the rough surface of mountain glaciers only the GLA 14 data product was employed in this thesis. In the GLA 14 product the surface elevation is derived from an average of up to six Gaussian fits to account for rougher land surfaces (e.g. [Kääb, 2008](#)). The [ICESat](#) mission was originally intended to measure elevation changes of the Greenland and Antarctic ice sheets ([Zwally et al., 2002](#)). Consequently, several methods were developed to derive time series of [ICESat](#) elevation changes in the polar regions (e.g. [Brenner et al., 2007](#); [Slobbe et al., 2008](#); [Moholdt et al., 2010](#)). When working with [ICESat](#) data on mid-latitude glaciers additional problems arise. (1) The data sampling is sparser than in the polar regions due to orbital constraints. (2) Repeat-tracks can be separated by several hundred meters as [ICESat](#)'s precision pointing control was not used in mid-latitudes. (3) The spatial distribution of glaciers is relatively small. (4) Slopes are generally larger than on the polar ice sheets as mid-latitude glaciers are located in mountainous terrain. (5) Due to crevasses the glacier surface can be relatively rough. However, two recent studies showed that [ICESat](#) is also suitable to measure elevation changes of mountain glaciers when combined with an adequate [DEM](#) and a complete glacier inventory ([Kääb et al., 2012](#); [Gardner et al., 2013](#)). The main idea is to group glaciers into sub-regions with a statistical sound [ICESat](#) data sample. To account for the cross-track slope between consecutive [ICESat](#) tracks a reference surface is employed. For this purpose global [DEMs](#), such as the ones acquired during the [SRTM](#), are commonly used.

2.3.3 Optical stereo photogrammetry

Optical stereo photogrammetry is the most traditional remote sensing technique for mapping the topography of the earth. For this it relies on the principle of stereoscopic parallax which is the apparent difference in the position of an object due to a change in viewing position (e.g. [Lillesand et al., 2007](#)). Overlapping aerial or space-borne images record parallax due to the motion of the platform. Surface heights can be measured from successive images as the amount of parallax decreases with increasing distance from the camera. To identify objects on the ground, image correlation techniques are employed, which is a limiting factor of stereo photogrammetry in featureless terrain. In [Paper D](#) stereoscopic images from the French Pléiades satellite mission were employed. Since 17 December 2011, Pléiades 1A is in space followed by Pléiades 1B on 2 December 2012. With both satellites in orbit, the French Space Agency (CNES) ensures a daily revisiting interval with almost world wide coverage. For DEM extraction, Pléiades provides along-track tristereo imagery (Figure 2.3c). Tristereo images are preferable to classic stereo imagery in mountainous terrain, as the quasi-nadir acquisition minimizes the risk of missing hidden items on the ground ([Astrium, 2012](#)).

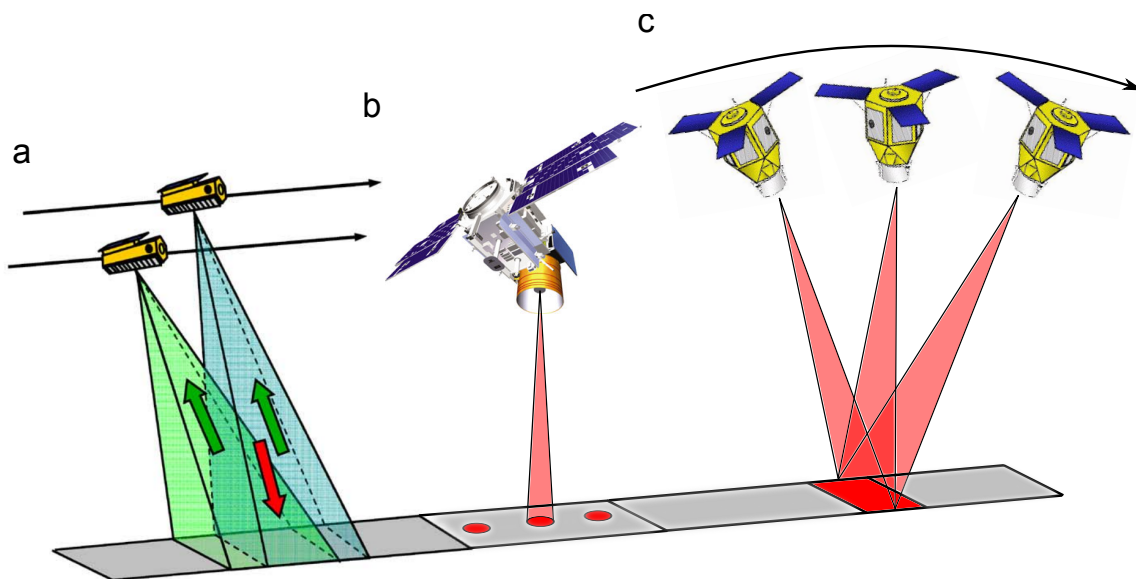


Figure 2.3: Satellite systems employed in this thesis, with (a) TerraSAR-X and TanDEM-X in bistatic acquisition mode (modified after [Krieger et al., 2007](#)), (b) ICESat/GLAS and (c) Pléiades in tristereo acquisition mode.

3 Research Summary

3.1 An overview of the spatial distribution of glacier mass balances on the Tibetan Plateau

Motivation: several recent studies report about rising lake-levels on the TP and attribute a certain amount of the lake-level rise to melt water released from glaciers (Zhang et al., 2011; Kropáček et al., 2012; Phan et al., 2012; Zhang et al., 2013). However, this amount was never quantified as *in situ* mass balance measurements are sparse on the TP and no measurements are available for the inner plateau (Yao et al., 2012). Furthermore, glacier mass balances are considered to be a good natural indicator for climate variability (e.g. Haeberli, 2011). Therefore, glacier mass balances and their differences in spatial distribution are important sources of information about climate variability. This is especially the case in remote regions such as the TP where meteorological station measurements are rare (e.g. Miehe et al., 2001).

Method: following studies from Kääb et al. (2012), Bolch et al. (2013) and Gardner et al. (2013) this is the fourth study which uses ICESat laser altimetry data to derive area-wide mass balances of mountain glaciers. For this purpose the TP was divided into eight climatological homogeneous sub-regions, including ~80% of the Tibetan glacier area. In these sub-regions, consecutive ICESat tracks over glaciers were compared relative to the SRTM C-band DEM resulting in a trend of surface elevation changes between 2003 and 2009. Relying on data of the CGI (Shi et al., 2009) and ice density assumptions these trends could be translated into area-wide mass balance estimates for the eight sub-regions (Figure 3.1). Employing information about watersheds on the TP, the amount of glacier melt water flowing into endorheic basins and hence is contributing to the local-lake level rise could be estimated for the first time.

Results & Conclusions: out of the total annual mass loss of $-15.6 \pm 10.1 \text{ Gt a}^{-1}$, $1.7 \pm 1.9 \text{ Gt a}^{-1}$ drained into endorheic basins on the plateau while $13.9 \pm 8.9 \text{ Gt a}^{-1}$ (or $0.04 \pm 0.02 \text{ mm a}^{-1}$ sea-level equivalent) contributed “directly” to the global sea-level rise. When combined with an accurate DEM, an actual glacier inventory and reasonable density assumptions, ICESat proved to be a valid data source to provide area-wide mass balances of mountain glaciers.

3.2. MASS BALANCE ESTIMATION OF A SINGLE MOUNTAIN GLACIER FROM ICESAT LASER ALTIMETRY DATA

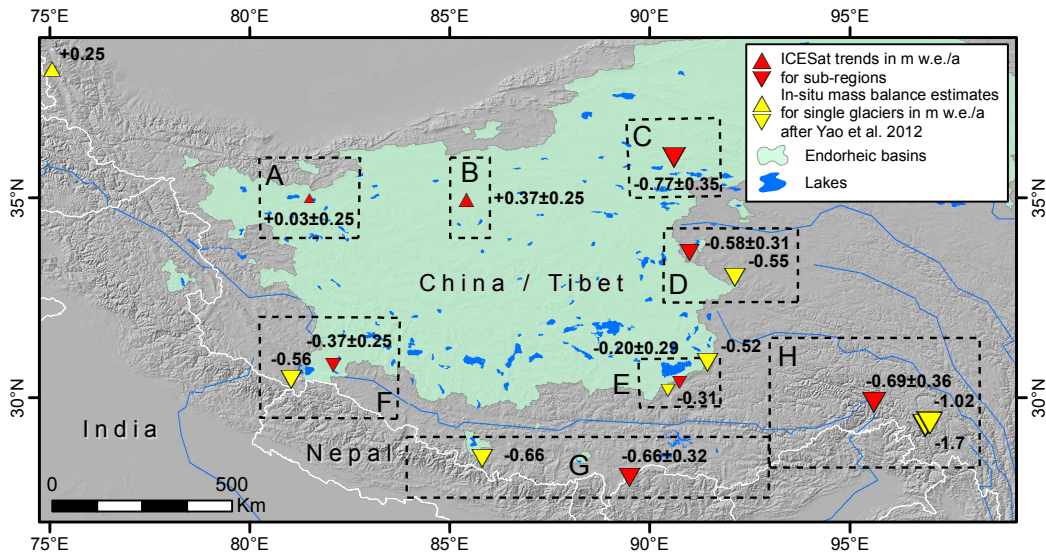


Figure 3.1: Spatial distribution of mass balance estimates in m w.eq. a⁻¹ derived from ICESat measurements for the eight sub-regions in comparison to *in situ* mass balance measurements of single glaciers (2006 – 2010, Yao et al., 2012). Reproduced from Paper A.

3.2 Mass balance estimation of a single mountain glacier from ICESat laser altimetry data

Motivation: in order to measure elevation changes of mountain glaciers on the TP from ICESat laser altimetry data, the Grosser Aletschgletscher located in the Swiss Alps was chosen as a test site. The ICESat data coverage is preferable on the glacier as several ICESat measurements are available in the accumulation area and the ablation area. Additionally, several DEMs are available including two precise airphoto DEMs (Figure 3.2). Furthermore, the Grosser Aletschgletscher is located in driving distance to the University of Tübingen.

Method: three separate areas of the Grosser Aletschgletscher are covered by one nominal ICESat track providing surface elevations for the period 2003 to 2009. To obtain surface elevation changes between 2003 and 2009 ICESat measurements were compared on the basis of a precise airphoto DEM and three different global DEMs. In order to validate the results, ICESat laser altimetry measurements were re-measured with a Differential Global Positioning System (DGPS) in 2012. Furthermore, the influence of the spatial sampling of ICESat measurements was investigated by subtracting two airphoto DEMs acquired in 1999 and 2009.

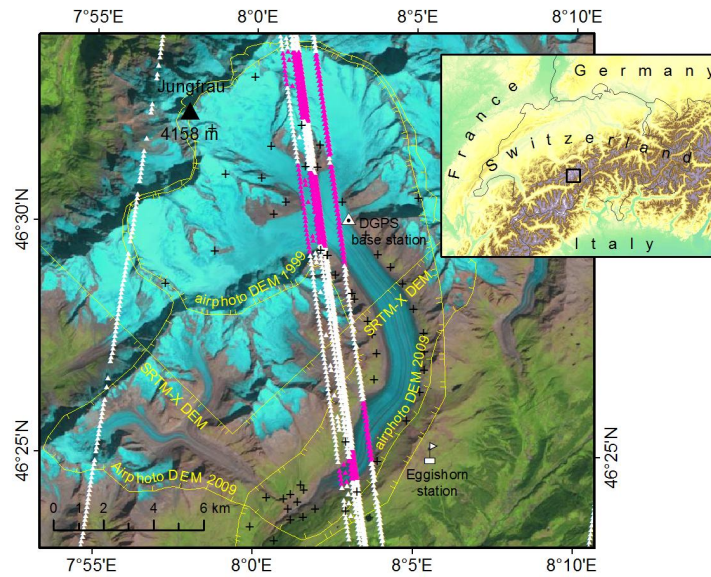


Figure 3.2: Data coverage of the Grosser Aletschglacier, Swiss Alps. In this study surface elevation changes were derived by combining [ICESat](#) data (indicated by small violet and white dots in on-glacier and off-glacier areas respectively) with several [DEMs](#) available in this region ([DEM](#) outlines with only partial coverage of the area are shown in yellow). Reproduced from [Paper B](#).

Results & Conclusions: depending on the [DEM](#) used as an elevation reference, an annual mass balance between -0.92 ± 0.18 m w.eq. a^{-1} and -1.04 ± 0.19 m w.eq. a^{-1} was estimated for the period 2003 to 2009 from [ICESat](#) laser altimetry data. The best estimate differs only for 9% when compared to the mass balance estimate derived from two airphoto [DEMs](#) acquired in 1999 and 2009. Although the use of global [DEMs](#) as an elevation reference leads to realistic estimates of surface lowering, the use of higher quality [DEMs](#) is preferable in terms of accuracy.

3.3 Recent mass balance of the Purogangri Ice Cap, Tibet's largest ice cap

Motivation: little is known about glacier variations and climate variability in the north-central part of the [TP](#). Therefore, the Purogangri Ice Cap ([PIC](#)) was chosen as one benchmark region of the [WET](#) project. Due to its extreme remoteness and an average altitude of 5,800 m, field work at the [PIC](#) would involve large logistical

3.3. RECENT MASS BALANCE OF THE PUROGANGRI ICE CAP, TIBET'S LARGEST ICE CAP

efforts and great physical strain, making remote sensing a promising alternative. The remote sensing data coverage of the PIC is preferable as 90% of the ice cap were mapped by X-band InSAR during the SRTM. Furthermore, this is the first study known to the author which uses data from the actual TanDEM-X mission to map surface elevation changes of a glacier.

Method: due to the preferable data situation at the PIC, surface elevation changes could be solely mapped by data from X-band InSAR. This simplifies assumptions about SAR penetration depth, a common issue in studies which employed data from the SRTM C-band DEM (e.g. Gardelle et al., 2012). Two different approaches were tested in this study to derive surface elevation changes. The first approach relies on Differential Interferometric Synthetic Aperture Radar (DInSAR) while the second approach uses common DEM differencing. Compared to the classical DEM differencing, the DInSAR approach relies on the subtraction of the interferometric phases of two InSAR acquisitions, rather than on the differencing of absolute surface heights.

Results & Conclusions: the mass balance of the PIC could be derived between 2000 and 2012. Only a slight mass loss of -44 ± 15 mm w.eq. a^{-1} and -38 ± 23 mm w.eq. a^{-1} was resolved by the DInSAR approach and from the DEM differencing respectively. The results of both methods suggest that the strong ablation in the lower regions of the ice cap is compensated by accumulation in the upper parts (Figure 3.3). The new TanDEM-X data turns out to be a very promising data source for geodetic mass balance measurements when compared to an older topographic dataset.

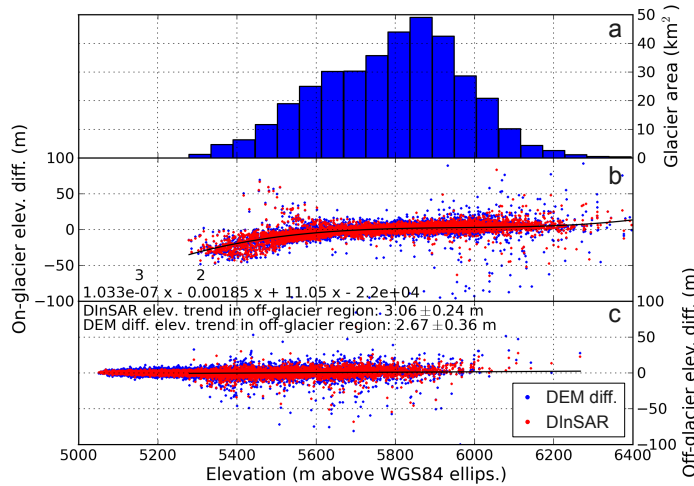


Figure 3.3: Glacier hypsometry of the Purogangri Ice Cap (PIC) in 50 m elevation bins (a). Surface elevation changes of the on-glacier area are shown as a function of elevation, a third order polynomial fit is shown as black solid line (b). Surface elevation changes in off-glacier regions are shown as a function of elevation, a linear trend is shown as black solid line (c). Reproduced from Paper C.

3.4 Comparing glacier mass balances derived from TanDEM-X and Pléiades data

Motivation: several new satellite missions provide large amounts of accurate elevation data in remote regions. However, so far little is known about their ability of mapping glacier elevation changes. In this study we took advantage of [TanDEM-X InSAR](#) data and stereoscopic Pléiades data acquired in 2012 and 2013 respectively. Several glaciers at the Gurla Mandhata massif were mapped by both data takes. The Gurla Mandhata massif is located in the south-western part of the [TP](#) and was chosen as another [WET](#) Benchmark region as its glaciers are believed to contribute to the lake-level changes of the large Mapam Yumco and La'nga Co.

Method: out of [CoSSC](#) data from the [TanDEM-X](#) acquisition a [DEM](#) was derived by interferometric means. Another [DEM](#) was calculated from tristereo Pléiades data employing stereo photogrammetry. In order to calculate geodetic mass balances between 2000, 2012 and 2013 the [SRTM](#) C-band [DEM](#) was subtracted from both [DEMs](#) after a proper horizontal and vertical alignment of the datasets. Also variations in glacier extent were mapped out of a declassified KH-7 Gambit-1 spy photograph from 1964, Landsat 7 ETM+ imagery from 2000, SPOT-5 imagery from 2010, TerraSAR-X data from 2011 and the 2013 Pléiades acquisition.

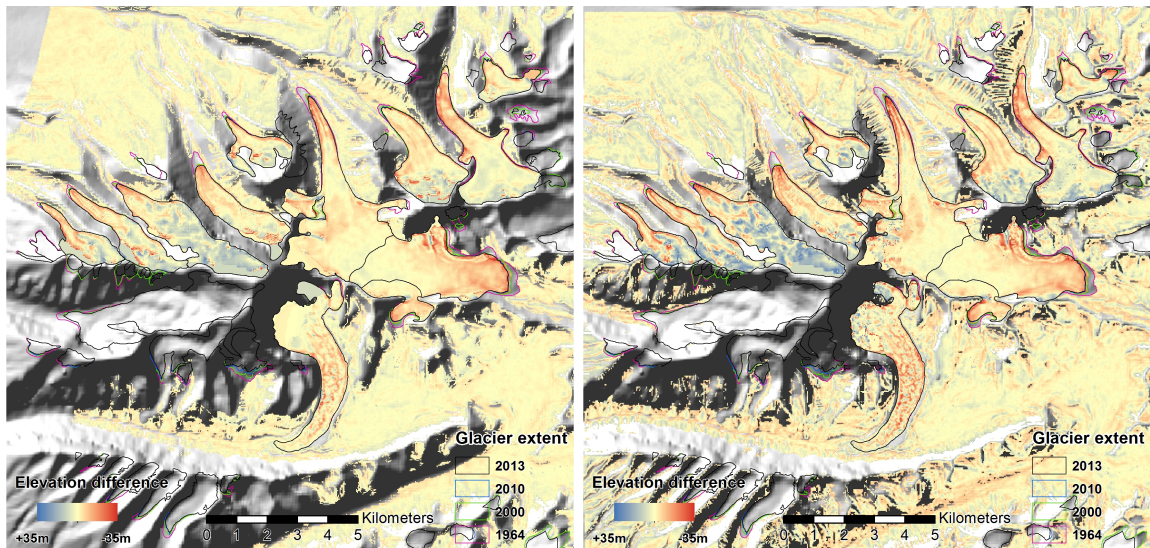


Figure 3.4: Surface elevation changes at the Gurla Mandhata study site from [TanDEM-X](#) (2012 acquisition) minus [SRTM](#) C-band (2000, left) and [Pléiades](#) (2013 acquisition) minus [SRTM](#) C-band (2000, right). Modified after [Paper D](#).

3.4. COMPARING GLACIER MASS BALANCES DERIVED FROM TANDEM-X AND PLÉIADES DATA

Results & Conclusions: for the Gurla Mandhata study site we calculated a mean annual mass balance of -0.11 ± 0.20 m w.eq. a^{-1} between 2000 and 2012 and of -0.07 ± 0.31 m w.eq. a^{-1} between 2000 and 2013. Our results agree within their error ranges, with both difference maps showing very similar patterns of glacier elevation changes (Figure 3.4). However, *in situ* measured mass balances from the north facing Gurla glacier appear to be more negative than our estimate (Yao et al., 2012). This difference is probably attributed to the penetration depth of the SRTM C-band DEM and the different time period of observations (i.e. the *in situ* mass balances from Yao et al. (2012) were measured between 2005 and 2009).

4 Discussion

In this thesis geodetic mass balances could be estimated for $\sim 80\%$ of the Tibetan glacier area. For this purpose different remote sensing techniques and datasets were employed which are briefly described in [Section 2.2](#). The first part of this chapter discusses the pros and cons of each remote sensing method applied in this thesis, while the second part of this chapter integrates the results into the wider context of the current environmental research on the TP.

In order to derive geodetic mass balances at the Purogangri study site and at the Gurla Mandhata study site ([Figure 1.1](#)) data from the current [TanDEM-X](#) mission were utilized. The great advantage of [InSAR](#) missions such as the [TanDEM-X](#) mission is the ability to map at all weather conditions during all daytimes. Furthermore, [InSAR](#) is able to map precise surface elevations in the accumulation area of glaciers which is a limiting factor for optical sensors which rely on visible structures on the glacier surface. However, penetration of the radar signal into snow and ice can have a significant influence on the results. Furthermore, foreshortening and layover effects are disadvantages when using this technique in mountainous terrain. This becomes a critical issue when investigating glaciers in steep mountain valleys such as at the Gurla Mandhata study site ([Paper D](#)). At the Purogangri study site this effect is only minor as the ice cap is relatively flat ([Paper C](#)). To attribute for foreshortening and layover effects, several data takes with different baselines, incident angles and acquisitions from ascending and descending orbits will be used in the production of the future global [TanDEM-X DEM](#) ([Krieger et al., 2007](#)). This procedure will enhance the quality of the [DEM](#), but will also induce a temporal inconsistency in the final [DEM](#).

So far, interferometric methods are widely employed to measure the topography and ice motion of ice sheets which have, compared to mountain glaciers, a larger size, narrower slopes and often lower accumulation and ablation rates ([Joughin et al., 2010](#)). However, new satellites such as TerraSAR-X or Radarsat-2 with a spatial resolution between one and three meters enhance the applicability of SAR data to smaller glaciers ([Short and Gray, 2004](#)). Today, data from TerraSAR-X is routinely employed for velocity measurements of glaciers by means of feature and speckle tracking ([Floricioiu et al., 2008](#); [Marsh et al., 2013](#); [Rankl et al., 2014](#), [Figure 2.1](#)) and for the first time experimental [TanDEM-X](#) interferometry was employed in this thesis to estimate multi-annual elevation changes ([Paper C](#), [Paper D](#)). The high temporal and

spatial resolution of the [TanDEM-X](#) mission and the high accuracy and precision of the data make it also a promising tool for measuring annual or even seasonal glacier elevation changes ([Leinss and Hajnesk, 2014](#)).

[ICESat](#) laser altimetry has similar attributes as [InSAR](#) except that the laser beam is not able to penetrate cloud cover. Also foreshortening and layover effects are not an issue due to the nadir looking laser instrument. The sparse data sampling, especially in mid-latitudes, is the main limiting factor when utilizing [ICESat](#) data to map surface elevations of glaciers. At the Grosser Aletschgletscher, the [ICESat](#) data sampling is preferable and meaningful estimates of glacier elevation changes could be derived for this single mountain glacier ([Paper B](#)). However, to assess glaciers with a sparser data sampling it is recommended to group glaciers into certain sub-regions as done for the entire [TP](#) in [Paper A](#) or in other recent studies ([Kääb et al., 2012](#); [Bolch et al., 2013](#); [Gardner et al., 2013](#)). As the [ICESat](#) mission ended in 2009 no new data is available and high expectations are on the [ICESat-2](#) mission which is planned for 2015 ([Abdalati et al., 2010](#)). Also altimetry data from the actual [CryoSat-2](#) mission might become interesting to estimate elevation changes of mountain glaciers.

The high spatial and temporal resolution of optical sensors such as [Pléiades](#) are advantages when compared to [InSAR](#) and laser altimetry data. However, the need of visible structures on the surface and the inability to penetrate cloud cover are disadvantages of optical stereo photogrammetry when mapping the topography of glaciers. However, compared to [InSAR](#) or laser altimetry, the principle of optical stereo photogrammetry is relatively old wherefore it is a very valuable technique to derive former glacier elevations. For this, several recent studies employed declassified spy imagery dating back to the 1960s and 1970s (e.g. [Bolch et al., 2011](#); [Pieczonka et al., 2013](#)). Early airborne photogrammetric surveys even date back to the 1930s providing precise topographic maps and hence past glacier elevations which also were used to assess longer time series of mass balance estimates (e.g. [Nuth et al., 2007](#)).

The glacier elevation changes derived in this thesis are depending, to a varying extent, on [SRTM DEM](#) data. The most critical issue when using data from the [SRTM](#) to derive glacier elevation changes is the penetration depth of the C-band (5.3 GHz) into snow and ice ([Rignot et al., 2001](#); [Gardelle et al., 2012](#)). This is especially an issue in [Paper D](#) where we assume a C-band penetration depth of 1.4 ± 1.0 m. A first order estimate can be derived when comparing [SRTM](#) C-band with [SRTM](#) X-band elevations in on- and off-glacier areas. Due to a lack of [SRTM](#) X-band data at the Gurla Mandhata study site we employed a similar value as [Gardelle et al. \(2013\)](#) in the Everest area ([Paper D](#)). The great advantage at the Purogangri study site is the large-scale coverage of [SRTM](#) X-band data which can be directly compared to data from the [TanDEM-X](#) mission as both datasets were acquired at X-band ([Paper C](#)).

In order to translate glacier elevation changes into glacier mass balances, assumptions about the glacier area and density are required. The new globally complete [RGI](#) ([Pfeffer et al., 2014](#)) provides an adequate data source for compiling glacier mass balances on a regional or even global scale ([Gardner et al., 2013](#)), to model the

global ice thickness and volume (Huss and Farinotti, 2012; Grinsted, 2013) and to predict future glacier changes. However, on a local scale the glacier outlines should be compared to recent satellite imagery as the quality of the RGI varies widely in time and space. Therefore, new glacier outlines were derived for the Purogangri study site and the Gurla Mandhata study site from optical satellite imagery and validated by recent 11-day TerraSAR-X coherence images (i.e. Paper C and Paper D). For the Grosser Aletschgletscher accurate glacier outlines were available via the GLIMS dataset (Paper B).

Without field measurements density assumptions are difficult to determine. Therefore several assumptions were made in this thesis relying on the relevant literature. However, as stated earlier this is considered to be the largest source of uncertainty in geodetic mass balance estimates (Fischer, 2011). This issue may be overcome in the future by employing firn densification models adapted for mountain glaciers (Bolch et al., 2013; Huss, 2013).

In this thesis contrasting patterns of glacier mass balances on the TP were found from different remote sensing datasets. In general, the results presented in this thesis agree with other studies which show similar regional patterns of glacier changes in the Himalaya (Bolch et al., 2012; Kääb et al., 2012; Gardelle et al., 2013, Figure 4.1) and on the TP (Yao et al., 2012; Gardner et al., 2013, Figure 4.1). Also the local studies at the Purogangri study site (Paper C) and at the Gurla Mandhata study site (Paper D) support the findings for the whole TP (Paper A). On average, glacier mass balances on the TP are clearly negative, with the most negative mass balances in the north-eastern and the south-eastern part of the plateau and in the central and eastern Tibetan Himalaya (Paper A). For the latter similar values were found by Gardner et al. (2013), but the results are clearly more negative than the results from Kääb et al. (2012). These differences are difficult to explain as slightly different regions and hence different glaciers were investigated. Also the ICESat derived mass balances for the south-eastern part of the plateau are more negative than the results based on DEM differencing between 1999 and 2010 (Gardelle et al., 2013). In their study Gardelle et al. (2013) state that ICESat derived mass balances tend to be more negative than their results. This statement holds also true for the Gurla Mandhata study site (Paper D) which revealed more positive mass balances from DEM differencing than from ICESat measurements. This is probably attributed to the fact that different glaciers were measured during slightly different time periods. Furthermore, the penetration depth of the SRTM C-band might introduce a significant bias in the DEM differencing. The latter might also be an issue when comparing the results from Bolch et al. (2011) and Gardelle et al. (2013) in the Mt. Everest area. While Gardelle et al. (2013) found an average mass balance of -0.41 ± 0.21 m w.eq. a⁻¹ between 1999 and 2011, Bolch et al. (2011) estimated an average mass balance of -0.79 ± 0.52 m w.eq. a⁻¹ between 2002 and 2007. Despite the slightly different time period between both studies, Gardelle et al. (2013) also referred to the SRTM-C DEM while Bolch et al. (2011) solely utilized DEMs derived from optical stereo photogrammetry.

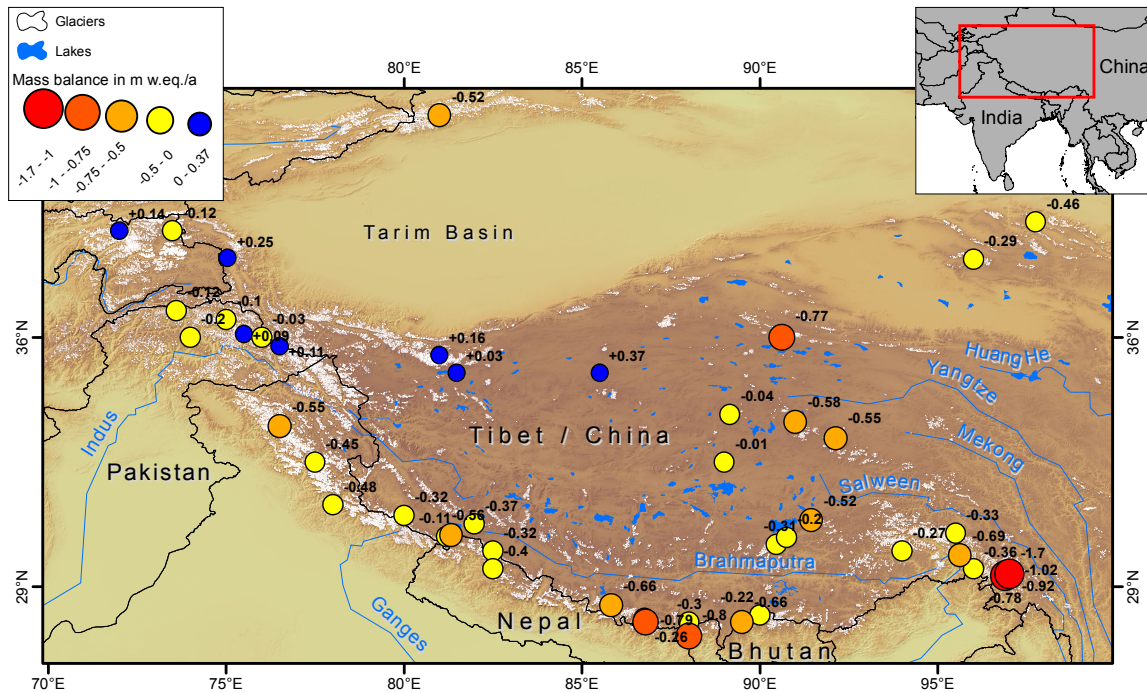


Figure 4.1: Overview of recent mass balance estimates in High Asia. Mass balance estimates are based on [Paper A](#), [Paper C](#), [Paper D](#), [Bolch et al. \(2011\)](#), [Kääb et al. \(2012\)](#), [Yao et al. \(2012\)](#), [Gardelle et al. \(2013\)](#) and [Gardner et al. \(2013\)](#). Glacier outlines are based on the Randolph Glacier Inventory (RGI) ([Pfeffer et al., 2014](#)).

The overall negative glacier mass balances are most probably attributed to an increase in air temperature on the TP as proposed in several studies (e.g. [Liu and Chen, 2000](#); [Qin et al., 2009](#); [Li et al., 2011](#); [Yao et al., 2012](#)). Also glacier terminus positions are in general retreat in the Himalaya ([Bolch et al., 2012](#)) and in the eastern part of the TP ([Bolch et al., 2010b](#); [Wei et al., 2014](#)). However, glaciers in the central and north-western part of the TP showed balanced or slightly positive mass changes in the last decade ([Paper A](#)). This is in agreement with the findings from [Yao et al. \(2012\)](#) who found positive glacier mass balances at the Mustagh Ata massif between 2006 and 2010 and with the findings from [Gardner et al. \(2013\)](#) who found positive mass balances in the western Kunlun Mountains between 2003 and 2009 (Figure 4.1). Also an increase in area was found for some glaciers in the western Kunlun Mountains between 1970 and 2001 ([Shangguan et al., 2007](#)). The latter is also known for the Karakoram where most glaciers showed a stable terminus position between 1976 and 2012 ([Rankl et al., 2014](#)). Also in the eastern Hindu Kush 24% of the investi-

gated glaciers showed a stable or advancing terminus position between 1976 and 2007 (Sarikaya et al., 2012). However, changes in glacier area cannot directly be compared to changes in mass balance as they only reflect a delayed signal to changes in climate. The positive elevation changes found for the large ice fields of Zangser Kangri and Songzhi Peak, located in the north-central part of the TP (Paper A) are in agreement with the almost neutral mass balance found for the Purogangri Ice Cap (Paper C). For these neighboring ice caps positive elevation changes were found in the accumulation area, while glacier thinning was observed in lower regions suggesting enhanced snow and firn accumulation (Paper A, Paper C). These heterogeneous patterns of mass balances may be related to similar mechanisms as causing the frequently mentioned Pamir-Karakoram anomaly (Hewitt, 2005; Gardelle et al., 2013). A possible explanation of this positive anomaly could be a compensation of the temperature driven glacier melt due to an increase in precipitation at higher altitudes. These thoughts are in agreement with the findings of Li et al. (2011), who showed a significant increase in annual temperature and precipitation between 1961 and 2008 from meteorological station measurements on the TP. However, meteorological stations are rare or even non-existing on the TP introducing large uncertainties in the spatial distribution of trends. Reanalysis data may help to fill this gap but are only available at a relative coarse spatial resolution. A recent study from Maussion et al. (2014) presents a new reanalysis dataset for High Asia (HAR) at 30 km and 10 km spatial resolution. However, as this dataset only covers a 12-year time period between 2001 and 2012 no meaningful climatic trends can be derived, making a direct comparison between glacier mass balances and atmospheric forces difficult.

The overall clearly negative mass balances found in this thesis are contrary to the gravitational findings of Jacob et al. (2012) and Yi and Sun (2014). In their study Jacob et al. (2012) showed an increase in mass of $7 \pm 7 \text{ Gt a}^{-1}$ on the TP from GRACE measurements acquired between 2003 and 2010. A more recent study even found an increase in mass of 30 Gt a^{-1} on the TP from GRACE measurements, but found it challenging to explain (Yi and Sun, 2014). A part of this mass gain can be attributed to an increase in lake level/mass rather than to an increase in glacier mass (Zhang et al., 2013). This is in agreement with this thesis papers as most of the studied regions showed a negative mass balance for the studied time period. However, not all of the estimated glacier mass loss could be detected by GRACE as many glaciers on the TP are draining into endorheic lake basins. The melt water released into endorheic basins stays on the plateau rather than “directly” contributing to the global sea-level rise. In Paper A this amount is estimated at $1.7 \pm 1.9 \text{ Gt a}^{-1}$ which can likely be linked to the observed rise of the local lake-levels on the TP (Zhang et al., 2011; Kropáček et al., 2012; Phan et al., 2012).

5 Conclusions and outlook

By quantifying glacier mass changes on the Tibetan Plateau (TP), the results of this thesis contribute to a better understanding of the effects of a changing climate to the water balance and ecosystems on the plateau. Furthermore, this work shows the spatial differences in glacier mass balances on the TP and quantifies the contribution of Tibetan glaciers to the global sea-level rise.

This work supports the current efforts to enhance *in situ* glacier mass balance measurements with large scale geodetic approaches as suggested in the recently published fifth Intergovernmental Panel on Climate Change (IPCC) Assessment Report (AR). Furthermore, traditional Digital Elevation Model (DEM) differencing is complemented by satellite altimetry measurements and at the first time new TanDEM-X data were utilized for geodetic mass balance estimates. In a co-authored study, these estimates could be complemented by recent Pléiades acquisitions. Both datasets show a great potential for deriving glacier elevation changes when compared to data from the global Shuttle Radar Topography Mission (SRTM) acquired in 2000. Additionally, Ice Cloud and Elevation Satellite (ICESat) laser altimetry measurements were successfully proofed to derive glacier elevation changes of the Grosser Aletschgletscher, located in the Swiss Alps. Applying an adjusted method to glaciers on the TP, elevation changes of $\sim 80\%$ of the Tibetan glacier area were quantified. Also the amount of glacier melt water draining into endorheic basins on the TP and hence does not contribute “directly” to the global sea-level rise was estimated for the first time.

According to the consistent results from the different recent remote sensing datasets glacier tend to gain mass in the north-western and central part of the plateau while a strong mass loss was found in the southern and eastern part of the TP. Considering $\sim 80\%$ of the glacier area on the TP a clearly negative mass budget of $-15.6 \pm 10.1 \text{ Gt a}^{-1}$ was found for the period 2003-2009 from ICESat laser altimetry data. These patterns correspond well to other recent studies relying on remote sensing data and *in situ* mass balance measurements, but are seemingly contrary to gravitational measurements from the Gravity Recovery and Climate Experiment (GRACE). This discrepancy can partly be explained by the drainage of glacial melt water into endorheic basins on the plateau which accounts for $1.7 \pm 1.9 \text{ Gt a}^{-1}$ of the ICESat derived mass loss. This amount does not leave the TP as stream flow but rather stays on the plateau and contributes to the recently observed lake-level rise.

Remote sensing turns out to be a promising data source for glacier mass balances, but much more research is needed to refine the results, both on a spatial and temporal scale. In order to validate remote sensing estimates of glacier mass balances it is also important to further enhance and pursue *in situ* mass balance measurements of mountain glaciers in remote areas such as the TP. Furthermore, high expectations are on new satellite altimetry missions such as the ICESat-2 and the CryoSat-2 mission. With the coming TanDEM-X WorldDEM^{TM1} another global DEM will become available. A combination of this dataset with the global SRTM DEM and the now globally complete Randolph Glacier Inventory (RGI) will allow for a comprehensive global mass balance estimate between 2000 and ~2012/2013. Such an estimate will lead to a further enhancement of global mass balance measurements from remote sensing data.

¹more information about the WorldDEMTM is available on the web via: www.astrium-geo.com/worlddem

References

- Abdalati, W., Zwally, H., Bindschadler, R., Csatho, B., Farrell, S., Fricker, H., Harding, D., Kwok, R., Lefsky, M., Markus, T., Marshak, A., Neumann, T., Palm, S., Schutz, B., Smith, B., Spinhirne, J., and Webb, C. (2010). The ICESat-2 Laser Altimetry Mission. *Proceedings of the IEEE*, 98(5):735–751.
- Albertz, J. (2009). *Einführung in die Fernerkundung. Grundlagen der Interpretation von Luft- und Satellitenbildern*. Wissenschaftliche Buchgesellschaft, Darmstadt.
- Astrium (2012). *Pléiades Imagery User Guide V2.0*. Astrium Geo-Information Services.
- Bader, H. (1954). Sorge's law of densification of snow on high polar glaciers. *Journal of Glaciology*, 2:319–323.
- Bakke, J. and Nesje, A. (2011). Equilibrium-Line Altitude (ELA). In Singh, V. P., Singh, P., and Haritashya, U. K., editors, *Encyclopedia of Snow, Ice and Glaciers*, pages 268–277. Springer, Dordrecht.
- Battle, W. R. B. (1951). Glacier movement in north-east Greenland, 1949. *Journal of Glaciology*, 1(10):559–563.
- Benn, D. I. and Evans, D. J. A. (2010). *Glaciers & Glaciation*. Hodder Education, London.
- Berthier, E., Arnaud, Y., Kumar, R., Ahmad, S., Wagnon, P., and Chevallier, P. (2007). Remote sensing estimates of glacier mass balances in the Himachal Pradesh (Western Himalaya, India). *Remote Sensing of Environment*, 108(3):327–338.
- Berthier, E., Schiefer, E., Clarke, G. K. C., Menounos, B., and Remy, F. (2010). Contribution of Alaskan glaciers to sea-level rise derived from satellite imagery. *Nature Geoscience*, 3(2):92–95.
- Bhutiyani, M. R. (2011). Ice Caps. In Singh, V. P., Singh, P., and Haritashya, U. K., editors, *Encyclopedia of Snow, Ice and Glaciers*, page 582. Springer, Dordrecht.
- Bindschadler, R., Dowdeswell, J., Hall, D., and Winther, J.-G. (2001). Glaciological applications with Landsat-7 imagery: Early assessments. *Remote Sensing of Environment*, 78(1–2):163–179. Landsat 7.
- Böhner, J. (2006). General climatic controls and topoclimatic variations in Central and High Asia. *Boreas*, 35(2):279–295.
- Bolch, T., Kulkarni, A., Kääb, A., Huggel, C., Paul, F., Cogley, J. G., Frey, H., Kargel, J. S., Fujita, K., Scheel, M., Bajracharya, S., and Stoffel, M. (2012). The State and Fate of Himalayan Glaciers. *Science*, 336(6079):310–314.
- Bolch, T., Menounos, B., and Wheate, R. (2010a). Landsat-based inventory of glaciers in western Canada, 1985–2005. *Remote Sensing of Environment*, 114(1):127–137.
- Bolch, T., Pieczonka, T., and Benn, D. I. (2011). Multi-decadal mass loss of glaciers in the Everest area (Nepal Himalaya) derived from stereo imagery. *The Cryosphere*, 5(2):349–358.
- Bolch, T., Sørensen, L. S., Simonsen, S. B., Mölg, N., Machguth, H., Rastner, P., and Paul, F. (2013). Mass loss of Greenland's glaciers and ice caps 2003–2008 revealed from ICESat laser altimetry data. *Geophysical Research Letters*, 40(5):875–881.
- Bolch, T., Yao, T., Kang, S., Buchroithner, M. F., Scherer, D., Maussion, F., Huintjes, E., and Schneider, C. (2010b). A glacier inventory for the western Nyainqentanglha Range and the Nam Co Basin, Tibet, and glacier changes 1976–2009. *The Cryosphere*, 4(3):419–433.
- Brenner, A. C., Bentley, C. R., Csatho, B. M., Harding, D. J., Hofton, M. A., Minster, J., Roberts, L., Saba, J. L., Schutz, R., Thomas, R. H., Yi, D., and Zwally, H. J. (2003). Derivation of Range and Range Distributions From Laser Pulse Waveform Analysis for Surface Elevations, Roughness, Slope, and Vegetation Heights. Technical report, NASA Goddard Space Flight Center.
- Brenner, A. C., DiMarzio, J. P., and Zwally, H. J. (2007). Precision and Accuracy of Satellite Radar and Laser Altimeter Data Over the Continental Ice Sheets. *IEEE Transactions on Geoscience and Remote Sensing*, 45(2):321–331.
- Bridge, J. and Demicco, R. (2008). *Earth Surface Processes, Landforms and Sediment Deposits*. Cambridge University Press, Cambridge.
- Church, J., Clark, P., Cazenave, A., Gregory, J., Jevrejeva, S., Levermann, A., Merrifield, M., Milne, G., Nerem, R., Nunn, P.D. abd Payne, A., Pfeffer, W., D.,

References

- S., and Unnikrishnan, A. (2013). Sea Level Change. In Stocker, T., Qin, D., Plattner, G., K., Tignor, M., Allen, S., Boschung, J., Nauels, A., Xia, Y., Bex, V., and Midgley, P., editors, *Climate Change 2013: The Physical Science Basis. Contribution of Working Group I to the Fifth Assessment Report of the Intergovernmental Panel on Climate Change*. Cambridge University Press, Cambridge, United Kingdom and New York, NY, USA.
- Cuffey, K. M. and Paterson, W. S. B. (2010). *The physics of glaciers*. Butterworth-Heinemann, Oxford.
- Ding, Y., Liu, S., Li, J., and Shangguan, D. (2006). The retreat of glaciers in response to recent climate warming in western China. *Annals of Glaciology*, 43:97–105.
- Dobhal, D. P. (2011). Glacier. In Singh, V. P., Singh, P., and Haritashya, U. K., editors, *Encyclopedia of Snow, Ice and Glaciers*, pages 376–377. Springer, Dordrecht.
- Draws, R., Rack, W., Wesche, C., and Helm, V. (2009). A Spatially Adjusted Elevation Model in Dronning Maud Land, Antarctica, Based on Differential SAR Interferometry. *Geoscience and Remote Sensing, IEEE Transactions on*, 47(8):2501–2509.
- Farr, T. G., Rosen, P. A., Caro, E., Crippen, R., Duren, R., Hensley, S., Kobrick, M., Paller, M., Rodriguez, E., Roth, L., Seal, D., Shaffer, S., Shimada, J., Umland, J., Werner, M., Oskin, M., Burbank, D., and Alsdorf, D. (2007). The Shuttle Radar Topography Mission. *Rev. Geophys.*, 45(2):RG2004.
- Fischer, A. (2011). Comparison of direct and geodetic mass balances on a multi-annual time scale. *The Cryosphere*, 5(1):107–124.
- Floricioiu, D., Eineder, M., Rott, H., and Nagler, T. (2008). Velocities of Major Outlet Glaciers of the Patagonia Icefield Observed by TerraSAR-X. In *Geoscience and Remote Sensing Symposium, 2008. IGARSS 2008. IEEE International*, volume 4, pages 347–350.
- Frey, H., Paul, F., and Strozzi, T. (2012). Compilation of a glacier inventory for the western Himalayas from satellite data: methods, challenges, and results. *Remote Sensing of Environment*, 124(0):832–843.
- Gardelle, J., Berthier, E., and Arnaud, Y. (2012). Impact of resolution and radar penetration on glacier elevation changes computed from DEM differencing. *Journal of Glaciology*, 58(208):419–422.
- Gardelle, J., Berthier, E., Arnaud, Y., and Kääb, A. (2013). Region-wide glacier mass balances over the Pamir-Karakoram-Himalaya during 1999–2011. *The Cryosphere*, 7(4):1263–1286.
- Gardner, A. S., Moholdt, G., Cogley, J. G., Wouters, B., Arendt, A. A., Wahr, J., Berthier, E., Hock, R., Pfeffer, W. T., Kaser, G., Ligtenberg, S. R. M., Bolch, T., Sharp, M. J., Hagen, J. O., van den Broeke, M. R., and Paul, F. (2013). A Reconciled Estimate of Glacier Contributions to Sea Level Rise: 2003 to 2009. *Science*, 340(6134):852–857.
- Grinsted, A. (2013). An estimate of global glacier volume. *The Cryosphere*, 7(1):141–151.
- Haerberli, W. (1998). Historical evolution and operational aspects of worldwide glacier monitoring. In *Into the second century of worldwide glacier monitoring: prospects and strategies*. UNESCO Publishing, Paris.
- Haerberli, W. (2011). Glacier Mass Balance. In Singh, V. P., Singh, P., and Haritashya, U. K., editors, *Encyclopedia of Snow, Ice and Glaciers*, pages 399–408. Springer, Dordrecht.
- Hagg, W. J., Braun, L. N., Uvarov, V. N., and Makarevich, K. G. (2004). A comparison of three methods of mass-balance determination in the Tuyuksu glacier region, Tien Shan, Central Asia. *Journal of Glaciology*, 50(171):505–510.
- Heid, T. and Kääb, A. (2012). Repeat optical satellite images reveal widespread and long term decrease in land-terminating glacier speeds. *The Cryosphere*, 6(2):467–478.
- Hewitt, K. (2005). The Karakoram Anomaly? Glacier Expansion and the ‘Elevation Effect,’ Karakoram Himalaya. *Mountain Research and Development*, 25(4):332–340.
- Hoffmann, J. and Walter, D. (2006). How Complementary are SRTM-X and -C Band Digital Elevation Models? *Photogrammetric Engineering & Remote Sensing*, 72:261–268.
- Huang, M. (1990). On the temperature distribution of glaciers in China. *Journal of Glaciology*, 36:210–216.
- Huss, M. (2013). Density assumptions for converting geodetic glacier volume change to mass change. *The Cryosphere*, 7(3):877–887.
- Huss, M. and Farinotti, D. (2012). Distributed ice thickness and volume of all glaciers around the globe. *J. Geophys. Res.*, 117(F4):F04010.
- Immerzeel, W., Droogers, P., de Jong, S., and Bierkens,

- M. (2009). Large-scale monitoring of snow cover and runoff simulation in Himalayan river basins using remote sensing. *Remote Sensing of Environment*, 113(1):40–49.
- Immerzeel, W. W., van Beek, L. P. H., and Bierkens, M. F. P. (2010). Climate change will affect the Asian water towers. *Science*, 328:1382–1385.
- Jacob, T., Wahr, J., Pfeffer, W. T., and Swenson, S. (2012). Recent contributions of glaciers and ice caps to sea level rise. *Nature*, 482(7386):514–518.
- Jansson, P., Hock, R., and Schneider, T. (2003). The concept of glacier storage: a review. *Journal of Hydrology*, 282(1–4):116–129. Mountain Hydrology and Water Resources.
- Joughin, I., Kwok, R., and Fahnestock, M. (1998). Interferometric estimation of three-dimensional ice-flow using ascending and descending passes. *IEEE Transactions on Geoscience and Remote Sensing*, 36:25–37.
- Joughin, I., Smith, B. E., and Abdalati, W. (2010). Glaciological advances made with interferometric synthetic aperture radar. *Journal of Glaciology*, 56(200):1026–1042.
- Kääb, A. (2008). Glacier Volume Changes Using ASTER Satellite Stereo and ICESat GLAS Laser Altimetry. A Test Study on Edgeøya, Eastern Svalbard. *IEEE Transactions on Geoscience and Remote Sensing*, 46:2823–2830.
- Kääb, A., Berthier, E., Nuth, C., Gardelle, J., and Arnaud, Y. (2012). Contrasting patterns of early twenty-first-century glacier mass change in the Himalayas. *Nature*, 488(7412):495–498.
- Kang, S., Xu, Y., You, Q., Flügel, W., Pepin, N., and Yao, T. (2010). Review of climate and cryospheric change in the Tibetan Plateau. *Environmental Research Letters*, 5(1):015101.
- Kaser, G., Großhauser, M., and Marzeion, B. (2010). Contribution potential of glaciers to water availability in different climate regimes. *Proceedings of the National Academy of Sciences*, 107(47):20223–20227.
- Kick, W. (1960). The first glaciologists in central asia. *Journal of Glaciology*, 3:687–689.
- Kramer, H. J. (2002). *Observation of the Earth and Its Environment*, chapter Earth Observation/Monitoring Missions, pages 329–553. Springer, Berlin, Heidelberg, New York.
- Krieger, G., Moreira, A., Fiedler, H., Hajnsek, I., Werner, M., Younis, M., and Zink, M. (2007). TanDEM-X: A Satellite Formation for High-Resolution SAR Interferometry. *Geoscience and Remote Sensing, IEEE Transactions on*, 45(11):3317–3341.
- Kropáček, J., Braun, A., Kang, S., Feng, C., Ye, Q., and Hochschild, V. (2012). Analysis of lake level changes in Nam Co in central Tibet utilizing synergistic satellite altimetry and optical imagery. *International Journal of Applied Earth Observation and Geoinformation*, 17(0):3–11.
- Kwok, R. and Fahnestock, M. A. (1996). Ice sheet motion and topography from radar interferometry. *IEEE Transactions on Geoscience and Remote Sensing*, 34:189–200.
- Leinss, S. and Hajnesk, I. (2014). Snow Accumulation, Melt Rates and Glacier Mass Balance Measured by TanDEM-X. In *7th EARSeL workshop on Land Ice and Snow*.
- Li, C. and Cheng, P. (1980). Recent research on glaciers on the Chinghai-Tibet Plateau. In *Proceedings of the Riederalp Workshop, Sep. 1978*.
- Li, Z., He, Y., An, W., Song, L., Zhang, W., Catto, N., Wang, Y., Wang, S., Liu, H., Cao, W., Theakstone, W. H., Wang, S., and Du, J. (2011). Climate and glacier change in southwestern China during the past several decades. *Environmental Research Letters*, 6(4):045404.
- Lillesand, T. M., Kiefer, R. W., and Chipman, J. W. (2007). *Remote Sensing and Image Interpretation*. John Wiley & Sons, New York.
- Liu, X. and Chen, B. (2000). Climatic warming in the Tibetan Plateau during recent decades. *International Journal of Climatology*, 20(14):1729–1742.
- Ludwig, K. (2010). *Tibet*. C. H. Beck. München.
- Mäder, H. (1997). *Tibet - Land mit Vergangenheit und Zukunft*. Mäder. Zürich.
- Marsh, O. J., Rack, W., Floricioiu, D., Gолledge, N. R., and Lawson, W. (2013). Tidally induced velocity variations of the Beardmore Glacier, Antarctica, and their representation in satellite measurements of ice velocity. *The Cryosphere*, 7(5):1375–1384.
- Maussion, F., Scherer, D., Mölg, T., Collier, E., Curio, J., and Finkelnburg, R. (2014). Precipitation Seasonality and Variability over the Tibetan Plateau as Resolved

References

- by the High Asia Reanalysis. *J. Climate*, 27(5):1910–1927.
- Miehe, G. (2004). Hochland von Tibet. In *Gebirge der Erde*, pages 349–359. Eugen Ulmer GmbH & Co., Stuttgart.
- Miehe, G., Winiger, M., Böhner, J., and Zhang, Y. (2001). The climatic diagram map of High Asia, Purpose and concepts. *Erdkunde*, 55:94–97.
- Moholdt, G., Nuth, C., Hagen, J. O., and Kohler, J. (2010). Recent elevation changes of Svalbard glaciers derived from ICESat laser altimetry. *Remote Sensing of Environment*, 114(11):2756–2767.
- Neckel, N., Drews, R., Rack, W., and Steinhage, D. (2012). Basal melting at the Ekström Ice Shelf, Antarctica, estimated from mass flux divergence. *Annals of Glaciology*, 53(60):294–302.
- Nuth, C., Kohler, J., Aas, H., Brandt, O., and Hagen, J. (2007). Glacier geometry and elevation changes on Svalbard (1936–90): a baseline dataset. *Annals of Glaciology*, 46(1):106–116.
- Nye, J. F. (1957). The Distribution of Stress and Velocity in Glaciers and Ice-Sheets. *Proceedings of the Royal Society of London. Series A. Mathematical and Physical Sciences*, 239(1216):113–133.
- Pfeffer, W. T., Arendt, A. A., Bliss, A., Bolch, T., Cogley, J. G., Gardner, A. S., Hagen, J. O., Hock, R., Kaser, G., Kienholz, C., Miles, E. S., Moholdt, G., Mölg, N., Paul, F., Radic, V., Rastner, P., Raup, B. H., Rich, J., Sharp, M. J., and the Randolph Consortium (2014). The Randolph Glacier Inventory (2014): a globally complete inventory of glaciers. *Journal of Glaciology*, 60(221):537–552.
- Phan, V. H., Lindenbergh, R., and Menenti, M. (2012). ICESat derived elevation changes of Tibetan lakes between 2003 and 2009. *International Journal of Applied Earth Observation and Geoinformation*, 17(0):12–22.
- Pieczonka, T., Bolch, T., Junfeng, W., and Shiyin, L. (2013). Heterogeneous mass loss of glaciers in the Aksu-Tarim Catchment (Central Tien Shan) revealed by 1976 KH-9 Hexagon and 2009 SPOT-5 stereo imagery. *Remote Sensing of Environment*, 130(0):233–244.
- Qin, J., Yang, K., Liang, S., and Guo, X. (2009). The altitudinal dependence of recent rapid warming over the Tibetan Plateau. *Climatic Change*, 97(1-2):321–327.
- Rabus, B., Eineder, M., Roth, A., and Bamler, R. (2003). The shuttle radar topography mission – a new class of digital elevation models acquired by spaceborne radar. *ISPRS Journal of Photogrammetry and Remote Sensing*, 57(4):241–262.
- Rankl, M., Kienholz, C., and Braun, M. (2014). Glacier changes in the Karakoram region mapped by multiresolution satellite imagery. *The Cryosphere*, 8(3):977–989.
- Rees, W. G. and Pellikka, P. (2010). Principles of remote sensing. In *Remote sensing of glaciers*, pages 1–20. Taylor & Francis Group, London.
- Richardson, S. D. and Reynolds, J. M. (2000). An overview of glacial hazards in the Himalayas. *Quaternary International*, 65-66(0):31–47.
- Rignot, E., Echelmeyer, K., and Krabill, W. (2001). Penetration depth of interferometric synthetic-aperture radar signals in snow and ice. *Geophys. Res. Lett.*, 28(18):3501–3504.
- Rignot, E., Rivera, A., and Casassa, G. (2003). Contribution of the Patagonia Icefields of South America to Sea Level Rise. *Science*, 302(5644):434–437.
- Rott, H. (2009). Advances in interferometric synthetic aperture radar (InSAR) in earth system science. *Progress in Physical Geography*, 33(6):769–791.
- Ryder, C. H. D. (1908). Dr. Sven Hedin’s Expedition in Tibet. *The Geographical Journal*, 32(6):585–590.
- Sarikaya, M. A., Bishop, M. P., Shroder, J. F., and Olsenholler, J. A. (2012). Space-based observations of Eastern Hindu Kush glaciers between 1976 and 2007, Afghanistan and Pakistan. *Remote Sensing Letters*, 3(1):77–84.
- Scambos, T. A., Dutkiewicz, M. J., Wilson, J. C., and Bindschadler, R. A. (1992). Application of Image Cross-Correlation to the Measurement of Glacier Velocity Using Satellite Image Data. *Remote Sensing of Environment*, 42:177–186.
- Schiemann, R., Lüthi, D., and Schär, C. (2009). Seasonality and Interannual Variability of the Westerly Jet in the Tibetan Plateau Region*. *J. Climate*, 22(11):2940–2957.
- Schutz, B. E., Zwally, H. J., Shuman, C. A., Hancock, D., and DiMarzio, J. P. (2005). Overview of the ICESat Mission. *Geophys. Res. Lett.*, 32(21):L21S01.
- Shangguan, D., Liu, S., Ding, Y., Li, J., Zhang, Y., Ding, L., Wang, X., Xie, C., and Li, G. (2007). Glacier changes in the west Kunlun Shan from 1970 to 2001

- derived from Landsat TM/ETM+ and Chinese glacier inventory data. *Annals of Glaciology*, 46(1):204–208.
- Shi, Y., Liu, C., and Kang, E. (2009). The Glacier Inventory of China. *Annals of Glaciology*, 50(53):1–4.
- Shih, Y., Hsieh, T., Cheng, P., and Li, C. (1980). Distribution, features and variations of glaciers in China. In *Proceedings of the Riederlapp Workshop, Sep. 1978*.
- Short, N. H. and Gray, A. L. (2004). Potential for RADARSAT-2 interferometry: glacier monitoring using speckle tracking. *Canadian Journal of Remote Sensing*, 30(3):504–509.
- Shugar, D. H., Rabus, B. T., and Clague, J. J. (2010). Elevation changes (1949–1995) of Black Rapids Glacier, Alaska, derived from a multi-baseline InSAR DEM and historical maps. *Journal of Glaciology*, 56(198):625–634.
- Slobbe, D., Lindenbergh, R., and Ditmar, P. (2008). Estimation of volume change rates of Greenland’s ice sheet from ICESat data using overlapping footprints. *Remote Sensing of Environment*, 112(12):4204–4213.
- Sørensen, L. S., Simonsen, S. B., Nielsen, K., Lucas-Picher, P., Spada, G., Adalgeirsdottir, G., Forsberg, R., and Hvidberg, C. S. (2011). Mass balance of the Greenland ice sheet (2003–2008) from ICESat data – the impact of interpolation, sampling and firn density. *The Cryosphere*, 5(1):173–186.
- Vaughan, D., Comiso, J., Allison, I., Carrasco, J., Kaser, G., Kwok, R., Mote, P., Murray, T., Paul, F., Ren, J., Rignot, E., Solomina, O., Steffen, K., and Zhang, T. (2013). Observations: Cryosphere. In Stocker, T., Qin, D., Plattner, G., K., Tignor, M., Allen, S., Boschung, J., Nauels, A., Xia, Y., Bex, V., and Midgley, P., editors, *Climate Change 2013: The Physical Science Basis. Contribution of Working Group I to the Fifth Assessment Report of the Intergovernmental Panel on Climate Change*. Cambridge University Press, Cambridge, United Kingdom and New York, NY, USA.
- Ward, F. K. and Smith, M. (1934). The Himalaya East of the Tsangpo. *The Geographical Journal*, 84(5):369–394.
- Wei, J., Liu, S., Guo, W., Yao, X., Xu, J., Bao, W., and Jiang, Z. (2014). Surface-area changes of glaciers in the Tibetan Plateau interior area since the 1970s using recent Landsat images and historical maps. *Annals of Glaciology*, 55(66):213–222.
- Yao, T., Thompson, L., Yang, W., Yu, W., Gao, Y., Guo, X., Yang, X., Duan, K., Zhao, H., Xu, B., Pu, J., Lu, A., Xiang, Y., Kattel, D. B., and Joswiak, D. (2012). Different glacier status with atmospheric circulations in Tibetan Plateau and surroundings. *Nature Climate Change*, 2(9):663–667.
- Yao, T., Wang, Y., Liu, S., Pu, J., Shen, Y., and Lu, A. (2004). Recent glacial retreat in High Asia in China and its impact on water resource in Northwest China. *Science in China Series D: Earth Sciences*, 47(12):1065–1075.
- Yi, S. and Sun, W. (2014). Evaluation of glacier changes in high-mountain Asia based on 10 year GRACE RL05 models. *Journal of Geophysical Research: Solid Earth*, 119(3):2504–2517.
- Yihui, D. and Chan, J. C. L. (2005). The East Asian summer monsoon: an overview. *Meteorology and Atmospheric Physics*, 89(1-4):117–142.
- Zhang, G., Xie, H., Kang, S., Yi, D., and Ackley, S. F. (2011). Monitoring lake level changes on the Tibetan Plateau using ICESat altimetry data (2003–2009). *Remote Sensing of Environment*, 115(7):1733–1742.
- Zhang, G., Yao, T., Xie, H., Kang, S., and Lei, Y. (2013). Increased mass over the Tibetan Plateau: From lakes or glaciers? *Geophysical Research Letters*, 40(10):2125–2130.
- Zwally, H., Schutz, B., Abdalati, W., Abshire, J., Bentley, C., Brenner, A., Bufton, J., Dezio, J., Hancock, D., Harding, D., Herring, T., Minster, B., Quinn, K., Palm, S., Spinhrne, J., and Thomas, R. (2002). ICESat’s laser measurements of polar ice, atmosphere, ocean, and land. *Journal of Geodynamics*, 34(3–4):405–445.

A Glacier mass changes on the Tibetan Plateau 2003-2009 derived from ICESat laser altimetry measurements

Author contribution: study design, data preparation, data analysis, figures and writing.

Current status: published, *Environmental Research Letters*.

Glacier mass changes on the Tibetan Plateau 2003–2009 derived from ICESat laser altimetry measurements

N Neckel¹, J Kropáček^{1,2}, T Bolch^{2,3} and V Hochschild¹

¹ Institute of Geography, University of Tübingen, Rümelinstraße 19-23, D-72070 Tübingen, Germany

² Institute for Cartography, Dresden University of Technology, Helmholtzstraße 10, D-01062 Dresden, Germany

³ Department of Geography, University of Zurich, Winterthurer Straße 190, 8057 Zürich, Switzerland

E-mail: Niklas.Neckel@uni-tuebingen.de

Received 17 May 2013, revised 13 December 2013

Accepted for publication 18 December 2013

Published 15 January 2014

Abstract

Glacier mass changes are a valuable indicator of climate variability and monsoon oscillation on the underexplored Tibetan Plateau. In this study data from the Ice Cloud and Elevation Satellite (ICESat) is employed to estimate elevation and mass changes of glaciers on the Tibetan Plateau between 2003 and 2009. In order to get a representative sample size of ICESat measurements, glaciers on the Tibetan Plateau were grouped into eight climatically homogeneous sub-regions. Most negative mass budgets of -0.77 ± 0.35 m w.e. a^{-1} were found for the Qilian Mountains and eastern Kunlun Mountains while a mass gain of $+0.37 \pm 0.25$ m w.e. a^{-1} was found in the westerly-dominated north-central part of the Tibetan Plateau. A total annual mass budget of -15.6 ± 10.1 Gt a^{-1} was estimated for the eight sub-regions sufficiently covered by ICESat data which represents $\sim 80\%$ of the glacier area on the Tibetan Plateau. 13.9 ± 8.9 Gt a^{-1} (or 0.04 ± 0.02 mm a^{-1} sea-level equivalent) of the total mass budget contributed ‘directly’ to the global sea-level rise while 1.7 ± 1.9 Gt a^{-1} drained into endorheic basins on the plateau.

Keywords: glacier mass changes, ICESat, Tibetan Plateau, endorheic lakes


 Online supplementary data available from stacks.iop.org/ERL/9/014009/mmedia

1. Introduction

The Tibetan Plateau (TP) with an average altitude of more than 4000 m above sea-level is characterized by the presence of many glaciers and ice caps. The climate of the TP is mainly governed by the westerlies, as well as the south Asian and the south-east Asian monsoons. Since the magnitude of these climatic influences varies, different types of glaciers are present from maritime or temperate-type glaciers in the south-east to continental or polar-type glaciers in the north-west (Shih *et al* 1980, Huang 1990). However, direct measurements of

climatic parameters are sparse, especially in the western part of the TP and the circulation pattern of the monsoon system is still not fully understood. The variability of glaciers is a valuable indicator for climate variability in remote regions (e.g. Yao *et al* 2012). Furthermore a quantification of melt water recharge of Tibetan glaciers would help to understand the role of different climate components (temperature, precipitation and evaporation) in the lake-level oscillation of numerous lakes on the TP (Zhang *et al* 2011, Kropáček *et al* 2012, Phan *et al* 2012, Zhang *et al* 2013). Lake-level changes are also of direct impact to the local population as increasing levels are flooding pastures (Yao *et al* 2007).

In the last decade several studies used remote sensing techniques to account for areal changes of glaciers in this large and remote region (e.g. Ding *et al* 2006, Liu *et al* 2006, Ye *et al*

 Content from this work may be used under the terms of the [Creative Commons Attribution 3.0 licence](http://creativecommons.org/licenses/by/3.0/). Any further distribution of this work must maintain attribution to the author(s) and the title of the work, journal citation and DOI.

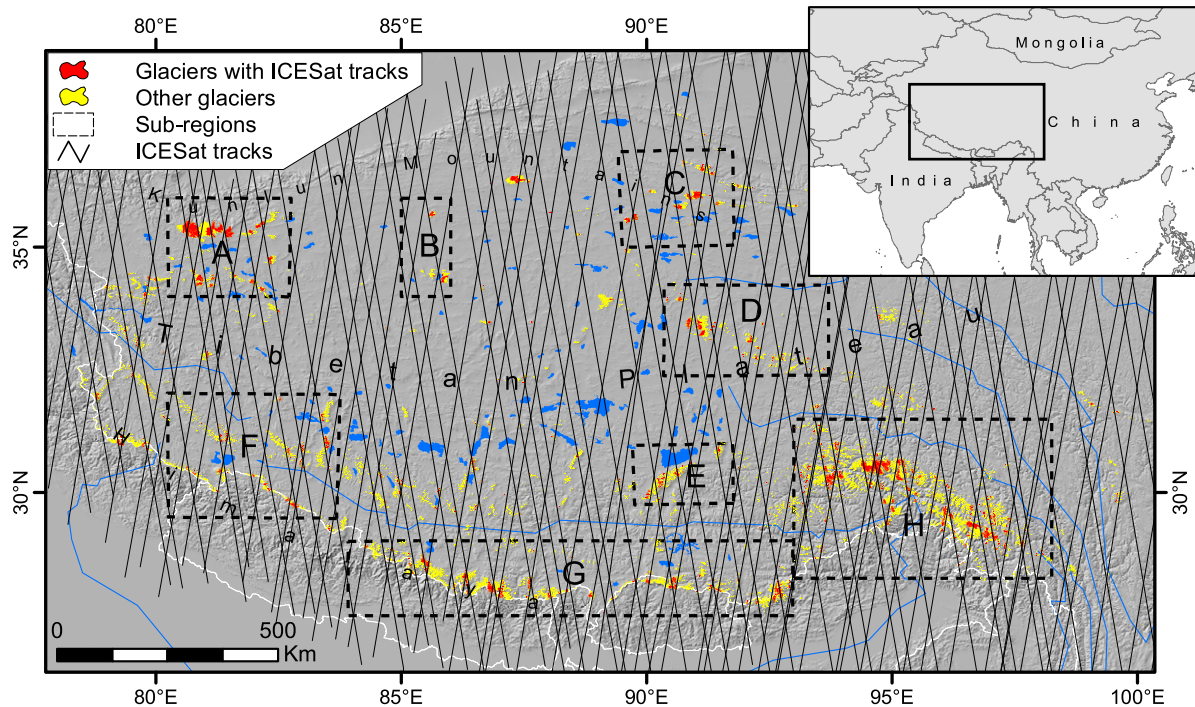


Figure 1. Overview of the study area including ICESat data coverage. Glacier outlines are based on the Chinese Glacier Inventory (CGI) (Li 2003, Shi *et al* 2009). Sub-regions are marked as black boxes and are sorted by alphabetical order with A = western Kunlun Mountains, B = Zangser Kangri and Songzhi Peak, C = Qilian Mountains and eastern Kunlun Mountains, D = Tanggula Mountains and Dongkemadi Ice Cap, E = western Nyainqentanglha range, F = Gangdise Mountains, G = central and eastern Tibetan Himalaya, H = eastern Nyainqentanglha range and Hengduan Mountains.

2006, Bolch *et al* 2010). However, glacier area changes provide only an indirect signal while the glacier mass budget shows the immediate reaction to climate variability (Oerlemans 2001). Laser altimetry data acquired by the Geoscience Laser Altimeter System (GLAS) carried on-board the Ice Cloud and Elevation Satellite (ICESat) were proven to be an accurate data source for the regional estimation of glacier elevation changes (Kääb *et al* 2012, Bolch *et al* 2013, Gardner *et al* 2013). Kääb *et al* (2012) estimated trends in glacier elevation changes for the Himalaya and Hindu Kush region leaving the TP unobserved. A recent study estimated global glacier mass changes using glaciological mass balance measurements, data from the Gravity Recovery And Climate Experiment (GRACE) and ICESat data, including High Mountain Asia (Gardner *et al* 2013). In this study we focus in detail on trends in glacier elevation and mass changes within eight sub-regions on the TP (figure 1) for the last decade and discuss our results in comparison to existing, but sparse, *in situ* measurements and recent remote sensing studies (e.g. Yao *et al* 2012, Gardner *et al* 2013, Neckel *et al* 2013). The investigated region contains a total ice cover of ~32 400 km² according to the first Chinese Glacier Inventory (CGI) (Li 2003, Shi *et al* 2009) which accounts for ~80% of the Tibetan ice cover.

2. Data and method

ICESat GLAS data and the digital elevation model (DEM) acquired by the Shuttle Radar Topography Mission (SRTM)

in February 2000 (Rabus *et al* 2003, Farr *et al* 2007) were employed to calculate volume changes of Tibetan glaciers. ICESat was launched in January 2003 hosting three laser sensors within the GLAS. The laser channels for surface altimetry operated at a wavelength of 1064 nm with footprints spaced at about 172 m along track and a diameter on the surface of about 70 m (Zwally *et al* 2002, Brenner *et al* 2003). The ICESat mission was conducted during 18 laser periods, each lasting between 12 and 55 days. As ICESat's precision spacecraft pointing control was not used in mid-latitudes between 59°S and 59°N individual repeated tracks do not match exactly but can be separated across track by up to 3000 m in our study area. Due to this fact and because of the rugged topography of the TP, cross-over and along-track processings of ICESat data (e.g. Brenner *et al* 2007, Slobbe *et al* 2008, Moholdt *et al* 2010) cannot be applied here. However, two recent studies proved the suitability of ICESat data in deriving elevation changes of mountain glaciers (Kääb *et al* 2012, Gardner *et al* 2013). Similar to Rinne *et al* (2011), Kääb *et al* (2012) and Gardner *et al* (2013) we used an independent DEM as a reference surface on which we compared ICESat elevation measurements. In this study we used version 3 of the SRTM C-band DEM (90 m grid spacing, hereinafter SRTM-C DEM).

Glaciers on the TP are small compared to the large polar ice sheets and ice caps and ICESat measurements over Tibetan glaciers are sparse. However, a sufficient number of ICESat measurements acquired in one track is needed in order to perform a statistical sound analysis. Therefore glaciers were

Table 1. Regional trends of glacier elevation changes are shown next to the area weighted mass balance, total glacier area in each sub-region and the percentage of the glacier area in each sub-region draining into endorheic basins. Geographic location of sub-regions is shown in figure 1 and trend lines are shown in figure 2. Statistical significant trends are illustrated as bold numbers.

Sub-region	ΔH trend accumulation area (m a ⁻¹)	ΔH trend ablation area (m a ⁻¹)	ΔH trend on-glacier area (m a ⁻¹)	ΔH trend off-glacier area (m a ⁻¹)	Mass balance (m w.e. a ⁻¹)	Total glacier area (km ²)	Drainage into endorheic basins (%)
A	—	+0.04 ± 0.29	+0.04 ± 0.29 ^a	-0.11 ± 0.08	+0.03 ± 0.25 ^a	6 483	43
B	+0.50 ± 0.30	-0.05 ± 0.26	+0.44 ± 0.26	+0.02 ± 0.02	+0.37 ± 0.25	464	100
C	-0.45 ± 0.31	-1.40 ± 0.51	-0.90 ± 0.28	-0.09 ± 0.05	-0.77 ± 0.35	1 491	100
D	+0.55 ± 0.33	-0.68 ± 0.35	-0.68 ± 0.29	-0.04 ± 0.02	-0.58 ± 0.31	1 859	30
E	-0.23 ± 0.33	—	-0.23 ± 0.33 ^b	+0.01 ± 0.02	-0.20 ± 0.29 ^b	1 056	38
F	-0.31 ± 0.28	-1.30 ± 0.47	-0.44 ± 0.26	+0.02 ± 0.02	-0.37 ± 0.25	2 371	42
G	-0.46 ± 0.31	-1.15 ± 0.44	-0.78 ± 0.27	+0.03 ± 0.04	-0.66 ± 0.32	6 632	2
H	-0.71 ± 0.38	-0.85 ± 0.41	-0.81 ± 0.32	+0.15 ± 0.07	-0.69 ± 0.36	12 017	0

^a Data only available in ablation area.

^b Data only available in accumulation area.

grouped into eight compact sub-regions where we assume climatologically homogeneous conditions (figure 1). In order to test if the selected sub-regions are sufficiently covered by ICESat measurements we compared the area elevation distribution of the ICESat measurements with the glacier hypsometry in all sub-regions (figure S1(a), available at stacks.iop.org/ERL/9/014009/mmedia). For most sub-regions the deviation is within ±15% with the highest deviation of +20% in sub-region F. Additionally, we conducted a bootstrapping analysis in which we iteratively included a random selection of ICESat footprints (figure S2, available at stacks.iop.org/ERL/9/014009/mmedia). Both analyses confirm that the eight sub-regions are covered relatively well by the ICESat dataset. The eight sub-regions contain a total ice cover of ~32 400 km² which accounts for ~80% of the glacier area on the TP. As the CGI tends to be spatially inaccurate, ICESat measurements on glaciers were manually selected based on the most recent cloud free Landsat scenes (Thematic Mapper, Level 1, acquisition between 2003 and 2011) obtained from the web archive of the USGS.

We used bilinear interpolation to extract the SRTM-C surface elevation, at the exact location of each ICESat measurement. ICESat measurements were excluded from the analysis if the difference between ICESat and SRTM-C elevation exceeded 150 m, which is attributed to cloud cover or atmospheric noise during the time of data acquisition. The elevation difference ΔH between each ICESat footprint and the SRTM-C DEM was calculated by

$$\Delta H = H^{\text{ICESat}} - H^{\text{SRTM}} \quad (1)$$

where H^{ICESat} and H^{SRTM} are the elevation measurements of both datasets. As on the TP most glaciers receive very low precipitation rates predominantly occurring in the summer (Ageta and Fujita 1996, Böhner 2006, Maussion *et al* 2013), multi-seasonal linear trends were fitted through all ΔH values. In order to make our results comparable to other studies we calculated mass balance estimates in water equivalent (w.e.), using the CGI for information on glacier area (Li 2003, Shi *et al* 2009). For volume to mass conversion we used an average ice density of $850 \pm 60 \text{ kg m}^{-3}$ (Huss 2013). Mass

balance estimates were calculated for all glaciers covered by ICESat. An area weighted upscaling was performed for each sub-region using the CGI for information on glacier area. For the calculation of the percentage of glacier area draining into endorheic basins we employed the HydroSHEDS dataset (Lehner *et al* 2006). Following Kääb *et al* (2012) mass balances were also calculated from ΔH trends, solely based on autumn acquisitions (table S2 and figure S8 available at stacks.iop.org/ERL/9/014009/mmedia).

Considering glacier flow, mass balance estimates were calculated for ΔH trends integrated over the entire glacier area. However, in order to look at differences in glacier thinning with respect to altitude, to detect unusual behavior such as glacier surging and to discuss the influence of surface elevation gain due to possible snow accumulation we also calculated ΔH trends separately for the accumulation and ablation areas in each sub-region (figure 2). The equilibrium line altitude (ELA) values used for the separation into accumulation and ablation areas are shown in table S1 available at stacks.iop.org/ERL/9/014009/mmedia.

3. Results

Our results reveal a heterogeneous wastage of glaciers and ice caps across the TP (figure 2, table 1). It should be noted, that ΔH trends were fitted through all ΔH values, however for a better visual representation only the ΔH median of each laser period is shown in figure 2. Due to this fact, small offsets may occur between the ΔH medians and the trend lines (e.g. in sub-region A). The separate calculation of ΔH trends in the accumulation and ablation area revealed an offset of several meters between both trends in each sub-region (figure 2) which can be attributed to the different penetration of the SRTM C-band into snow, firn and ice (Rignot *et al* 2001, Gardelle *et al* 2012).

We determined on average a decrease of glacier surface elevations between 2003 and 2009 but also found positive trends for two sub-regions. The highest specific mass loss was found for the Qilian Mountains and eastern Kunlun Mountains ($-0.77 \pm 0.35 \text{ m w.e. a}^{-1}$) located in the north-eastern part of

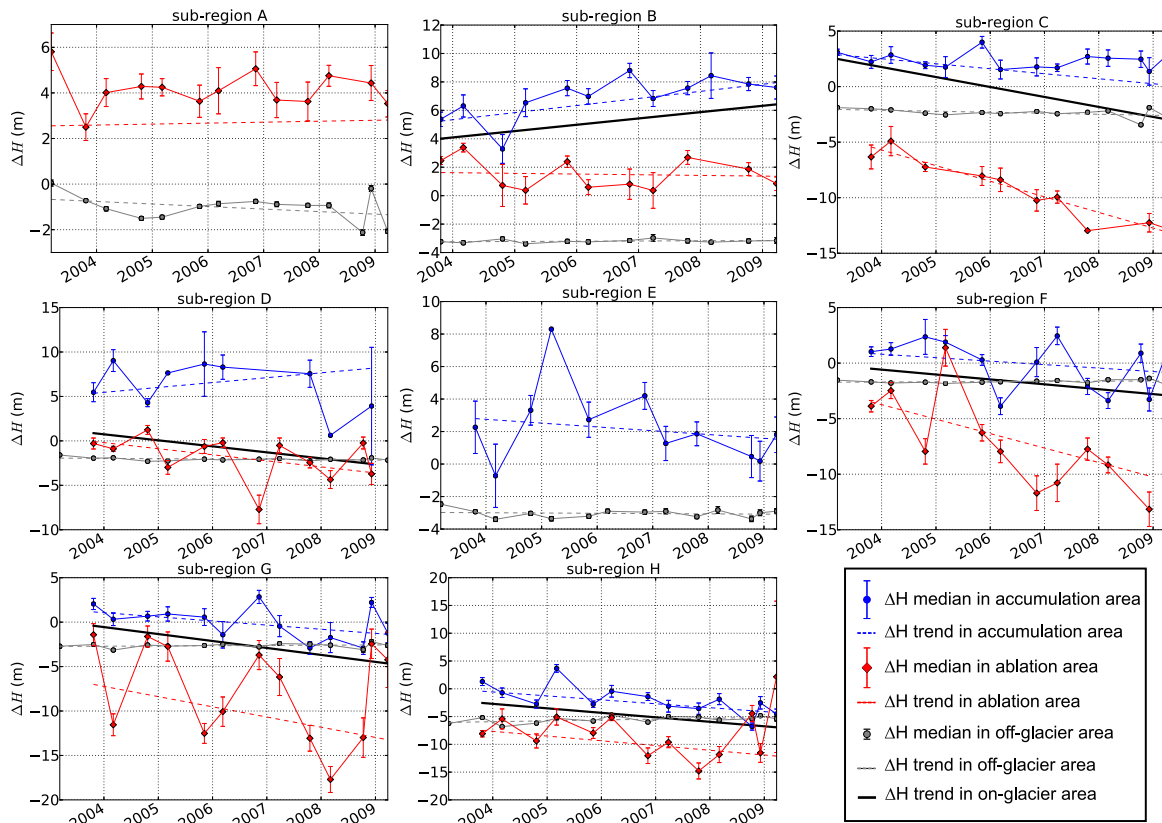


Figure 2. Estimated trends for selected geographic sub-regions as shown in figure 1. Trends were fitted through all ΔH values in on- and off-glacier areas. For on-glacier areas trends are shown separately for the accumulation and ablation areas as well as for the whole glacier area. For clarity reasons only the ΔH median of each laser period is shown. Year dates correspond to 1 January of each year.

the TP, the eastern Nyainqentanglha range and Hengduan Mountains ($-0.69 \pm 0.36 \text{ m.w.e. a}^{-1}$) and the central and eastern Tibetan Himalaya ($-0.66 \pm 0.32 \text{ m.w.e. a}^{-1}$), regions which are predominantly monsoon-influenced. In contrast, the continental westerly-influenced north-western (western Kunlun Mountains) and north-central mountains (Zangser Kangri and Songzhi Peak) showed evidence for balanced mass budgets or a slight mass gain. For the latter peaks which are covered by ice caps, we detected glacier thinning at lower elevations while a simultaneous glacier thickening was observed at higher elevations (figure 2, sub-region B). The same altitude depended pattern is found for the Tanggula Mountains and Dongkemadi Ice Cap (figure 2, sub-region D), except that the overall mass balance is negative in this sub-region ($-0.58 \pm 0.31 \text{ m.w.e. a}^{-1}$). The western Kunlun Mountains (sub-region A) are characterized by a heterogeneous behavior of glacier elevation changes. Here we found significant surface lowering in the accumulation areas of some glaciers with a simultaneous elevation increase at ICESat footprints in ablation areas, indicating the occurrence of glacier surges in this sub-region. The highest mass loss and contribution to sea-level rise is comprised from the strongly glacierized eastern Nyainqentanglha range and Hengduan Mountains with $-8.3 \pm 4.3 \text{ Gt a}^{-1}$ (or $0.02 \pm 0.01 \text{ mm a}^{-1}$ sea-level equivalent, sub-region H). In sum, we estimated a total annual mass budget of $-15.6 \pm 10.1 \text{ Gt a}^{-1}$ for the eight sub-regions, of which $1.7 \pm 1.9 \text{ Gt a}^{-1}$ were not leaving the TP as stream

flow but drained into endorheic lakes on the plateau. Glaciers draining into the endorheic Tarim Basin in the north of the TP showed on average balanced mass budgets.

4. Discussion

In this study two almost global datasets, the ICESat GLA 14 product and the SRTM-C DEM were used to conduct a regional study of trends in glacier surface elevation changes. The main problem when utilizing ICESat data to estimate elevation changes of glaciers in mid-latitudes is the large distance between ICESat tracks and the corresponding limited data coverage of mountain glaciers. However, recent studies have proven that ICESat is an accurate data source if the available data sample is statistically suitable for a region, i.e. if the investigated region and its ice covered area is large enough (Kääb *et al* 2012, Bolch *et al* 2013, Gardner *et al* 2013). In our approach, we assume no prominent snow accumulation period in high elevations on the TP and fitted trends through multi-seasonal ICESat acquisitions. This way, the statistical significance increased due to a higher number of measurements in the data-sparse sub-regions. On the TP a multi-seasonal data fit can be justified for several reasons. (1) The north-western part of the plateau receives very low precipitation rates in winter, although winter precipitation is predominant in this region (Böhner 2006). (2) In the south-eastern part accumulation and ablation at higher elevations is related to monsoon precipitation

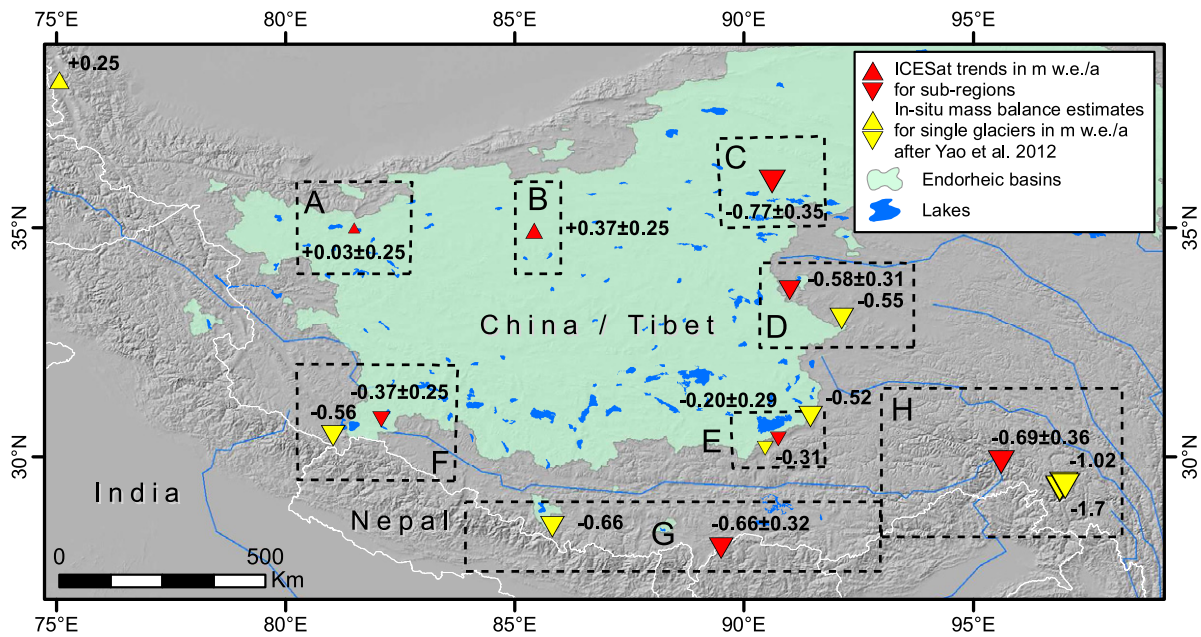


Figure 3. Mass balance estimates in m.w.e. a^{-1} derived from ICESat measurements in comparison to *in situ* mass balance measurements of single glaciers (2006–2010, Yao *et al* 2012).

in summer (Ageta and Fujita 1996, Kang *et al* 2009). (3) A recent study of Maussion *et al* (2013) showed that the majority of glaciers on the central TP are accumulating mass in summer. (4) We also conducted our analysis solely based on autumn acquisitions (figure S8 and table S2, available at stacks.iop.org/ERL/9/014009/mmedia). The resulting trends are similar as for the multi-seasonal data and agree within their error bars. The mean and maximum difference between the multi-seasonal ΔH trends and the autumn ΔH trends were estimated at 0.06 m a^{-1} and 0.33 m a^{-1} respectively. However, the sparser sampling distribution of the autumn laser periods led to statistical insignificant ΔH trends in some of the sub-regions.

Our study tends to agree with other studies which show similar regional patterns of glacier changes in the Himalaya (Bolch *et al* 2012, Käab *et al* 2012, Gardelle *et al* 2013) and on the TP (figure 3) (Yao *et al* 2012, Gardner *et al* 2013). However, we show some more details on the spatial variability within Tibet and consider also the drainage into endorheic basins separately.

The bigger picture shows an overall negative trend in glacier mass budgets with the highest specific mass loss in the monsoon-influenced north-eastern and south-eastern margins and balanced mass budgets in the more westerly-influenced north-western regions. A direct comparison between the studies is difficult as the studied sub-regions are not identical and the time span of observations is also partly different.

For the western Kunlun Mountains (sub-region A), we estimated slightly positive trends in glacier elevation changes. However, we found strong data noise of up to $\pm 80 \text{ m}$ for ΔH in the accumulation area so that no meaningful trend could be derived here. Although our estimate of $+0.04 \pm 0.29 \text{ m a}^{-1}$ in the ablation area is not statistically significant a balanced glacier regime can be assumed for the western

Kunlun Mountains which is in agreement with Gardner *et al* (2013). It should be noted that large variations in glacier area changes with several advancing glaciers are reported in this region (Shangguan *et al* 2007, Scherler *et al* 2011, Yao *et al* 2012). Also the results of Maussion *et al* (2013) suggest different accumulation regimes for the north and south facing slopes of the western Kunlun Mountains. Our study seems to confirm that the western Kunlun Mountains show a similar anomaly than the neighboring Pamir and also the Karakoram Mountains (Gardelle *et al* 2013). However, this possible western Kunlun anomaly needs further investigation as our study revealed that the ICESat estimate stretches its limits in sub-regions with heterogeneous behavior of glaciers. It is therefore recommended to calculate ΔH trends separately for the accumulation and ablation areas.

Possible positive mass budgets were also found for the large ice fields of Zangser Kangri and Songzhi Peak (sub-region B). Here we found a positive trend in the accumulation area, while glacier thinning was observed in lower regions suggesting strong firn and snow accumulation. We therefore tested a lower density of 600 kg m^{-3} for the conversion from volume to mass which revealed a smaller mass gain of $+0.26 \pm 0.18 \text{ m.w.e. a}^{-1}$. This value seems more appropriate than the proposed estimate of $+0.37 \pm 0.25 \text{ m.w.e. a}^{-1}$ (table 1) but is also covered by our error estimate.

For the Tanggula Mountains and Dongkemadi Ice Cap (sub-region D) the overall trend follows the trend of the ablation area due to sparse data sampling in the accumulation area. However, strong mass loss in ablation regions led to an overall significant negative mass budget for this sub-region. Such a behavior is also common for ice caps in arctic regions (Gardner *et al* 2011, Bolch *et al* 2013) while on the central TP (e.g. in sub-region B) the mass loss in the ablation area is

probably compensated by strong accumulation (Neckel *et al* 2013).

Our results for the central and eastern Tibetan Himalaya are in agreement with Gardner *et al* (2013) (sub-region G, this study: $-0.78 \pm 0.27 \text{ m a}^{-1}$, Gardner *et al* (2013): $-0.89 \pm 0.18 \text{ m a}^{-1}$) but are clearly more negative than the values from Kääb *et al* (2012). The difference is difficult to investigate as the sample regions do not match and therefore different glaciers were sampled. Similar to the Himalayan region, the ICESat derived mass budgets for the eastern Nyainqentanglha range and the Hengduan Mountains (sub-region H) are more negative than the results based on DEM differencing between 1999 and 2010 (Gardelle *et al* 2013). The authors of the latter study state in their paper that mass losses measured with ICESat tend to be slightly larger than their estimates. In addition, different glaciers were measured over a slightly different time span in both studies, making a direct comparison difficult.

Our results seem to be in contradiction to the findings of Jacob *et al* (2012) which showed an increase in mass from GRACE measurements between 2003 and 2010 on the TP. However, a recent study by Zhang *et al* (2013) attributed this increase in mass predominately to an increase in lake level/mass rather than to an increase in glacier mass. This observation is in agreement with our study as most of the eight sub-regions showed a negative mass balance for the studied time period. However, the estimated negative mass budgets could not be detected by GRACE as many glaciers on the TP drain into endorheic lakes. This amount is estimated at $1.7 \pm 1.9 \text{ Gt a}^{-1}$ in this study. It should therefore be noted that only $13.9 \pm 8.9 \text{ Gt a}^{-1}$ (or $0.04 \pm 0.02 \text{ mm a}^{-1}$ sea-level equivalent) of our total annual mass budget estimate can directly contribute to the global sea-level rise, while the majority of the remaining mass loss can likely be linked to the observed rise of the lake levels (Zhang *et al* 2011, Kropáček *et al* 2012, Phan *et al* 2012). Similar to the fact that the rising sea-level threatens coastal areas on the globe, the rising lake levels pose problems to the local population as pastures are often situated close to the lakes and will be flooded (e.g. Yao *et al* 2007).

5. Conclusions

This study presents glacier surface elevation changes and mass budget estimations for almost the entire TP for the period 2003–2009 including central TP where no previous mass balance estimates exist. The fitting of multi-seasonal ICESat elevation differences in combination with density assumptions enabled us to derive meaningful estimates of glacier mass changes for eight detailed sub-regions on the TP. A total annual mass budget of $-15.6 \pm 10.1 \text{ Gt a}^{-1}$ was estimated for the eight sub-regions which includes $\sim 80\%$ of the glacier area on the TP. Of the estimated total mass budget $13.9 \pm 8.9 \text{ Gt a}^{-1}$ (or $0.04 \pm 0.02 \text{ mm a}^{-1}$ sea-level equivalent) contributed directly to the global sea-level rise while $1.7 \pm 1.9 \text{ Gt a}^{-1}$ drained into endorheic basins, i.e. were not leaving the TP as stream flow. Glaciers in the north-central part of the TP were probably gaining mass while glaciers in the south-eastern part were

significantly losing mass between 2003 and 2009. These trends were found to be in agreement with the few existing *in situ* mass balance measurements and several recent remote sensing studies. Hence, this study confirms that ICESat data in combination with a detailed DEM provides a valuable source of information about elevation changes of mountain glaciers on a regional scale.

Acknowledgments

This work was supported by the German Federal Ministry of Education and Research (BMBF) Programme Central Asia—Monsoon Dynamics and Geo-Ecosystems (CAME) within the WET project (Variability and Trends in Water Balance Components of Benchmark Drainage Basins on the Tibetan Plateau) under the code 03G0804D and by the German Research Foundation (DFG) Priority Programme 1372, Tibetan Plateau: Formation—Climate—Ecosystems within the DynRG-TiP (Dynamic Response of Glaciers on the Tibetan Plateau to Climate Change) project under the code BU 949/20-3. T Bolch acknowledges the funding through DFG (BO 3199/2-1) and the European Space Agency (ESA) project Glaciers_cci (400010177810I-AM). We are thankful for the cooperation with the Institute for Tibetan Plateau Research (ITP), Beijing. We acknowledge NSIDC for hosting the ICESat data and the CGI dataset. SRTM-C data and Landsat imagery were obtained from the USGS. The valuable comments of two anonymous referees and of the scientific editor significantly improved the letter.

References

- Ageta Y and Fujita K 1996 Characteristics of mass balance of summer-accumulation type glaciers in the Himalayas and the Tibetan Plateau *Z. Gletscherkunde G.* **32** 61–5
- Böhner J 2006 General climatic controls and topoclimatic variations in central and high Asia *Boreas* **35** 279–95
- Bolch T, Sørensen L S, Simonsen S B, Mölg N, Machguth H, Rastner P and Paul F 2013 Mass loss of Greenland's glaciers and ice caps 2003–2008 revealed from ICESat laser altimetry data *Geophys. Res. Lett.* **40** 875–81
- Bolch T, Yao T, Kang S, Buchroithner M F, Scherer D, Maussion F, Huintjes E and Schneider C 2010 A glacier inventory for the western Nyainqentanglha range and the Nam Co Basin, Tibet, and glacier changes 1976–2009 *Cryosphere* **4** 419–33
- Bolch T *et al* 2012 The state and fate of Himalayan glaciers *Science* **336** 310–4
- Brenner A C, DiMarzio J P and Zwally H J 2007 Precision and accuracy of satellite radar and laser altimeter data over the continental ice sheets *IEEE Trans. Geosci. Remote Sens.* **45** 321–31
- Brenner A C *et al* 2003 Derivation of range and range distributions from laser pulse waveform analysis for surface elevations, roughness, slope, and vegetation heights *Technical Report NASA Goddard Space Flight Center*
- Ding Y, Liu S, Li J and Shanguan D 2006 The retreat of glaciers in response to recent climate warming in western China *Ann. Glaciol.* **43** 97–105
- Farr T G *et al* 2007 The Shuttle Radar Topography Mission *Rev. Geophys.* **45** RG2004
- Gardelle J, Berthier E and Arnaud Y 2012 Impact of resolution and radar penetration on glacier elevation changes computed from DEM differencing *J. Glaciol.* **58** 419–22

- Gardelle J, Berthier E, Arnaud Y and Kääb A 2013 Region-wide glacier mass balances over the Pamir–Karakoram–Himalaya during 1999–2011 *Cryosphere* **7** 1263–86
- Gardner A S, Moholdt G, Wouters B, Wolken G J, Burgess D O, Sharp M J, Cogley J G, Braun C and Labine C 2011 Sharply increased mass loss from glaciers and ice caps in the Canadian Arctic archipelago *Nature* **473** 357–60
- Gardner A S et al 2013 A reconciled estimate of glacier contributions to sea level rise: 2003 to 2009 *Science* **340** 852–7
- Huang M 1990 On the temperature distribution of glaciers in China *J. Glaciol.* **36** 210–6
- Huss M 2013 Density assumptions for converting geodetic glacier volume change to mass change *Cryosphere* **7** 877–87
- Jacob T, Wahr J, Pfeffer W T and Swenson S 2012 Recent contributions of glaciers and ice caps to sea level rise *Nature* **482** 514–8
- Kääb A, Berthier E, Nuth C, Gardelle J and Arnaud Y 2012 Contrasting patterns of early twenty-first-century glacier mass change in the Himalayas *Nature* **488** 495–8
- Kang S, Chen F, Gao T, Zhang Y, Yang W, Yu W and Yao T 2009 Early onset of rainy season suppresses glacier melt: a case study on Zhadang glacier, Tibetan Plateau *J. Glaciol.* **55** 755–8
- Kropáček J, Braun A, Kang S, Feng C, Ye Q and Hochschild V 2012 Analysis of lake level changes in Nam Co in central Tibet utilizing synergistic satellite altimetry and optical imagery *Int. J. Appl. Earth Observ. Geoinform.* **17** 3–11
- Lehner B, Verdin K and Jarvis A 2006 *HydroSHEDS Technical Documentation* (Washington, DC: World Wildlife Fund US) available at <http://hydrosheds.cr.usgs.gov>
- Li X 2003 *GLIMS Glacier Database* (Boulder, CO: National Snow and Ice Data Center/World Data Center for Glaciology) Digital Media www.glims.org
- Liu S, Shangguan D, Ding Y, Han H, Xie C, Zhang Y, Li J, Wang J and Li G 2006 Glacier changes during the past century in the Gangrigabu mountains, southeast Qinghai-Xizang (Tibetan) Plateau, China *Ann. Glaciol.* **43** 187–93
- Maussion F, Scherer D, Mölg T, Collier E, Curio J and Finkelnburg R 2013 Precipitation seasonality and variability over the Tibetan Plateau as resolved by the High Asia Reanalysis *J. Clim.* in press
- Moholdt G, Hagen J O, Eiken T and Schuler T V 2010 Geometric changes and mass balance of the Austfonna ice cap, Svalbard *Cryosphere* **4** 21–34
- Neckel N, Braun A, Kropáček J and Hochschild V 2013 Recent mass balance of the Purogangri Ice Cap, central Tibetan Plateau, by means of differential X-band SAR interferometry *Cryosphere* **7** 1623–33
- Oerlemans J 2001 *Glaciers and Climate Change* (Rotterdam: A. A. Balkema Publishers)
- Phan V H, Lindenberg R and Menenti M 2012 ICESat derived elevation changes of Tibetan lakes between 2003 and 2009 *Int. J. Appl. Earth Observ. Geoinform.* **17** 12–22
- Rabus B, Eineder M, Roth A and Bamler R 2003 The shuttle radar topography mission—a new class of digital elevation models acquired by spaceborne radar *ISPRS J. Photogramm. Remote Sens.* **57** 241–62
- Rignot E, Echelmeyer K and Krabill W 2001 Penetration depth of interferometric synthetic-aperture radar signals in snow and ice *Geophys. Res. Lett.* **28** 3501–4
- Rinne E J, Shepherd A, Palmer S, van den Broeke M R, Muir A, Ettema J and Wingham D 2011 On the recent elevation changes at the Flade Isblink Ice Cap, northern Greenland *J. Geophys. Res.* **116** F03024
- Scherler D, Bookhagen B and Strecker M R 2011 Spatially variable response of Himalayan glaciers to climate change affected by debris cover *Nature Geosci.* **4** 156–9
- Shangguan D, Liu S, Ding Y, Li J, Zhang Y, Ding L, Wang X, Xie C and Li G 2007 Glacier changes in the west Kunlun Shan from 1970 to 2001 derived from Landsat TM/ETM+ and Chinese glacier inventory data *Ann. Glaciol.* **46** 204–8
- Shi Y, Liu C H and Kang E S 2009 The Glacier Inventory of China *Ann. Glaciol.* **50** 1–4
- Shih Y, Hsieh T, Cheng P and Li C 1980 Distribution, features and variations of glaciers in China *Proc. Riederalp Workshop (Sep. 1978)* **126** 111–6
- Slobbe D, Lindenberg R and Ditmar P 2008 Estimation of volume change rates of Greenland's ice sheet from ICESat data using overlapping footprints *Remote Sens. Environ.* **112** 4204–13
- Yao T, Pu J, Lu A, Wang Y and Yu W 2007 Recent glacial retreat and its impact on hydrological processes on the Tibetan Plateau, China, and surrounding regions *Arctic, Antarctic, Alpine Res.* **39** 642–50
- Yao T et al 2012 Different glacier status with atmospheric circulations in Tibetan Plateau and surroundings *Nature Clim. Change* **2** 663–7
- Ye Q, Kang S, Chen F and Wang J 2006 Monitoring glacier variations on Geladandong mountain, central Tibetan Plateau, from 1969 to 2002 using remote-sensing and GIS technologies *J. Glaciol.* **179** 537–45
- Zhang G, Xie H, Kang S, Yi D and Ackley S F 2011 Monitoring lake level changes on the Tibetan Plateau using ICESat altimetry data (2003–2009) *Remote Sens. Environ.* **115** 1733–42
- Zhang G, Yao T, Xie H, Kang S and Lei Y 2013 Increased mass over the Tibetan Plateau: from lakes or glaciers? *Geophys. Res. Lett.* **40** 2125–30
- Zwally H et al 2002 ICESat's laser measurements of polar ice, atmosphere, ocean, and land *J. Geodyn.* **34** 405–45

Glacier mass changes on the Tibetan Plateau 2003 – 2009 derived from ICESat laser altimetry measurements (Supplementary Material)

N. Neckel¹, J. Kropáček^{1,2}, T. Bolch^{2,3}, and V. Hochschild¹

¹Institute of Geography, University of Tübingen, Rümelinstr. 19-23, 72070 Tübingen, Germany

²Institute for Cartography, Dresden University of Technology, Helmholtzstr. 10, 01062 Dresden, Germany

³Department of Geography, University of Zurich, Winterthurer Str. 190, 8057 Zürich, Switzerland

E-mail: Niklas.Neckel@uni-tuebingen.de

Additional information on data

In this study we chose the GLA 14 product over the GLA 06 product, which is frequently used to derive ice sheet elevations, because of the mountainous topography and crevassed glacier surfaces in our study area (Kääb, 2008). The main difference between the GLA 06 and GLA 14 data product is the higher number of Gaussian fits applied to the return signal of the GLA 14 data. The GLAS elevation data, originally referenced to the Topex/Poseidon ellipsoid, were adjusted to the WGS84 ellipsoid following Bhang et al. (2007) and corrected for EGM96-geoid variations obtained from the GLA 14 dataset. The recently announced range determination error of ± 6 cm in the ICESat data can be neglected as the GLA 14 product seems to be not affected by this error (Zwally, 2013). The approximate June laser periods (2C, 3C, 3F) were excluded from the analysis as they only include the first three years of ICESat's lifetime and could therefore bias the results. Also laser period 2F was excluded from the analysis due to a failure of the laser in this period.

In this study we use version 3 of the SRTM-C DEM (90 m grid spacing) which is available to the public via the U.S. Geological Survey (USGS) at dds.cr.usgs.gov/srtm/version2_1/SRTM3/. Compared to version 4 of the DEM no timely inconsistent data patches and interpolation artifacts are present in version 3 and no horizontal misalignment between version 3 and the ICESat data is found which is in agreement with Kääb et al. (2012, their supplementary information). However, data gaps are present in version 3 of the DEM but are located in off-glacier areas in our study region. The vertical reference of the SRTM-C DEM is the EGM96-geoid.

Additional information on methods

For the separation into accumulation and ablation areas in each sub-region, Equilibrium Line Altitude (ELA) values were selected from the literature (Table S 1). The data describing the ELA on the TP are sparse and heterogeneous both in terms of the acquisition method and date taken. Some authors used field measurements (Ageta et al., 1989; Pu et al., 2008; Fujita and Nuimura, 2011) while others reconstructed the ELA using a model (Ageta and Kadota, 1992; Benn and Lehmkühl, 2000; Caidong and Sorteberg, 2010). Due to the sparse spatial data coverage of published ELA values, additional information was derived from recent Landsat imagery acquired in September/October 2010 (Thematic Mapper, Level 1, acquisition). The snowline was manually selected for several glaciers with different angles of inclination and slope in the relevant sub-regions. The mean of the snowline elevations was used as an approximate ELA in the respective sub-regions. For comparison we calculated the median glacier elevation in each sub-region which gives a rough approximation of the ELA if the glaciers are in equilibrium (Raper and Braithwaite, 2009). In order to test the sensitivity to a changing ELA we added ± 150 m to our ELA estimates, which revealed a mean difference of $\pm 30\%$ for the derived ΔH trends.

Supplementary Table S 1. Equilibrium line altitude (ELA) values for the eight sub-regions. Also shown glacier median elevation in each sub-region, year of ELA estimate and data source.

sub-region	median (m)	ELA (m)	year	source
A	5,944	5,930	1987	Ageta et al. (1989)
B	5,867	5,835	2010	Landsat estimate
C	5,372	5,300	2010	Landsat estimate
D	5,635	5,740	2002	Pu et al. (2008)
E	5,756	5,770	2005	Caidong and Sorteberg (2010)
F	5,757	5,600	2005	Fujita and Nuimura (2011)
G	5,512	5,500	2010	Landsat estimate
H	4,871	4,860	1989	Ageta and Kadota (1992)

It is known that ICESat measurements tend to get inaccurate on slopes $>10^\circ$ (e.g. Hilbert and Schmullius, 2012). We therefore tested the sensitivity of ΔH trends on slopes $<10^\circ$, which revealed a mean difference of -0.04 m a^{-1} for the ΔH trends in all sub-regions with the highest deviation of -0.26 m a^{-1} in sub-region G where 50% of on-glacier ICESat footprints were excluded. Due to the large number of discarded ICESat measurements no slope threshold was applied for our final estimate.

Error computation

In order to test the representativeness of ICESat coverage we employed a bootstrapping analysis (e.g. Kääh et al., 2012). Here we included random ICESat footprints in 10% intervals and calculated ΔH trends after each iteration. After 200 iterations we calculated the standard deviation of trends which is shown in Figure S 2 (all acquisitions) and Figure S 7 (autumn acquisitions) and fitted a polynomial to the data. As at some point the standard deviation of trends reaches a stable value we included the polynomial value where 100% of the ICESat footprints are included in the analysis as an error for the uneven spatial data sampling in our error estimate. This value reaches from 0.09 m a^{-1} for sub-region B to 0.21 m a^{-1} for sub-region E. We also detected a temporal trend in the ICESat data which is shown in Figure S 4. However, as our bootstrapping analysis shows a stable value at $\sim 60\%$ of included ICESat footprints we conclude that the temporal trend of decreasing ICESat measurements ($-5.9 \pm 3.8\% \text{ a}^{-1}$) and the differences of the area-elevation distribution ($\pm 15\%$, Figure S 1a) are covered by our error estimate. The overall error in surface elevation changes is given by

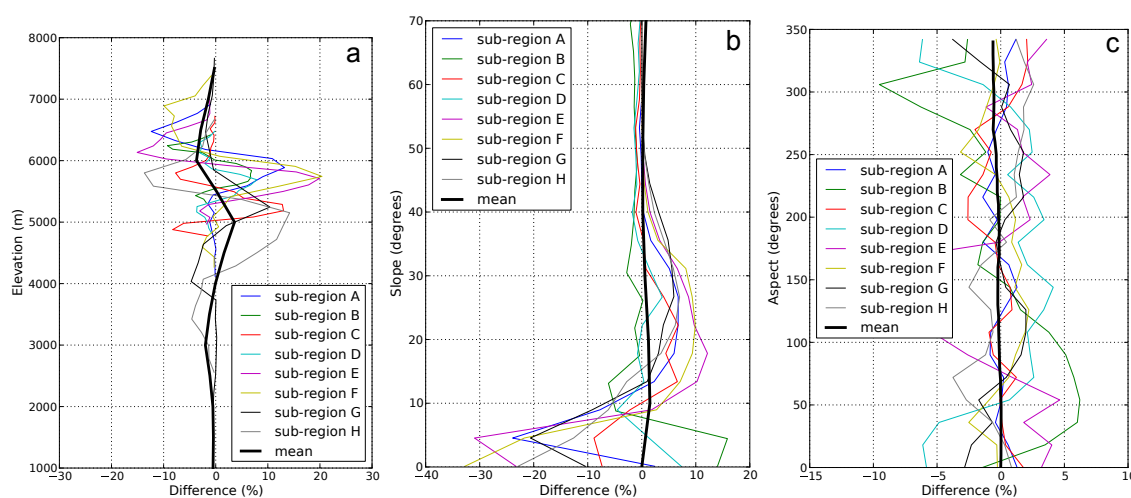
$$e_{trend} = \sqrt{\sigma_{trend}^2 + trend_{land}^2 + e_{bias}} \quad (1)$$

where σ_{trend} is the error from the bootstrapping analysis and $trend_{land}$ is the estimated off-glacier ΔH trend in each sub-region. The off-glacier trend was calculated in the same way as the on-glacier trend employing all off-glacier ICESat measurement in each sub-region. Following Gardner et al. (2013) we also included a systematic inter campaign bias of 0.06 m a^{-1} (e_{bias}). For the error estimate of the separate ΔH trends (i.e. in the accumulation area and the ablation area) we additionally included a $\pm 30\%$ ELA uncertainty.

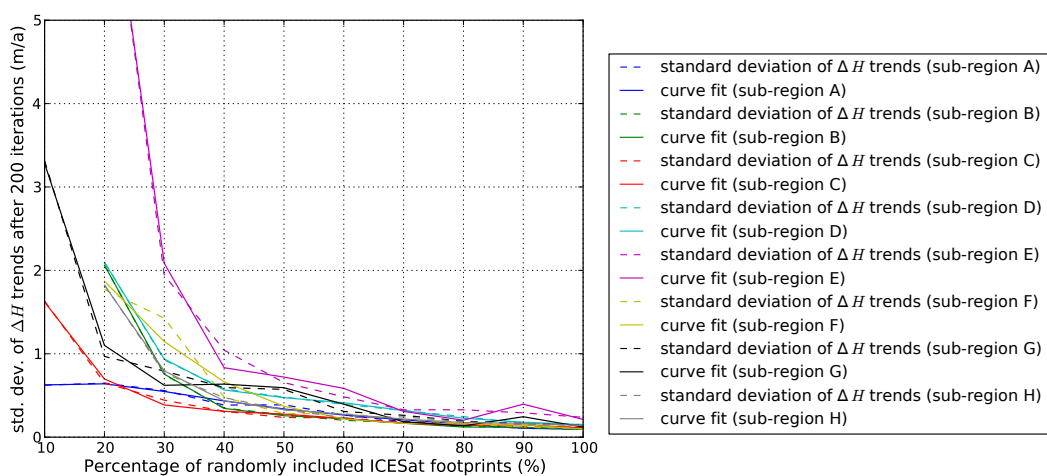
For the error computation of mass balances we added an error of $\pm 60 \text{ kg m}^{-3}$ in ice density (Huss, 2013) and of $\pm 20\%$ in glacier area. For the latter we randomly selected 11 glaciers all of which are included in our analysis. The areas of these glaciers were digitized manually, based on the mentioned Landsat imagery (Thematic Mapper, Level 1, acquisition between 2003 and 2011). From the differences between the digitized glacier outlines and the CGI we estimated the error in glacier area.

In order to test the statistical significance (Z) of the derived ΔH trends we employed a Mann-Kendall trend test. If $|Z| \geq 1.96$ the estimated trend is assumed to be statistical significant at the 5% level.

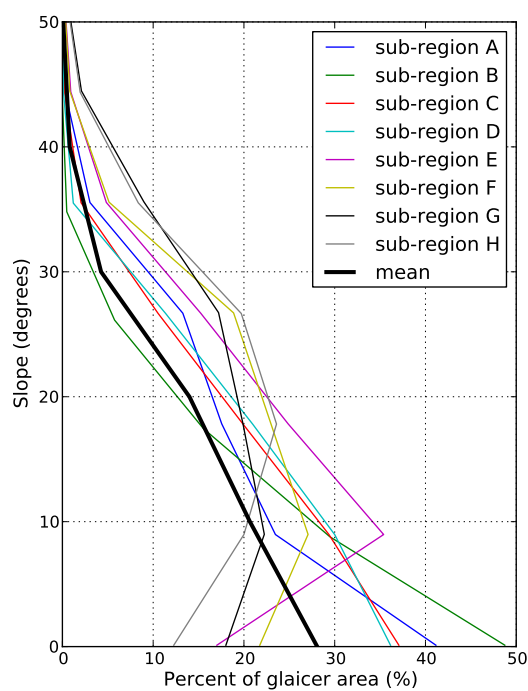
ICESat footprint distribution



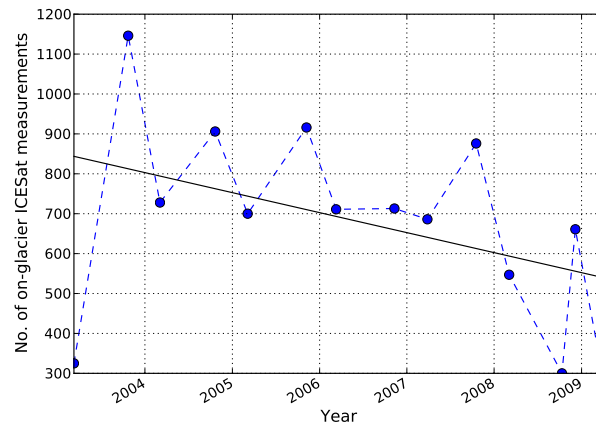
Supplementary Figure S 1. Difference between the area-elevation distribution and the ICESat elevation distribution for all glaciers in the eight sub-regions (a, after Bolch et al., 2013). In order to translate the ICESat footprint distribution to an area-elevation estimate we employed the 90 m grid posting of the SRTM-C DEM and the SRTM-C elevation at each ICESat footprint location. Difference between the glacier slope distribution and the ICESat slope distribution (b) and difference between the glacier aspect distribution and the ICESat aspect distribution (c).



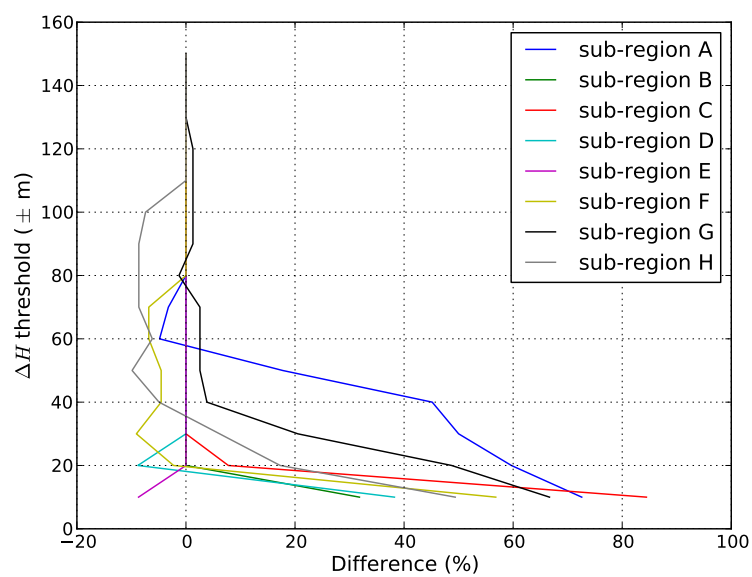
Supplementary Figure S 2. Standard deviation of ΔH trends from randomly selected 10% intervals of ICESat measurements after 200 iterations. The curves reach a stable value at $\sim 60\%$ of included ICESat footprints, showing the representativeness of the ICESat data sample in each sub-region.



Supplementary Figure S 3. Glacier slope distribution for the eight sub-regions.

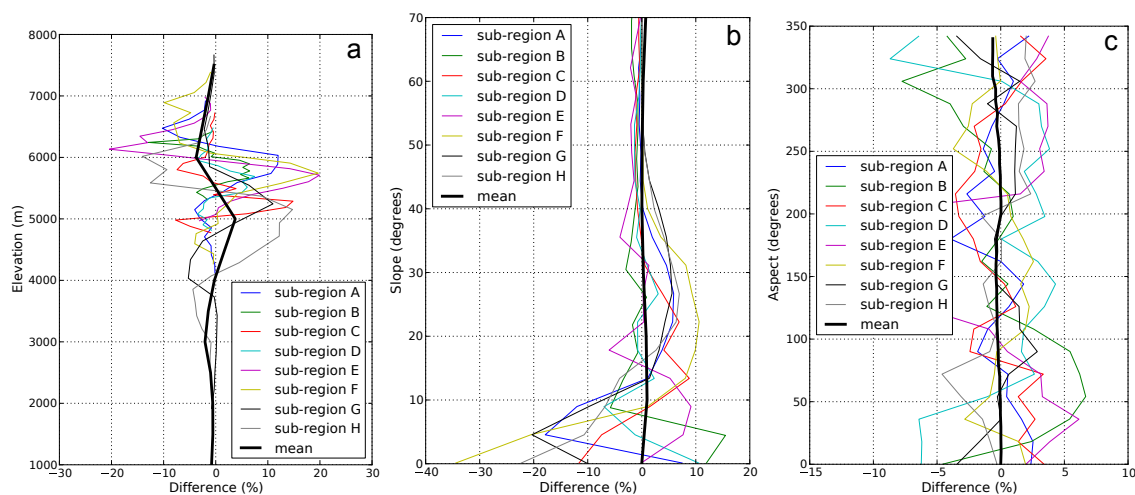


Supplementary Figure S 4. Temporal trend in the ICESat data sample. Blue dots represent the number of on-glacier ICESat measurements from each laser period (except for laser period 2C, 3C, 3F and 2F). The number of ICESat measurements is decreasing by $-5.9 \pm 3.8\% \text{ a}^{-1}$ between 2003 and 2009.

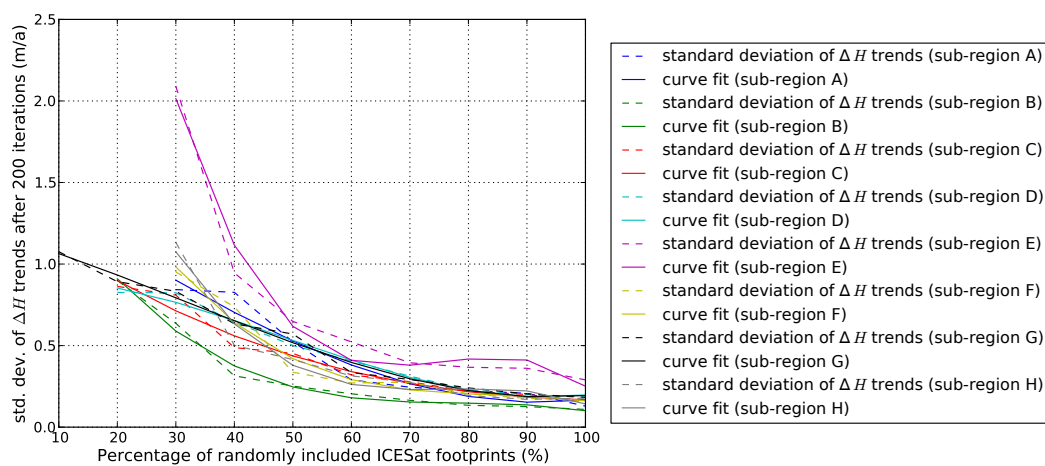


Supplementary Figure S 5. Difference of ΔH trends for a varying ΔH threshold in each sub-region. In order to select cloud-free ICESat footprints a ΔH threshold of ± 150 m was applied to the data.

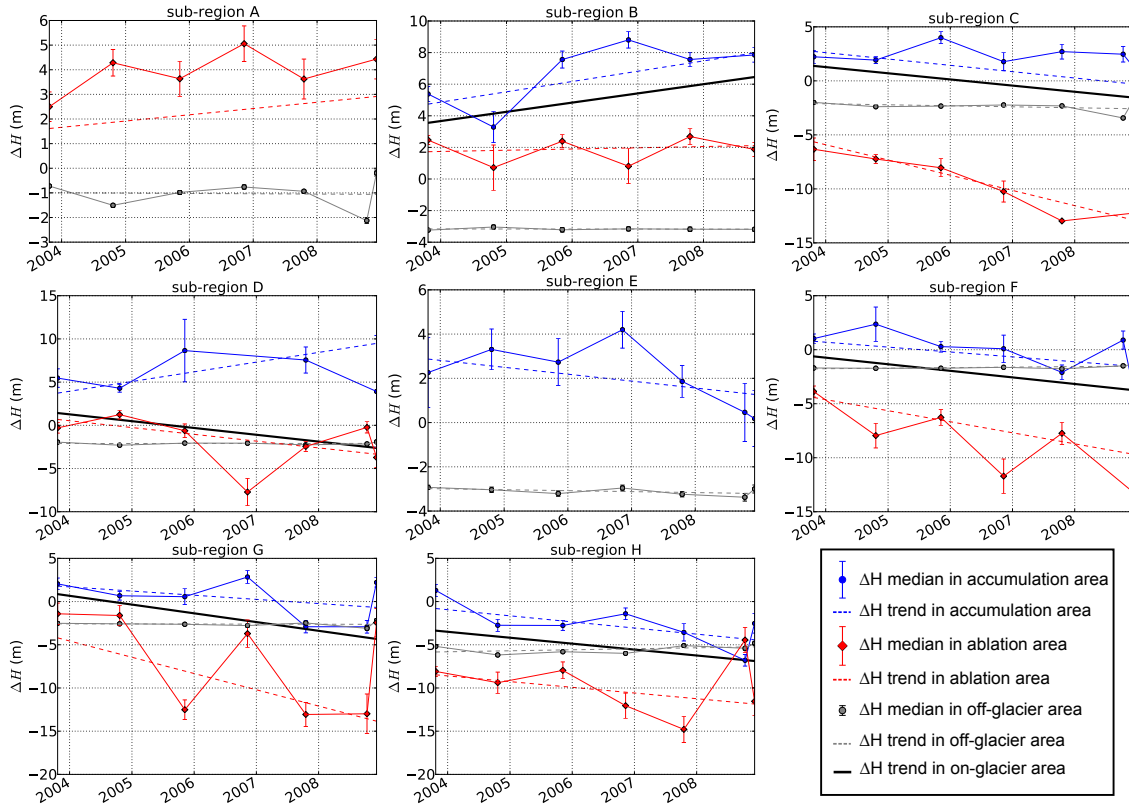
ICESat autumn measurements



Supplementary Figure S 6. Same plot as Figure S 1 except that only autumn acquisitions are employed.



Supplementary Figure S 7. Same plot as Figure S 2 except that only autumn acquisitions are employed. A stable value is reached after including $\sim 90\%$ of ICESat measurements.



Supplementary Figure S 8. Estimated trends for selected geographic sub-regions solely based on autumn acquisitions. Geographic sub-regions are shown in Figure 1 in the manuscript. Trends were fitted through all ΔH values in on- and off-glacier areas. For on-glacier areas trends are shown separately for the accumulation and ablation areas as well as for the whole glacier area. For clarity reasons only the ΔH median of each laser period is shown. Year dates correspond to 1 January of each year.

Supplementary Table S 2. Regional trends of glacier elevation changes solely based on autumn acquisitions are shown next to the area weighted mass balance and total glacier area in each sub-region. Geographic location of sub-regions is shown in Figure 1 in the manuscript and trend lines are shown in Figure S 8. Statistical significant trends are illustrated as bold numbers.

Sub-region	ΔH trend (m a^{-1}) accumulation area	ΔH trend (m a^{-1}) ablation area	ΔH trend (m a^{-1}) on-glacier area	ΔH trend (m a^{-1}) off-glacier area	Mass balance (m w.e. a^{-1})	Total glacier area (km^2)
A	-	$+0.25 \pm 0.30$	$+0.25 \pm 0.30^a$	-0.01 ± 0.14	$+0.21 \pm 0.26^a$	6,483
B	$+0.65 \pm 0.33$	$+0.08 \pm 0.27$	$+0.58 \pm 0.26$	-0.01 ± 0.02	$+0.49 \pm 0.28$	464
C	-0.59 ± 0.36	-1.41 ± 0.52	-0.57 ± 0.31	-0.09 ± 0.11	-0.48 ± 0.31	1,491
D	$+1.12 \pm 0.46$	-0.79 ± 0.39	-0.79 ± 0.31	$+0.01 \pm 0.03$	-0.67 ± 0.35	1,859
E	-0.31 ± 0.37	-	-0.31 ± 0.37^b	-0.12 ± 0.03	-0.26 ± 0.33^b	1,056
F	-0.45 ± 0.33	-1.02 ± 0.43	-0.61 ± 0.30	$+0.05 \pm 0.02$	-0.52 ± 0.31	2,371
G	-0.48 ± 0.34	-1.88 ± 0.64	-1.01 ± 0.31	-0.01 ± 0.06	-0.86 ± 0.39	6,632
H	-0.71 ± 0.37	-0.66 ± 0.37	-0.69 ± 0.31	$+0.12 \pm 0.10$	-0.59 ± 0.33	12,017

^a data only available in ablation area.

^b data only available in accumulation area.

References

- Ageta, Y. and Kadota, T. (1992). Predictions of changes of glacier mass balance in the Nepal Himalaya and Tibetan Plateau: a case study of air temperature increase for three glaciers. *Annals of Glaciology*, 16:89–94.
- Ageta, Y., Zhang, W., and Nakawo, M. (1989). Mass balance studies on Chongce Ice Cap in the West Kunlun Mountains. *Bulletin of Glacier Research*, 7:37–43.
- Benn, D. I. and Lehmkuhl, F. (2000). Mass balance and equilibrium-line altitudes of glaciers in high-mountain environments. *Quaternary International*, 6566(0):15–29.
- Bhang, K. J., Schwartz, F. W., and Braun, A. (2007). Verification of the Vertical Error in C-Band SRTM DEM Using ICESat and Landsat-7, Otter Tail County, MN. *IEEE Transactions on Geoscience and Remote Sensing*, 45(1):36–44.
- Bolch, T., Sørensen, L. S., Simonsen, S. B., Mölg, N., Machguth, H., Rastner, P., and Paul, F. (2013). Mass loss of Greenland’s glaciers and ice caps 2003-2008 revealed from ICESat laser altimetry data. *Geophysical Research Letters*, 40(5):875–881.
- Caidong, C. and Sorteberg, A. (2010). Modelled mass balance of Xibu glacier, Tibetan Plateau: sensitivity to climate change. *Journal of Glaciology*, 56:235–248.
- Fujita, K. and Nuimura, T. (2011). Spatially heterogeneous wastage of Himalayan glaciers. *Proceedings of the National Academy of Sciences*, 108:14011–14014.
- Gardner, A. S., Moholdt, G., Cogley, J. G., Wouters, B., Arendt, A. A., Wahr, J., Berthier, E., Hock, R., Pfeffer, W. T., Kaser, G., Ligtenberg, S. R. M., Bolch, T., Sharp, M. J., Hagen, J. O., van den Broeke, M. R., and Paul, F. (2013). A Reconciled Estimate of Glacier Contributions to Sea Level Rise: 2003 to 2009. *Science*, 340(6134):852–857.
- Hilbert, C. and Schmullius, C. (2012). Influence of Surface Topography on ICESat/GLAS Forest Height Estimation and Waveform Shape. *Remote Sensing*, 4(8):2210–2235.
- Huss, M. (2013). Density assumptions for converting geodetic glacier volume change to mass change. *The Cryosphere*, 7(3):877–887.
- Kääb, A. (2008). Glacier Volume Changes Using ASTER Satellite Stereo and ICESat GLAS Laser Altimetry. A Test Study on Edgeøya, Eastern Svalbard. *IEEE Transactions on Geoscience and Remote Sensing*, 46:2823–2830.
- Kääb, A., Berthier, E., Nuth, C., Gardelle, J., and Arnaud, Y. (2012). Contrasting patterns of early twenty-first-century glacier mass change in the Himalayas. *Nature*, 488(7412):495–498.
- Pu, J., Yao, T., Yang, M., Tian, L., Wang, N., Ageta, Y., and Fujita, K. (2008). Rapid decrease of mass balance observed in the Xiao (Lesser) Dongkemadi Glacier, in the central Tibetan Plateau. *Hydrological Processes*, 22(16):2953–2958.
- Raper, S. C. B. and Braithwaite, R. J. (2009). Glacier volume response time and its

links to climate and topography based on a conceptual model of glacier hypsometry. *The Cryosphere*, 3(2):183–194.

Zwally, J. (2013). Correction to the ICESat Data Product Surface Elevations due to an Error in the Range Determination from Transmit-Pulse Reference-Point Selection (Centroid vs Gaussian). Retrieved from: <http://nsidc.org/data/icesat/pdf/ICESat%20G-C%20statement.pdf>.

B Estimation of Mass Balance of the Grosser Aletschgletscher, Swiss Alps, from ICESat Laser Altimetry Data and Digital Elevation Models

Author contribution: contribution to the study design, contribution to the data preparation and data analysis, contribution to the writing.

Current status: published, *Remote Sensing*.

Article

Estimation of Mass Balance of the Grosser Aletschgletscher, Swiss Alps, from ICESat Laser Altimetry Data and Digital Elevation Models

Jan Kropáček^{1,2,*}, Niklas Neckel² and Andreas Bauder³

¹ Institute for Cartography, TU-Dresden, Helmholtzstr. 10., 01062 Dresden, Germany

² Institute of Geography, University of Tuebingen, Rümelinstr. 19–23, 72070 Tübingen, Germany; E-Mail: niklas.neckel@uni-tuebingen.de

³ Laboratory of Hydraulics, Hydrology and Glaciology, ETH Zurich, Wolfgang-Pauli-Str. 27, 8093 Zürich, Switzerland; E-Mail: bauder@vaw.baug.ethz.ch

* Author to whom correspondence should be addressed; E-Mail: jan.kropacek@uni-tuebingen.de; Tel.: +49-351-463-36223; Fax: +49-351-463-37028.

Received: 19 November 2013; in revised form: 30 May 2014 / Accepted: 30 May 2014 /

Published: 17 June 2014

Abstract: Traditional glaciological mass balance measurements of mountain glaciers are a demanding and cost intensive task. In this study, we combine data from the Ice Cloud and Elevation Satellite (ICESat) acquired between 2003 and 2009 with air and space borne Digital Elevation Models (DEMs) in order to derive surface elevation changes of the Grosser Aletschgletscher in the Swiss Alps. Three different areas of the glacier are covered by one nominal ICESat track, allowing us to investigate the performance of the approach under different conditions in terms of ICESat data coverage, and surface characteristics. In order to test the sensitivity of the derived trend in surface lowering, several variables were tested. Employing correction for perennial snow accumulation, footprint selection and adequate reference DEM, we estimated a mean mass balance of -0.92 ± 0.18 m w.e. a⁻¹ for the whole glacier in the studied time period. The resulting mass balance was validated by a comparison with another geodetic approach based on the subtraction of two DEMs for the years 1999 and 2009. It appears that the processing parameters need to be selected depending on the amount of available ICESat measurements, quality of the elevation reference and character of the glacier surface.

Keywords: Grosser Aletschgletscher; ICESat; mass balance; surface lowering; DEM

1. Introduction

Worldwide rapid retreat of mountain glaciers has been reported by numerous authors for the past few decades (e.g., [1,2]). Glacier fluctuations are regarded as a good indicator for climate variability. This holds true especially for changes in ice volume rather than in glacier extent as glacier area changes tend to show a delayed signal to a changing climate [3]. Precise estimates of glacier volume changes are still challenging and, especially for inaccessible mountain glaciers, remote sensing is a promising data source. In this study, we used data from the Ice Cloud and Elevation Satellite (ICESat) to derive surface elevation changes and volume changes of the Grosser Aletschgletscher in the Swiss Alps. This is the first time that ICESat data was used to estimate changes in geometry of a glacier in the European Alps.

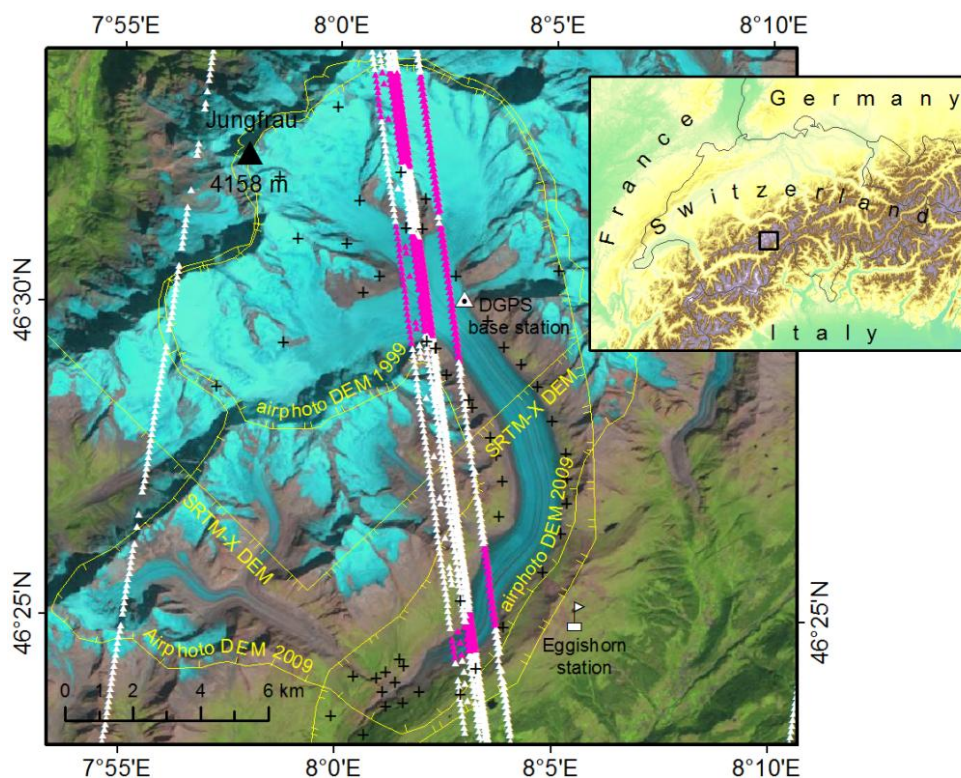
The ICESat mission, which was primarily dedicated for the observation of polar ice sheets, provides precise elevation measurements along nadir tracks acquired between 2003 and 2009. The major obstacle in deriving a time series of elevation changes between consecutive ICESat tracks is that the individual repeated tracks do not match exactly but can be horizontally separated by several hundred meters. This is especially the case in mid-latitudes between 59°S and 59°N for which ICESat's precision spacecraft pointing control was not used [4]. In order to circumvent this problem, several methods have been developed lately, however they have mostly been of value for the large polar ice sheets and ice caps [5–9]. Compared to mid-latitude mountain glaciers, polar ice sheets and ice caps feature an enormous size, good data coverage in terms of satellite orbits, and relatively homogeneous surface characteristics and slope. Due to these characteristics, several methods of analysis exist. One method makes use of crossover points between ascending and descending satellite tracks (e.g., [10]). This method yields accurate results at the cost of sample density. However, the number of crossovers decreases as the distance to the equator decreases and no crossovers exist over the Grosser Aletschgletscher. Another method compares overlapping repeat tracks by projecting a younger profile onto an older one [6,7]. For this method, the tracks must be spatially close which is a limiting factor for the amount of available data. A third method uses the average slope derived from neighboring ICESat tracks in pre-defined boxes (e.g., [5,7]) to account for the cross-track slope. This method is restricted to a relatively gentle and homogeneous surface structure and is therefore not suitable for the mountainous topography in our study area. However, three recent studies proved the suitability of ICESat data in also deriving elevation changes for mountain glaciers [11–13]. Similar to them, we used a DEM as reference surface on which we compare the acquired ICESat data. In these studies [11–13], ICESat measurements are integrated over a large number of glaciers of different orientation and elevation in order to derive a statistically valid region wide mass balance estimate. Although slightly different approaches were applied by these authors, the results in the overlapping areas are in good agreement. In contrast to these studies, we aim at the derivation of detailed elevation changes for a single mountain glacier. Therefore, in this study, several data processing approaches and various reference DEMs were investigated in terms of their influence on the derived trend in elevation change and on the resulting mass balance. A number of ICESat footprints were re-measured by DGPS and serve as ground truth for the derived surface elevation changes.

2. Study Area and Data

2.1. Study Area

The Grosser Aletschgletscher located in the Bernese Alps in the central part of Switzerland is the longest (22.6 km) and largest (83.0 km²) glacier in the Swiss Alps (Figure 1) [14]. It features a rich archive of glaciological records and climate data dating back to 1841 when the first ablation measurements on this glacier were carried out [15]. The accumulation area, which is located on the southern slopes of the main mountain range, is marked by the two prominent summits of Jungfrau and Mönch. The main tongue is formed by the confluence of three tributaries (Grosser Aletschfirn, Jungfraufirn and Ewig Schneefeld) at the so-called Konkordiaplatz. The Grosser Aletschgletscher reaches an ice thickness of 890 m in its central part [16]. The glacier has been losing volume since the Little Ice Age [14] with a considerably increased speed since the late 1980s [14,17]. Its mean annual mass balance in the period from 1880–1999 has been estimated as $-0.42 \text{ m w.e. a}^{-1}$ which corresponds to more than 50 m mean thickness loss [14]. A mass balance monitoring program was set up in the 1960s in the framework of a hydropower project but the data was too sparse to obtain an area-averaged mass balance [18]. Point based surface mass balance has been measured on one site in the accumulation area at the Jungfernfirn since 1920 [18].

Figure 1. Ground tracks of ICESat cross the surface of Grosser Aletschgletscher in three separate places: Ewig Schneefeld (A1), Konkordiaplatz (A2) and the lower part close to the terminus (A3). ICESat measurements on the glacier are highlighted in violet. Outlines of the DEMs with only partial coverage of the area are in yellow. The points used as ground control for the airphoto DEMs are shown as black crosses. In the background is a Landsat TM image from 28 August 2011.



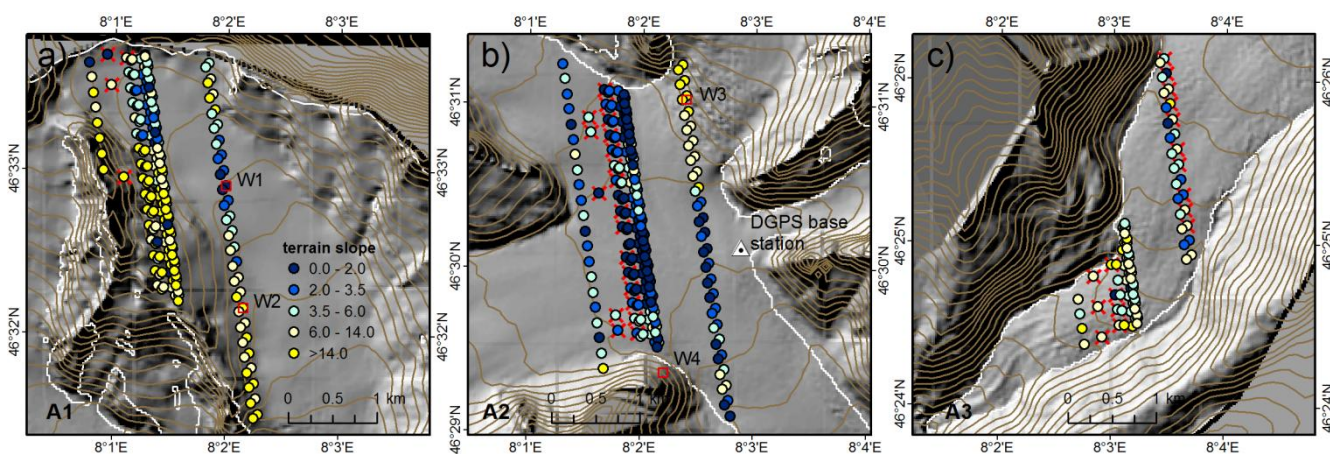
2.2. Data

2.2.1. ICESat/GLASS Data

NASA’s Ice Cloud and Elevation Satellite (ICESat) mission provides accurate along-track elevation measurements derived from the two-way travel time of the emitted laser pulse. Measurements are acquired in nadir every 172 m with a footprint diameter of 70 m [19]. The instrument was operational in the period 2003–2009. The launch of ICESat-2 with an improved instrument is planned for early 2016 [20]. Data acquisitions were carried out every 3–6 months during 18 one-month campaigns. In the ideal case of no cloud cover, each campaign typically resulted in one repeat-pass track for a nominal track. In this study, we used the ICESat/GLAS product L2 Global Land Surface Altimetry Data, release 33 [21] denoted as GLA14, provided by the National Snow & Ice Data Center (NSIDC). It contains information on land surface elevation, geolocation, reflectance as well as geodetic atmospheric and instrument corrections.

The Grosser Aletschgletscher is crossed by one nominal ICESat track which yields 14 ground tracks out of which one track provides only sparse measurements. The ground tracks run parallel in a stripe of 1.37 km width and cross the glacier in three separate areas (Figure 2). The first area with a mean elevation of 3400 m a.s.l. called Ewig Schneefeld, denoted here as A1, belongs to the accumulation area of the glacier. The second area (A2) which is located in the relative flat glacier confluence called Konkordiaplatz belongs to the ablation area of the glacier. This area with a mean elevation of 2800 m a.s.l. is crossed by a number of crevasses and by distinct medial moraines. The third area (A3) is located close to the terminus at a mean elevation of 2100 m a.s.l., some 1600 meters lower than the highest ICESat measurements of area A1. These three areas (A1, A2 and A3) which represent different units in terms of slope, surface roughness and glacier dynamics were treated separately.

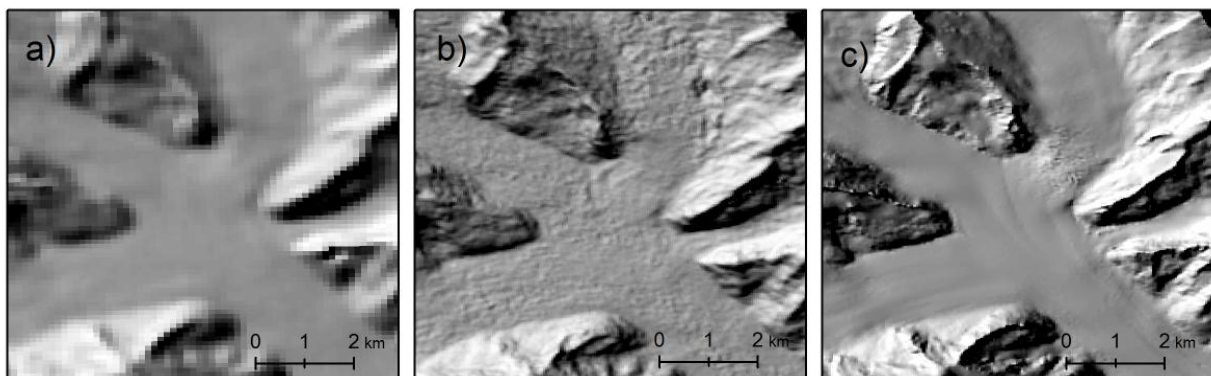
Figure 2. Terrain slope at ICESat points in the three areas A1 (a), A2 (b) and A3 (c) on the Grosser Aletschgletscher. Red crosses indicate canceled points with erroneous elevations due to cloud cover. Glacier outlines are from the Global Land Ice Measurements from Space (GLIMS) dataset. The red squares mark the points for which the waveforms are shown in below.



2.2.2. SRTM DEM

The Shuttle Radar Topography Mission (SRTM) conducted during 11 days in February 2000 provided data for two high resolution digital elevation models [22,23] acquired at C- and X-band. The data was interferometrically processed by the National Aeronautics and Space Administration (NASA) and the German Aerospace Center (DLR), respectively. The homogeneous freely available DEMs cover the entire land mass of the Earth between latitudes 60N and 57S. However, the SRTM-X DEM was acquired with a swath width of 45 km leading to larger data gaps [22]. Due to the gaps between the acquisition stripes, the SRTM-X DEM is only available for area A3. In this study, we use the SRTM-C DEM version 3 which is available via the U.S. Geological Survey (USGS) with a grid posting of three arc seconds and the SRTM-X DEM which is available via the German Aerospace Center (DLR) with a grid posting of one arc second. The vertical accuracy of the SRTM-C DEM as specified in the mission requirements is ± 16 m at 90% confidence [22]. It has been repeatedly confirmed that these requirements were met [24–26]. A mean and standard deviation of 0.60 ± 3.46 m between ICESat and SRTM C elevations were found by [27] in a low relief area with sparse tree cover in the Western United States. However, Gorokhovich and Voustianiouk [26] showed that the error of the SRTM values have a strong correlation with slope and aspect, particularly for slope values $>10^\circ$.

Figure 3. The area A2 (Konkordiaplatz) on different DEMs shown as shaded relief. (a) The SRTM-C DEM features a smooth surface with little detail. Artifacts are clearly visible on the glacier surface in the case of the ASTER GDEM (b) while the Airphoto DEM (c) has a smooth surface with a distinct medial moraine.



2.2.3. ASTER GDEM

The Advanced Spaceborne Thermal Emission and Reflection Radiometer Global Digital Elevation Model (ASTER GDEM) covers the land mass of the World between 83° N and 83° S with a resolution of 30 m. It was produced by feature matching techniques using optical stereo-pairs acquired by nadir- and backward-looking infrared cameras of the ASTER instrument onboard the Terra Satellite between 2000 and 2010. Multiple stereo pairs were processed for each point. The vertical accuracy is a function of the number of used stereo pairs and is specified as 17 m at the 95% confidence level [28]. For the Grosser Aletschgletscher, between four and 19 stereo-images were employed. A visual comparison of a shaded relief calculated from GDEM version 2 with high resolution DEMs revealed that the GDEM over Grosser Aletschgletscher contains a high level of noise (Figure 3) which

corresponds to the findings of [29]. To account for the noise, we used a smoothed version obtained by a 5×5 low pass filter besides the original dataset.

2.2.4. Airphoto DEM

Two DEMs were derived from aerial photographs from 2009 and 1999 [14] by means of digital stereo-photogrammetry whereas the former was used further as an elevation reference for the ICESat data processing. A two-phase procedure with automatic terrain extraction and manual post-processing for blunder elimination was applied. As a ground control, 50 permanently marked geodetic points were used (Figure 1). The resulting DEMs cover the glacier and its immediate surroundings and have a spatial resolution of 25 m. The expected accuracy is in the order of <0.3 m which was confirmed by a cross validation using independent check points outside the glacier.

2.2.5. Glacier Outlines

Glacier outlines from 1998 are available via the Global Land Ice Measurements from Space (GLIMS) database [30] and were used for the selection of ICESat footprints on the glacier. The glacier outline was provided to GLIMS by F. Paul who used a band ratio of Landsat Thematic Mapper data for the delineation of the ice body.

3. Methods

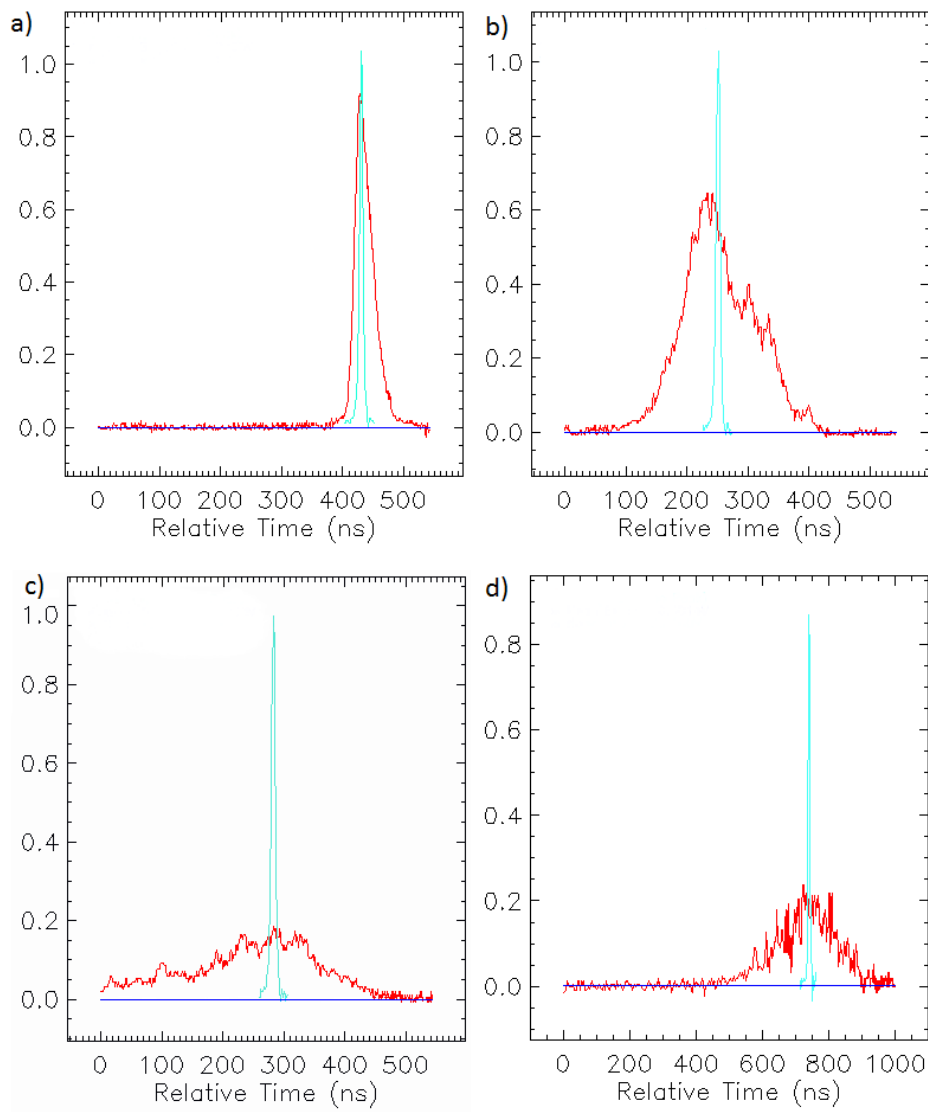
To ensure that the ICESat elevation measurements are comparable between the non-identical tracks on the tilted and irregular shaped glacier surface, this method, similarly to [11–13], makes use of a static elevation reference. Therefore, the surface elevation for each ICESat point was extracted from existing DEM data using bilinear interpolation of the four closest cells in the DEM following [25]. The elevation difference between both datasets (ICESat-DEM) is further denoted as ΔH .

First of all, the DEMs had to be checked for horizontal shifts with respect to the ICESat profiles. Following [31], all values of ΔH in off-glacier regions were normalized by the local slope inclination and were plotted against the terrain aspect. The horizontal shift was estimated by the amplitude of a fitted sinusoid and then removed by an adjustment of the reference coordinates of the DEMs (Table 1). The Airphoto DEM did not provide enough ΔH values for the fitting as it is limited mainly to the glacier area. Its shift with respect to the ICESat measurements could be derived by calculating the displacement between the Airphoto DEM and the adjusted SRTM-C DEM (Table 1).

Table 1. Horizontal shifts of the reference DEMs with respect to the ICESat measurements which had to be removed before the extraction of ΔH values.

DEM	Horizontal Shift (m)	Azimuth of the Shift (deg.)
SRTM-C	70.8	124.2
SRTM-X	40.0	72.1
Airphoto DEM	55.1	-106.3
ASTER GDEM	17.1	200.6

Figure 4. Waveforms of ICESat pulses recorded on 24 October 2003 over (a) flat glacier surface in A1 (slope = 1.7°), (b) steeper glacier surface (slope = 14.9°), (c) rough glacier surface marked by a number of crevasses that form between Ewig Schneefeld and Konkordiaplatz and (d) steep off-glacier slope south of Konkordiaplatz. The raw waveform is in red and the fit is in blue. One hundred ns corresponds to 15.1 m of the elevation difference. Positions of the points labeled as W1, W2, W3 and W4, respectively, are shown in Figure 2.



Since the ICESat data is referenced to the TOPEX/Poseidon ellipsoid [19], the ICESat measurements were converted to WGS-84 heights following [32,33]. In the next step, the ellipsoidal elevations were recalculated to heights above the EGM2008 geoid using information on geoidal heights contained in the GLA14 records. Then, the ICESat points were filtered based on the distance to the reference DEM. The threshold of 100 m appears to effectively sort out all measurements affected by clouds. In order to sort out short tracks with too high variation of ΔH which can provide no meaningful elevation information, a threshold for the in-track standard deviation of ΔH was set to 20 m. Since the vertical error of ICESat elevations increases with the incidence angle between the laser vector and the surface normal [27,34], an upper limit of terrain slope of 10° suggested by [34] was applied to account for the effect of the inaccuracy induced by the Gaussian fitting of the wide

waveforms (see Figure 4b). Further, the effect of the slope threshold on the resultant trend was investigated. The effect of terrain slope and surface roughness is illustrated by waveforms recorded over different surfaces (Figure 4). Furthermore, the impact of smoothing of the ΔH values along the track and the elimination of outliers on the derived surface lowering trend was explored. Outliers were replaced by the average of two neighboring values, and for the smoothing, a running mean was applied. To exclude the influence of a systematic bias in the ICESat data (differences between the lasers used during different ICESat campaigns, instrument drift, *etc.*), off-glacier measurements from the surrounding area were checked for a possible trend.

In order to estimate trends in surface elevation change, assuming a linear trend of surface lowering of the glacier, a linear function was fitted through all ΔH values per ICESat track and area. This way, the trend is independent of the absolute elevation of the reference. The statistical significance of the estimated trends was checked with an f-test and the error of the regression was shown by its standard deviation. Irregularities in glacier surface changes caused by variation in albedo, debris cover and glacier flow together with processing artifacts of the DEM introduce a noise to the derived values of ΔH . However, the variation of ΔH along the tracks can also indicate the quality of the reference data set. A low variation indicates a good match between the ICESat profiles and their vertical projection on the DEM. Various DEMs were used as a reference and were compared in terms of variation of ΔH for all three areas.

Seasonal snow cover introduces a variation into the time series of glacier elevations measured by ICESat. For testing of the snow pack correction of ICESat elevations, we used snow depths for days of ICESat flyovers measured at Eggishorn Station (2495 m a.s.l.) which is located 1.7 km to the SE from the lower part of the glacier (Figure 1). The multi-seasonal ICESat measurements were corrected for snow pack depth by subtraction of the snow depth measured at the station. The resulting trend was compared to the trend derived from measurements acquired after the ablation period (*i.e.*, autumn trends).

4. Results

4.1. Trends in the Surface Lowering

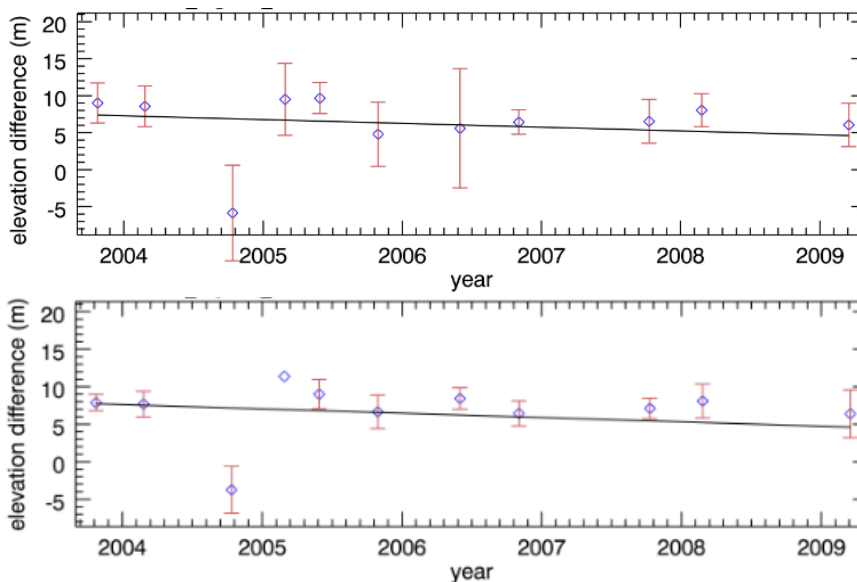
The surface lowering of the Grosser Aletschgletscher observed from ICESat elevations appears to be nearly zero in the accumulation area (A1) (Figure 5). The lowering in the upper part of the ablation area (A2) is 2.2 m/a and it increases towards the terminus (area A3) where it approximately doubles (Table 2). This is a common pattern observed at alpine glaciers in the last decade [14,18]. The analysis of ΔH for the surrounding area not covered by the glacier did not produce any statistically significant trend (Figure 6), which is in an agreement with [11–13], and it confirms that the use of different lasers for the ICESat campaigns or a possible instrument drift did not affect the trends extracted on the glacier.

In area A1, no elevation changes could be detected by ICESat because the derived low trends are not statistically significant (Table 2). The in-track variation in ΔH over this area appears to be high. The application of a slope threshold of 5° led to a strong reduction of measurements (Figure 5). The best results in terms of ΔH variations are achieved when using the Airphoto DEM. When comparing the two global DEMs, the SRTM DEM outperforms the ASTER GDEM which confirms the superiority of the InSAR technique in snow covered areas due to a lack of features for stereo-processing.

Table 2. Mean surface lowering for areas A1, A2 and A3 using different DEMs as elevation reference. The snow pack correction and the threshold of the terrain slope were applied. F-values in italics indicate a statistically non-significant trend.

Elevation Reference	Area	Mean ΔH (m)	σ of ΔH (m)	Mean Surface Lowering (m/a)	f-Value	Canceled Points (%)	Canceled Tracks (No)
SRTM-C	A1	8.1	4.7	-0.2 ± 0.32	<i>0.41</i>	55.8	1
ASTER GDEM original	A1	-13.4	12.9	0.2 ± 1.05	<i>0.02</i>	76.1	2
ASTER GDEM smoothed	A1	-12.7	10.2	0.1 ± 0.67	<i>0.04</i>	58.9	1
Airphoto DEM	A1	5.5	3.9	-0.0 ± 0.30	<i>0.02</i>	54.3	1
SRTM-C	A2	-6.1	2.8	-2.5 ± 0.13	380.6	14.9	1
ASTER GDEM original	A2	-3.8	4.2	-2.2 ± 0.20	125.9	33.2	1
ASTER GDEM smoothed	A2	-3.3	3.5	-2.1 ± 0.15	183.8	15.9	1
Airphoto DEM	A2	10.7	1.9	-2.6 ± 0.10	759.8	16.8	1
DGPS	A2	15.0	0.9	-2.6 ± 0.08	788.5	7.5	1
SRTM-C	A3	-25.6	4.4	-5.1 ± 0.35	209.06	28.2	2
ASTER GDEM original	A3	-18.2	4.6	-4.3 ± 0.52	68.32	56.4	2
ASTER GDEM smoothed	A3	-17.1	4	-5.1 ± 0.34	217.44	30.8	2
Airphoto DEM	A3	17	3.8	-3.3 ± 0.36	84.77	39.7	2
SRTM-X	A3	-22.6	4.4	-5.3 ± 0.39	189.23	33.3	2

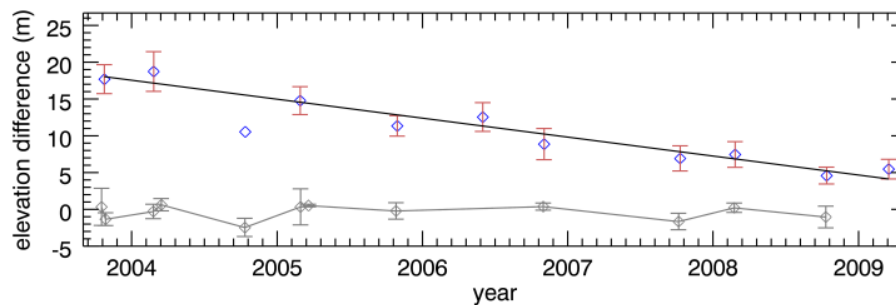
Figure 5. Linear trend of the surface lowering in area A1 fitted through multi-seasonal ICESat data. Snow corrections and a threshold for the local terrain slope of 10 °(above) and 5 °(below) were applied to reduce the high in-track variation of ΔH .



The trend in surface lowering derived for A2 (Figure 6) based on the Airphoto DEM (2.6 ± 0.10 m/a) is equal to the one based on the DGPS measurements (Table 2). Very similar results were also achieved using the SRTM-C DEM. The trends derived using the ASTER GDEM slightly underestimate the rates of the surface lowering. The smoothing reduces the variation of ΔH but does not affect the trend significantly. The estimation of surface lowering in this area benefits from long

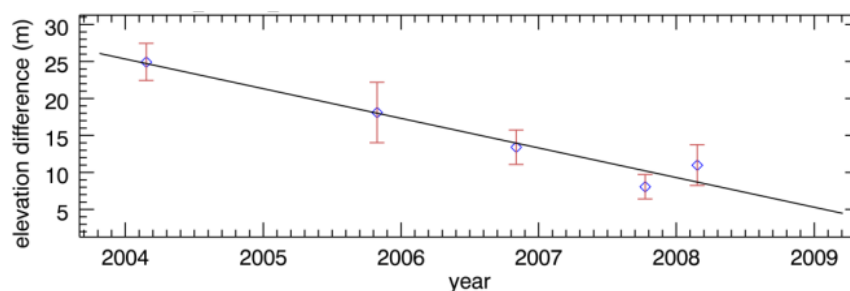
intersections of ICESat tracks with the glacier surface (Figure 2). The smooth surface topography leads generally to a relatively low variation of ΔH (Figure 6).

Figure 6. Linear trend of the surface lowering in area A2 fitted through multi-seasonal ICESat data using the Airphoto DEM as elevation reference. A terrain slope threshold of 10° and snow pack corrections were applied. Values of mean ΔH for off-glacier area (in grey) do not show a statistically significant trend.



The use of the DEMs provided by space borne platforms led to similar results in case of A3. Both, the trend and the variations in ΔH are almost identical when comparing the SRTM-X DEM with the SRTM-C DEM. Nevertheless, they differ from the results which use the Airphoto DEM as elevation reference (-3.3 ± 0.36) (Figure 7). This difference is probably due to changes of the surface geometry between different acquisition dates taking into account the high dynamics of the retreating glacier terminus. A number of ICESat measurements acquired in winter were sorted out due to erroneous elevations caused by the presence of low clouds (Figure 2).

Figure 7. Linear trend of the surface lowering in area A3 fitted through multi-seasonal ICESat data using the Airphoto DEM as elevation reference. A terrain slope threshold of 10° and snow pack corrections were applied.



It appeared that different approaches in data processing of the ICESat data as listed in Table 3 have only a limited effect on the resulting mass balance. The difference is in all cases within 6% (Table 3). When looking at the differences in surface lowering (Table 3), it can be seen that the listed processing approaches affects also the error ranges and the statistical significance. For instance, the application of the slope threshold of 10° has little effect on the surface lowering but it leads to an increase of the statistical significance of the trend and to a narrowing of the error range in A2. In this area, this threshold leads to cancelation of the points over the highly dynamic inflow of Ewig Schneefeld, where the surface velocity reaches 90 cm/day [35] which is likely the reason for this improvement. A weak contrary effect can be observed for A3. In A1, the f-value more than doubles but the trend

remains non-significant. The correction for snow pack depth using the *in-situ* data results in an increase in the statistical significance of the derived trend in surface lowering for A2. The effect is less strong in A3. The trend in both A2 and A3 stays almost unaffected. Finally, the selection of autumn measurements led to a change in trend of 18.9% in A3 resulting in a trend value of 2.6 m/a, which diverges substantially from the value obtained by the DEM subtraction. This is connected to a high increase in the error range and a substantial decrease in the statistical significance. Only small changes were observed for area A2 in which the flat surface and abundance of measurements ensure a robust result. The high variations in A1 between the tested approaches are caused by the fluctuation of the non-significant trend near zero. The results for A1 were shown for completeness. The smoothing of the ΔH values along the tracks did not significantly affect the trend in both regions, A2 and A3. However, its effect on the error ranges and the statistical significance is contradictory.

Table 3. The effect of various approaches in the processing of ICESat data on the trend in ΔH , the error range, the statistical significance and the resulting mass balance are expressed in percentages. The calculation is based on the Airphoto DEM for 2009.

Tested Change	Area	Surface Lowering	Sigma	f-Value	Mass Balance
threshold for terrain slope 10°	A1	50.0%	0.0%	120.5%	
	A2	3.2%	-30.8%	119.7%	1.74%
	A3	0.0%	9.1%	-15.1%	
snow pack correction	A1	-15.7%	2.6%	-33.3%	
	A2	-1.9%	22.2%	-33.7%	0.44%
	A3	3.0%	5.6%	-5.3%	
selection of autumn measurements	A1	-70.6%	34.2%	-95.2%	
	A2	6.8%	7.7%	0.3%	-5.8%
	A3	-18.9%	63.6%	-75.4%	
smoothing of ΔH profiles	A1	58.8%	-15.8%	237.3%	
	A2	-0.4%	-23.1%	71.0%	-4.8%
	A3	0.9%	60.6%	-59.1%	

4.2. Estimation of Mass Balance

Since no surface lowering was detected for the accumulation area, the interpolation of the trend was limited entirely to the ablation area using solely the surface lowering trends in the areas A2 and A3. The trend was interpolated in elevation bands of 100 m by piecewise linear interpolation in an altitude range from 1800 to 3000 m a.s.l., the upper one being an approximate position of the equilibrium line. The volume change was then obtained by multiplication of these trends by the area delimited by the elevation range of each band and summing up of the products. The volume to mass conversion was then calculated assuming an ice density of $850 \pm 60 \text{ kg}\cdot\text{m}^{-3}$ following [36]. The utilization of the Airphoto DEM as elevation reference produced a total mass balance of $-0.92 \pm 0.18 \text{ m w.e. a}^{-1}$ using the snow corrected multi-seasonal data and a slope threshold of 10° . The use of the different DEMs resulted in a range of mass balances from $-0.90 \pm 0.17 \text{ m}$ to $-1.04 \pm 0.19 \text{ m w.e. a}^{-1}$ (Table 4). The error of the mass balance was quantified as a combination of the following contributions: error of derived trends, uncertainty of

the glacier outlines and the error of the ice density. Following [11,12], the accuracy of the glacier area delimited by the GLIMS outlines was estimated to be 10%.

Table 4. Mass balance of the Grosser Aletschgletscher estimated from ICESat measurements for the period 2003–2009 using different DEMs as elevation reference and from the subtraction of the DEMs for the years 1999 and 2009.

DEM	Mass Balance (m w.e. a ⁻¹)
Airphoto DEM	-0.92 ± 0.18
SRTM-C	-1.04 ± 0.19
GDEM ASTER original	-0.90 ± 0.17
GDEM ASTER smoothed	-0.94 ± 0.18
subtraction of DEMs	-1.02 ± 0.34

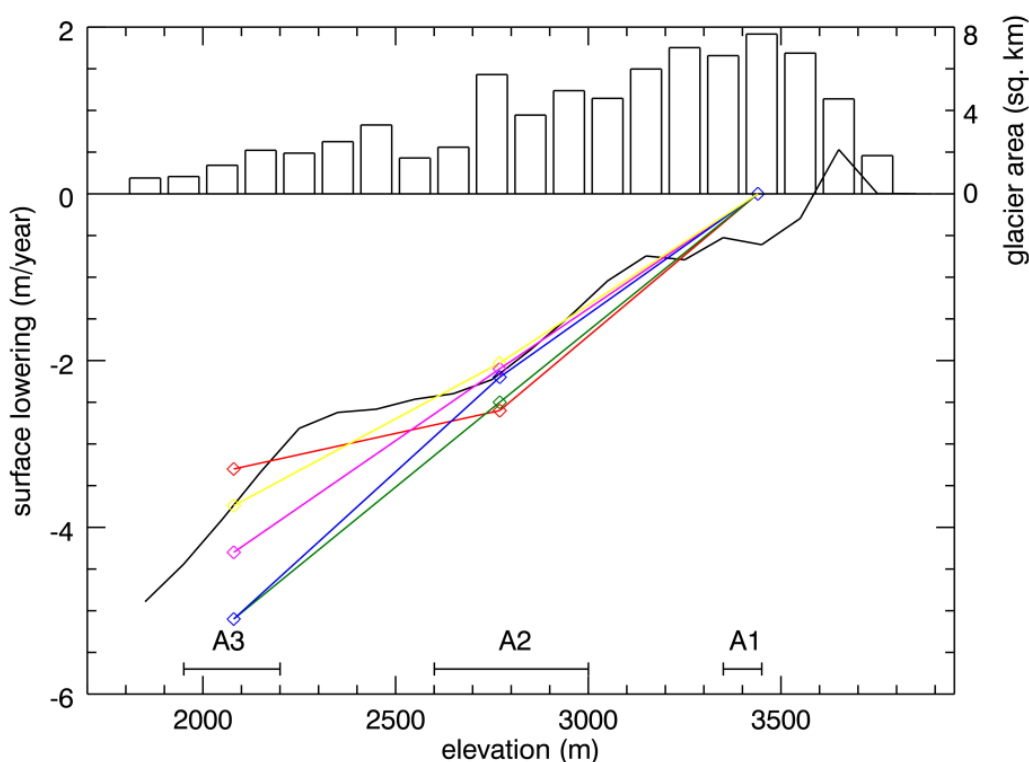
4.3. Validation

In order to get a high accuracy elevation reference for comparison with the DEMs, elevations of ICESat footprints were measured *in-situ* by Differential Global Positioning System (DGPS) during a four day field campaign in July 2012. Elevations of 57% of the footprint center points in area A2 were obtained in static mode with a relative accuracy in the order of centimeters. To provide a comparison with the DEMs, the DGPS measurements were used as elevation reference and values of ΔH were calculated for each point. The resulting surface lowering (Table 2) is almost identical to the surface lowering obtained when using the Airphoto DEM. The ΔH has considerably lower standard deviation in comparison to the use of all the DEMs. This shows that an analysis of ICESat data of flat areas well sampled by ICESat measurements leads to a highly accurate result when using a good quality DEM.

To validate the calculated mass balance, we applied another geodetic method based on the subtraction of two DEMs produced by aerial stereo-photogrammetry. For this purpose, the Airphoto DEMs for the years 2009 and 1999 were co-registered, re-sampled to the same spatial resolution (25 m) and subtracted from each other under the mask for the whole glacier area. The obtained volume was converted to mass balance using again the assumption about the ice density of $850 \pm 60 \text{ kg}\cdot\text{m}^{-3}$. The thickness change was then calculated in elevation bands of 100 m and plotted against elevation (Figure 8). This plot shows a non-linearity between surface lowering and altitude around 2200 m a.s.l. This non-linearity is not captured by the ICESat data due to the gaps in data coverage along the elevation range. Another non-linearity occurs in the accumulation area which could be due to difficulties of optical stereoscopy over snow covered areas. The error estimation of the DEM subtraction employed the uncertainty of the elevation difference of the two DEMs, error of the ice density and the uncertainty of the glacier outlines. The uncertainty of the elevation difference of the two DEMs was calculated after [37] using statistics of an off-glacier area calculated from each 20th pixel in the sample in order to account for the autocorrelation inherent to the stereoscopically derived DEMs. The resulting mass balance ($-1.02 \pm 0.34 \text{ m w.e. a}^{-1}$) is in a good agreement with the values calculated from the ICESat measurements using different DEMs (Table 4). The lowest and highest difference is for the SRTM-C (2%) and GDEM ASTER without smoothing (12%), respectively. It should be noted that the two above mentioned nonlinearities which divert from the lowering rates derived from ICESat measurements compensate each other which contributes to this good agreement.

It also has to be noted that different methods of mass balance estimation do not lead to identical results and that great care has to be taken when comparing them [38].

Figure 8. Glacier hypsometry (upper panel) and surface lowering in elevation bands of 100 m derived from the subtraction of two Airphoto DEMs (black line) and surface lowering from ICESat measurements using the Airphoto DEM (red), SRTM-C DEM (green), the ASTER GDEM original (blue) and the ASTER GDEM smoothed version (magenta) as elevation reference and from SIMU-Laser (yellow). The subtraction of the two DEMs and the ICESat measurements cover slightly different periods: 1999–2009 and 2003–2009, respectively. The elevation ranges covered with the ICESat data (A1, A2 and A3) are marked by horizontal lines in the lower part of the image.



Further, we checked the representativeness of the sparse ICESat sampling distribution using simu-laser approach proposed by [39]. The simu-laser elevation changes were extracted at the locations of the ICESat footprints in the areas A2 and A3 from the difference image calculated from the two airphoto DEMs. These differences were averaged over the studied areas to obtain surface lowering (Figure 8). These values were then converted to mass balance applying the same method as for the ICESat measurements. The resulting mass balance $0.81 \text{ m w.e. a}^{-1}$ is only 3% higher with respect to the subtraction of the two DEMs if this subtraction is limited to the ablation area. The resulting lower value of the mass balance is due to the above mentioned non-linearity around the altitude 2200 m a.s.l. This good agreement shows that the ICESat sampling is representative and it supports the validity of the approach.

5. Discussion

The ICESat coverage of the Grosser Aletschgletscher allowed us to test the derivation of the trend of surface lowering under different conditions. Ground DGPS measurements on Konkordiaplatz provided an accurate elevation reference which validates the results achieved by various DEMs. Even though there is a certain variation of ΔH present when using the DGPS data, it is lower than in the case of the DEMs. This residual variation can be attributed to terrain undulations in the ICESat footprints and probably also to the effects of the horizontal component of glacier movements. The trend for Konkordiaplatz based on DGPS is equal to the one for the Airphoto DEM and very close to the one for the SRTM-C DEM.

The available DEMs that were used for the analysis differ in terms of detail level, amount of noise and spatial coverage. The use of the Airphoto DEM for the elevation reference provided results comparable with the ground truth measurements. When comparing the global DEMs, the use of the SRTM-C DEM as elevation reference provides a more robust estimate of ΔH for all three areas than the ASTER GDEM which provides the worse results, especially in the snow-covered accumulation area. The different penetration depth of the C-band signal into firn and ice discussed by several authors [11,40,41] did not affect the results since the accumulation area was treated separately. The penetration depth of C-band signal during the SRTM data acquisition can be estimated as a difference between ΔH values for C- and X-band in the area A3 (Table 2). The resulting value of 3.0 m seems to be a realistic estimate of the C-band signal penetration. The spatially limited SRTM-X DEM does not seem to provide a better result than the SRTM-C DEM.

Although the snow cover depth of alpine glaciers, especially in the accumulation area, can be highly variable [42], the use of *in-situ* snow depth measurements led to suppression of a seasonal signal in the data. This allowed us to take multi-seasonal ICESat measurements which can be essential in areas with only few ICESat tracks. Multi-seasonal data was similarly used by [12,13]. The representativeness of snow depth measurement from a close meteorological station is biased by the spatial irregularity of precipitation, the redistribution of snow cover by wind and a depth gradient with elevation. Regardless, in our case, the application of the snow correction leads to a higher statistical significance of the derived trends.

A recent study of [34] showed that ICESat measurements tend to be inaccurate for slope values higher than 10° . The comparison of waveforms over various glacier surfaces in terms of slope and roughness in Figure 4 showed that higher slope and higher roughness results in a wider and more complex waveform which can in turn lead to an error in elevation estimation. The application of a threshold for terrain slope seems to be an effective approach in areas with complex topography as was shown for area A1. It leads to a reduction of error ranges and to an increase of statistical significance even over the relatively flat surface of Konkordiaplatz. However, this approach did not bring any improvements in area A3. Moreover, a trade-off between this positive effect and the reduction of number of measurements has to be considered.

Unfortunately, there are no glaciological mass balance measurements for the studied period that could be used for a comparison. However, the mass balance derived from the combination of ICESat data with the SRTM-C DEM matches well to the results of another geodetic method based on the subtraction of two DEMs from the years 1999 and 2009 (Table 4) and to a detailed reconstruction of

mass balance by [43]. Certain underestimation of trends derived from ICESat measurements for areas A2 and A3 and a non-linearity of the surface lowering with altitude revealed by the DEM subtraction lead to an underestimation of the mass balance due to the sparse ICESat sampling (Figure 8). This suggests that proper attention has to be paid to the distribution of ICESat data over the elevation range when considering this method for a single glacier. The differences of the trend in surface lowering in area A3 (Table 2) are difficult to explain. As this area is close to the terminus, a high variability of the surface shape can be assumed between the different DEMs acquired at different times. It is evident from Figure 8 that the ICESat-derived trend in ΔH using the Airphoto DEM as an elevation reference is the best match to the subtraction of DEMs. Nevertheless, the impact of these differences on the resulting mass balance is rather small.

6. Conclusions

In this study, the mass balance of the Grosser Aletschgletscher in the Swiss Alps was estimated from ICESat laser altimetry combined with a digital elevation model (DEM). This is the first time that the mass balance of a single mountain glacier was estimated using ICESat measurements. The mass balance differs only 9.8% when comparing with the result of another geodetic approach based on the subtraction of two DEMs produced by aerial stereo-photogrammetry. Depending on the DEM used as an elevation reference, an annual mass balance between -0.90 ± 0.17 m w.e. a^{-1} and -1.02 ± 0.34 m w.e. a^{-1} was estimated for the period 2003–2009. Various processing approaches were tested including a threshold for terrain slope, snowpack correction, selection of autumn measurements and along-track smoothing of ICESat-DEM elevation differences. Comparison of the various approaches resulted in differences in mass balance in the range from 0.4% to 5.8%, comparing to the other geodetic approach. It was shown that even the use of global DEMs as elevation reference can lead to a good estimate of surface lowering. The use of the SRTM-C and ASTER-GDEM results in differences of 3.8% and 15.3% from the surface lowering based on Differential Global Positioning System measurements as an elevation reference. However, the use of a higher quality DEM provides better results in terms of variation of ICESat-DEM elevation differences which in turn leads to a higher significance of the estimated trends and to a more accurate mass balance. Global availability of a detailed high quality DEM in the future will indeed improve the accuracy of the derived mass balance of mountain glaciers. In this context, there are high expectations for the global DEM derived from data of the TanDEM-X mission and for the ICESat-2 mission. The results of the Grosser Aletschgletscher indicate that, for a single glacier, surface lowering can be realistically assessed by interpolation across the elevation range, if the ICESat measurements are favorably distributed over the glacier surface. However, the actual surface lowering may locally differ due to non-linearities caused by glacier geometry. This approach indeed cannot compete with a glaciological approach in terms of accuracy; it appears however that it can lead to a realistic estimate of mass balance of a single glacier. As there is only a small fraction of mountain glaciers covered by mass balance measurements worldwide, ICESat data in combination with a DEM can help to fill this gap.

Acknowledgments

This work was supported by the German Research Foundation (DFG) Priority Programme 1372, “Tibetan Plateau: Formation–Climate–Ecosystems” within the DynRG-TiP (“Dynamic Response of Glaciers on the Tibetan Plateau to Climate Change”) project under the code BU 949/20-3, and by the German Federal Ministry of Education and Research (BMBF) Programme “Central Asia–Monsoon Dynamics and Geo-Ecosystems” (CAME) within the WET project (“Variability and Trends in Water Balance Components of Benchmark Drainage Basins on the Tibetan Plateau”) under the code 03G0804D. We acknowledge support by Open Access Publishing Fund of the University of Tuebingen. ICESat data was provided by NSIDC, SRTM-C DEM was obtained from the USGS and the SRTM-X DEM was provided by the DLR. ASTER GDEM is a product of METI and NASA. The field measurements of the snow depth were provided by the Institute for Snow and Avalanche Research in Davos, Switzerland. The Landsat scene was provided by the USGS. Thanks to B. Schröter for support during the field survey.

Author Contributions

The authors contributed to the reported research and writing of this paper as follows Jan Kropáček: 60%, 65%, Niklas Neckel: 25%, 25%, Andreas Bauder: 15%, 10%.

Conflicts of Interest

The authors declare no conflict of interest.

References and Notes

1. WGMS. *Global Glacier Changes: Facts and Figures*; Zemp, M., Roer, I., Kääb, A., Hoelzle, M., Paul, F., Haeberli, W., Eds.; World Glacier Monitoring Service: Zurich, Switzerland, 2008.
2. WGMS. *Fluctuations of Glaciers 2005–2010 (Vol. X)*; Zemp, M., Frey, H., Gärtner-Roer, I., Nussbaumer, S.U., Hoelzle, M., Paul, F., Haeberli W., Eds.; World Glacier Monitoring Service: Zurich, Switzerland, 2012.
3. Oerlemans, J. *Glaciers and Climate Change*; CRC Press: Rotterdam, The Netherlands, 2001.
4. NSIDC. Available online: http://nsidc.org/data/icesat/orbit_grnd_trck.html (accessed on 24 October 2013).
5. Howat, I.M.; Smith, B.E.; Joughin, I.; Scambos, T.A. Rates of southeast Greenland ice volume loss from combined ICESat and ASTER observations. *Geophys. Res. Lett.* **2008**, doi:10.1029/2008GL034496.
6. Slobbe, D.; Lindenbergh, R.; Ditmar, P. Estimation of volume change rates of Greenland’s ice sheet from ICESat data using overlapping footprints. *Remote Sens. Environ.* **2008**, *112*, 4204–4213.
7. Moholdt, G.; Nuth, C.; Hagen, J.O.; Kohler, J. Recent elevation changes of Svalbard glaciers derived from ICESat laser altimetry. *Remote Sens. Environ.* **2010**, *114*, 2756–2767.
8. Rinne, E.J.; Shepherd, A.; Palmer, S.; van den Broeke, M.R.; Muir, A.; Ettema, J.; Wingham, D. On the recent elevation changes at the Flade Isblink Ice Cap, northern Greenland. *J. Geophys. Res.: Earth Surface* **2011**, doi:10.1029/2011JF001972.

9. Sørensen, L.S.; Simonsen, S.B.; Nielsen, K.; Lucas-Picher, P.; Spada, G.; Adalgeirsdottir, G.; Forsberg, R.; Hvidberg, C.S. Mass balance of the Greenland ice sheet (2003–2008) from ICESat data—The impact of interpolation, sampling and firn density. *Cryosphere* **2011**, *5*, 173–186.
10. Brenner, A.C.; DiMarzio, J.P.; Zwally, H.J. Precision and accuracy of satellite radar and LASER altimeter data over the continental ice SHEETS. *IEEE Trans. Geosci. Remote Sens.* **2007**, *45*, 321–331.
11. Kääb, A.; Berthier, E.; Nuth, C.; Gardelle, J.; Arnaud, Y. Contrasting patterns of early twenty-first-century glacier mass change in the Himalayas. *Nature* **2012**, *488*, 495–498.
12. Gardner, A.S.; Moholdt, G.; Cogley, J.G.; Wouters, B.; Arendt, A.A.; Wahr, J.; Berthier, E.; Hock, R.; Pfeffer, W.T.; Kaser, G.; *et al.* A reconciled estimate of glacier contributions to sea level rise: 2003 to 2009. *Science* **2013**, *340*, 852–857.
13. Neckel, N.; Kropáček, J.; Bolch, T.; Hochschild, V. Glacier mass changes on the Tibetan Plateau 2003–2009 derived from ICESat laser altimetry measurements. *Environ. Res. Lett.* **2014**, doi:10.1088/1748-9326/9/1/014009.
14. Bauder, A.; Funk, M.; Huss, M. Ice-volume changes of selected glaciers in the Swiss Alps since the end of the 19th century. *Ann. Glaciol.* **2007**, *46*, 145–149.
15. Holzhauser, H. Die bewegte Vergangenheit des Grossen Aletschgletschers. *Blätter aus der Walliser Geschichte* **2009**, *41*, 103–121.
16. Thyssen, F.; Ahmad, M. Ergebnisse seismischer Messungen auf dem Aletschgletscher. *Polarforschung, Bremerhaven, Alfred Wegener Institute for Polar and Marine Research & German Society of Polar Research* **1969**, *39*, 283–293.
17. Huss, M.; Hock, R.; Bauder, A.; Funk, M. 100-year mass changes in the Swiss Alps linked to the Atlantic Multidecadal Oscillation. *Geophys. Res. Lett.* **2010**, doi:10.1029/2010GL042616.
18. Huss, M.; Bauder, A.; Funk, M.; Hock, R. Determination of the seasonal mass balance of four Alpine glaciers since 1865. *J. Geophys. Res.: Earth Surface* **2008**, doi:10.1029/2007JF000803.
19. Schutz, B.E.; Zwally, H.J.; Shuman, C.A.; Hancock, D.; Di Marzio, J.P. Overview of the ICESat mission. *Geophys. Res. Lett.* **2005**, doi:10.1029/2005GL024009.
20. Abdalati, W.; Zwally, H.J.; Bindschadler, R.; Csatho, B.; Farrell, S.L.; Fricker, H.A.; Harding, D.; Kwok, R.; Lefsky, M.; Markus, T.; *et al.* The ICESat-2 laser altimetry mission. *Proc. IEEE* **2010**, *98*, 735–751.
21. Zwally, H.J.; Schutz, R.; Bentley, C.; Bufton, J.; Herring, T.; Minster, J.; Spinhirne, J.; Thomas R. *GLAS/ICESat L2 Global Land Surface Altimetry Data, Version 33*; National Snow and Ice Data Center: Boulder, CO, USA, 2003.
22. Rabus, B.; Eineder, M.; Roth, A.; Bamler, R. The shuttle radar topography mission, a new class of digital elevation models acquired by spaceborne radar. *ISPRS J. Photogramm. Remote Sens.* **2003**, *57*, 241–262.
23. Farr, T.G.; Rosen, P.A.; Caro, E.; Crippen, R.; Duren, R.; Hensley, S.; Kobrick, M.; Paller, M.; Rodriguez, E.; Roth, L.; *et al.* The shuttle radar topography mission. *Rev. Geophys.* **2007**, doi:10.1029/2005RG000183.
24. Sun, G.; Ranson, K.J.; Kharuk, V.I.; Kovacs, K. Validation of surface height from shuttle radar topography mission using shuttle laser altimeter. *Remote Sens. Environ.* **2003**, *88*, 401–411.

25. Hoffman, D.; Walter, J. How complementary are SRTM-X and -C band digital elevation models? *Photogramm. Eng. Remote Sens.* **2006**, *72*, 261–268.
26. Gorokhovich, Y.; Voustianiouk, A. Accuracy assessment of the processed SRTM-based elevation data by CGIAR using field data from USA and Thailand and its relation to the terrain characteristics. *Remote Sens. Environ.* **2006**, *104*, 409–415.
27. Carabajal, C.C.; Harding, D.J. ICESat validation of SRTM C-band digital elevation models. *Geophys. Res. Lett.* **2005**, doi:10.1029/2005GL023957.
28. Tachikawa, T.; Kaku, M.; Iwasaki, A.; Gesch, D.; Oimoen, M.; Zhang, Z.; Danielson, J.; Krieger, T.; Curtis, B.; Haase, J.; *et al.* ASTER Global Digital Elevation Model Version 2—Summary of Validation Results. Available online: <http://www.ersdac.or.jp/GDEM/ver2Validation/> (accessed on 1 November 2013).
29. Frey, H.; Paul, F. On the suitability of the SRTM DEM and ASTER GDEM for the compilation of topographic parameters in glacier inventories. *Int. J. Appl. Earth Observ. Geoinf.* **2011**, doi:10.1016/j.jag.2011.09.020.
30. Armstrong, R.; Raup, B.; Khalsa, S.; Barry, B.; Kargel, J.; Helm, C.; Kieffer, H. *GLIMS Glacier Database*; National Snow and Ice Data Center: Boulder, CO, USA, 2005.
31. Nuth C.; Kääb A. Co-registration and bias corrections of satellite elevation data sets for quantifying glacier thickness change. *Cryosphere* **2011**, *5*, 271–290.
32. Bhang, K.J.; Schwartz, F.W.; Braun, A. Verification of the vertical error in C-band SRTM DEM using ICESat and Landsat-7, Otter Tail County, MN. *IEEE Trans. Geosci. Remote Sens.* **2007**, *45*, 36–44.
33. Wesche, C.; Riedel, S.; Steinhage, D. Precise surface topography of the grounded ice ridges at the Ekströmsisen, Antarctica, based on several geophysical data sets. *ISPRS J. Photogramm. Remote Sens.* **2009**, *64*, 381–386.
34. Hilbert, C.; Schmillius, C. Influence of surface topography on ICESat/GLAS forest height estimation and waveform shape. *Remote Sens.* **2012**, *4*, 2210–2235.
35. Schubert, A.; Faes, A.; Kääb, A.; Meier, E. Glacier surface velocity estimation using repeat TerraSAR-X images: Wavelet- vs. correlation-based image matching. *ISPRS J. Photogramm. Remote Sens.* **2013**, *82*, 49–62.
36. Huss, M. Density assumptions for converting geodetic glacier volume change to mass change. *Cryosphere* **2013**, *7*, 877–887.
37. Koblet, T.; Gärtner-Roer, I.; Zemp, M.; Jansson, P.; Thee, P.; Haeberli, W.; Holmlund P. Reanalysis of multi-temporal aerial images of Storglaciären, Sweden (1959–99)—Part 1: Determination of length, area, and volume changes. *Cryosphere* **2010**, *4*, 333–343.
38. Fischer, A. Comparison of direct and geodetic mass balances on a multi-annual scale. *Cryosphere* **2011**, *5*, 107–124.
39. Berthier, E.; Schiefer, E.; Clarke, G.K.C.; Menounos, B.; Rémy, F. Contribution of Alaskan glaciers to sea-level rise derived from satellite imagery. *Nature Geosc.* **2010**, doi:10.1038/ngeo737.
40. Rignot, E.; Echelmeyer, K.A.; Krabill, W. Penetration depth of interferometric synthetic-aperture radar signals in snow and ice. *Geophys. Res. Lett.* **2001**, *28*, 501–504.
41. Gardelle, J.; Berthier, E.; Arnaud, Y. Impact of resolution and radar penetration on glacier elevation changes computed from DEM differencing. *J. Glaciol.* **2012**, *58*, 419–422.

42. Machguth, H.; Paul, F.; Hoelzle, M. Strong spatial variability of snow accumulation observed with helicopter-borne GPR on two adjacent Alpine glaciers. *Geophys. Res. Lett.* **2006**, doi:10.1029/2006GL026576.
43. Farinotti, D.; Usselman, S.; Huss, M.; Bauder, A.; Funk, M. Runoff evolution in the Swiss Alps: Projections for selected high-alpine catchments based on ENSEMBLES scenarios. *Hydrol. Process.* **2012**, *26*, 1909–1924.

© 2014 by the authors; licensee MDPI, Basel, Switzerland. This article is an open access article distributed under the terms and conditions of the Creative Commons Attribution license (<http://creativecommons.org/licenses/by/3.0/>).

C Recent mass balance of the Purogangri Ice Cap, central Tibetan Plateau, by means of differential X-band SAR interferometry

Author contribution: study design, data preparation, data analysis, figures and writing.

Current status: published, *The Cryosphere*.



Recent mass balance of the Purogangri Ice Cap, central Tibetan Plateau, by means of differential X-band SAR interferometry

N. Neckel, A. Braun, J. Kropáček, and V. Hochschild

Institute of Geography, University of Tübingen, Rümelinstr. 19–23, 72070 Tübingen, Germany

Correspondence to: N. Neckel (niklas.neckel@uni-tuebingen.de)

Received: 11 February 2013 – Published in The Cryosphere Discuss.: 21 March 2013

Revised: 30 August 2013 – Accepted: 9 September 2013 – Published: 24 October 2013

Abstract. Due to their remoteness, altitude and harsh climatic conditions, little is known about the glaciological parameters of ice caps on the Tibetan Plateau. This study presents a geodetic mass balance estimate of the Purogangri Ice Cap, Tibet's largest ice field between 2000 and 2012. We utilized data from the actual TerraSAR-X mission and its add-on for digital elevation measurements and compared it with elevation data from the Shuttle Radar Topography Mission. The employed data sets are ideal for this approach as both data sets were acquired at X-band at nearly the same time of the year and are available at a fine grid spacing. In order to derive surface elevation changes we employed two different methods. The first method is based on differential synthetic radar interferometry while the second method uses common DEM differencing. Both approaches revealed a slightly negative mass budget of -44 ± 15 and -38 ± 23 mm w.eq. a⁻¹ (millimeter water equivalent) respectively. A slightly negative trend of -0.15 ± 0.01 km² a⁻¹ in glacier extent was found for the same time period employing a time series of Landsat data. Overall, our results show an almost balanced mass budget for the studied time period. Additionally, we detected one continuously advancing glacier tongue in the eastern part of the ice cap.

of the TP (Thompson et al., 2006). In this study, we take a closer look at the recent mass balance of the Purogangri Ice Cap (PIC), Tibet's largest ice field (Shi et al., 2009). The PIC is located at 33°05' N, 89°10' E in the continental westerly-dominated north-central part of the TP (Thompson et al., 2006). Due to its remoteness and high altitude of 5800 m a.s.l, on average, field work at the PIC would involve high costs, large logistical efforts and great physical strain. Therefore, remote sensing is a promising alternative to conduct mass balance measurements of this ice cap.

In this study, we estimate the mass balance by geodetic means. In general, the geodetic mass balance is calculated by subtracting data sets of glacier surface elevation acquired at different times (e.g., Rignot et al., 2003; Kääb, 2008; Haug et al., 2009; Bolch et al., 2011). For the PIC two such data sets are available. The ice cap was almost completely mapped by X-band SAR Interferometry (InSAR) in February 2000 during the Shuttle Radar Topography Mission (SRTM) resulting in a Digital Elevation Model (DEM). Almost exactly 12 years later, on January 26, 2012, the ice cap was mapped by single-pass X-band InSAR from TerraSAR-X and its add-on for digital elevation measurements (TanDEM-X) (Krieger et al., 2007).

Utilizing these interferometric data sets, we followed two different approaches to estimate the geodetic mass balance of the PIC between 2000 and 2012. First, we employed Differential Synthetic Aperture Radar Interferometry (DInSAR). In this approach we subtracted a simulated SRTM-X interferogram from a single-pass TSX/TDX (TerraSAR-X/TanDEM-X) interferogram. In order to compare the DInSAR derived estimate with a more common method, we constructed a DEM from the TSX/TDX acquisition and calculated the surface elevation differences between the two InSAR derived

1 Introduction

The Tibetan Plateau (TP), also known as the third pole, is characterized by many glaciers and ice caps. Information of whether that ice is losing or gaining mass is a valuable indicator to understand the climate variability on the TP (Yao et al., 2012). This is of high importance as direct measurements of climatic parameters are sparse, especially in the central part

DEMs. Finally, the results of both approaches were converted to mass changes showing the enormous potential of the new TSX/TDX data for geodetic mass balance estimates in remote regions.

2 Data

2.1 Shuttle Radar Topography Mission

The SRTM was conducted from 11 to 22 February 2000 in order to derive a near-global DEM (Rabus et al., 2003; Farr et al., 2007). For this purpose, data from C- and X-band SAR were acquired. In this study we used the X-band DEM, which was processed at the German Aerospace Center (DLR). In comparison to the C-band ScanSAR system with a swath width of 225 km, the X-band SAR system was operated with a swath width of only 45 km leaving large data gaps in the resulting X-band DEM (Rabus et al., 2003). Fortunately, 90 % of the PIC is covered by the data set (Fig. 1). The DEM is sampled to a grid posting of one arc second and is referenced to the WGS84 ellipsoid.

2.2 TerraSAR-X and its add-on for digital elevation measurements (TanDEM-X)

TSX was launched in June 2007 followed by its twin satellite TDX in June 2010. The two satellites are flying in a unique helical formation acting as a single-pass InSAR system with a flexible baseline configuration (Krieger et al., 2007). The main goal of the TanDEM-X mission is the generation of a global consistent DEM with a 12 m × 12 m grid posting and a vertical accuracy of < 2 m (Moreira et al., 2004).

In this study, we employed the experimental Co-registered Single look Slant range Complex (CoSSC) product acquired in bistatic InSAR stripmap mode on 26 January 2012 (Table 1). The data were acquired on an ascending satellite pass with an incident angle of 44° and VV polarization. The CoSSC product has already been focused and co-registered at the TanDEM-X Processing and Archiving Facility (PAF) via the integrated TanDEM processor (Duque, 2012). For the interferometric processing of the CoSSC product we employed the GAMMA SAR and interferometric processing software (e.g., Werner et al., 2000).

Besides the tandem acquisition, we employed two TSX stripmap scenes acquired on 2 and 13 August 2011 (Table 1). The data were acquired on a descending satellite pass with an incident angle of 31° and HH polarization. From the phases of these scenes a coherence image was calculated, which was used to support and validate the Landsat derived glacier outlines shown in Fig. 1. Further details concerning the production of the DEM and the generation of the glacier outlines are described in the Methods section.

Table 1. Overview of satellite data and date of data acquisition. Perpendicular baseline, B_{\perp} and pass direction are given for SAR acquisitions (Fig. 1). For Landsat data path and row number is given next to the spatial resolution.

SAR sensor	date	B_{\perp} (m)	pass
SRTM-X	11–22 February 2000	155*	ascend.
TSX	2/13 August 2011	403	descend.
TSX/TDX	26 January 2012	155	ascend.
optical sensor	date	path / row	res. (m)
Landsat ETM+	25 August 1999	140/036	15
Landsat ETM+	7 October 2000	139/037	15
Landsat ETM+	28 October 2005	140/036	15
Landsat ETM+	16 September 2007	140/036	15
Landsat TM	15 August 2010	140/036	30
Landsat TM	19 September 2011	140/036	30
Landsat ETM+	13 September 2012	140/036	15
Landsat ETM+	29 September 2012	140/036	15

* In this study the baseline was simulated from the TSX/TDX pass, the original SRTM-X baseline is 59.9 m (Rabus et al., 2003).

2.3 Landsat

In order to compare the interferometrically derived results with changes in glacier extent, we utilized six Landsat Enhanced Thematic Mapper Plus (ETM+) and two Landsat Thematic Mapper (TM) scenes (Table 1). We used all bands of the orthorectified level T1 products provided by the United States Geological Survey (USGS). No horizontal shift was observed by visual comparison amongst the Landsat imagery, the co-registered TerraSAR-X coherence image and the SRTM-X DEM. In order to reduce data gaps induced by scanline errors in the 2012 ETM+ data, we combined two ETM+ scenes acquired in September 2012 (e.g., Chen et al., 2011). To enhance the spatial resolution of the Landsat ETM+ scenes to 15 m, pan-sharpening employing principal component analysis was performed.

3 Methods

3.1 Delineation of ice

In order to measure any glaciological parameter, the delineation of the ice body is an essential step. Glacier outlines are available globally through the Randolph Glacier Inventory (Arendt et al., 2012). However, for the PIC these glacier outlines are spatially inaccurate when compared to the Landsat scenes listed in Table 1.

Due to the high spectral contrast between glacier area and non-glacier area in our study region, we conducted an unsupervised 2-class classification to delineate the ice body for the years 2000 and 2012. This classification was performed on the pan-sharpened Landsat ETM+ scenes of 2000 and 2012, which incorporate the principal components of all

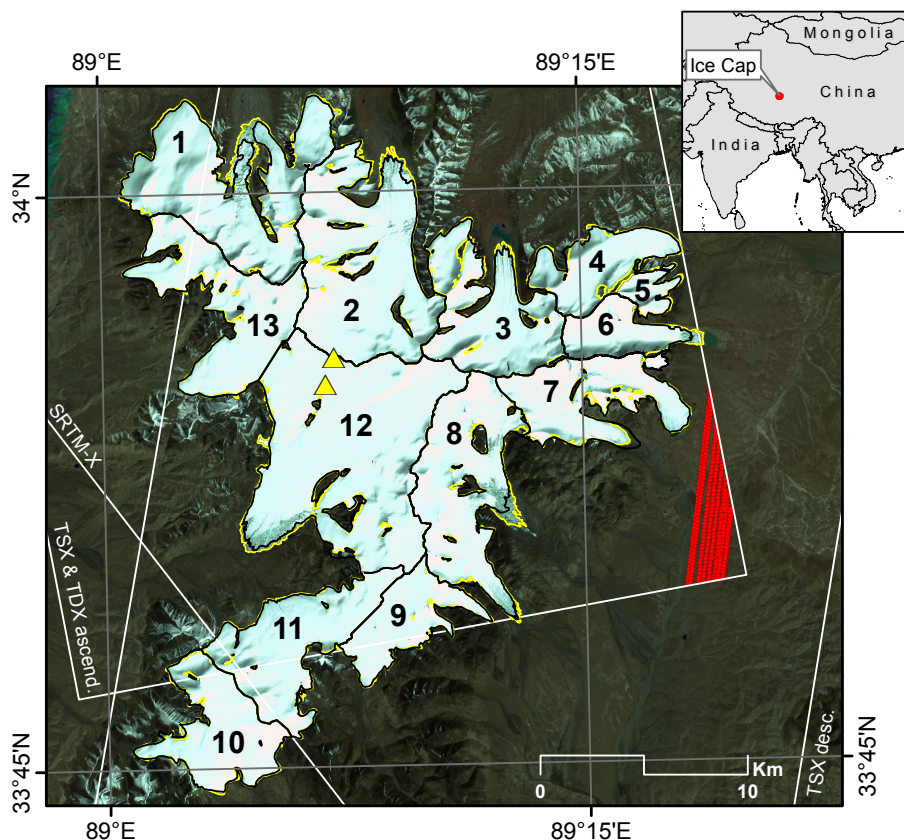


Fig. 1. Landsat ETM+ image, acquired on 7 October 2000, of the Purogangri Ice Cap (PIC) overlaid by SAR image footprints and glacier outlines for the years 2000 (yellow) and 2012 (black). Bands 4, 3, and 2 are combined as red, green, and blue, respectively. ICESat footprints are indicated as small red dots. Ice core drill sites of the Byrd Polar Research Center are shown as yellow triangles.

Landsat bands. We also tested a method based on band ratios and the use of a specific threshold as suggested by Paul et al. (2004) and Bolch et al. (2010b). For our study region, a visual comparison showed a good match between both methods.

Choosing only two classes revealed a general determination of on-glacier and off-glacier areas. Due to a few snow covered mountain ridges and remains of snow avalanches, the derived glacier masks were adjusted manually according to the Global Land Ice Measurements from Space standards (Rau et al., 2005). In consequence of occasional cloud cover in the Landsat ETM+ data of 2012, we employed an additional coherence image of an 11 day repeat-pass of TerraSAR-X acquired on 2 and 13 August 2011 (Table 1). Due to the short wavelength of TerraSAR-X (3.1 cm) and the changing surface characteristics of the ice cap (e.g., precipitation, wind drift, melting, freezing), a low coherence was calculated for ice covered areas whereas the coherence outside the glacier was distinguishably high (e.g., Frey et al., 2012). Two small cloudy patches in the 2012 glacier mask were fixed manually on the basis of the coherence image. Ice divides were estimated on the basis of watersheds extracted from the SRTM-X DEM utilizing the *r. watershed*

tool implemented in the *GRASS GIS* software (GRASS Development Team, 2012).

An error estimation of the resulting glacier masks was performed based on a modified approach from Granshaw and Fountain (2006) and Bolch et al. (2010a) who compared their semi-automatically generated results to independently digitized glacier outlines from high resolution aerial imagery at random locations. In this study, we used the additional TerraSAR-X coherence image as a reference base. Randomly selected parts of the TerraSAR-X coherence image were digitized manually and compared to the 2012 Landsat derived glacier extent. On the basis of these differences we calculated a mean relative error of $\pm 2.3\%$ for the estimated glacier area. It should be noted that this error estimate is rather conservative as it also includes one year of glacier change. As the 2000 glacier mask was derived with the same method we assume a similar error for the 2000 glacier extent.

3.2 Glacier elevation changes

In this study, glacier elevation changes were calculated using two different methods. The first method is based on differential SAR interferometry while the second method uses

common DEM differencing. Both approaches are using the TSX/TDX acquisition from January 2012 and the SRTM-X DEM acquired in February 2000 (Table 1). The main focus of this section is on the DInSAR approach followed by a brief description of the DEM differencing.

The interferometric phase of the single-pass TSX/TDX interferogram may be described by

$$\Delta\phi_{\text{TSX/TDX}} = \Delta\phi_{\text{orbit}} + \Delta\phi_{\text{topo}} + \Delta\phi_{\text{atm}} + \Delta\phi_{\text{scat}}, \quad (1)$$

where $\Delta\phi_{\text{TSX/TDX}}$ is the difference of phases ϕ_{TSX} and ϕ_{TDX} simultaneously acquired by TSX and TDX in January 2012 (Fig. 2, upper left). As the baseline of this satellite pass is relatively small (155 m) and the data were acquired simultaneously, the same atmospheric conditions are assumed for both SAR antennas, which sets the atmospheric contribution $\Delta\phi_{\text{atm}}$ in Eq. (1) to zero. The same applies for $\Delta\phi_{\text{scat}}$, which describes the phase difference due to different scattering on the ground. This only leaves $\Delta\phi_{\text{orbit}}$, which is the phase difference induced by the different acquisition geometry of the SAR sensors, and $\Delta\phi_{\text{topo}}$, which describes the phase difference induced by topography.

The DInSAR approach applied in this study can be described by

$$\Delta\phi'_{\text{diff}} = \Delta\phi_{\text{TSX/TDX}} - \Delta\phi_{\text{SRTM-X}}, \quad (2)$$

where $\Delta\phi_{\text{SRTM-X}}$ is the interferometric phase of the February 2000 SRTM-X acquisition. However, as the raw interferometric data of the SRTM-X acquisition is not available, $\Delta\phi_{\text{SRTM-X}}$ was simulated from SRTM-X DEM data using the satellite geometry and baseline model of the TSX/TDX pass from January 2012 (Fig. 2, lower part). Since the same satellite geometry and baseline model was used for both interferograms, the differential phase $\Delta\phi'_{\text{diff}}$ is solely based on changes in $\Delta\phi_{\text{topo}}$ between data acquisitions (Fig. 2, bottom). In order to solve the $2\text{-}\pi$ ambiguity of the difference interferogram, a phase unwrapping step was performed using *GAMMA*'s minimum cost flow (MCF) algorithm (Costantini, 1998). In the next step 20 ground control points (GCPs) were selected randomly in off-glacier regions across the entire scene. The relative differential phase was set to zero at these points as no changes in topography were assumed in these regions between 2000 and 2012.

Before calculating the difference interferogram and prior to the simulation of $\Delta\phi_{\text{SRTM-X}}$, precise horizontal offset registration and fitting between the TSX/TDX and the SRTM-X data set is mandatory. Therefore, we calculated a DEM from the TSX/TDX interferogram. For this we removed the orbital contribution from the interferogram ($\Delta\phi_{\text{orbit}}$) by subtracting a simulated flat-earth phase trend (e.g., Rosen et al., 2000). The resulting flattened interferogram was unwrapped using *GAMMA*'s MCF algorithm and converted to a DEM (Fig. 2, upper part). For the calculation of absolute heights, GCPs were obtained from the respective off-glacier pixel locations in the SRTM-X DEM. In the interferometric processing of the TSX/TDX DEM we observed an artificial linear

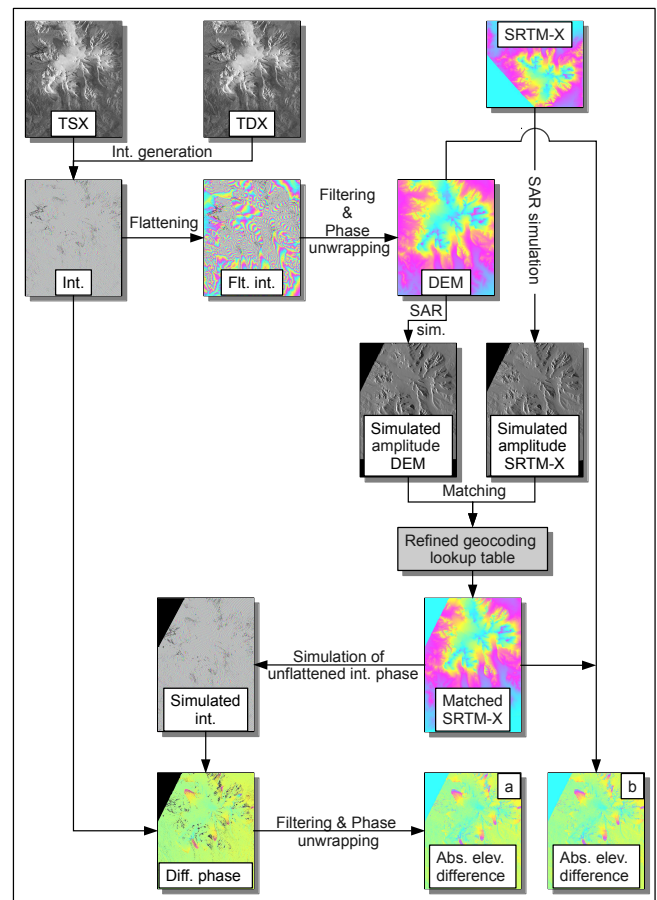


Fig. 2. Scheme of the DInSAR approach and the DEM differencing applied in this study. The abbreviations used in this figure are as follows: TSX, TerraSAR-X SSC; TDX, TanDEM-X SSC; SRTM-X, SRTM-X DEM; Int., interferogram; Flt. int., flattened interferogram; DEM, TSX/TDX DEM; SAR sim., SAR simulation; Simulated int., simulated interferogram; Diff. phase, differential phase; Abs. elev. difference, absolute surface elevation differences derived by DInSAR (a), and absolute surface elevation differences derived by DEM differencing (b).

phase ramp presumably related to an inaccurate flat-earth estimate. This linear phase ramp was minimized by an additional baseline refinement based on off-glacier phase values from the differential interferogram. In order to calculate horizontal offsets between both data sets, two SAR images were simulated from the DEMs using the orbital parameters of the TSX/TDX pass (e.g., Kropáček et al., 2012). Offsets were calculated using cross correlation optimization of the simulated SAR images employing *GAMMA*'s *offset_pwrn* module. These offsets were used to refine the horizontal data registration via a refined geocoding lookup table, which was used to translate the SRTM-X DEM from geographic coordinates into SAR coordinates (Fig. 2, central part) and, conversely, the final difference map from SAR coordinates to geographic coordinates (Fig. 5a).

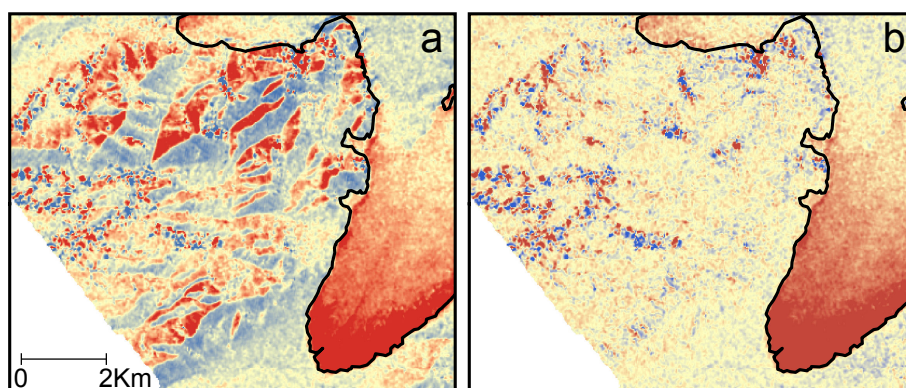


Fig. 3. Elevation differences estimated from DEM differencing before (a) and after the co-registration via a refined geocoding lookup table (b). Location of the data example is shown in Fig. 5b.

In order to compare the DInSAR derived elevation changes, we also constructed a difference map by common DEM differencing (Fig. 5b). Here we used the DEM that was created to estimate the horizontal offsets between the TSX/TDX data set and the SRTM-X DEM (Fig. 2, upper part). This DEM was geocoded to geographic coordinates with a grid posting of one arc second using the refined geocoding lookup table created above (Fig. 2, central part). This way both DEMs feature the same grid posting and are horizontally aligned. Figure 3 shows a subset of the map derived by common DEM differencing before (Fig. 3a) and after applying the refined geocoding lookup table to the data (Fig. 3b).

In the next step, a constant vertical offset and a linear trend were removed from both difference maps. The latter was estimated by a two dimensional first order polynomial fit in off-glacier regions and is probably a residual not covered by the baseline refinement mentioned above. The same linear trend was also removed from the TSX/TDX DEM. Finally, the data sets were translated to a metric cartographic coordinate system with a grid spacing of $25\text{ m} \times 25\text{ m}$ employing bilinear interpolation.

3.3 Estimation of mass changes and error computation

In order to translate the derived surface elevation changes into volume changes, an estimate of the glacier area is needed. To respect changes in glacier extent between the dates of data acquisition, we employed the geometric union of the 2000 and 2012 glacier masks (Li et al., 2012). We then multiplied the mean surface elevation changes of the 13 separated glaciers (Fig. 1) and of the entire ice cap by the respective area estimate. Finally, we applied an average ice density of $900 \pm 17\text{ kg m}^{-3}$ to convert volume changes to mass changes (Gardner et al., 2013). This was done separately for the DInSAR results and for the results of the DEM differencing. For a first accuracy assessment of the SRTM-X DEM we utilized data from the Geoscience Laser Altime-

ter System (GLAS) carried on-board the Ice Cloud and Elevation Satellite (ICESat). We employed the GLA 14 data product from all ICESat campaigns provided by the National Snow and Ice Data Center (NSIDC). SRTM-X surface elevations were extracted by bilinear interpolation at each ICESat footprint location. ICESat measurements were excluded from the analysis if the difference between GLA 14 and SRTM-X elevation exceeded 150 m, which can be attributed to cloud cover during the time of data acquisition. Compared to the ICESat data, we found a mean and standard deviation of $3.93 \pm 2.07\text{ m}$ for the SRTM-X DEM (SRTM-X DEM higher). We also compared the InSAR derived TSX/TDX DEM with the ICESat data sample available in our study region. Applying the same procedure as for the SRTM-X DEM, we found a mean and standard deviation of $3.24 \pm 1.11\text{ m}$ against the spatially limited ICESat sample (TSX/TDX DEM higher). As off-glacier SRTM-X values were used to translate the unwrapped TSX/TDX interferogram into absolute heights, a similar vertical bias is found for both DEMs. However, it should be noted that ICESat measurements are only available in a relatively flat off-glacier region (Fig. 1) making the ICESat sample distribution not fully representative for our study region.

For an error estimate of the derived surface elevation changes we used the Normalized Median Absolute Deviation (NMAD) in off-glacier regions, which is considered to be less sensitive to outliers than the standard deviation (Höhle and Höhle, 2009). As a certain degree of autocorrelation can be assumed in DEMs, we analyzed semivariograms and detected a decorrelation distance of $\sim 100\text{ m}$ (e.g., Nuth and Kääb, 2011). To avoid the effect of autocorrelation we reduced the grid spacing of non-glacier grid cells to $200\text{ m} \times 200\text{ m}$. In order to calculate the NMAD for a reasonable number of grid cells close to the glacier, we only employed grid cells located in a 1 km buffer around the ice cap. We estimated a NMAD of 2.38 m for the DInSAR approach and of 3.70 m for the DEM differencing.

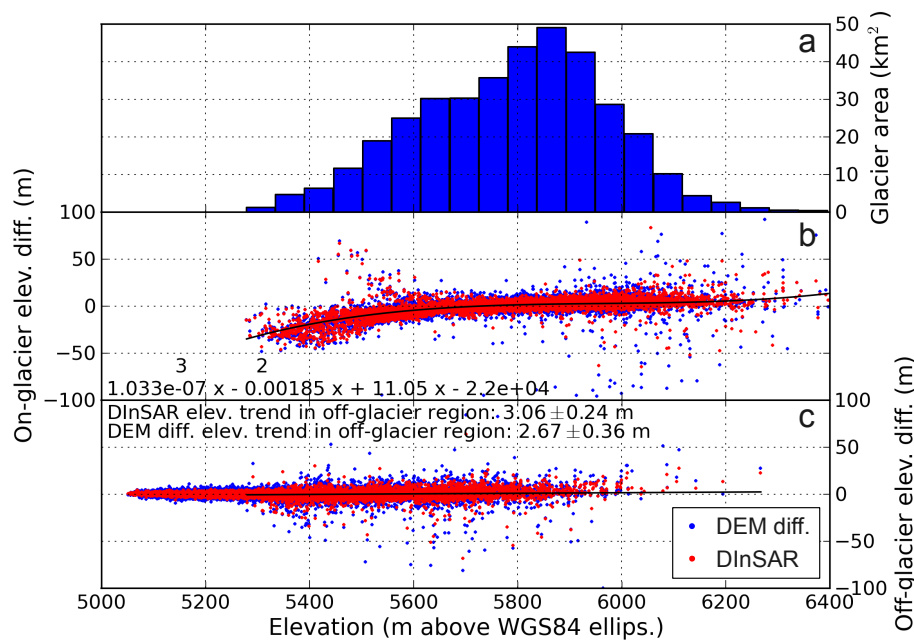


Fig. 4. Glacier hypsometry in 50 m elevation bins (a). Surface elevation changes of the PIC are shown as a function of elevation, a third order polynomial fit is shown as black solid line (b). Surface elevation changes in off-glacier regions are shown as a function of elevation, a linear trend is shown as black solid line (c).

In this study, the overall error of the derived surface elevation changes is given by

$$e = \sqrt{\text{NMAD}^2 + \text{wRMSE}^2}, \quad (3)$$

where the NMAD is the random part of the error while the systematic part of the error is estimated by a weighted root mean squared error (wRMSE) of the off-glacier trend residuals (Fig. 4c). From the residuals that represent the center points of the histogram bins shown in Fig. 4a we calculated a RMSE which was weighted by the histogram frequency. In this way, we estimated a systematic error of 0.32 m for the DInSAR approach and of 0.27 m for the DEM differencing.

For the overall error of mass changes we used the root of sum of squares of the estimated errors of glacier area and surface elevation differences and an error of $\pm 17 \text{ kg m}^{-3}$ for the density assumption.

4 Results

Similar to Lei et al. (2012), who estimated surface elevation changes of the PIC between 1974 and 2000, we found predominant surface lowering on outlet glaciers and glacier thickening in the interior of the ice cap (Fig. 5). However, on average the mass budget of the ice cap was close to equilibrium between 2000 and 2012. Table 2 lists the surface elevation changes next to the area changes and the annual mass budget between 2000 and 2012 for the observed part of the PIC. For the observed time period we estimated an annual

change rate of $-0.15 \pm 0.01 \text{ km}^2 \text{ a}^{-1}$ for the entire glacier area, suggesting a general but slow retreat of the ice cap in the last decade. It is evident in Figs. 4b and 5 that rapid thinning occurred in the lower regions of the ice cap while simultaneously a modest thickening occurred in the upper parts where the major glacier area is located (Fig. 4a).

The slightly negative mass budget of the PIC is in agreement with Yao et al. (2012), Gardner et al. (2013) and Neckel et al. (2013), who estimated balanced mass changes in the northwestern part of the TP for a similar time period, contrary to the remaining parts of the TP. Also, Lei et al. (2012) found that the PIC retreats at a much slower rate than other glaciers on the TP.

Prominent positive elevation changes were found for one glacier tongue in the eastern part of the Ice Cap (Fig. 6, World Glacier Monitoring Service id: 5Z213E0012). Between August 1999 and September 2011, the glacier terminus advanced by 515 m at an average rate of 43 m per year.

5 Discussion

In this study, elevation changes were calculated in two different ways. The first approach makes use of the interferometric phase of a differential interferogram, while the second approach starts from two co-registered DEMs. The results of both methods show a very similar pattern of surface elevation changes with a slightly smaller error estimate for the DInSAR approach (Table 2). The different noise level of the results is evident from the histograms shown in Fig. 5 and

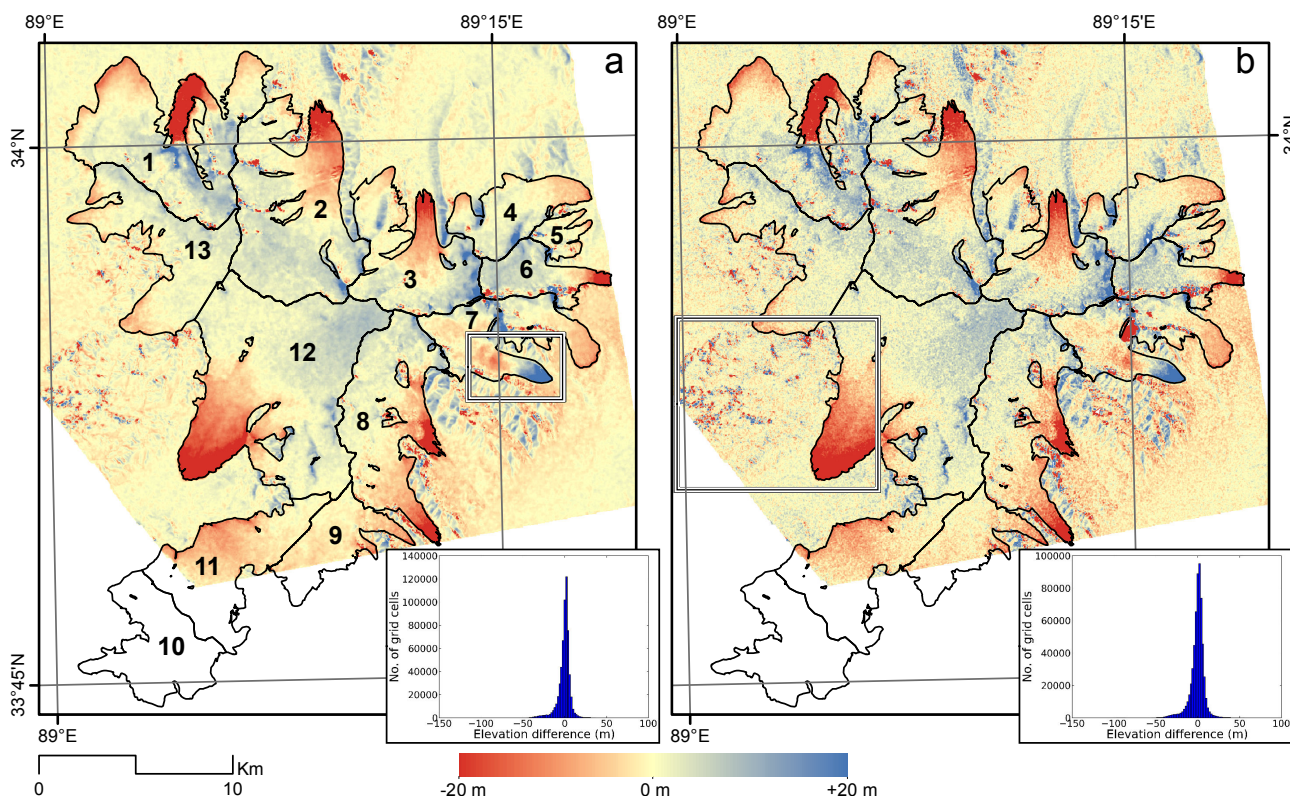


Fig. 5. Elevation changes of the PIC between February 2000 and January 2012. Figure (a) shows the difference map derived by DInSAR while Fig. (b) shows the difference map derived from absolute heights. The glacier outline is based on the geometric union of the 2000 and 2012 Landsat derived glacier extent. Histograms show the on-glacier elevation differences.

Table 2. Mean surface elevation changes estimated by DInSAR and from DEM differencing are listed next to the area changes and the annual mass budgets for the single glaciers shown in Figs. 1 and 5a. The geometric union of the 2000 glacier area (A_{2000}) and the 2012 glacier area (A_{2012}) is also shown. The error of the surface elevation changes is estimated as ± 2.40 m for the DInSAR approach and as ± 3.71 m for the DEM differencing, which also applies for the listed single glaciers.

id	mean ΔH DInSAR (m)	mean ΔH DEM diff. (m)	area change (km ²)	$A_{2000} \cup A_{2012}$ (km ²)	budget DInSAR (mm w.eq. a ⁻¹)	budget DEM diff. (mm w.eq. a ⁻¹)
1	-0.42	-0.31	-1.84 ± 0.04	48.00 ± 1.10	-31 ± 15	-23 ± 23
2	+0.07	+0.35	-0.50 ± 0.01	51.88 ± 1.19	$+5 \pm 15$	$+26 \pm 23$
3	+0.35	+0.58	$+0.07 \pm 0.01$	30.78 ± 0.71	$+26 \pm 15$	$+43 \pm 23$
4	+0.86	+0.83	$+0.42 \pm 0.01$	17.01 ± 0.39	$+65 \pm 15$	$+62 \pm 23$
5	+0.13	-0.16	-0.14 ± 0.01	4.51 ± 0.10	$+10 \pm 15$	-12 ± 23
6	+1.46	+1.17	-0.32 ± 0.01	12.66 ± 0.29	$+109 \pm 15$	$+88 \pm 23$
7	+1.05	+0.22	$+1.3 \pm 0.03$	25.56 ± 0.59	$+79 \pm 15$	$+16 \pm 23$
8	-2.35	-2.21	-0.73 ± 0.02	37.1 ± 0.85	-176 ± 16	-166 ± 24
9*	-2.79	-2.70	-0.01 ± 0.01	16.77 ± 0.39	-210 ± 16	-203 ± 24
10*	-	-	$+0.02 \pm 0.01$	24.35 ± 0.56	-	-
11*	-4.08	-4.05	-0.38 ± 0.01	30.54 ± 0.7	-306 ± 17	-304 ± 24
12	-1.20	-1.05	-0.12 ± 0.01	76.74 ± 1.77	-90 ± 15	-79 ± 23
13	+0.74	+0.91	$+0.41 \pm 0.01$	32.08 ± 0.74	$+56 \pm 15$	$+68 \pm 23$
total	-0.59 ± 2.40	-0.51 ± 3.71	-1.81 ± 0.04	407.97 ± 9.38	-44 ± 15	-38 ± 23

* Glacier is not or only partially covered by the interferometric data set.

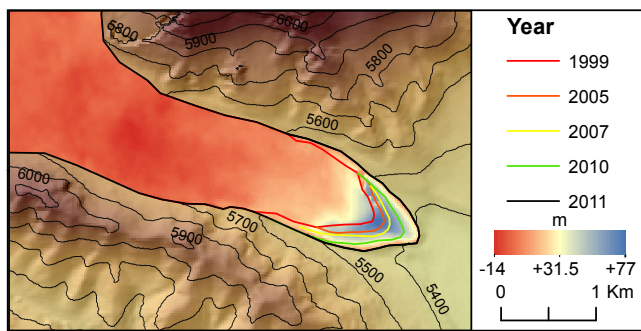


Fig. 6. Positive surface elevation changes in glacier tongue region of glacier 5Z213E0012 (World Glacier Monitoring Service id). DInSAR derived surface elevation changes are color-coded. In the background is the TSX/TDX DEM. Glacier terminus positions are based on Landsat imagery. Location is shown in Fig. 5a.

in Fig. 4, which shows a higher amount of noise for the result from the DEM differencing. This may be attributed to the fact that no filter was applied to the SRTM-X DEM in the case of the DEM differencing. As shown in the flowchart (Fig. 2), both approaches are using adaptive filtering prior to phase unwrapping (Goldstein and Werner, 1998). However, in the case of the DInSAR approach this filter is applied to both data sets, i.e., the filtering takes place after the differencing (Fig. 2, lower part), while for the DEM differencing the filtering is solely applied to the TSX/TDX interferogram (Fig. 2, upper part). For this reason, more noise is present in the result of the DEM differencing. The difference between both approaches (i.e., the difference between Fig. 5a and b) shows a normal distribution with a mean and standard deviation of 0.14 ± 2.18 m, suggesting that the noise, which we attribute to the SRTM-X DEM, is random.

The systematic error of the DInSAR approach, on the other hand, is estimated to be slightly higher than that of the DEM differencing. This is probably due to residual inaccuracies of the baseline refinement not covered by the additional first order polynomial fit.

A crucial point in both methods is an accurate horizontal co-registration between the input data sets. An accurate horizontal co-registration was achieved with the help of a refined geocoding lookup table (Fig. 3). As we used the same lookup table for both methods, we can assume that the differences between the two methods are not affected by a different horizontal data registration, but rather by vertical differences.

Even though we estimated a lower random error for the DInSAR approach, we cannot conclude that the DInSAR approach is more reliable. The DInSAR approach, however, provides a more homogeneous result because the random noise of both input data sets is minimized simultaneously during the adaptive phase filtering of the differential interferogram.

In general, both methods agree within their error bars (Table 2). However, the mean elevation differences of the listed

individual glaciers show rather large variations for glaciers 2, 5, 6 and 7 when comparing the two methods. We attribute these variations to the random noise, as the estimated surface elevation changes are rather low for these specific glaciers.

Penetration effects of SAR signals in snow and ice are widely discussed in the literature (e.g., Rignot et al., 2001; Gardelle et al., 2012a). The uncertainty induced by these effects are difficult to quantify when comparing InSAR derived DEMs with other data sets (e.g., Sauber et al., 2005; Berthier et al., 2006; Nuth and Kääb, 2011). The great advantage of this study is that the data sets used were acquired at the same wavelength at nearly the same time of the year. However, a certain bias introduced by the X-band penetration depth may have affected our results as the snow pack properties in 2000 and 2012 were probably not identical. Another bias can be expected from snow depth variations between 2000 and 2012 for which no measurements are available.

In 2000 two ice cores were drilled near the main ice divide of the PIC by the Byrd Polar Research Center in a joint US–Chinese project (Thompson et al., 2006). The location of the drill sites is shown in Figure 1. Personal communication with Davis (2013) and Thompson et al. (2006) suggest that the PIC has no obvious firn layer, therefore we applied an ice density of 900 ± 17 kg m⁻³ for the conversion from volume to mass changes for the entire ice cap. In order to test the sensitivity to a change in ice density, we also applied an ice density of 800 kg m⁻³, which resulted in a 10 % decrease of the total mass balance estimates shown in Table 2.

Our results suggest an almost balanced glacier regime for the PIC between 2000 and 2012, which is in agreement with Neckel et al. (2013), who found a slightly positive trend in mass balance between 2003 and 2009 for the Zangser Kangri ice cap, located ~ 300 km to the northwest. However, this behavior is contrary to the remaining parts of the TP where glacier mass balances are negative (Yao et al., 2012; Gardner et al., 2013; Neckel et al., 2013). The slightly negative mass budget of the PIC may be related to the same mechanisms as the frequently mentioned Pamir–Karakoram anomaly (e.g., Hewitt, 2005; Gardelle et al., 2012b, 2013). A possible mechanism could be a compensation of the temperature driven melt-off due to an increase of precipitation at high altitudes. This is in agreement with Li et al. (2011), who showed a significant increase in annual temperature and precipitation during the period 1961–2008 from meteorological station measurements on the TP. Also Dyurgerov and Dwyer (2000) found an increase in vertical gradient due to an annual ablation increase and a simultaneous increase in accumulation at higher altitudes on several glaciers in the Northern Hemisphere. According to Raper and Braithwaite (2009), such a behavior is typical for glaciers in wet and warm climate conditions rather than in a dry and cold continental climate.

Overall, we found negative elevation changes in glacier tongue regions except for one glacier in the eastern part of the ice cap. This glacier shows thickening at the terminus while negative values are found further up the glacier (Fig. 6).

These areas could be interpreted as reservoir and receiving areas of a surging glacier (Paterson, 1994).

6 Conclusions

In this study, we estimated the recent mass budget for large parts of the PIC by geodetic means. We employed SRTM-X DEM data from February 2000 and compared it with TSX/TDX data acquired in January 2012 following two different approaches. Very similar results were achieved by a DInSAR based approach and DEM differencing. We estimated modest positive elevation changes in the accumulation area of the ice cap while rapid negative elevation changes were found in glacier tongue regions. This behavior might be connected to an increase in ablation due to warmer climate conditions with a simultaneous increase in accumulation due to higher precipitation rates. Overall, the mass budget of the PIC is close to equilibrium with a mean annual mass budget of -44 ± 15 and -38 ± 23 mm w.eq. a^{-1} (millimeter water equivalent) estimated from the DInSAR approach and from the DEM differencing respectively. In the same time period, the ice cap retreated at a relatively slow rate of -0.15 ± 0.01 km² a^{-1} . Contrary to the remaining glacier tongues, we detected one continuously advancing glacier tongue in the eastern part of the ice cap. This study shows the enormous potential of the new TSX/TDX data to derive glacier elevation changes when combined with an older elevation data set. The data situation at the PIC is preferable as the SRTM-X DEM was acquired with the same method as the new TSX/TDX data.

Acknowledgements. This work was supported by the German Research Foundation (DFG) Priority Programme 1372, Tibetan Plateau: Formation–Climate–Ecosystems within the DynRG-TiP (Dynamic Response of Glaciers on the Tibetan Plateau to Climate Change) project under the codes SCHE 750/4-1, SCHE750/4-2, SCHE 750/4-3, and by the German Federal Ministry of Education and Research (BMBF) Programme Central Asia – Monsoon Dynamics and Geo-Ecosystems (CAME) within the WET project (Variability and Trends in Water Balance Components of Benchmark Drainage Basins on the Tibetan Plateau) under the code 03G0804D. SRTM-X, TerraSAR-X and TanDEM-X data were provided by the German Aerospace Center (DLR) under project ID HYD0534 and XTI_GLAC1054 respectively. We acknowledge NSIDC for hosting the ICESat data. All SAR processing was done with the GAMMA SAR and interferometric processing software. Thanks to U. Wegmüller, W. Rack and V. Helm for some hints and discussion in the processing of the TSX/TDX DEM. Information about the drill site locations was provided by M. Davis. The valuable comments of E. Berthier, C. Nuth, M. Pelto, K. Scharrer and the scientific editor A. Kääb improved the quality of the manuscript significantly.

Edited by: A. Kääb

References

- Arendt et al.: Randolph Glacier Inventory [v2.0]: A Dataset of Global Glacier Outlines. Global Land Ice Measurements from Space, Boulder Colorado, USA. Digital Media., 2012.
- Berthier, E., Arnaud, Y., Vincent, C., and Remy, F.: Biases of SRTM in high-mountain areas: Implications for the monitoring of glacier volume changes, *Geophys. Res. Lett.*, 33, 5, <http://dx.doi.org/10.1029/2006GL025862>, 2006.
- Bolch, T., Menounos, B., and Wheate, R.: Landsat-based inventory of glaciers in western Canada, 1985–2005, *Remote Sensing of Environment*, 114, 127–137, doi:10.1016/j.rse.2009.08.015, <http://www.sciencedirect.com/science/article/pii/S0034425709002661>, 2010a.
- Bolch, T., Yao, T., Kang, S., Buchroithner, M. F., Scherer, D., Mausson, F., Huintjes, E., and Schneider, C.: A glacier inventory for the western Nyainqentanglha Range and the Nam Co Basin, Tibet, and glacier changes 1976–2009, *The Cryosphere*, 4, 419–433, doi:10.5194/tc-4-419-2010, <http://www.the-cryosphere.net/4/419/2010/>, 2010b.
- Bolch, T., Pieczonka, T., and Benn, D. I.: Multi-decadal mass loss of glaciers in the Everest area (Nepal Himalaya) derived from stereo imagery, *The Cryosphere*, 5, 349–358, doi:10.5194/tc-5-349-2011, <http://www.the-cryosphere.net/5/349/2011/>, 2011.
- Chen, J., Zhu, X., Vogelmann, J. E., Gao, F., and Jin, S.: A simple and effective method for filling gaps in Landsat ETM+ SLC-off images, *Remote Sensing of Environment*, 115, 1053–1064, doi:10.1016/j.rse.2010.12.010, <http://www.sciencedirect.com/science/article/pii/S0034425710003482>, 2011.
- Costantini, M.: A novel phase unwrapping method based on network programming, *Geoscience and Remote Sensing, IEEE Transactions on*, 36, 813–821, doi:10.1109/36.673674, 1998.
- Duque, S.: CoSSC Generation and Interferometric Considerations. TD-PGS-TN-3129, 2012.
- Dyurgerov, M. and Dwyer, J.: The steepening of glacier mass balance gradients with northern hemisphere warming, *Zeitschrift für Gletscherkunde und Glazialgeologie*, 36, 107–118, 2000.
- Farr, T. G., Rosen, P. A., Caro, E., Crippen, R., Duren, R., Hensley, S., Kobrick, M., Paller, M., Rodriguez, E., Roth, L., Seal, D., Shaffer, S., Shimada, J., Umland, J., Werner, M., Oskin, M., Burbank, D., and Alsdorf, D.: The Shuttle Radar Topography Mission, *Rev. Geophys.*, 45, RG2004, <http://dx.doi.org/10.1029/2005RG000183>, 2007.
- Frey, H., Paul, F., and Strozzi, T.: Compilation of a glacier inventory for the western Himalayas from satellite data: methods, challenges, and results, *Remote Sensing of Environment*, 124, 832–843, doi:10.1016/j.rse.2012.06.020, <http://www.sciencedirect.com/science/article/pii/S0034425712002568>, 2012.
- Gardelle, J., Berthier, E., and Arnaud, Y.: Impact of resolution and radar penetration on glacier elevation changes computed from DEM differencing, *Journal of Glaciology*, 58, 419–422, 2012a.
- Gardelle, J., Berthier, E., and Arnaud, Y.: Slight mass gain of Karakoram glaciers in the early twenty-first century, *Nature Geosci.*, 5, 322–325, <http://dx.doi.org/10.1038/ngeo1450>, 2012b.
- Gardelle, J., Berthier, E., Arnaud, Y., and Kääb, A.: Region-wide glacier mass balances over the Pamir-Karakoram-Himalaya during 1999–2011, *The Cryosphere*, 7, 1263–1286, doi:10.5194/tc-7-1263-2013, <http://www.the-cryosphere.net/7/1263/2013/>, 2013.

- Gardner, A. S., Moholdt, G., Cogley, J. G., Wouters, B., Arendt, A. A., Wahr, J., Berthier, E., Hock, R., Pfeffer, W. T., Kaser, G., Ligtenberg, S. R. M., Bolch, T., Sharp, M. J., Hagen, J. O., van den Broeke, M. R., and Paul, F.: A Reconciled Estimate of Glacier Contributions to Sea Level Rise: 2003 to 2009, *Science*, 340, 852–857, doi:10.1126/science.1234532, <http://www.sciencemag.org/content/340/6134/852.abstract>, 2013.
- Goldstein, R. M. and Werner, C. L.: Radar interferogram filtering for geophysical applications, *Geophysical Research Letters*, 25, 4035–4038, doi:10.1029/1998GL900033, <http://dx.doi.org/10.1029/1998GL900033>, 1998.
- Granshaw, F. D. and Fountain, A. G.: Glacier change (1958–1998) in the North Cascades National Park Complex, Washington, USA, *Journal of Glaciology*, 52, 251–256, doi:10.3189/172756506781828782, <http://www.ingentaconnect.com/content/igsoc/jog/2006/0000052/00000177/art00009>, 2006.
- GRASS Development Team: Geographic Resources Analysis Support System (GRASS GIS) Software, Open Source Geospatial Foundation, USA, <http://grass.osgeo.org>, 2012.
- Haug, T., Rolstad, C., Elvehoy, H., Jackson, M., and Maalen-Johansen, I.: Geodetic mass balance of the western Svartisen ice cap, Norway, in the periods 1968–1985 and 1985–2002, *Annals of Glaciology*, 50, 119–125, doi:10.3189/172756409787769528, <http://www.ingentaconnect.com/content/igsoc/agl/2009/0000050/0000050/art00017>, 2009.
- Hewitt, K.: The Karakoram Anomaly? Glacier Expansion and the ‘Elevation Effect,’ *Karakoram Himalaya, Mountain Research and Development*, 25, 332–340, doi:10.1659/0276-4741(2005)025[0332:TKAGEA]2.0.CO;2, 2005.
- Höhle, J. and Höhle, M.: Accuracy assessment of digital elevation models by means of robust statistical methods, *ISPRS Journal of Photogrammetry and Remote Sensing*, 64, 398–406, doi:10.1016/j.isprsjprs.2009.02.003, <http://www.sciencedirect.com/science/article/pii/S0924271609000276>, 2009.
- Kääb, A.: Glacier Volume Changes Using ASTER Satellite Stereo and ICESat GLAS Laser Altimetry. A Test Study on Edgeøya, Eastern Svalbard, *IEEE Transactions on Geoscience and Remote Sensing*, 46, 2823–2830, 2008.
- Krieger, G., Moreira, A., Fiedler, H., Hajnsek, I., Werner, M., Younis, M., and Zink, M.: TanDEM-X: A Satellite Formation for High-Resolution SAR Interferometry, *Geoscience and Remote Sensing, IEEE Transactions on*, 45, 3317–3341, doi:10.1109/TGRS.2007.900693, 2007.
- Kropáček, J., De Grandi, G., and Rauste, Y.: Geo-referencing of continental-scale JERS-1 SAR mosaics based on matching homologous features with a Digital Elevation Model: theory and practice, *International Journal of Remote Sensing*, 33, 2413–2433, doi:10.1080/01431161.2011.609843, <http://www.tandfonline.com/doi/abs/10.1080/01431161.2011.609843>, 2012.
- Lei, Y., Yao, T., Yi, C., Wang, W., Sheng, Y., Li, J., and Joswiak, D.: Glacier mass loss induced the rapid growth of Linggo Co on the central Tibetan Plateau, *Journal of Glaciology*, 58, 177–184, doi:10.3189/2012JoG11J025, <http://www.ingentaconnect.com/content/igsoc/jog/2012/0000058/00000207/art00015>, 2012.
- Li, Z., He, Y., An, W., Song, L., Zhang, W., Catto, N., Wang, Y., Wang, S., Liu, H., Cao, W., Theakstone, W. H., Wang, S., and Du, J.: Climate and glacier change in southwestern China during the past several decades, *Environmental Research Letters*, 6, 24, <http://stacks.iop.org/1748-9326/6/i=4/a=045404>, 2011.
- Li, Z., Xing, Q., Liu, S., Zhou, J., and Huang, L.: Monitoring thickness and volume changes of the Dongkemadi Ice Field on the Qinghai-Tibetan Plateau (1969–2000) using Shuttle Radar Topography Mission and map data, *International Journal of Digital Earth*, 5, 516–532, doi:10.1080/17538947.2011.594099, <http://www.ingentaconnect.com/content/tandf/ijde/2012/0000005/0000006/art00004>, 2012.
- Moreira, A., Krieger, G., Hajnsek, I., Hounam, D., Werner, M., Riegger, S., and Settlemyer, E.: TanDEM-X: a TerraSAR-X add-on satellite for single-pass SAR interferometry, in: *Geoscience and Remote Sensing Symposium, 2004. IGARSS '04. Proceedings. 2004 IEEE International*, vol. 2, pp. 1000 – 1003 vol.2, doi:10.1109/IGARSS.2004.1368578, 2004.
- Neckel, N., Kropáček, J., Bolch, T., and Hochschild, V.: Glacier mass changes on the Tibetan Plateau 2003 – 2009 derived from ICESat laser altimetry measurements, *Environmental Research Letters*, publication in review, 2013.
- Nuth, C. and Kääb, A.: Co-registration and bias corrections of satellite elevation data sets for quantifying glacier thickness change, *The Cryosphere*, 5, 271–290, doi:10.5194/tc-5-271-2011, <http://www.the-cryosphere.net/5/271/2011/>, 2011.
- Paterson, W.: *The Physics of Glaciers* 3rd ed., New York: Pergamon, 1994.
- Paul, F., Huggel, C., and Kääb, A.: Combining satellite multi-spectral image data and a Digital Elevation Model for mapping debris-covered glaciers, *Remote Sensing of Environment*, 89, 510–518, doi:10.1016/j.rse.2003.11.007, <http://www.sciencedirect.com/science/article/pii/S0034425703003444>, 2004.
- Rabus, B., Eineder, M., Roth, A., and Bamler, R.: The shuttle radar topography mission – a new class of digital elevation models acquired by spaceborne radar, *ISPRS Journal of Photogrammetry and Remote Sensing*, 57, 241 – 262, doi:10.1016/S0924-2716(02)00124-7, <http://www.sciencedirect.com/science/article/pii/S0924271602001247>, 2003.
- Raper, S. C. B. and Braithwaite, R. J.: Glacier volume response time and its links to climate and topography based on a conceptual model of glacier hypsometry, *The Cryosphere*, 3, 183–194, doi:10.5194/tc-3-183-2009, <http://www.the-cryosphere.net/3/183/2009/>, 2009.
- Rau, F., Mauz, F., Vogt, S., Khalsa, S., and Raup, B.: *Illustrated GLIMS Glacier Classification Manual*, NSIDC, 2005.
- Rignot, E., Echelmeyer, K., and Krabill, W.: Penetration depth of interferometric synthetic-aperture radar signals in snow and ice, *Geophys. Res. Lett.*, 28, 3501–3504, <http://dx.doi.org/10.1029/2000GL012484>, 2001.
- Rignot, E., Rivera, A., and Casassa, G.: Contribution of the Patagonia Icefields of South America to Sea Level Rise, *Science*, 302, 434–437, doi:10.1126/science.1087393, <http://www.sciencemag.org/content/302/5644/434.abstract>, 2003.
- Rosen, P., Hensley, S., Joughin, I., Li, F., Madsen, S., Rodriguez, E., and Goldstein, R.: Synthetic aperture radar interferometry, *Proceedings of the IEEE*, 88, 333–382, doi:10.1109/5.838084, 2000.
- Sauber, J., Molnia, B., Carabajal, C., Luthcke, S., and Muskett, R.: Ice elevations and surface change on the Malaspina Glacier,

- Alaska, *Geophys. Res. Lett.*, 32, L23S01, <http://dx.doi.org/10.1029/2005GL023943>, 2005.
- Shi, Y., Liu, C., and Kang, E.: The Glacier Inventory of China, *Annals of Glaciology*, 50, 1–4, doi:10.3189/172756410790595831, <http://www.ingentaconnect.com/content/igsoc/agl/2010/00000050/00000053/art00001>, 2009.
- Thompson, L. G., Yao, T., Davis, M. E., Mosley-Thompson, E., Mashiotta, T. A., Lin, P.-N., Mikhalevko, V. N., and Zagorodnov, V. S.: Holocene climate variability archived in the Purogangri Ice Cap on the central Tibetan Plateau, *Annals of Glaciology*, 43, 61–69, doi:10.3189/172756406781812357, <http://www.ingentaconnect.com/content/igsoc/agl/2006/00000043/00000001/art00010>, 2006.
- Werner, C., Wegmüller, U., Strozzi, T., and Wiesmann, A.: GAMMA SAR and Interferometric Processing Software, in: ERS - ENVISAT Symposium, Gothenburg, Sweden, 2000.
- Yao, T., Thompson, L., Yang, W., Yu, W., Gao, Y., Guo, X., Yang, X., Duan, K., Zhao, H., Xu, B., Pu, J., Lu, A., Xiang, Y., Kattel, D. B., and Joswiak, D.: Different glacier status with atmospheric circulations in Tibetan Plateau and surroundings, *Nature Clim. Change*, 2, 663–667, <http://dx.doi.org/10.1038/nclimate1580>, 2012.

D Glacier variations at Gurla Mandhata (Naimona'nyi), Tibet: a multi-sensoral approach including TanDEM-X, Pléiades and KH-7 Gambit-1

Author contribution: contribution to the study design, [SAR](#) data analysis, contribution to the writing.

Current status: in review, *Remote Sensing of Environment*.

Glacier variations at Gurla Mandhata (Naimona'nyi), Tibet: a multi-sensoral approach including TanDEM-X, Pléiades and KH-7 Gambit-1

Nicolai Holzer^{a,*}, Niklas Neckel^b, Manfred Buchroithner^a, Noël Gourmelen^{c,d}, Jérôme Colin^e, Tobias Bolch^{a,f}

^a*Institut für Kartographie, Technische Universität Dresden, Helmholtzstraße 10, 01069 Dresden, Germany*

^b*Institut für Geographie, Universität Tübingen, Rümelinstraße 19-23, 72070 Tübingen, Germany*

^c*Institut de Physique du Globe de Strasbourg, Université de Strasbourg, 5 rue René Descartes, 67084 Strasbourg Cedex, France*

^d*School of Geosciences, University of Edinburgh, Geography Building Drummond Street, Edinburgh EH8 9XP, United Kingdom*

^e*Laboratoire ICube, UMR 7357 CNRS, Université de Strasbourg, 300 Boulevard Sébastien Brant, 67412 Illkirch-Graffenstaden Cedex, France*

^f*Geographisches Institut, Universität Zürich, Winterthurerstrasse 190, 8057 Zürich, Switzerland*

Abstract

Long-term glacier variations were determined at Gurla Mandhata (30.4° N, 81.2° E), situated in the Central Himalaya at the headwaters of the rivers Indus, Sutlej, Ganges and Brahmaputra. Its glaciers drain either in the endorheic Manasarovar Basin or via the exorheic Karnali Basin in the Indian Ocean. Glaciers are mapped from declassified KH-7 Gambit-1 spy photography of 1964 as well as from Landsat 7 ETM+ (2000), SPOT-5 (2010) and Pléiades (2013) imagery. Geodetic mass balance estimates are based on Digital Elevation Models (DEMs) relative to SRTM-3 (1999), generated from both TanDEM-X SAR interferometry (2012) and optical tri-stereo Pléiades data (2013). A third DEM of coarser quality from SPOT-5 HRG stereo imagery (2010) was used to validate the determined results. Glacier shrinkage from $79.0 \pm 1.6 \text{ km}^2$ in 1964 to $74.3 \pm 0.2 \text{ km}^2$ in 2013 corresponds to a loss of $6.0 \pm 2.1 \%$ during the study time period ($-0.12 \pm 0.04 \%$ a⁻¹). One advancing but thinning glacier tongue could be observed, while an average glacier retreat of $175.0 \pm 5.0 \text{ m}$ was measured at the same time ($-3.6 \pm 0.1 \text{ m a}^{-1}$). Glacier mass balances of in mean $-0.07 \pm 0.31 \text{ m w.e.a}^{-1}$ from Pléiades to $-0.11 \pm 0.20 \text{ m w.e.a}^{-1}$ from TanDEM-X show comparatively low but similar results by considering a SRTM-3 C-band radar penetration depth of $1.4 \pm 1.0 \text{ m}$ in all clean-ice glaciers. Layover and shadowing effects in this high mountain environment for TanDEM-X and low contrast in snow covered glacier areas for Pléiades and SPOT-5 are the main issues for terrain extraction by these two different approaches. This is the first glaciological study that combines KH-7 Gambit-1, TanDEM-X and Pléiades to provide data of glacier variations in a region, where such information is scarce.

Keywords: TanDEM-X, Pléiades, SPOT-5, KH-7 Gambit-1, SRTM-3, Digital Elevation Model, glacier mass balance, glacier area change, Gurla Mandhata, Naimona'nyi, climate change

1. Introduction

The glaciers of high mountain Asia are among the most sensitive key indicators of terrestrial climate change and regulate with its snow and ice reserves the upstream headwaters of the major south-east Asian rivers (IPCC, 2013; Pfeffer et al., 2014). Station records and most climate models indicate a near-surface warming trend (e.g. 0.2° C per decade by Ding et al. (2006)), with uncertain effects for the downstream water supply due to glacier melting (Kang et al., 2010; Immerzeel et al., 2013; IPCC, 2013). Strong spatial glacier variations associated with topographic and climatic effects were observed in the Himalayas while their

averaged mass loss is similar to other glaciers elsewhere in the world (Bolch et al., 2012; Yao et al., 2012a). The mean mass balance for the Pamir–Karakoram–Himalaya was estimated at $-0.14 \pm 0.08 \text{ m w.e. a}^{-1}$ between 1999 and 2011 (Gardelle et al., 2013) and for the Hindu Kush–Karakoram–Himalaya region at $-0.21 \pm 0.05 \text{ m w.e. a}^{-1}$ from 2003 and 2008 (Kääb et al., 2012). The highest retreat (-16.6 m a^{-1}) and shrinkage (-0.42% a⁻¹) as well as the most negative mass balance ($-0.91 \text{ m w.e. a}^{-1}$) was observed in the Himalaya (Yao et al., 2012a), with measured mass balances in West Nepal of $-0.32 \pm 0.13 \text{ m w.e. a}^{-1}$ by Gardelle et al. (2013) and of $-0.34 \pm 0.05 \text{ m w.e. a}^{-1}$ by Kääb et al. (2012). A recent study of Neckel et al. (2014) estimate a mass loss of $0.37 \pm 0.25 \text{ m w.e. a}^{-1}$ from ICESat laser altimetry measurements between 2003 and 2009 for the Gangdise Mountains including Gurla Mandhata.

Investigations of glacier area and length changes can be efficiently employed in such remote areas by taking advantage of satellite data. However, glacier shrinkage

*Corresponding author at: Institut für Kartographie, Technische Universität Dresden, Helmholtzstraße 10, 01069 Dresden, Germany. Telephone: +49 (0351) 463-33281, fax number: +49 (0351) 463-37028

Email address: nicolai.holzer@tu-dresden.de (Nicolai Holzer)

and retreat is only a delayed signal of climate variability, while glacier mass changes are an immediate reaction of glaciers to climate forcing. The geodetic glacier mass balance approach relies on the assumption that a change in glacier elevation can be translated to a change in ice mass, based on the expectation that the ice density has not changed and that there was no change in bedrock elevation (Bamber & Rivera, 2007). Several recent studies extracted Digital Elevation Models (DEMs) from optical stereo data such as from SPOT-5 (e.g. Gardelle et al., 2013; Vincent et al., 2013) or from declassified Keyhole Corona or Hexagon stereo imagery (e.g. Bolch et al., 2008; Holzer et al., 2012; Pieczonka et al., 2013) and compared them with elevation data from the Shuttle Radar Topography Mission (SRTM) conducted in 2000 to obtain glacier mass balance estimates in High Asia.

Pléiades and TanDEM-X are among the most modern high resolution optical and SAR satellites that are currently existing for geodetic glacier mass balance studies based on their extracted DEMs. Neckel et al. (2013) for TanDEM-X and Wagnon et al. (2013) for Pléiades are one of the first that used DEMs on glaciated regions from these new sensors. This is the first geodetic glacier mass balance study known to the authors that combines both tri-stereoscopic Pléiades and interferometric TanDEM-X remote sensing data by also taking advantage of declassified KH-7 Gambit-1 spy photography to investigate glacier area and length changes back to the year 1964. The aim of this detailed study at Gurla Mandhata is on the one hand to fill a knowledge gap since little is known about glacier variations in this remote region, and on the other hand to evaluate the potentials and limitations of these two very new sensors.

2. Study area

Gurla Mandhata (or Naimona'nyi in Chinese) is an isolated dome-shaped massif in the Central Himalaya (Nalankankar Himal) in Burang County, Ngari Prefecture, at 30.4° N, 81.2° E (Figure 1). It is the highest peak in the Central Himalaya (7694 m a.s.l.) and situated south of Mt. Kailash at the transition zone of the Indian monsoon and the Westerlies. Many of the cold glaciers originate from the shallowly-sloping subcontinental ice field at 6050 m a.s.l and do not extent below 5320 m a.s.l (Owen et al., 2010; ICIMOD, 2011). With other glaciers in this region they form the headwaters of the rivers Indus, Sutlej, Ganges and Brahmaputra. At Gurla Mandhata, they drain in two different watersheds: the endorheic Manasarovar Basin with its lakes Mapam Yumco (Manasarovar, 4586 m a.s.l.) and La'nga Co (Rakshas Tal, 4572 m a.s.l.) situated ~ 5 km north of the mountain range, and the exorheic Karnali Basin that drains as later affluent of the Ganges in the Indian Ocean by directly contributing to global sea-level rise.

The precipitation at Gurla Mandhata is significantly higher to the south and east by reason of the Indian sum-

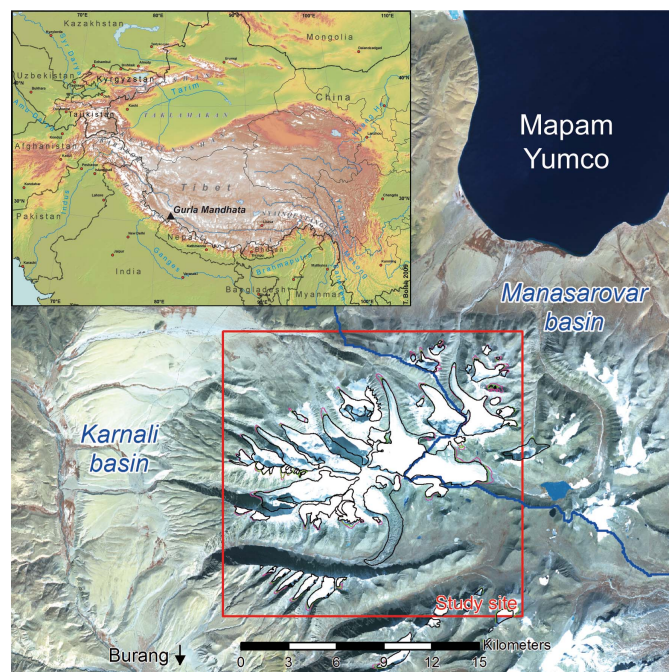


Figure 1: Overview of the Gurla Mandhata study site (red box) with overview map and drainage basins (background image SPOT-5)

mer monsoon and to the west due to winter Westerlies, however most of the glaciers (80% in the Kailash-Gurla Region) are orientated northwards. The resulting two precipitation peaks of approximately equal magnitude reflect a typical pattern in the transition zone controlled by both climate systems (Owen et al., 2010; ICIMOD, 2011; Mölg et al., 2013). The semi-arid continental-type climate was becoming drier and warmer in the past decades. From 1973 to 1984, the mean annual temperature in Burang (30° 17'N, 81° 15'E, 3900 m a.s.l.) was measured at 3° C and the total mean annual precipitation at 176 mm (Miehe et al., 2001; Owen et al., 2010). In Burang, an increase of air temperature at a rate of ~0.5° C per decade was observed from 1973 to 2008, while mean annual precipitation shows a decreasing trend from 177 mm (1973 to 1988) to 135 mm (1999 to 2008) (IGSNRR, 2010; Liao et al., 2011). Yao et al. (2012a) states that a weakening Indian monsoon and strengthening Westerlies might explain this precipitation decrease in the Himalayas, with the highest temperature rise that was observed at altitudes from 4800 m to 6200 m a.s.l.

Owen et al. (2010) could proof that the Gurla Mandhata massif was previously covered by an expanded ice cap before deep valley glaciers were formed. Kehrwald et al. (2008) suggest no net accumulation of ice mass since at least 1950 due to the lack of distinctive marker horizons in the Naimona'nyi ice core collected in 2006 near the summit and concludes that the glaciers are thinning at all elevations. With an elevation of 6050 m a.s.l. at the ice field summit, this is the highest documented occurrence of surface mass loss (Kehrwald et al., 2008).

3. Data

The study site at Gurla Mandhata covers an area of $\sim 340 \text{ km}^2$. All remote sensing data as summarized in Table 1 is referenced to WGS 84 (UTM zone 44N) and the EGM 96-geoid.

3.1. TerraSAR-X and its add-on for Digital Elevation Measurements (TanDEM-X)

TerraSAR-X (TSX) and TanDEM-X (TDX) are two almost identical radar satellites operated by the German Aerospace Center (DLR). TerraSAR-X was launched in June 2007 followed by TanDEM-X in June 2010. Both satellites are equipped with a X-band Synthetic Aperture Radar (SAR) system and flying in close formation to act as a single-pass SAR interferometer. The main goal of the TanDEM-X mission is the generation of a global consistent Digital Elevation Model (DEM) fulfilling the high DTED-3 specifications (Krieger et al., 2007; Buckreuss et al., 2009).

In this study, we employed the experimental Co-registered Single look Slant range Complex (CoSSC) product acquired in bistatic stripmap mode on 26 April 2012. The data was provided by DLR and acquired on a descending satellite pass with an incident angle of 36° and VV polarization. The CoSSC product has already been focused and co-registered via the integrated TanDEM processor (Duque, 2012). Two TerraSAR-X stripmap scenes recorded on 17 and 28 August 2011 were moreover used to support and validate mapped glacier outlines from optical imagery. This data was also acquired on a descending satellite pass and VV polarization, at an incident angle of 37° .

3.2. Pléiades

Pléiades (PLE) is an optical earth observation system for both civilian and military purpose developed by the French Space Agency CNES as part of the intergovernmental agreement ORFEO between France and Italy. With Pléiades 1A launched on 17 December 2011 and Pléiades 1B on 2 December 2012, it consists of two similar but not identical satellites that are flying at an altitude of 694 km. The nadir resolution of the panchromatic band is 0.7 m and of the four multi-spectral bands (blue, green, red and near-infrared) 2.8 m, resampled to 0.5 m and 2.0 m respectively. Pléiades offers an image swath of 20 km at nadir, and by adapting its viewing angle of up to 47° it can enlarge the width of the image to achieve a daily revisit interval of almost world wide coverage with its two satellites. Along-track tri-stereoscopic (triplet) mode implies the acquisition of three images focusing on the same area at one single pass under difference incidence angles, with one of the images being quasi-nadir for increasing altimetric accuracy at DEM extraction (Astrium, 2012; Gleyzes et al., 2012; Durand et al., 2013).

Within the framework of the ORFEO RTU Pléiades program of CNES we could take advantage of a tri-stereoscopic bundle mosaic recorded on 18 and 26 October 2013.

The images provided in Dimap format and processed at level 1A have for their stereoscopic pairs a base-to-height (b/h) factor ranging from 0.20 to 0.48 which equals to a difference of the along-track incidence angle of $5.75^\circ - 13.57^\circ$. The image of 18 October covers most of the study site while the most eastern part is covered by the image of 26 October.

3.3. SPOT-5

The SPOT-5 satellite flying at an altitude of 822 km at the equator was launched on 4 May 2002 and is equipped with imaging instruments known as High Resolution Geometric (HRG) and High Resolution Stereoscopic (HRS). While the latter sensor offers in-track stereo capability from the same orbit by a forward and backward looking camera with viewing angles of $\pm 20^\circ$, stereoscopy with pushbroom HRG data at an imaging swath of 60 km can be obtained from two different orbits by adjusting the viewing angle of up to $\pm 27^\circ$ relative to the vertical with thus a recommended resulting b/h-ratio in between 0.6 and 1.1 (b/h of HRS sensor: ~ 0.80). Contrary to in-track stereo imagery, across-track approaches have the disadvantage of radiometric image variations due to temporal changes in between both image captures from different points in time (Bouillon et al., 2003; Büyüksalih et al., 2005; Toutin, 2006).

In this study we obtained two SPOT-5 HRG level-1A multispectral mode image pairs of 2 and 6 November 2010 in Dimap format by the program ISIS of CNES. Both images have a pixel resolution of 2.5 m and to each other a cross-track difference of the viewing angle of 40.53° , resulting in a b/h-factor of 0.74. Unfortunately the second stereo image pair recorded on 2 November 2010 has serious quality problems in saturation that cannot be fixed, with saturations of 22.5% in band 1, 48.3% in band 2 and 8.6% in band 3.

3.4. Gambit-1 KH-7

The Keyhole KH-7 surveillance system was a military intelligence satellite program of the United States with codename Gambit-1 and flown from July 1963 to June 1967 (Mission numbers 4001–4038). Gambit-1 was the first high-resolution surveillance satellite flown at a relatively low orbital altitude of 60–150 nautical miles (90 miles nominal). It was equipped with a 77 inch focal length telescopic strip camera with a clear aperture of 19.5 inches developed by Eastman Kodak, acquiring images on thin film in continuous lengthwise sweeps of the terrain. Gambit-1 was able to carry a film of 3000 feet of length and 9.46 inches of width, taking photograph shots with film lengths varying from 4 inches to 500 feet. Image retrieval was realized through single film recovery capsules that returned to earth after each mission. Considerable KH-7 and KH-9 imagery was declassified in 2002 in accordance with executive order 12951 (NRO, 2011b,a; CSNR, 2012).

The KH-7 film stripe of this study was recorded on 5 December 1964 during mission 4014 with a resolutions

Table 1: Overview of SAR and optical remote sensing data used in this study

SAR Sensor	Date	Baseline [m]	Pass
SRTM-3 C-band v4.1	11 – 22 Feb. 2000	60	-
TSX	17 / 28 Aug. 2011	155	descend.
TSX/TDX	26 Apr. 2012	225	descend.
Optical sensor (stereo)	Date	b/h-factor (viewing angle)	Res. [m]
SPOT-5 HRG	02 / 06 Nov. 2010	0.74 (40.53°)	2.5
Pléiades HR 1A/1B	18 / 26 Oct. 2013	0.20 – 0.48 (5.75° – 13.57°)	0.5 (pan)
Optical sensor (mono)	Date	Product	Res. [m]
Gambit-1 KH-7	5 Dec. 1964	scanned film (3600 dpi)	0.6 – 1.2
Landsat 7 ETM+	24 Sep. 2000 (and others)	L1 t	30.0 (pan: 15.0)
Orbview-3	Nov. 2004 – Dec. 2005	L1 Gst	1.0 (pan)

of up to 2.1 feet (~ 0.6 m) (NRO, 2011b). Other sources (NRO, 2011a) document that for imagery recorded until 1966 a resolution of up to four feet (~ 1.2 m) at nadir could be obtained and that resolution improved to two feet (~ 0.6 m) during later missions. The photograph film was scanned at 7 microns (3600 dpi) in six overlapping subsets of 9.5 inch (0.24 m) of length for each section and provided as digital product by the U.S. Geological Survey (USGS) without any geo-reference or geo-correction.

3.5. Landsat 7 ETM+ and Orbview-3

A level T1 terrain corrected satellite image of the Landsat Enhanced Thematic Mapper 7 (ETM+) recorded on 24 September 2000 was used for glacier delineation of the year 2000. Because of the higher image resolution of 1 m in the panchromatic channel, multiple level 1 Gst orthorectified Orbview-3 images recorded from November 2004 to December 2005 were achieved for Ground Control Point (GCP) measurements. Both Landsat 7 ETM+ and Orbview-3 images were provided by USGS and show no horizontal offsets by visual comparison with other remote sensing ortho-imagery of this study.

3.6. Shuttle Radar Topography Mission (SRTM)

The Shuttle Radar Topography Mission (SRTM) was conducted from 11 to 22 February 2000 in order to derive a near-global DEM between 60° N and 57° S. Data acquisition was employed by C- and X-band SAR at 90 m and 30 m pixel resolution respectively, while the X-band DEM shows large data gaps due to a smaller swath width of the X-SAR interferometer (Falorni et al., 2005; Rodriguez et al., 2006).

In this study, we use the hole-filled SRTM-3 C-band DEM version 4.1 provided by the Consultative Group for International Agricultural Research (CGIAR). The vertical reference is in orthometric heights with respect to the WGS 84 reference system and the EGM 96-geoid (Gorokhovich & Voustianiouk, 2006; Reuter et al., 2007). The provided data mask proofed that only few areas at steep slopes particularly at ridges were gap filled and that almost the entire glacier area consists of original non-interpolated SRTM data.

4. Data processing

Data processing for later geodetic mass balance estimates includes the extraction of DEMs by use of Ground Control Points (GCPs), cleanup of erroneous elevation values, DEM co-registration to the SRTM-3 height model, and correction of elevation dependent biases. Glaciers are named according to their ID in the GLIMS database (GLIMS, 2005) (see Figure 2).

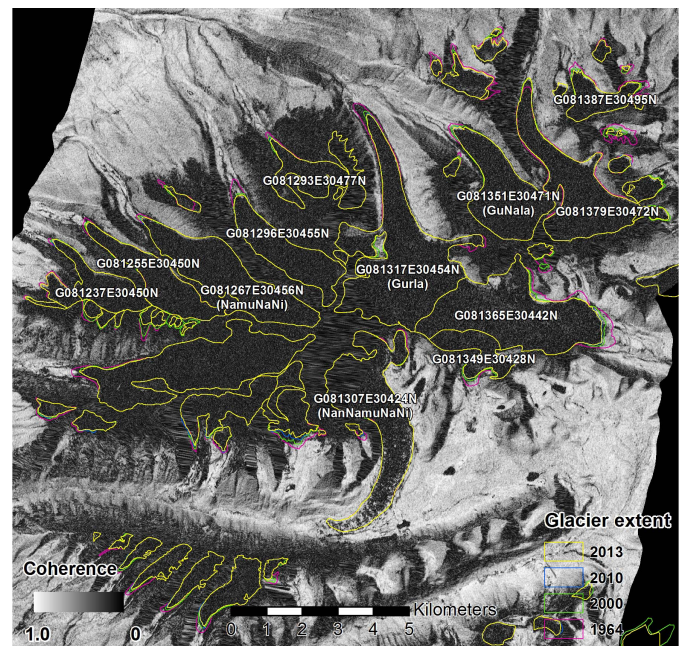


Figure 2: Generated TerraSAR-X coherence image of 17/28 Aug. 2011 used for validation of glacier outlines, where dark areas show low coherence compared to bright areas with high coherence. Glaciers of mass balance estimate are named according to their ID in GLIMS (GLIMS, 2005)

4.1. Ground Control Points

The x and y coordinates of the GCPs were measured on stable terrain in the orthorectified Orbview-3 images, ideally at anthropogenic objects such as bridges, cross roads and house corners. Since elevation accuracy in SRTM degrades with steeper slope (Falorni et al., 2005), we tried to measure GCPs in plain areas below a slope of 10°. If moreover available, we measured GCPs close to available

laser altimetry measurements from the Ice Cloud and Elevation Satellite (ICESat) for obtaining accurate height reference values combined with SRTM-3. All of our GCPs were finally cross checked in ortho-imagery of Landsat 7 ETM+ as well as Google EarthTM and showed no serious deviance.

4.2. InSAR DEM extraction (TanDEM-X)

For the interferometric processing of the CoSSC product we used the GAMMA SAR and interferometry processing software. From the CoSSC data product provided by DLR we calculated an interferogram by employing 5×5 multi-looking. A flat-earth trend was simulated from the satellite orbits and removed from the interferogram. The flattened interferogram was filtered and unwrapped using a minimum cost flow algorithm (Costantini, 1998). In order to minimize an artificial linear phase ramp evident in the unwrapped interferogram we adjusted the spatial baseline by measuring 50 GCPs which are evenly distributed over the satellite scene. With the help of the refined baseline file a DEM was created using GAMMA's *hgt_map* module. The final DEM was gridded to $30 \text{ m} \times 30 \text{ m}$ and geocoded via a refined geocoding look-up table (c.f. Neckel et al., 2013). A subset of the hillshade from this DEM is shown in Figure 3.

4.3. DEM extraction from optical stereo data (Pléiades and SPOT-5)

Terrain extraction from optical stereo data was realized with the software package Orthoengine of PCI Geomatica by using the *Rational Functions* model for Pléiades and *Toutin's Model* for SPOT-5 stereo images. Based on ephemeris information, an image location accuracy with usually a shift in absolute coordinates of 60 m for SPOT-5 HRG (Bouillon et al., 2003) and of 8.5 m at CE90 (As trium, 2012) for Pléiades with delivered Rational Polynomial Coefficients (RPCs) can be reached. For planimetric adjustment, we measured seven evenly distributed GCPs for the Pléiades mosaic and thirteen for the larger area of the SPOT-5 image. Tie points generated automatically by PCI with residuals higher as half of the image pixel size resolution were eliminated. After bundle block adjustment (with first order RPC adjustment for Pléiades), the residuals of the GCPs in the stereo model were 0.20 m in x-direction and 0.23 m in y-direction for Pléiades, and 2.0 m and 1.93 m respectively for SPOT-5.

We calculated one epipolar image pair from both SPOT-5 images and two epipolar pairs from the backward and nadir as well as from the nadir and forward looking views of the Pléiades tri-stereoscopic data. For terrain extraction we applied Wallis filtering to locally enhance the contrast and used for Pléiades the highest score of both generated DEMs. With a resolution of 0.5 m for Pléiades and 2.5 m for SPOT-5 imagery, we derived a Pléiades-DEM at 1 m and a SPOT-5 DEM at 10 m pixel resolution. Figure 3 shows a subset of the hillshade from the DEM of Pléiades.

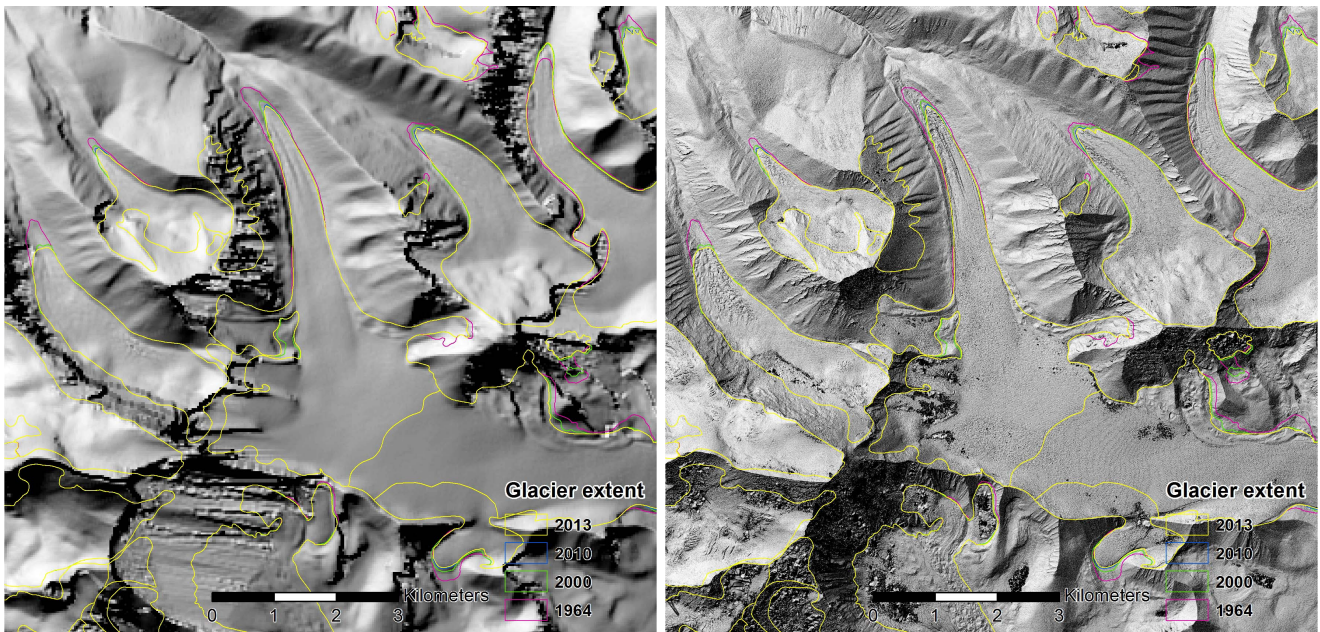
4.4. DEM enhancement and post-processing

Before post-processing, we resampled the acquired SRTM-3 and all generated DEMs to a resolution of 30 m with a common raster grid extent and at EGM96 orthometric heights by cubic convolution.

Clean-up of erroneous elevation values. PCI Orthoengine generates an additional score channel image that represents the correlation result for each extracted elevation value. The DEM of Pléiades shows good results even in case of low correlation coefficients, thereof a threshold of only 0.3 was used and elevation values below this value were considered as inaccurate and set to nodata. A higher threshold of 0.7 for SPOT-5 was set because of the much worse DEM quality due to a saturation problem in the second image pair. To identify erroneous height values in the DEM of TanDEM-X we calculated a coherence image from the CoSSC data product and set DEM elevations at a coherence below 0.3 to nodata. Due to unwrapping errors evident in the interferogram of the complex and mountainous terrain, some areas with erroneous height values of several meters still remained in the TanDEM-X DEM after thresholding and were subsequently set to nodata.

DEM co-registration. Proper alignment of multitemporal DEMs is a primary concern for the estimation of elevation changes (Paul et al., 2013b). We used an analytical approach as published by Nuth & Kääb (2011) that optimizes the co-registration based on the corresponding aspect and slope of each pixel in the difference image of two elevation models. For each DEM we calculated their difference image relative to SRTM-3 by excluding non-stable terrain such as glaciers, rock glaciers, ice cored moraines and water pixels. Only height differences (Δh) above a slope of 10° were considered by reason of the slope dependency of the method. We set the bounds to the 5% and 95% quantiles to eliminate most extreme outliers, and subsequently only examined values in between the two-tailed 1.5 times interquartile range to evaluate the horizontal fitting of our DEMs to SRTM-3 (c.f. Pieczonka et al., 2013). The determined x and y offsets were added to the image extent and the shifted DEMs were afterwards resampled back to the SRTM raster grid extent by cubic convolution.

Elevation-dependent bias correction. In all DEMs we detected systematic linear elevation trend offsets in form of a tilt relative to SRTM-3. For the DEMs extracted out of optical data this is probably caused by the spatial distribution of GCPs, and for the SAR TanDEM-X DEM due to a slightly inaccurate flat-earth estimate. After horizontal bias correction we calculated for each DEM two dimensional first order polynomial trend surfaces relative to SRTM-3. These are based on off-glacier difference images of the co-registered DEMs to SRTM-3 by only considering Δh values below a slope of 10° . Ice volume loss might be underestimated if SRTM is the older topography in a geodetic mass balance approach (Berthier et al.,



(a) TanDEM-X DEM of 26 Apr. 2012 (30 m res.)

(b) Pléiades DEM of 18 / 26 Oct. 2013 (1 m res.)

Figure 3: Subset of hillshades from generated project DEMs

2006) which is attributed to diverse resolutions in DEM differencing (Paul, 2008). To exclude resulting curvature effects we therefore only examined Δh values within the two-tailed 1.5 times interquartile range bounded by the 5% and 95% quantiles. This is similar as in case of horizontal shift correction, while other studies considered e.g. the terrain maximum curvature (c.f. Gardelle et al., 2012; Vincent et al., 2013). This bias correction minimizes the mean height offset to SRTM-3 to zero (see Table 2).

4.5. Orthorectification

Gambit-1 KH-7. Large ground coverage of KH-7 photographs was realized by a spaceborne panoramic camera which resulted in complex image distortions that are also an issue when working with data from earlier Keyhole missions such as Corona (e.g. Bolch et al., 2008; Pieczonka et al., 2011). Our study area is situated within the space of two scanned subsets near the center of the photograph (i.e. the image principle point) where the effect of the panoramic distortion is low compared to the margins of the film stripe.

Since no optimized mathematical model for this image geometry was available, we eliminated the complex panoramic distortions empirically by means of GCPs. First we generated a mosaic from both subsets by pixel based radiometric matching. Geometric correction was then employed by projective transformation (RPC order of 2) to a pixel resolution of 0.60 m, based on SRTM-3 and 26 evenly distributed GCPs. Measurements of GCPs was challenging due to the smaller coverage of the KH-7 film stripe

and the longer period of time in between the acquisition of the KH-7 and the reference Orbview-3 data. Since the resulting RMSE of ~ 40 m showed high inaccuracies, we subsequently employed non-linear rubber sheeting based on additionally 100 measured points that resulted in a final RMSE well within the uncertainties of ± 5 m.

Pléiades and SPOT-5. We orthorectified the Pléiades nadir views of the image mosaic based on its DEM derived from the same stereo imagery. Orthorectification of the SPOT-5 image of 6 November (which is not afflicted to saturation quality problems) was however based on SRTM-3 due to the poor quality of its own extracted DEM.

5. Glacier mapping and assessing glacier mass balance

5.1. Glacier area and length changes

By taking advantage of Pléiades VHR ortho-imagery and its extracted DEMs, glaciers were mapped manually for the year 2013 and subsequently adjusted to the situations of the years 1964 and 2010 based on the orthorectified KH-7 Gambit-1 and SPOT-5 satellite data. Glacier delineation for the year 2000 was employed in an automated way by using Landsat 7 ETM+ ratio techniques of band 4 divided by band 5 with a threshold of 2.0, followed by 3×3 median filtering to eliminate isolated pixels and by smoothing of the resulting glacier polygons (e.g. Racoviteanu et al., 2009; Paul et al., 2013b). Such techniques rely on high reflectivity of snow and ice in the VNIR

Table 2: Vertical accuracy measures of DEMs at stable terrain in respect to SRTM-3

DEM	Median [m]	NMAD [m]	68.3 % quantile [m]	95 % quantile [m]	Mean [m]	RMSE [m]	STD [m]
TDX	-0.08	2.74	2.91	5.85	0.00	2.89	2.89
PLE	-0.01	4.83	5.13	9.71	0.00	4.92	4.92
SPOT-5	-0.06	6.11	6.24	11.59	0.00	5.93	5.93

wavelengths compared to low reflectivity in the shortwave infrared (SWIR) (Dozier, 1989). Ice divides were automatically obtained from DEM watershed analysis. Glacier length changes were measured along the central glacier flow lines. We validated and corrected glacier outlines particularly in debris-covered areas by use of a coherence image derived from a 11-day TerraSAR-X repeat-pass acquisition of August 2011. This coherence image was calculated after proper co-registration of both SAR scenes, where contrary to the single-pass acquisition high decorrelation is evident for most of the glacierized areas (Figure 2). This can be attributed to a change of scattering on the glacier surface due to e.g. motion, melting, snow accumulation and wind drift between data acquisitions (e.g. Frey et al., 2012). Final cross-checks in Orbview-3 and Google EarthTM confirmed accurate fits. Some few outlines of three glaciers in the most eastern part of the study site were at some extent located outside of the KH-7 film stripe and therefore mapped from a Landsat 2 MSS image recorded on 6 December 1976.

5.2. Glacier mass balance

Twelve larger glaciers at all expositions were chosen for geodetic glacier mass balance estimates by employing both SAR and optical remote sensing approaches. Glacier volume changes for later ice mass conversion are derived from difference images by subtracting the DEM of the older date (SRTM-3) from both generated DEMs of Pléiades and TanDEM-X which are of newer date. Gap-filled areas of SRTM-3 were set to no-data and the largest glacier extent (i.e. the geometric union) of the mapped glacier outlines of 2000, 2010 and 2013 was used. Annual glacier mass balances with an assumed glacier ice density of $850 \pm 60 \text{ kg m}^{-3}$ (Huss, 2013) were finally calculated based on the gap-filled and SRTM-3 C-band penetration depth corrected mean elevation changes for each glacier from both Pléiades and TanDEM-X difference images. Due to its poor quality, the SPOT-5 DEM was only used to validate glacier thickness changes from its difference image to SRTM-3.

Data gap handling. Small nodata gaps below 0.01 km^2 were filled with a closing operator based on a mean filter for all Δh areas. To exclude very few but extreme outliers that still remained or appeared due to previous data post-processing, we employed a uniform threshold value of $\pm 35 \text{ m}$ in all difference images and set Δh values outside of this range to nodata. This threshold was determined by evaluating Δh quantiles from Pléiades, TanDEM-X and SPOT-5 to SRTM-3 which for the offset had to reside beyond the 5 % and 95 % quantiles in all difference images.

Remaining nodata gaps were afterwards separately filled for the glacier accumulation and ablation zones based on a height estimate of the equilibrium line altitude (ELA). Yao et al. (2012a) measured specific ELAs for Gurla Glacier (GLIMS ID *G081317E30454N*) at 6300 m for 2004/06, 6480 m for 2007/08, 6200 m for 2008/09 and 6150 m for 2009/10. By considering this variation, we assumed an ELA of 6200 m in our entire study area from 1999 to 2013. For the glacier ablation zones we locally calculated for every 25 m height section a mean Δh value that was used to fill nodata gaps within each section. Due to the relatively high ELA, there were often not sufficient Δh pixel values in the glacier accumulation zones to calculate confident nodata replacement values, such as the mode value. We thereof decided to use zero by also assuming very little elevation changes in such areas over time (Schwitter & Raymond, 1993). Gap-filling was cross-checked for every glacier, and in rare cases particularly at accumulation areas a more suitable nodata replacement value based on surrounding Δh pixel values from either Pléiades or TanDEM-X difference images was chosen if the automatic method did not produce confident results. Table 3 provides information about the extent and percentage of gap filled glacier areas separated in ablation and accumulation zones for Pléiades and TanDEM-X as well as for nodata glacier areas in SPOT-5 for that no gap-filling was employed.

Seasonality and correction of the SRTM-3 C-band penetration. Geodetic glacier mass balances should be based on data recorded at the same time of the year since seasonality can influence possible mass changes as well as the density by reason of varying layers of firn and snow (Gardelle et al., 2013). Imagery of Pléiades was recorded in October 2013 and of SPOT-5 in November 2010, but TanDEM-X SAR data was acquired in April 2012 and the SRTM mission was conducted in February 2000. We observed thin snow coverage and mostly snow-free glacier tongues in an acquired Landsat 7 ETM+ image of 18 April 2012. This is comparable to the image content of Pléiades and SPOT-5, and as a result no seasonal correction was employed to the DEM of TanDEM-X. Similar snow cover conditions are also apparent in Landsat 7 ETM+ imagery recorded on 28 January and 29 February 2000, presuming that a slight penetration of the SRTM-3 C-band signal should be considered. Due to penetration of the C-band beam into snow and firn refers the altitude of the SRTM-3 DEM to the glacier surface at the end of the melt season in 1999 (c.f. Pieczonka et al., 2013; Vincent et al., 2013). By reason of no SRTM-3 X-band coverage at our study site it was not possible to quantify the local penetration depth of the

Table 3: Gap filled / nodata glacier areas of DEMs that are splitted in accumulation (A_{acc}) and ablation (A_{abl}) zones compared to total glacier area A_{Σ} and valid stable terrain ($A_{stable-terrain}$) for DEM accuracy measurements

Glacier (GLIMS ID)	A_{Σ} [km ²]	TDX [km ²]			PLE [km ²]			SPOT-5 [km ²]
		$A_{gap-filled}$	A_{acc}	A_{abl}	$A_{gap-filled}$	A_{acc}	A_{abl}	A_{nodata}
G081237E30450N	1.99	0.36 (18.09 %)	0.28	0.08	0.09 (4.52 %)	0.08	0.01	1.55 (77.89 %)
G081255E30450N	2.92	0.32 (10.96 %)	0.32	0.00	0.12 (4.11 %)	0.12	0.00	2.30 (78.77 %)
G081267E30456N (NamuNaNi)	5.08	0.66 (12.99 %)	0.66	0.00	0.54 (10.63 %)	0.54	0.00	4.78 (94.09 %)
G081296E30455N	3.16	0.43 (13.61 %)	0.40	0.03	0.14 (4.43 %)	0.14	0.00	2.34 (74.05 %)
G081293E30477N	1.87	0.05 (2.67 %)	0.02	0.03	0.00 (0.00 %)	0.00	0.00	1.61 (86.10 %)
G081317E30454N (Gurla)	9.11	1.04 (11.42 %)	0.60	0.44	0.52 (5.71 %)	0.29	0.23	6.29 (69.05 %)
G081307E30424N (NanNamuNaNi)	6.34	1.70 (26.81 %)	0.01	1.69	0.47 (7.41 %)	0.00	0.47	2.48 (39.12 %)
G081351E30471N (GuNala)	4.23	0.22 (5.20 %)	0.21	0.01	0.01 (0.23 %)	0.01	0.00	2.87 (67.85 %)
G081365E30442N	7.47	0.18 (2.41 %)	0.03	0.15	0.06 (0.80 %)	0.01	0.05	5.59 (74.83 %)
G081349E30428N	1.69	0.05 (2.96 %)	0.00	0.05	0.00 (0.00 %)	0.00	0.00	1.19 (70.41 %)
G081379E30472N	5.18	0.30 (5.79 %)	0.02	0.28	0.04 (0.77 %)	0.01	0.03	3.76 (72.59 %)
G081387E30495N	1.45	0.26 (17.93 %)	0.02	0.24	0.00 (0.00 %)	0.00	0.00	0.18 (12.41 %)
Σ glaciers	50.49	5.57 (11.03 %)	2.57	3.00	1.99 (3.94 %)	1.20	0.79	34.94 (69.20 %)
Σ no glaciers	262.28	$A_{stable-terrain}$ 109.30			$A_{stable-terrain}$ 164.71			$A_{stable-terrain}$ 112.27

C-band signal by comparing C-band with X-band elevation values at off- and on-glacier areas (c.f. Gardelle et al., 2013). Hence we assumed the same penetration depth as it was published by Gardelle et al. (2013) for West Nepal as determined from their nearest Everest study site, however with an adapted error assumption: This is 1.4 ± 1.0 m for all clean-ice glaciers, except for the almost entirely debris covered NanNamuNaNi Glacier (*G081307E30424N*). We also calculated glacier mass balances by assuming either no penetration of the C-band beam and by assuming a penetration depth of 2.8 ± 2.0 m which is the double as used by Gardelle et al. (2013). No seasonality was corrected for SRTM-3 since the C-band radar penetration depth clearly dominates the uncertainty.

6. Uncertainty computation

6.1. Uncertainties of glacier area and length changes

The uncertainty for glacier mapping primarily depends on the image resolution and – in case of multiple data – on the registration technique (Hall et al., 2003; Bolch et al., 2010b). Other error sources include the method of glacier delineation, the glacier size, debris cover, the scene quality in regard of clouds and shadow, and seasonal snow that can tend to an overestimated result in glacier extent (Bolch et al., 2010a). In the study of Paul et al. (2013a) it turned out that automated mapping of clean ice glaciers is at least as accurate as manual mapping. Accuracy estimates on debris covered glaciers are more problematic since glacier ice below surface debris is difficult to distinguish due to a spectral reflectance similar to the surrounding moraine (Hall et al., 2003). A rough estimate for the precision of clean ice glacier mapping can be approximated by a one-pixel variability of the imagery out of that the glaciers were mapped from (Bolch et al., 2010b; Paul et al., 2013a).

We thereof buffered the glacier area by at least half of the pixel size resolution of the correspondent ortho-images. This is ± 0.5 m for the Pléiades images as mapping reference (2013), ± 1.5 m for SPOT-5 (2010) and ± 15 m for automated mapping from Landsat 7 ETM+ (2000). By visual comparison, co-registration of our orthorectified data shows accurate fits, except for the KH-7 ortho-photograph that still indicates slight inaccuracies even after rubber-sheeting. As a result, we used a much higher buffer size of ± 5 m for the mapping of 1964 which is about four to eight times the initial image resolution. The inaccuracies of glacier area changes are estimated as the root of sum of squares of each mapping dependent error and are shown in Table 4. The uncertainties of length changes are dominated by the accuracy of the KH-7 ortho-image and were thereof assumed to be in the range of ± 5 m (Table 5).

6.2. Uncertainties of glacier mass balances

The accuracy of DEM differencing depends on the quality of the DEMs, the processing chain for co-registration, and the post-processing including the removal of altitudinal or other biases. Major issue in regard of the subsequent conversion to ice mass is a suitable ice density assumption (Paul et al., 2013b). Other errors include the seasonality and the error of the SRTM C-band penetration correction (Gardelle et al., 2013).

After co-registration, our DEMs show sub-pixel horizontal accuracy to SRTM-3 of ± 1.89 m in x-direction and ± 1.51 m in y-direction for Pléiades and of ± 5.79 m and ± 4.86 m for SPOT-5 respectively. The DEM of TanDEM-X was already co-registered to SRTM-3 by a refined geocoding look-up table and had lower offsets to correct, with remaining inaccuracies of ± 2.81 m in x-direction and ± 2.60 m in y-direction. To measure vertical DEM accuracy on unglacierized terrain, we calculated the Normalized Median Absolute Deviation (NMAD), the 68.3 % quantile as

well as the 95 % quantile for all difference images relative to SRTM-3 (c.f. [Höhle & Höhle, 2009](#)), as shown in Table 2. We hereby only considered elevation difference values at stable terrain below a slope of 35° which is about the 95 % slope quantile of all glaciers. Due to curvature effects, we only considered Δh values within the two-tailed 1.5 times interquartile range bounded by the 5 % and 95 % quantiles, based on the same approach as employed for DEM co-registration.

[Gardelle et al. \(2013\)](#) mention for their determined SRTM-3 C-band penetration correction ranging from 1.4 m to 3.4 m an uncertainty of ± 1.5 m, but for the expected penetration depth of 1.4 m this seems overestimated, and as a result we suppose an uncertainty of ± 1.0 m in this study. The total error of glacier-mass balance uncertainties is the root of sum of each squared error term, i.e. the NMAD of each DEM, the uncertainty of the ice-density assumption of $\pm 60 \text{ kg m}^{-3}$ (c.f. [Huss, 2013](#)), and in case of clean-ice glaciers an uncertainty of the SRTM-3 C-band penetration correction, converted to water equivalent. The mean offset of the Pléiades DEM (18/26 Oct. 2013) to the DEM of TanDEM-X (26 Apr. 2012) proved to be 0.22 m on unglacierized terrain with a standard deviation of 2.78 m (Figure 8).

7. Results

7.1. Glacier area and length changes

An area of $79.0 \pm 1.6 \text{ km}^2$ as defined by our study site was covered by glacier ice in 1964. Glaciers shrank by $2.7 \pm 5.0 \text{ km}^2$ to $76.3 \pm 4.7 \text{ km}^2$ in 2000, subsequently by $1.7 \pm 4.8 \text{ km}^2$ to $74.6 \pm 0.5 \text{ km}^2$ in 2010 and by $0.3 \pm 0.5 \text{ km}^2$ to $74.3 \pm 0.2 \text{ km}^2$ in 2013. The overall shrinkage during the 49 years of investigation was measured at $4.7 \pm 1.7 \text{ km}^2$ which corresponds to a loss of $6.0 \pm 2.1 \%$ for the entire glaciated area of 1964 and to an annual rate of $-0.10 \pm 0.03 \text{ km}^2 \text{ a}^{-1}$ ($-0.12 \pm 0.04 \%$ a^{-1}). All twelve glaciers which were investigated for their mass balance shrank in total from $51.8 \pm 0.8 \text{ km}^2$ in 1964 to $49.8 \pm 0.08 \text{ km}^2$ in 2013 and showed clear tendency of continued glacier shrinkage (Table 4). Its recession rate of $3.7 \pm 1.5 \%$ ($\sim 1.9 \pm 0.8 \text{ km}^2$) is much less as it was determined for the entire glacierized area of the study site which can be explained by the longer response time of large glaciers that were investigated for their mass balance. Glacier outlines of the year 2000 show higher uncertainties by reason of the poorer Landsat 7 ETM+ pixel size resolution but are in line with the determined tendencies.

For one single glacier (*G081379E30472N*) we could observe a significant advance of its glacier tongue by $+260.0 \pm 5.0$ m, which was however coming along with an area loss of $0.12 \pm 0.07 \text{ km}^2$ ($2.3 \pm 1.3 \%$). The average retreat of the glaciers investigated for mass balance is with 178.0 ± 5.0 m similar to other glaciers of the study area with 175.0 ± 5.0 m, which corresponds to an annual retreat of $3.6 \pm 0.1 \text{ m a}^{-1}$ (Table 5). Figure 4 shows the frontal area changes of three

glaciers close to the peak of Mt. Gurla Mandhata, including Gurla Glacier (*G081317E30454N*, most western) and the advancing glacier *G081379E30472N* (most eastern).

7.2. Glacier mass balances

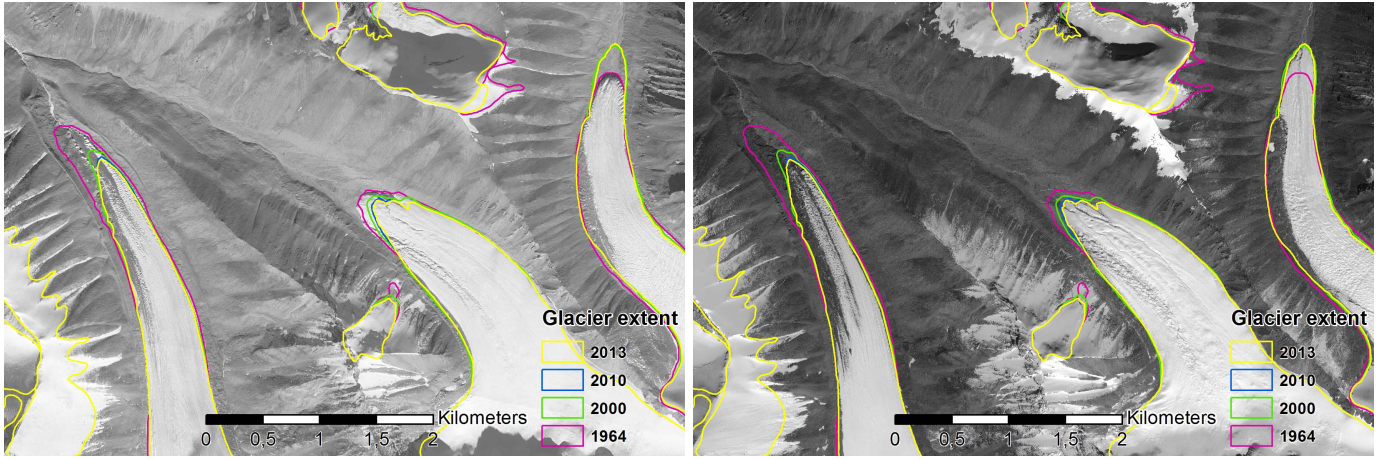
Table 6 presents results of mean glacier elevation and volume changes as well as annual glacier mass balances as calculated by TanDEM-X (2012) and Pléiades (2013) and by assuming a SRTM-3 C-band penetration depth of 1.4 ± 1.0 m in all twelve glaciers. Glacier mass balances from TanDEM-X show a slight loss of in mean $0.12 \pm 0.20 \text{ m w.e.a}^{-1}$ and a volume loss of $0.10 \pm 0.15 \text{ km}^3$ from 1999 to 2012 which is comparable to a negative mass balance of $0.08 \pm 0.31 \text{ m w.e.a}^{-1}$ and to the volume deficit of $0.08 \pm 0.25 \text{ km}^3$ as determined from Pléiades (1999-2013). In case of no penetration, this would lead to a mass budget which is close to zero, with in mean $-0.02 \pm 0.19 \text{ m w.e.a}^{-1}$ for TanDEM-X (volume change of $-0.03 \pm 0.14 \text{ km}^3$) and $+0.01 \pm 0.30 \text{ m w.e.a}^{-1}$ for Pléiades (volume change $-0.01 \pm 0.24 \text{ km}^3$) (Table 7). A deeper SRTM-3 C-band penetration depth of 2.8 ± 2.0 m results in more negative glacier mass balances, with in mean $-0.22 \pm 0.24 \text{ m w.e.a}^{-1}$ and a volume change of $-0.17 \pm 0.17 \text{ km}^3$ for TanDEM-X compared to $-0.16 \pm 0.33 \text{ m w.e.a}^{-1}$ and $-0.15 \pm 0.26 \text{ km}^3$ for Pléiades respectively (Table 8). NanNamuNaNi (*G081307E30424N*) is the only glacier in the study area that is largely covered by debris while the other investigated glaciers are virtually free of debris cover. For the final mass balance we thereof assumed for all clean-ice glaciers except of the debris-covered NanNamuNaNi glacier a C-band radar penetration depth of 1.4 ± 1.0 m in ice and snow. Based on this assumption we obtain for the observed glaciers of our Gurla Mandhata study site a mean mass balance in the range of $-0.07 \pm 0.31 \text{ m w.e.a}^{-1}$ with a volume change of $-0.07 \pm 0.25 \text{ km}^3$ as determined from optical Pléiades (1999-2013) to $-0.11 \pm 0.20 \text{ m w.e.a}^{-1}$ and $-0.09 \pm 0.15 \text{ km}^3$ as determined from SAR TanDEM-X (1999-2012) relative to SRTM-3.

Figure 5 for TanDEM-X and Figure 6 for Pléiades show their DEM difference image to SRTM-3 before and after post-processing for glacier mass balance calculation and error computation. Figure 10 represents the hypsometry by Δh values from difference images of both TanDEM-X and Pléiades DEMs to SRTM-3 for selected glaciers at Gurla Mandhata.

8. Discussion

8.1. Glacier area and length changes

Analysis of glacier area changes were restricted by the ground coverage of the KH-7 film stripe of 1964 that does not cover some few glaciers south-east which were previously investigated with ASTER and Landsat imagery ([Ye et al., 2006, 2009](#)). These studies however omitted the only south exposed and at the same time debris covered NanNamuNaNi Glacier (*G081307E30424N*), and as a result



(a) KH-7 ortho image of 5 Dec. 1964

(b) Pléiades ortho image of 18 Oct. 2013

Figure 4: Glacier length changes from 1964 – 2013 for the glaciers $G081317E30454N$ (Gurla Glacier), $G081351E30471N$ (GuNala Glacier) and the advancing glacier $G081379E30472N$ (from west to east)

only the relative change can be compared due to variations in total glacier area. The shrinkage of 8.8% equals to

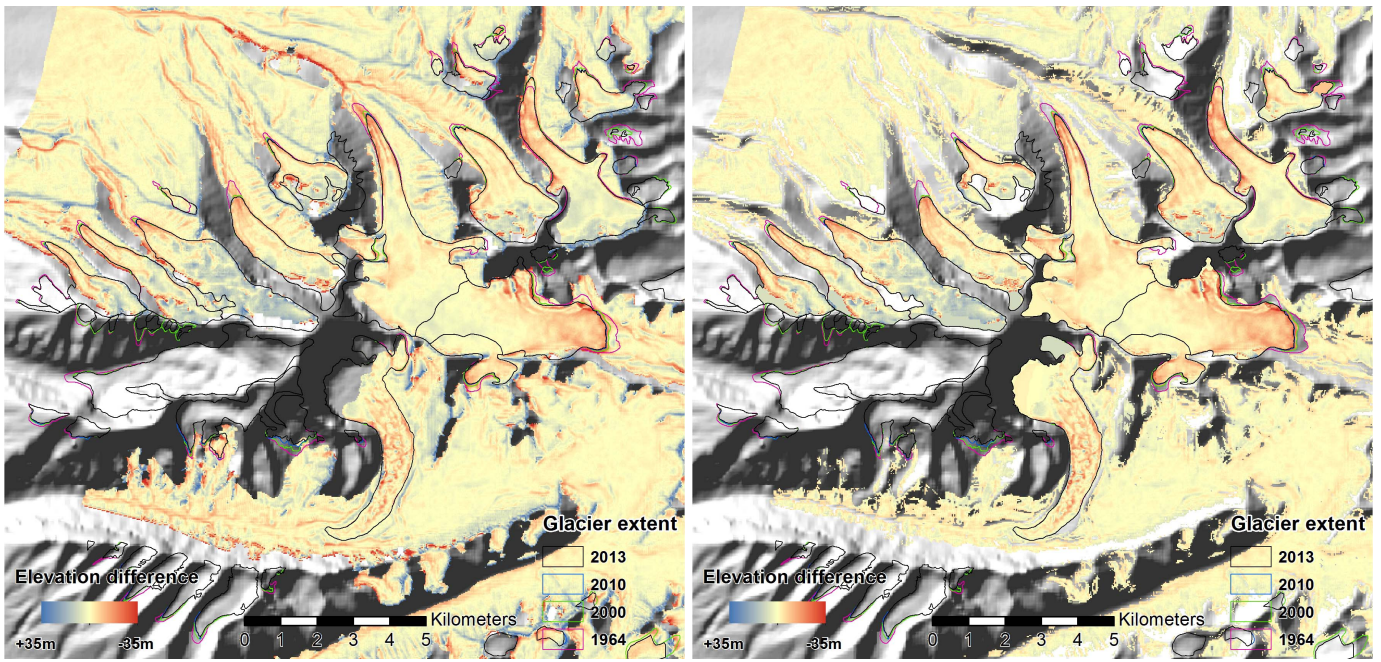
an area loss of 7.6 km² from 87.0 km² in 1976 to 79.4 km² in 2003 and is equivalent to an annual rate of $-0.31\% \text{ a}^{-1}$ (Ye

Table 4: Glacier area (A) and changes (ΔA) from 1964 – 2013 at Gurla Mandhata for selected glaciers of mass balance estimates and for all glaciers of the entire study area

Glacier (GLIMS ID)	A_{1964} [km ²]	A_{2000} [km ²]	A_{2010} [km ²]	A_{2013} [km ²]	$\Delta A_{2013-1964}$ [km ²]
G081237E30450N	2.00 ± 0.04	1.99 ± 0.12	1.98 ± 0.01	1.98 ± 0.004	-0.02 ± 0.04 (-1.00 \pm 2.00 %)
G081255E30450N	2.95 ± 0.05	2.92 ± 0.16	2.90 ± 0.01	2.90 ± 0.006	-0.05 ± 0.05 (-1.69 \pm 1.69 %)
G081267E30456N (NamuNaNi)	5.11 ± 0.07	5.08 ± 0.22	5.08 ± 0.02	5.07 ± 0.007	-0.04 ± 0.07 (-0.78 \pm 1.37 %)
G081296E30455N	3.29 ± 0.06	3.16 ± 0.15	3.14 ± 0.02	3.14 ± 0.005	-0.15 ± 0.06 (-4.56 \pm 1.82 %)
G081293E30477N	1.91 ± 0.05	1.87 ± 0.15	1.85 ± 0.02	1.85 ± 0.005	-0.06 ± 0.05 (-3.14 \pm 2.62 %)
G081317E30454N (Gurla)	9.33 ± 0.13	9.09 ± 0.37	9.01 ± 0.04	9.00 ± 0.013	-0.33 ± 0.13 (-3.54 \pm 1.39 %)
G081307E30424N (NanNamuNaNi)	6.36 ± 0.10	6.33 ± 0.29	6.33 ± 0.03	6.33 ± 0.010	-0.03 ± 0.10 (-0.47 \pm 1.57 %)
G081351E30471N (GuNala)	4.26 ± 0.05	4.23 ± 0.15	4.18 ± 0.01	4.17 ± 0.005	-0.09 ± 0.05 (-2.11 \pm 1.17 %)
G081365E30442N	7.95 ± 0.08	7.46 ± 0.22	7.30 ± 0.02	7.28 ± 0.007	-0.67 ± 0.08 (-8.43 \pm 1.01 %)
G081349E30428N	1.77 ± 0.04	1.69 ± 0.13	1.65 ± 0.01	1.64 ± 0.004	-0.13 ± 0.04 (-7.34 \pm 2.26 %)
G081379E30472N	5.26 ± 0.07	5.18 ± 0.23	5.14 ± 0.03	5.14 ± 0.008	-0.12 ± 0.07 (-2.28 \pm 1.33 %)
G081387E30495N	1.59 ± 0.04	1.45 ± 0.10	1.40 ± 0.01	1.39 ± 0.004	-0.20 ± 0.04 (-12.58 \pm 2.52 %)
\sum selected glaciers	51.78 ± 0.78	50.45 ± 2.29	49.96 ± 0.23	49.80 ± 0.078	-1.89 ± 0.78 (-3.65 \pm 1.51 %)
\sum glaciers study area	78.99 ± 1.64	76.26 ± 4.74	74.56 ± 0.46	74.27 ± 0.15	-4.72 ± 1.65 (-5.98 \pm 2.09 %)

Table 5: Glacier length changes (ΔL) from 1964 – 2013 at Gurla Mandhata for selected glaciers of mass balance estimates and for all glaciers of the entire study area

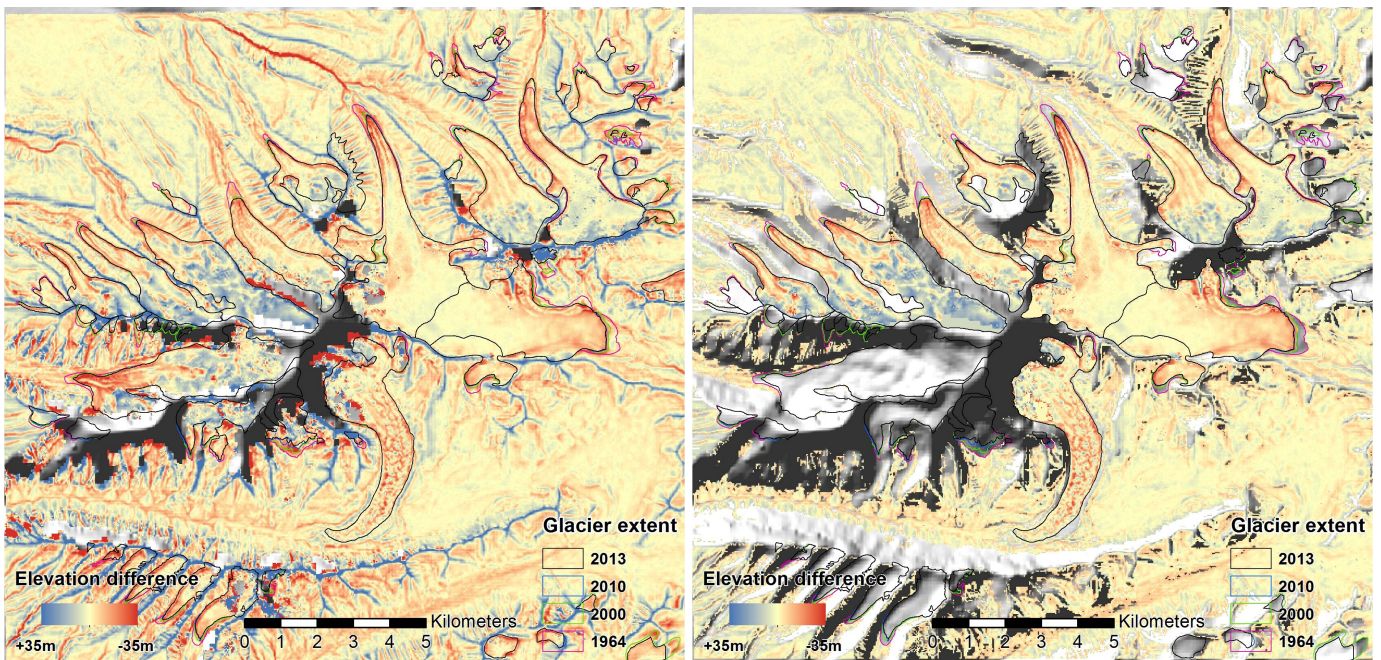
Glacier (GLIMS ID)	$\Delta L_{2013-1964}$ [m]
G081237E30450N	-120.0 ± 5.0
G081255E30450N	-150.0 ± 5.0
G081267E30456N (NamuNaNi)	-160.0 ± 5.0
G081296E30455N	-490.0 ± 5.0
G081293E30477N	-220.0 ± 5.0
G081317E30454N (Gurla)	-450.0 ± 5.0
G081307E30424N (NanNamuNaNi)	$+0.0$
G081351E30471N (GuNala)	-130.0 ± 5.0
G081365E30442N	-330.0 ± 5.0
G081349E30428N	-210.0 ± 5.0
G081379E30472N	$+260.0 \pm 5.0$
G081387E30495N	-140.0 ± 5.0
\bar{X} selected glaciers	-178.33 ± 5.0
\bar{X} glaciers study area	-174.77 ± 5.0



(a) Before post-processing

(b) After post-processing

Figure 5: Difference image of TanDEM-X DEM (26 Apr. 2012) minus SRTM-3 DEM (11–22 Feb. 2000) before and after post-processing for glacier mass balance calculation (glaciers) and error computation (stable terrain) by considering a SRTM-3 C-band penetration depth of 1.4 m in all glaciers except of NanNamuNaNi Glacier (*G081307E30424N*)



(a) Before post-processing

(b) After post-processing

Figure 6: Difference image of Pléiades DEM (18/26 Oct. 2013) minus SRTM-3 DEM (11–22 Feb. 2000) before and after post-processing for glacier mass balance calculation (glaciers) and error computation (stable terrain) by considering a SRTM-3 C-band penetration depth of 1.4 m in all glaciers except of NanNamuNaNi Glacier (*G081307E30424N*)

Table 7: Glacier mean Δh differences, glacier volume changes and annual glacier mass balances measured from TanDEM-X (2012) and Pliádes (2013) DEMs by comparison to SRTM-3 (1999) and by consideration of no SRTM-3 C-band penetration in ice and snow

Glacier (GLIMS ID)	Mean Δh [m]	TDX	Mean Δh [m]	PLE	Volume change [km ³ · 10 ⁻³]	TDX	Volume change [km ³ · 10 ⁻³]	PLE	Annual balance TDX [w.e.a ⁻¹]	mass TDX [m]	Annual balance PLE [w.e.a ⁻¹]	mass PLE [m]	Annual mass balance diff. PLE to TDX [m w.e.a ⁻¹]
G081237E30450N	+1.26 ± 2.74		+2.18 ± 4.83		+2.50 ± 5.44		+4.32 ± 9.59		+0.09 ± 0.19		+0.14 ± 0.30		-0.05
G081255E30450N	+1.65 ± 2.74		+3.56 ± 4.83		+4.83 ± 8.00		+10.41 ± 14.11		+0.12 ± 0.19		+0.22 ± 0.30		-0.10
G081267E30456N (Nannu-NaNi)	+5.92 ± 2.74		+8.26 ± 4.83		+30.08 ± 13.93		+41.99 ± 24.55		+0.41 ± 0.19		+0.51 ± 0.30		-0.10
G081296E30455N	-1.39 ± 2.74		-1.45 ± 4.83		-4.39 ± 8.65		-4.58 ± 15.25		-0.10 ± 0.19		-0.09 ± 0.30		-0.01
G081293E30477N	+0.65 ± 2.74		+1.12 ± 4.83		+1.21 ± 5.10		+2.08 ± 8.99		+0.05 ± 0.19		+0.07 ± 0.30		-0.02
G081317E30454N (Gurja)	-1.43 ± 2.74		-1.59 ± 4.83		-12.98 ± 24.95		-14.47 ± 43.99		-0.10 ± 0.19		-0.10 ± 0.30		+0.00
G081307E30424N (Nannu-NaNi)	-1.97 ± 2.74		-3.36 ± 4.83		-12.51 ± 17.37		-21.28 ± 30.61		-0.14 ± 0.19		-0.21 ± 0.30		+0.07
G081351E30471N (GüNala)	-0.42 ± 2.74		+0.66 ± 4.83		-1.79 ± 11.58		+2.78 ± 20.40		-0.03 ± 0.19		+0.04 ± 0.30		+0.01
G081365E30442N	-3.86 ± 2.74		-3.28 ± 4.83		-28.79 ± 20.46		-24.49 ± 36.06		-0.27 ± 0.19		-0.20 ± 0.30		-0.07
G081349E30428N	-2.67 ± 2.74		-2.32 ± 4.83		-4.51 ± 4.63		-3.92 ± 8.16		-0.19 ± 0.19		-0.14 ± 0.30		-0.05
G081379E30472N	-0.40 ± 2.74		+0.27 ± 4.83		-2.09 ± 14.19		+1.39 ± 25.01		-0.03 ± 0.19		+0.02 ± 0.30		-0.05
G081387E30495N	-1.01 ± 2.74		-1.56 ± 4.83		-1.45 ± 3.94		-2.24 ± 6.95		-0.07 ± 0.19		-0.10 ± 0.30		+0.03
\sum glaciers	-0.31 ± 2.74		+0.21 ± 4.83		-29.89 ± 138.24		-8.01 ± 243.67		-0.02 ± 0.19		+0.01 ± 0.30		-0.03

Table 6: Glacier mean Δh differences, glacier volume changes and annual mass balances measured from TanDEM-X (2012) and Pliádes (2013) DEMs by comparison to SRTM-3 (1999) and by consideration of an assumed SRTM-3 C-band penetration depth of 1.4 ± 1.0 m in ice and snow

Glacier (GLIMS ID)	Mean Δh [m]	TDX	Mean Δh [m]	PLE	Volume change [km ³ · 10 ⁻³]	TDX	Volume change [km ³ · 10 ⁻³]	PLE	Annual balance TDX [w.e.a ⁻¹]	mass TDX [m]	Annual balance PLE [w.e.a ⁻¹]	mass PLE [m]	Annual mass balance diff. PLE to TDX [m w.e.a ⁻¹]
G081237E30450N	-0.14 ± 2.92		+0.78 ± 4.93		-0.27 ± 5.78		+1.54 ± 9.78		-0.01 ± 0.20		+0.05 ± 0.31		-0.06
G081255E30450N	+0.25 ± 2.92		+2.16 ± 4.93		+0.73 ± 8.52		+6.31 ± 14.41		+0.02 ± 0.20		+0.13 ± 0.31		-0.11
G081267E30456N (Nannu-NaNi)	+4.52 ± 2.92		+6.86 ± 4.93		+22.96 ± 14.82		+34.87 ± 25.07		+0.31 ± 0.20		+0.43 ± 0.31		-0.12
G081296E30455N	-2.79 ± 2.92		-2.85 ± 4.93		-8.81 ± 9.21		-9.01 ± 15.57		-0.19 ± 0.20		-0.18 ± 0.31		-0.01
G081293E30477N	-0.75 ± 2.92		-0.28 ± 4.93		-1.40 ± 5.43		-0.52 ± 9.18		-0.05 ± 0.20		-0.02 ± 0.31		-0.03
G081317E30454N (Gurja)	-2.83 ± 2.92		-2.99 ± 4.93		-25.73 ± 26.56		-27.22 ± 44.92		-0.20 ± 0.20		-0.19 ± 0.31		-0.01
G081307E30424N (Nannu-NaNi)	-3.37 ± 2.92		-4.76 ± 4.93		-21.38 ± 18.49		-30.15 ± 31.26		-0.24 ± 0.20		-0.30 ± 0.31		+0.06
G081351E30471N (GüNala)	-1.82 ± 2.92		-0.74 ± 4.93		-7.71 ± 12.32		-3.13 ± 20.84		-0.13 ± 0.20		-0.05 ± 0.31		-0.08
G081365E30442N	-5.26 ± 2.92		-4.68 ± 4.93		-39.24 ± 21.78		-34.95 ± 36.82		-0.37 ± 0.20		-0.29 ± 0.31		-0.08
G081349E30428N	-4.07 ± 2.92		-3.72 ± 4.93		-6.88 ± 4.93		-6.29 ± 8.34		-0.28 ± 0.20		-0.23 ± 0.31		-0.05
G081379E30472N	-1.80 ± 2.92		-1.13 ± 4.93		-9.34 ± 15.10		-5.85 ± 25.54		-0.13 ± 0.20		-0.07 ± 0.31		-0.06
G081387E30495N	-2.41 ± 2.92		-2.96 ± 4.93		-3.47 ± 4.19		-4.26 ± 7.09		-0.17 ± 0.20		-0.18 ± 0.31		+0.01
\sum glaciers	-1.71 ± 2.92		-1.19 ± 4.93		-100.54 ± 147.13		-78.66 ± 248.82		-0.12 ± 0.20		-0.08 ± 0.31		-0.04

Table 8: Glacier mean Δh differences, glacier volume changes and annual mass balances measured from TanDEM-X (2012) and Pléiades (2013) DEMs by comparison to SRTM-3 (1999) and by consideration of an assumed SRTM-3 C-band penetration depth of 2.8 ± 2.0 m in ice and snow

Glacier (GLIMS ID)	Mean Δh [m]	Mean Δh TDX [m]	Mean Δh PLE [m]	Volume change [km ³ · 10 ⁻³]	Volume change TDX [km ³ · 10 ⁻³]	Volume change PLE [km ³ · 10 ⁻³]	Annual balance TDX [m w.e.a ⁻¹]	Annual mass balance PLE [m w.e.a ⁻¹]	Annual mass balance PLE [m w.e.a ⁻¹]	Annual mass balance diff. PLE to TDX [m w.e.a ⁻¹]
G081237E30450N	-1.54 ± 3.39	-0.62 ± 5.23	-0.62 ± 5.23	-3.05 ± 6.73	-1.23 ± 10.37	-0.11 ± 0.24	-0.04 ± 0.33	-0.04 ± 0.33	-0.07	
G081255E30450N	-1.15 ± 3.39	+0.76 ± 5.23	+0.76 ± 5.23	-3.36 ± 9.92	+2.22 ± 15.28	-0.08 ± 0.24	+0.05 ± 0.33	+0.05 ± 0.33	-0.13	
G081267E30456N (NamuNaNi)	+3.12 ± 3.39	+5.46 ± 5.23	+5.46 ± 5.23	+15.85 ± 17.24	+27.76 ± 26.57	+0.22 ± 0.24	+0.34 ± 0.33	+0.34 ± 0.33	-0.12	
G081296E30455N	-4.19 ± 3.39	-4.25 ± 5.23	-4.25 ± 5.23	-13.23 ± 10.71	-13.43 ± 16.50	-0.29 ± 0.24	-0.26 ± 0.33	-0.26 ± 0.33	-0.03	
G081293E30477N	-2.15 ± 3.39	-1.68 ± 5.23	-1.68 ± 5.23	-4.00 ± 6.31	-3.13 ± 9.72	-0.15 ± 0.24	-0.10 ± 0.33	-0.10 ± 0.33	-0.05	
G081317E30454N (Gurla)	-4.23 ± 3.39	-4.39 ± 5.23	-4.39 ± 5.23	-38.48 ± 30.89	-39.97 ± 47.61	-0.29 ± 0.24	-0.27 ± 0.33	-0.27 ± 0.33	-0.02	
G081307E30424N (NamuNaNi)	-4.77 ± 3.39	-6.16 ± 5.23	-6.16 ± 5.23	-30.26 ± 21.50	-39.03 ± 33.13	-0.33 ± 0.24	-0.38 ± 0.33	-0.38 ± 0.33	+0.05	
G081351E30471N (GunaNa)	-3.22 ± 3.39	-2.14 ± 5.23	-2.14 ± 5.23	-13.62 ± 14.33	-9.04 ± 22.08	-0.22 ± 0.24	-0.13 ± 0.33	-0.13 ± 0.33	-0.09	
G081365E30442N	-6.66 ± 3.39	-6.08 ± 5.23	-6.08 ± 5.23	-49.70 ± 25.33	-45.40 ± 39.03	-0.46 ± 0.24	-0.38 ± 0.33	-0.38 ± 0.33	-0.08	
G081349E30428N	-5.47 ± 3.39	-5.12 ± 5.23	-5.12 ± 5.23	-9.24 ± 5.73	-8.66 ± 8.84	-0.38 ± 0.24	-0.32 ± 0.33	-0.32 ± 0.33	-0.06	
G081379E30472N	-3.20 ± 3.39	-2.53 ± 5.23	-2.53 ± 5.23	-16.59 ± 17.56	-13.10 ± 27.07	-0.22 ± 0.24	-0.16 ± 0.33	-0.16 ± 0.33	-0.06	
G081387E30495N	-3.81 ± 3.39	-4.36 ± 5.23	-4.36 ± 5.23	-5.48 ± 4.88	-6.28 ± 7.52	-0.27 ± 0.24	-0.27 ± 0.33	-0.27 ± 0.33	+0.00	
\sum glaciers	-3.11 ± 3.39	-2.59 ± 5.23	-2.59 ± 5.23	-171.16 ± 171.13	-149.29 ± 263.72	-0.22 ± 0.24	-0.16 ± 0.33	-0.16 ± 0.33	-0.06	

et al., 2009; Yao et al., 2012a). Our results as defined by the study site indicate a glacier shrinkage of 4.7 ± 1.7 km² from 1964 to 2013. This is equivalent to -6.0 ± 2.1 % or -0.12 ± 0.04 % a⁻¹ (see Table 4) and less as half as observed by Ye et al. (2006, 2009). The previously observed higher shrinkage is probably less influenced by diverging study definitions, but by the way of mapping from different sensors at a poorer resolutions which eventually might have led to an overestimation in the results of Ye et al. (2006, 2009).

Several branches of Gurla Glacier (*G081317E30454N*) separated from the main glacier body during the period of 1976 to 2006 which was going along with a total retreat of 155 m (~ 5 m a⁻¹) (Yao et al., 2012a). Our ortho images indicate a retreat of 450 m from 1964 to 2013 or ~ 9 m a⁻¹ (Figure 4) along the central flow line of Gurla Glacier (Table 5). Probably due to movement of debris and lateral moraines is de-correlation however still apparent at the recession area in the TerraSAR-X coherence image of 2011 (Figure 2) which might have resulted in ambiguous delineations at the tongue of Gurla Glacier (*G081317E30454N*).

8.2. Glacier mass balances

Mass balance measurements are sparse in this harsh and remote environment. In this study they range in mean from -0.07 ± 0.31 m w.e.a⁻¹ (Pléiades) to -0.11 ± 0.20 m w.e.a⁻¹ (TanDEM-X) and are lower as previously published in less detailed studies covering the site (e.g. Käab et al., 2012; Gardelle et al., 2013; Neckel et al., 2014). A mass deficit of in mean -0.56 m w.e. was observed for the period of 2005/06 to 2009/10 by means of 16 measuring stakes for Gurla Glacier (*G081317E30454N*) (Yao et al., 2012a), a reference glacier of the Third Pole Environment (TPE) program (Yao et al., 2012b). Our geodetic approach indicates a lower loss for this glacier, with -0.20 ± 0.20 m w.e.a⁻¹ as determined from TanDEM-X and -0.19 ± 0.31 m w.e.a⁻¹ from Pléiades (see Table 6). If no SRTM C-band penetration was considered, the mass balance would only lead to -0.10 ± 0.30 m w.e.a⁻¹ (see Table 7) and at a penetration depth of 2.8 ± 2.0 m it would range from -0.27 ± 0.33 m w.e.a⁻¹ (Pléiades) to -0.29 ± 0.24 m w.e.a⁻¹ (TanDEM-X) (see Table 8). The in-situ measurements of Yao et al. (2012a) however show strong annual variations (from -0.28 m w.e in 2009/10 to -0.72 m w.e in 2007/08), and we detected that a C-band radar penetration depth of almost 7.0 m would have to be considered in our data to obtain a mean mass loss of ~ 0.56 m w.e. for Gurla Glacier (*G081317E30454N*).

Our results show in most cases strong mass losses at the glacier tongues (Figure 5, 6, 10). Mass gain in the upper glacier areas with positive glacier mass budgets are particularly observed for some north-west exposed glaciers such as NamuNaNi Glacier (*G081267E30456N*), probably by reason of their higher altitudes and the wind direction of the Westerlies. Evident is the high altitude of the ELA as measured for Gurla Glacier (*G081317E30454N*) by Yao et al. (2012a), which is however low compared to

e.g. NamuNaNi Glacier (*G081267E30456N*). NanNamuNaNi Glacier (*G081307E30424N*) is the only larger and south-exposed glacier of the study site that at the same time is almost entirely debris-covered and located at comparatively low altitudes. The relatively high surface lowering at the central part of its glacier tongue is also found elsewhere on debris covered glaciers (c.f. [Bolch et al., 2011](#); [Pieczonka et al., 2013](#)). Strong mass loss for large areas of the advancing glacier tongue came along with the shrinkage of glacier *G081379E30472N*. Gap filled areas for that constant replacement values were calculated can be identified as linear features in the hypsometry by Δh values (Figure 10).

8.3. Issues of geodetic mass balances from SAR and optical data

The advantage of SAR compared to optical data is the ability to map at all weather conditions during all day-times. As InSAR is independent of visible structures and contrast of the glacier surface, it also performs well in accumulation areas of glaciers, such as the ice field of Naimona'nyi. The single-pass configuration of TerraSAR-X and TanDEM-X ensures a high coherence on glaciers which is advantageous compared to repeat-pass InSAR. However, due to the side-looking SAR antennae, foreshortening and layover effects are common issues in mountainous terrain (e.g. [Rott, 2009](#); [Shugar et al., 2010](#)). These effects result in incoherent areas which can not be adequately unwrapped, as visible in Figure 3 at steep slopes close to the peak of Mt. Gurla Mandhata. Several data takes with different baselines, incident angles and acquisitions from ascending and descending orbits will be used for such difficult terrain in the coming global DEM of TanDEM-X ([Krieger et al., 2007](#)).

Geodetic mass balance measurements by means of optical stereo data is promising on rough crevassed or debris-covered glacier surfaces, but difficult in case of snow cover. Infrequent variations of albedo might cause a lack of contrast which can result in extensive areas without elevation estimates ([Bamber & Rivera, 2007](#)). Image matching algorithms might also fail in case of clouds, shadow and fresh snow coverage due to high saturation or low contrast alterations. The higher pixel depth of Pléiades with 12 bit and thus 4096 available digital numbers (DNs) compared to 8 bit of SPOT-5 (256 DN) allows to quantify for finer albedo variations during acquisition and lowers the risk of saturation. Combined with the higher geometric resolution in the panchromatic channel of 0.5 m for Pléiades (2.5 m for SPOT-5) can more large-scale variations on the glacier surface be detected. This led to a high quality of our extracted Pléiades DEM even in areas of poor contrast such as the glacier accumulation zones (see Figure 3). The b/h-factor at mountainous areas should be rather moderate to reduce the rate of hidden items and to achieve good matching identification. Pléiades stereo images are recorded virtually instantaneously under different along-track incidence angles, and its tri-stereoscopic acquisition

mode with an additional quasi vertical image can minimize this factor and increase the altimetric accuracy. The b/h-factor of our tri-stereoscopic Pléiades imagery ranges from 0.20 to 0.48 for each stereo pair (recommended ~ 0.25 by [Astrium \(2012\)](#)). SPOT-5 HRG stereo images are acquired from two different orbits with a parallax that is obtained by a difference of the across track incidence angle. Temporal decorrelation can lead to problems in terrain extraction due to varying image content since data is recorded at two different points in time. SPOT-5 images of this study were recorded with only four days of difference in acquisition (2 and 6 November 2010) and at a b/h-factor of 0.74, but the saturation quality problem in the second image pair is the major reason of its poor DEM.

8.4. Accuracy of glacier mass balances

The DEM of TanDEM-X appears with a NMAD of 2.74 m more accurate as the DEM of Pléiades (NMAD of 4.83 m) or SPOT-5 (NMAD of 6.11 m), as summarized in Table 2. The histograms in Figure 9 however show wider spread in the optical DEMs as compared to the SAR-DEM which is reflected by the NMAD value. This is presumably caused by the much higher initial resolution of the generated DEMs (up to 1 m for Pléiades) when comparing elevation differences to the coarser resolution of SRTM-3 (90 m). Prior to post-processing, DEM differencing to SRTM-3 indicates low Δh values at gentle slopes but high offsets at mountain ridges (blue colors) and highly negative offsets in deep valleys (red colors). This is particularly the case for Pléiades (Figure 6), but also for TanDEM-X (Figure 5) and SPOT-5 (Figure 7). These offsets however are resolution implicated and only occur at extreme topographies with high curvature ([Paul, 2008](#)). The absolute vertical accuracy of the SRTM-3 C-band DEM is ± 16 m (± 6 m relative) and the horizontal accuracy is ± 20 m ([Rabus et al., 2003](#); [Farr et al., 2007](#)). The vertical accuracy is strongly related to topographic characteristics and is better in flat areas, but can exceed the accuracy specifications in high-relief terrain ([Falorni et al., 2005](#); [Rodriguez et al., 2006](#)). By reason of the quality dependence of the SRTM-3 reference dataset we would expect a lower uncertainty of our DEMs in flat terrain if a more accurate reference such as from differential GPS or LIDAR measurement was available. We set in this regard constraints to the Δh values of stable terrain to achieve accurate elevation bias correction as well as uncertainty estimates by the NMAD.

The post-processed difference images of TanDEM-X (Figure 5) and Pléiades (Figure 6) show similar glacier trends and accurate fits to SRTM-3 on stable terrain. The high relative accuracy of the optical Pléiades to the SAR TanDEM-X DEM with a mean offset of 0.22 ± 2.78 m on unglacierized terrain is also proofed by their difference image in Figure 8 which shows almost no change in elevation on both glacier and stable areas. Table 6 indicates slight mass balance variations with some positive and in most cases negative budgets, but with generally similar trends.

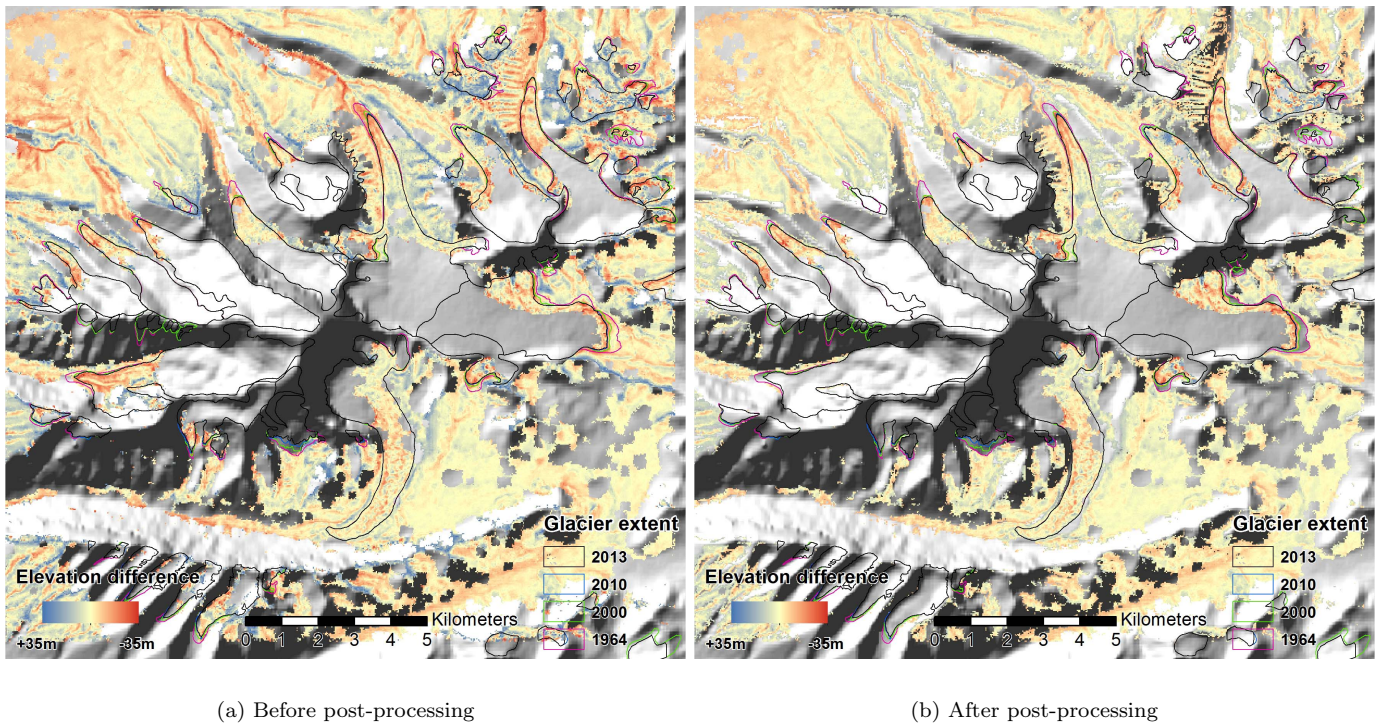


Figure 7: Difference image of SPOT-5 DEM (02 / 06 Nov. 2010) minus SRTM-3 DEM (11 – 22 Feb. 2000) before and after post-processing for visual glacier thickness change interpretation and error computation (stable terrain) by considering a SRTM-3 C-band penetration depth of 1.4 m in all glaciers except of NanNamuNaNi Glacier (*G081307E30424N*)

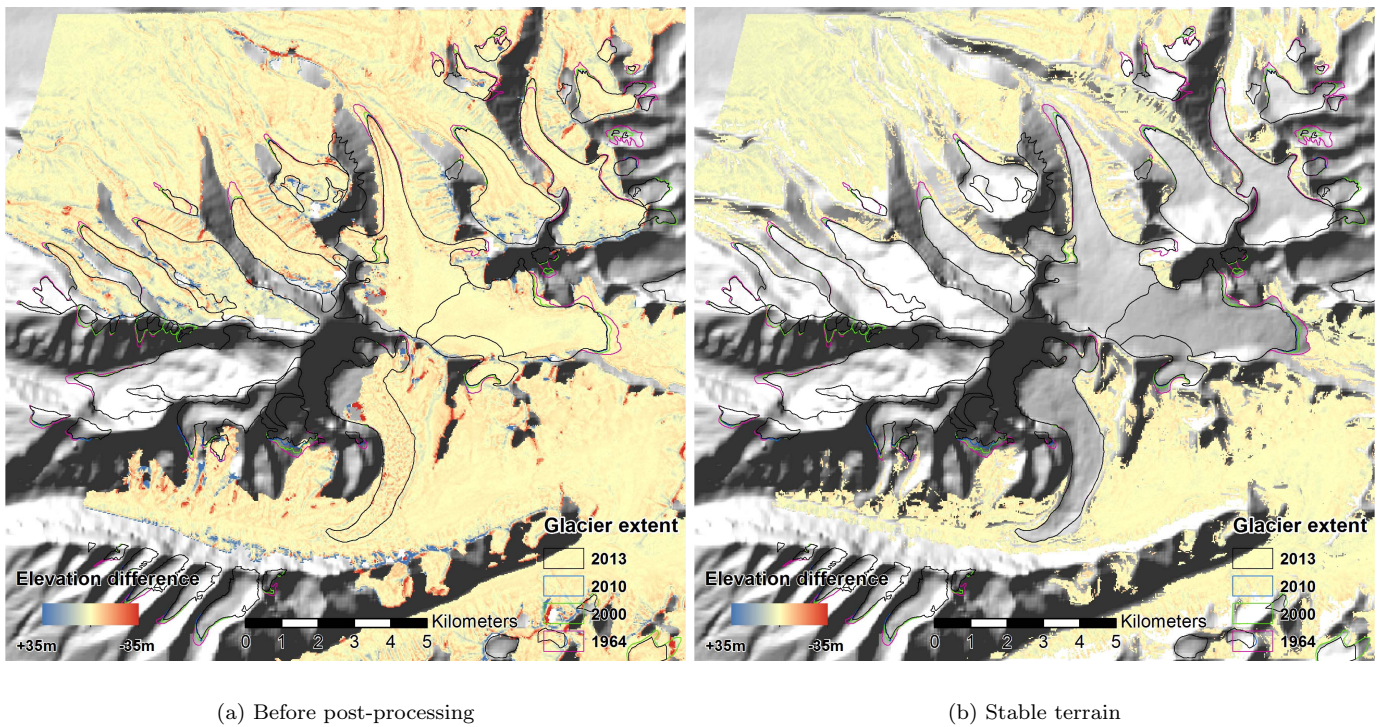


Figure 8: Difference image of Pléiades DEM (18 / 26 Oct. 2013) minus TanDEM-X DEM (26 Apr. 2012) before and after post-processing for error computation (stable terrain)

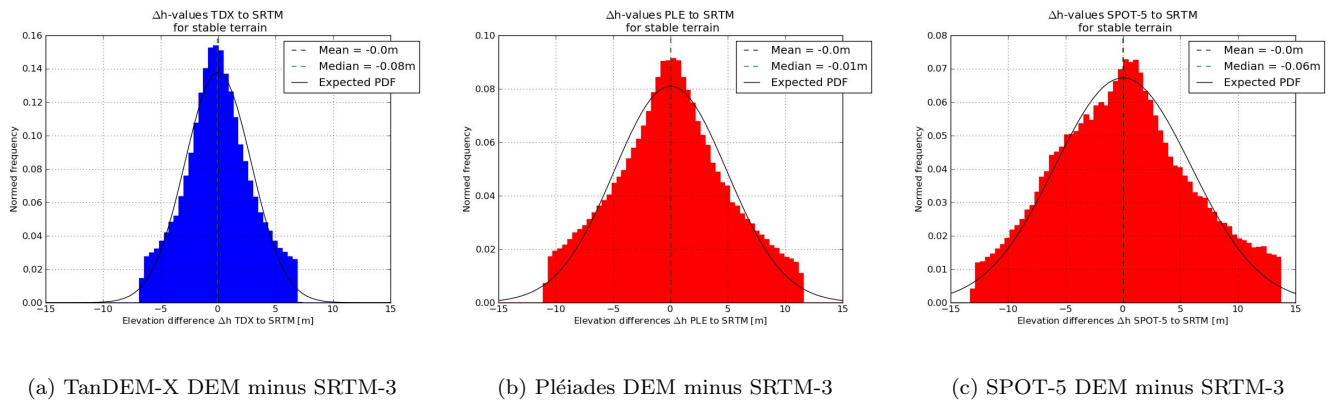


Figure 9: Histograms of DEMs representing Δh distribution on stable terrain relative to SRTM-3

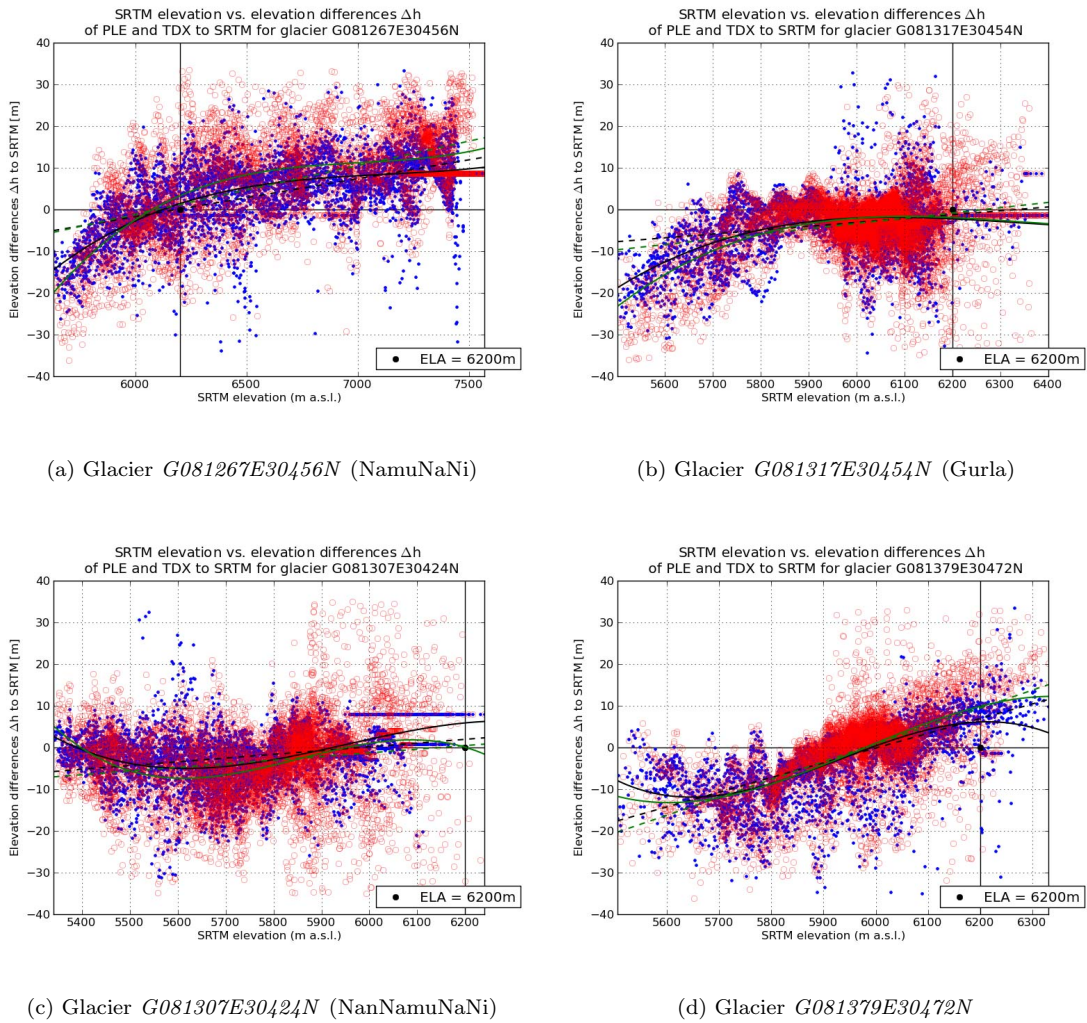


Figure 10: Hypsometry by Δh values from DEMs of TanDEM-X (blue dots / black lines) and Pléiades (red dots / green lines) relative to SRTM-3 with linear and polynomial (third order) fits for selected glaciers at the Gurla Mandhata study site. The ELA was determined for Gurla Glacier (*G081317E30454N*) by Yao et al. (2012a)

This is also proofed in the hypsometry by Δh values for selected glaciers when comparing linear and polynomial fits for both TanDEM-X and Pléiades DEMs to SRTM-3 in Figure 10, where higher spread at snow covered glacier areas of low image contrast in Pléiades is obvious. No glacier mass balance was estimated out of the SPOT-5 DEM due to its poor DEM quality with extensive data gaps, and we subsequently only used its difference image to SRTM-3 (Figure 7) to validate glacier elevation changes which are consistent to the trends as observed by Pléiades (Figure 6) and TanDEM-X (Figure 5).

8.5. Remaining uncertainties of glacier mass balances

Gap filling of missing Δh values is based on an assumption of the ELA, but such estimates are scarce and show high variations. Our ELA (6200 m) is based on multi-annual in-situ measurements at Gurla Glacier by Yao et al. (2012a) that fluctuate strongly, while Gardelle et al. (2013) mentions an ELA of only 5590 ± 138 m for West Nepal based on snowline mapping from ~ 2000 Landsat data.

The penetration of the SAR C-band signal of SRTM-3 into snow and ice can lead to an underestimation of surface elevations particularly in glacier accumulation zones and subsequently to biased estimates in glacier mass balance. As a result, specific penetration depths must be considered for each region due to different weather and snow cover conditions in February 2000 (Rignot et al., 2001; Gardelle et al., 2012; Kääb et al., 2012). Gardelle et al. (2013) observed an increasing penetration gradient in High Asia from east to west, caused by different westerly and monsoonal precipitation patterns in February 2000. Rignot et al. (2001) measured C-band penetration depths of up to 10 m in dry cold firn and less than 2 m in exposed ice, confirmed by Langley et al. (2007) that distinguished layers of superimposed ice in depths of up to 14 m. Kääb et al. (2012) document a mean penetration of 1.5 ± 0.4 m into glacier ice and of 2.3 ± 0.6 m into firn and snow within their Himachal Pradesh, Uttarakhand and West Nepal study site. We thereof also calculated mass balances by considering both no penetration of the SRTM-3 C-band beam (see Table 7) and by considering a penetration depth of 2.8 ± 2.0 m (see Table 8) by reason of the maybe underestimated correction of 1.4 ± 1.0 m (see Table 6).

9. Conclusion

Declassified historical spy-photographs from the U.S. Keyhole missions offer a vast archive of still largely untouched high resolution data. We took advantage of imagery from Gambit-1 KH-7 at less than 1 m resolution and observed at our study site that glaciers shrank from 79.0 ± 1.6 km² in 1964 to 74.3 ± 0.2 km² in 2013. This corresponds to an area loss of 0.12 ± 0.04 % per year and is less as previously published by other studies. Most glaciers retreated with in average 3.6 ± 0.1 m per year, while one advancing but thinning glacier tongue could be observed.

Optical stereo DEM approaches depend on images which are free of clouds and shadow and might fail on areas of poor contrast such as the glacier accumulation zones. A high resolution DEM could be generated from Pléiades tri-stereoscopic imagery at 0.5 m resolution which even performs well on snow and ice covered areas by reason of its high radiometric quality (12-bit). A SPOT-5 DEM from imagery at lower geometric (2.5 m) and radiometric (8-bit) resolution is of worse quality which in this case is primarily caused by a saturation problem in one image pair. SAR approaches are independent of weather conditions and visible structures, but have limitations in high mountain terrain. This is apparent as areas of nodata in the DEM of TanDEM-X due to problems in phase unwrapping as well as layover and shadowing. Both optical and SAR approaches offer ideal means to combine the advantages of both techniques and show similar results, which is also confirmed by DEM differencing to SPOT-5.

By geodetic means from both optical and SAR approaches to SRTM-3, an overall volume loss (1999–2012/13) of 0.07 ± 0.25 km³ (Pléiades) to 0.09 ± 0.15 km³ (TanDEM-X) and a mean glacier mass balance of -0.07 ± 0.31 m w.e.a⁻¹ (Pléiades) to -0.11 ± 0.20 m w.e.a⁻¹ (TanDEM-X) was determined for Gurla Mandhata. Uncertainty estimates of 2.74 m for TanDEM-X and 4.83 m for Pléiades based on the NMAD relative to SRTM-3 are rather conservative and proof the high accuracy. The radar penetration depth of the SRTM-3 C-band signal was in this study assumed to be 1.4 ± 1.0 m in all clean-ice glaciers and is probably the dominating factor for uncertainty that might have led to underestimated glacier mass balances. Further research should be employed in this regard, and this is why mass budgets at different C-band penetration depths were calculated.

Acknowledgements

This study was supported by the German Federal Ministry of Education and Research (BMBF) program "Central Asia – Monsoon Dynamics and Geo-Ecosystems" (CAMÉ) within the WET project ("Variability and Trends in Water Balance Components of Benchmark Drainage Basins on the Tibetan Plateau") under the codes 03G0804D and 03G0804F. Gambit-1 KH-7, Landsat 7 ETM+ and Orbview-3 satellite imagery was provided by the U.S. Geological Survey (USGS). Hole-filled SRTM-3 v4.1 data was obtained from the Consortium for Spatial Information of the Consultative Group for International Agricultural Research (CGIAR-CSI). TerraSAR-X and TanDEM-X data was provided by the German Aerospace Center (DLR) under project ID HYD0534 and XTI.GLAC1054 respectively. SPOT-5 (Satellite Pour l'Observation de la Terre) imagery was provided by the program ISIS (Incitation à l'utilisation Scientifique des Images SPOT) of CNES (Centre National d'Etudes Spatiales) under the project ID 661 and distributed by Spot Image SA (<http://www.isis-cnes.fr>). Pléiades imagery was provided to the Institut de Physique

du Globe and the ICube Laboratory (UMR 7357 CNRS) of the University of Strasbourg as part of the second call of the program RTU (Recette Thématique Utilisateurs) within the satellite program ORFEO (Optical and Radar Federation for Earth Observation) of the French Space Agency CNES and processed by the Institute of Cartography of the Dresden University of Technology, Germany (<https://rtu-pleiades.kalimsat.eu>).

We particularly thank Hervé Yesou of SERTIT Strasbourg for his kind support and help with Pléiades imagery as well as Felix Wiemann for glacier mapping and data processing of the KH-7 photograph. T. Bolch acknowledges funding through DFG (BO 3199/2-1) and the European Space Agency (ESA), project Glaciers_cci (400010177810-IAM).

References

- Astrium (2012). *Pléiades Imagery - User Guide V2.0*. Astrium Geo-Information Services.
- Bamber, J. L., & Rivera, A. (2007). A review of remote sensing methods for glacier mass balance determination. *Global and Planetary Change*, *59*, 138–148. doi:10.1016/j.gloplacha.2006.11.031.
- Berthier, E., Arnaud, Y., Vincent, C., & Rémy, F. (2006). Biases of SRTM in high-mountain areas: Implications for the monitoring of glacier volume changes. *Geophysical Research Letters*, *33*, 1–4. doi:10.1029/2006GL025862.
- Bolch, T., Buchroithner, M., Pieczonka, T., & Kunert, A. (2008). Planimetric and volumetric glacier changes in the Khumbu Himal, Nepal, since 1962 using Corona, Landsat TM and ASTER data. *Journal of Glaciology*, *54*, 592–600. doi:10.3189/002214308786570782.
- Bolch, T., Kulkarni, A. V., Kääb, A., Huggel, C., Paul, F., Cogley, J. G., Frey, H., Kargel, J. S., Fujita, K., Scheel, M., Bajracharya, S., & Stoffel, M. (2012). The State and Fate of Himalayan Glaciers. *Science*, *336*, 310–314. doi:10.1126/science.1215828.
- Bolch, T., Menounos, B., & Wheate, R. (2010a). Landsat-based inventory of glaciers in western Canada, 1985–2005. *Remote Sensing of Environment*, *114*, 127–137. doi:10.1016/j.rse.2009.08.015.
- Bolch, T., Pieczonka, T., & Benn, D. I. (2011). Multi-decadal mass loss of glaciers in the Everest area (Nepal Himalaya) derived from stereo imagery. *The Cryosphere*, *5*, 349–358. doi:10.5194/tc-5-349-2011.
- Bolch, T., Yao, T., Kang, S., Buchroithner, M. F., Scherer, D., Mausson, F., Huintjes, E., & Schneider, C. (2010b). A glacier inventory for the western Nyainqentanglha Range and the Nam Co Basin, Tibet, and glacier changes 1976–2009. *The Cryosphere*, *4*, 419–433. doi:10.5194/tc-4-419-2010.
- Bouillon, A., Breton, E., De Lussy, F., & Gachet, R. (2003). SPOT5 HRG and HRS first in-flight geometric quality results. *Proceedings SPIE*, *4881*, 212–223. doi:10.1117/12.462637.
- Buckreuss, S., Werninghaus, R., & Pitz, W. (2009). The German satellite mission TerraSAR-X. *Aerospace and Electronic Systems Magazine*, *IEEE*, *24*, 4–9. doi:10.1109/MAES.2009.5344175.
- Büyüksalih, G., Kocak, G., Topan, H., Oruc, M., & Marangoz, A. (2005). SPOT revisited: Accuracy assessment, DEM generation and validation from stereo SPOT 5 HRG images. *The Photogrammetric Record*, *20*, 130–146. doi:10.1111/j.1477-9730.2005.00314.x.
- Costantini, M. (1998). A novel phase unwrapping method based on network programming. *Geoscience and Remote Sensing, IEEE Transactions on*, *36*, 813–821. doi:10.1109/36.673674.
- CSNR (2012). *Hexagon (KH-9) - Mapping camera program and evolution*. National Reconnaissance Office, Center for the Study of National Reconnaissance (CSNR) Chantilly, VA, United States.
- Ding, Y., Liu, S., Jing, L., & Shanguan, D. (2006). The retreat of glaciers in response to recent climate warming in western China. *Annals of Glaciology*, *43*, 97–105. doi:10.3189/172756406781812005.
- Dozier, J. (1989). Spectral Signature of Alpine Snow Cover from the Landsat Thematic Mapper. *Remote Sensing of Environment*, *28*, 9–22. doi:10.1016/0034-4257(89)90101-6.
- Duque, S. (2012). *TanDEM-X Payload Ground Segment: CoSSC Generation and Interferometric Considerations. Doc.: TD-PGS-TN-3129*. Remote Sensing Technology Institute of the German Aerospace Center (DLR).
- Durand, A., Michel, J., de Franchis, C., Allenbach, B., & Giros, A. (2013). Qualitative assessment of four DSM generation approaches using Pléiades-HR data. In R. Lasaponara (Ed.), *33rd EARSeL Symposium Towards Horizon 2020*. Matera, Italy: EARSeL.
- Falorni, G., Teles, V., Vivoni, E. R., L. Bras, R., & Amaratunga, K. S. (2005). Analysis and characterization of the vertical accuracy of digital elevation models from the Shuttle Radar Topography Mission. *Journal of Geophysical Research*, *110*, 1–20. doi:10.1029/2003JF000113. F02005.
- Farr, T. G., Rosen, P. A., Caro, E., Crippen, R., Duren, R., Hensley, S., Kobrick, M., Paller, M., Rodriguez, E., Roth, L., Seal, D., Shaffer, S., Shimada, J., Umland, J., Werner, M., Oskin, M., Burbank, D., & Alsdorf, D. (2007). The Shuttle Radar Topography Mission. *Reviews of Geophysics*, *45*, RG2004. doi:10.1029/2005RG000183.
- Frey, H., Paul, F., & Strozzi, T. (2012). Compilation of a glacier inventory for the western Himalayas from satellite data: methods, challenges, and results. *Remote Sensing of Environment*, *124*, 832–843. doi:10.1016/j.rse.2012.06.020.
- Gardelle, J., Berthier, E., & Arnaud, Y. (2012). Impact of resolution and radar penetration on glacier elevation changes computed from DEM differencing. *Journal of Glaciology*, *58*, 419–422. doi:10.3189/2012JoG11J175.
- Gardelle, J., Berthier, E., Arnaud, Y., & Kääb, A. (2013). Region-wide glacier mass balances over the Pamir-Karakoram-Himalaya during 1999–2011. *The Cryosphere*, *7*, 1263–1286. doi:10.5194/tc-7-1263-2013.
- Gleyzes, M. A., Perret, L., & Kubik, P. (2012). Pléiades system architecture and main performances. In *International Archives of the Photogrammetry, Remote Sensing and Spatial Information Sciences (XXII ISPRS Congress)* (pp. 537–542). Melbourne, Australia: ISPRS volume XXXIX-B1.
- GLIMS (2005). Global Land Ice Measurements from Space glacier database. Compiled and made available by the international GLIMS community and the National Snow and Ice Data Center (NSIDC), Boulder CO, U.S.A. doi:10.7265/N5V98602 updated 2013.
- Gorokhovich, Y., & Voustantiyouk, A. (2006). Accuracy assessment of the processed SRTM-based elevation data by CGIAR using field data from USA and Thailand and its relation to the terrain characteristics. *Remote Sensing of Environment*, *104*, 409–415. doi:10.1016/j.rse.2006.05.012.
- Hall, D. K., Bayr, K. J., Schöner, W., Bindschadler, R. A., & Chien, J. Y. (2003). Consideration of the errors inherent in mapping historical glacier positions in Austria from the ground and space (18932001). *Remote Sensing of Environment*, *86*, 566–577. doi:10.1016/S0034-4257(03)00134-2.
- Höhle, J., & Höhle, M. (2009). Accuracy assessment of digital elevation models by means of robust statistical methods. *ISPRS Journal of Photogrammetry and Remote Sensing*, *64*, 398–406. doi:10.1016/j.isprsjprs.2009.02.003.
- Holzer, N., Vijay, S., Buchroithner, M. F., & Manjoi, A. K. (2012). Analysis of glacier mass balance and rheology of Kekesayi Glacier using Hexagon KH-9, ALOS-PRISM and SAR data. In *ESA Earth Observation and Cryosphere Science Conference Proceedings of extended abstracts*. 13–16.11.2012, Frascati, Italy: European Space Agency (ESA).
- Huss, M. (2013). Density assumptions for converting geodetic glacier volume change to mass change. *The Cryosphere*, *7*, 877–887. doi:10.5194/tc-7-877-2013.
- ICIMOD (2011). *Kailash Sacred Landscape Conservation Initiative: Feasibility Assessment Report*. International Centre for In-

- egrated Mountain Development (ICIMOD), Kathmandu, Nepal. URL: <http://lib.icimod.org/record/26968> ICIMOD technical publication.
- IGSNRR (2010). *Kailash Sacred Landscape Conservation Initiative, Feasibility Assessment Report of China*. Institute of Geographic Sciences and Natural Resources Research, Chinese Academy of Sciences (IGSNRR).
- Immerzeel, W. W., Pellicciotti, F., & Bierkens, M. F. P. (2013). Rising river flows throughout the twenty-first century in two Himalayan glacierized watersheds. *Nature Geoscience*, 6, 742–745. doi:10.1038/NGEO1896.
- IPCC (2013). *Climate Change 2013: The Physical Science Basis. Contribution of Working Group I to the Fifth Assessment Report of the Intergovernmental Panel on Climate Change*. Cambridge, United Kingdom and New York, NY, USA: Cambridge University Press.
- Kääb, A., Berthier, E., Nuth, C., Gardelle, J., & Arnau, Y. (2012). Contrasting patterns of early twenty-first-century glacier mass change in the Himalayas. *Nature*, 488, 495–498. doi:10.1038/nature11324.
- Kang, S., Xu, Y., You, Q., Flügel, W.-A., Pepin, N., & Yao, T. (2010). Review of climate and cryospheric change in the Tibetan Plateau. *Environmental Research Letters*, 5, 015101. doi:10.1088/1748-9326/5/1/015101.
- Kehrwald, N. M., Thompson, L. G., Tandong, Y., Mosley-Thompson, E., Schotterer, U., Alfimov, V., Beer, J., Eikenberg, J., & Davis, M. E. (2008). Mass loss on Himalayan glacier endangers water resources. *Geophysical Research Letters*, 35, 1–6. doi:10.1029/2008GL035556.
- Krieger, G., Moreira, A., Fiedler, H., Hajnsek, I., Werner, M., Younis, M., & Zink, M. (2007). TanDEM-X: A Satellite Formation for High-Resolution SAR Interferometry. *Geoscience and Remote Sensing, IEEE Transactions*, 45, 3317–3341. doi:10.1109/TGRS.2007.900693.
- Langley, K., Hamran, S.-E., Hogda, K., Storbald, R., Brandt, O., Hagen, J., & Kohler, J. (2007). Use of C-Band Ground Penetrating Radar to Determine Backscatter Sources Within Glaciers. *IEEE Transactions on Geoscience and Remote Sensing*, 45, 1236–1246. doi:10.1109/TGRS.2007.892600.
- Liao, J., Shen, G., & Huang, W. (2011). The response of lake variations to climate change in Tibetan Plateau in last 40 years. In *ASPRS Annual Conference*. 01.- 05.05.2011, Milwaukee, Wisconsin, USA.
- Miehe, G., Winiger, M., Böhner, J., & Zhang, Y. (2001). The climatic diagram map of High Asia. Purpose and Concepts. *Erdkunde*, 55, 94–97.
- Mölg, T., Maussion, F., & Scherer, D. (2013). Mid-latitude westerlies as a driver of glacier variability in monsoonal High Asia. *Nature Climate Change*, 4, 68–73. doi:10.1038/nclimate2055.
- Neckel, N., Braun, A., Kropáček, J., & Hochschild, V. (2013). Recent mass balance of the Purogangri Ice Cap, central Tibetan Plateau, by means of differential X-band SAR interferometry. *The Cryosphere*, 7, 1623–1633. doi:10.5194/tc-7-1623-2013.
- Neckel, N., Kropáček, J., Bolch, T., & Hochschild, V. (2014). Glacier mass changes on the Tibetan Plateau 2003 – 2009 derived from ICESat laser altimetry measurements. *Environmental Research Letters*, 9, 014009. doi:10.1088/1748-9326/9/1/014009.
- NRO (2011a). *Gambit and Hexagon Declassification Guidelines*. National Reconnaissance Office (NRO) Unites States. NRO approved for release 6 December 2011.
- NRO (2011b). *The Gambit Story*. National Reconnaissance Office (NRO) Unites States. NRO approved for release 17 September 2011.
- Nuth, C., & Kääb, A. (2011). Co-registration and bias corrections of satellite elevation data sets for quantifying glacier thickness change. *The Cryosphere*, 5, 271–290. doi:10.5194/tc-5-271-2011.
- Owen, L. A., Yi, C., Finkel, R. C., & Davis, N. K. (2010). Quaternary glaciation of Gurla Mandhata (Naimon'anyi). *Quaternary Science Reviews*, 29, 1817–1830. doi:10.1016/j.quascirev.2010.03.017.
- Paul, F. (2008). Calculation of glacier elevation changes with SRTM: is there an elevation dependent bias? *Journal of Glaciology*, 54, 945–946. doi:10.3189/002214308787779960.
- Paul, F., Barrand, N., Baumann, S., Berthier, E., Bolch, T., Casey, K., Frey, H., Joshi, S., Kononov, V., Bris, R. L., Mölg, N., Nosenko, G., Nuth, C., Pope, A., Racoviteanu, A., Rastner, P., Raup, B., Scharrer, K., Steffen, S., & Winsvold, S. (2013a). On the accuracy of glacier outlines derived from remote-sensing data. *Annals of Glaciology*, 54, 171–182. doi:10.3189/2013AoG63A296.
- Paul, F., Bolch, T., Kääb, A., Nagler, T., Nuth, C., Scharrer, K., Shepherd, A., Strozzi, T., Ticconi, F., Bhambri, R., Berthier, E., Bevan, S., Gourmelen, N., Heid, T., Jeong, S., Kunz, M., Lauknes, T. R., Luckman, A., Boncori, J. P. M., Moholdt, G., Muir, A., Neelmeijer, J., Rankl, M., VanLooy, J., & Niel, T. V. (2013b). The glaciers climate change initiative: Methods for creating glacier area, elevation change and velocity products. *Remote Sensing of Environment*, . doi:10.1016/j.rse.2013.07.043. In Press, Corrected Proof.
- Pfeffer, W., Arendt, A., Bliss, A., Bolch, T., Cogley, J., Gardner, A., Hagen, J.-O., Hock, R., Kaser, G., Kienholz, C., Miles, E., Moholdt, G., Mölg, N., Paul, F., Radic, V., Rastner, P., Raup, B., Rich, J., Sharp, M., & the Randolph Consortium, M. (2014). The Randolph Glacier Inventory: a globally complete inventory of glaciers. *Journal of Glaciology*, . Accepted for publication.
- Pieczonka, T., Bolch, T., & Buchroithner, M. (2011). Generation and evaluation of multitemporal digital terrain models of the Mt. Everest area from different optical sensors. *ISPRS Journal of Photogrammetry and Remote Sensing*, 66, 927–940. doi:10.1016/j.isprsjprs.2011.07.003.
- Pieczonka, T., Bolch, T., Wei, J., & Liu, S. (2013). Heterogeneous mass loss of glaciers in the Aksu-Tarim Catchment (Central Tien Shan) revealed by 1976 KH-9 Hexagon and 2009 SPOT-5 stereo imagery. *Remote Sensing of Environment*, 130, 233–244. doi:10.1016/j.rse.2012.11.020.
- Rabus, B., Eineder, M., Roth, A., & Bamler, R. (2003). The shuttle radar topography mission – a new class of digital elevation models acquired by spaceborne radar. *ISPRS Journal of Photogrammetry and Remote Sensing*, 57, 241–262. doi:10.1016/S0924-2716(02)00124-7.
- Racoviteanu, A. E., Paul, F., Raup, B., Khalsa, S. J. S., & Armstrong, R. (2009). Challenges and recommendations in mapping of glacier parameters from space: results of the 2008 Global Land Ice Measurements from Space (GLIMS) workshop, Boulder, Colorado, USA. *Annals of Glaciology*, 50, 53–69. doi:10.3189/172756410790595804.
- Reuter, H. I., Nelson, A., & Jarvis, A. (2007). An evaluation of void-filling interpolation methods for SRTM data. *International Journal of Geographical Information Science*, 21, 983–1008. doi:10.1080/13658810601169899.
- Rignot, E., Echelmeyer, K., & Krabill, W. (2001). Penetration depth of interferometric synthetic-aperture radar signals in snow and ice. *Geophysical Research Letters*, 28, 3501–3504. doi:10.1029/2000GL012484.
- Rodriguez, E., Morris, C. S., & Belz, E. J. (2006). A Global Assessment of the SRTM Performance. *Photogrammetric Engineering and Remote Sensing*, 72, 249–260.
- Rott, H. (2009). Advances in interferometric synthetic aperture radar (InSAR) in earth system science. *Progress in Physical Geography*, 33, 769–791. doi:10.1177/0309133309350263.
- Schwitzer, M. P., & Raymond, C. F. (1993). Changes in the longitudinal profiles of glaciers during advance and retreat. *Journal of Glaciology*, 39, 582–290.
- Shugar, D. H., Rabus, B. T., & Clague, J. J. (2010). Elevation changes (1949–1995) of Black Rapids Glacier, Alaska, derived from a multi-baseline InSAR DEM and historical maps. *Journal of Glaciology*, 56, 625–634. doi:10.3189/002214310793146278.
- Toutin, T. (2006). Generation of DSMs from SPOT-5 in-track HRS and across-track HRG stereo data using spatiotriangulation and autocalibration. *ISPRS Journal of Photogrammetry and Remote Sensing*, 60, 170–181. doi:10.1016/j.isprsjprs.2006.02.003.
- Vincent, C., Ramanathan, A., Wagnon, P., Dobhal, D. P., Linda, A., Berthier, E., Sharma, P., Arnaud, Y., Azam, M. F., Jose, P. G.,

- & Gardelle, J. (2013). Balanced conditions or slight mass gain of glaciers in the Lahaul and Spiti region (northern India, Himalaya) during the nineties preceded recent mass loss. *The Cryosphere*, *7*, 569–582. doi:[10.5194/tc-7-569-2013](https://doi.org/10.5194/tc-7-569-2013).
- Wagnon, P., Vincent, C., Arnaud, Y., Berthier, E., Vuillermoz, E., Gruber, S., Ménégoz, M., Gilbert, A., Dumont, M., Shea, J. M., Stumm, D., & Pokhrel, B. K. (2013). Seasonal and annual mass balances of Mera and Pokalde glaciers (Nepal Himalaya) since 2007. *The Cryosphere*, *7*, 1769–1786. doi:[10.5194/tc-7-1769-2013](https://doi.org/10.5194/tc-7-1769-2013).
- Yao, T., Thompson, L., Yang, W., Yu, W., Gao, Y., Guo, X., Yang, X., Duan, K., Zhao, H., Xu, B., Pu, J., Lu, A., Xiang, Y., Kattel, D. B., & Joswiak, D. (2012a). Different glacier status with atmospheric circulations in Tibetan Plateau and surroundings. *Nature Climate Change*, *2*, 663–667. doi:[10.1038/nclimate1580](https://doi.org/10.1038/nclimate1580).
- Yao, T., Thompson, L. G., Mosbrugger, V., Zhang, F., Ma, Y., Luo, T., Xu, B., Yang, X., Joswiak, D. R., Wang, W., Joswiak, M. E., Devkota, L. P., Tayal, S., Jilani, R., & Fayziev, R. (2012b). Third Pole Environment (TPE). *Environmental Development*, *3*, 52–64. doi:[10.1016/j.envdev.2012.04.002](https://doi.org/10.1016/j.envdev.2012.04.002).
- Ye, Q., Chen, F., Stein, A., & Zhong, Z. (2009). Use of a multi-temporal grid method to analyze changes in glacier coverage in the Tibetan Plateau. *Progress in Natural Science*, *19*, 861–872. doi:[10.1016/j.pnsc.2008.12.002](https://doi.org/10.1016/j.pnsc.2008.12.002).
- Ye, Q., Yao, T., Kang, S., Chen, F., & Wang, J. (2006). Glacier variations in the Naimona'nyi region, western Himalaya, in the last three decades. *Annals of Glaciology*, *43*, 385–389. doi:[10.3189/172756406781812032](https://doi.org/10.3189/172756406781812032).

Acknowledgements



This doctoral thesis has been written within the [WET](#) project, initiated by Dieter Scherer at the TU-Berlin. Thank you Dieter for making this great project possible. Also special thanks to Fabien and Julia who did a great job in coordinating things, whether in Germany or in Tibet. Furthermore I want to thank the whole [WET](#) group including Benny, Christoph, Eva, Frank, Jörg, 2 × Manfred, Marinka, Nicolai and Sophie. Last but not least I want to thank Tobias Bolch who agreed in correcting my thesis and helped me with a lot of effort on numerous glaciological and remote sensing related issues, thank you Tobias.

EBERHARD KARLS
UNIVERSITÄT
TÜBINGEN

On the Tübingen side I want to thank Volker Hochschild who provided me with an excellent work environment, financial support and a lot of remote sensing data. Special thanks to Jan Kropacek who helped me with several remote sensing related issues and initiated the great Halji expedition in 2013 and 2014. Also many questions were solved between climbing pitches and cold beer, thank you Jan. Furthermore I want to thank the whole Tübingen working group including Andi, Bernd, Christian, Felix, Gebhard, Geraldine, Hans, Joachim, Mansour and Sandy. Finally, I want to thank Ilka Weikusat and Erwin Appel for attending my defense.